VENEZUELA-MEM/USA-DOE FOSSIL ENERGY REPORT IV-11

DOE/BC-00/2/SP
OSTI ID: 753416

SUPPORTING TECHNOLOGY FOR ENHANCED OIL RECOVERY

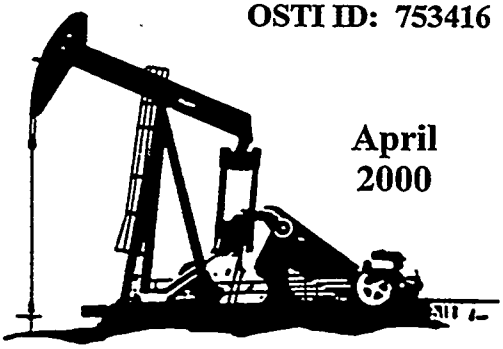

April
2000

EOR THERMAL PROCESSES

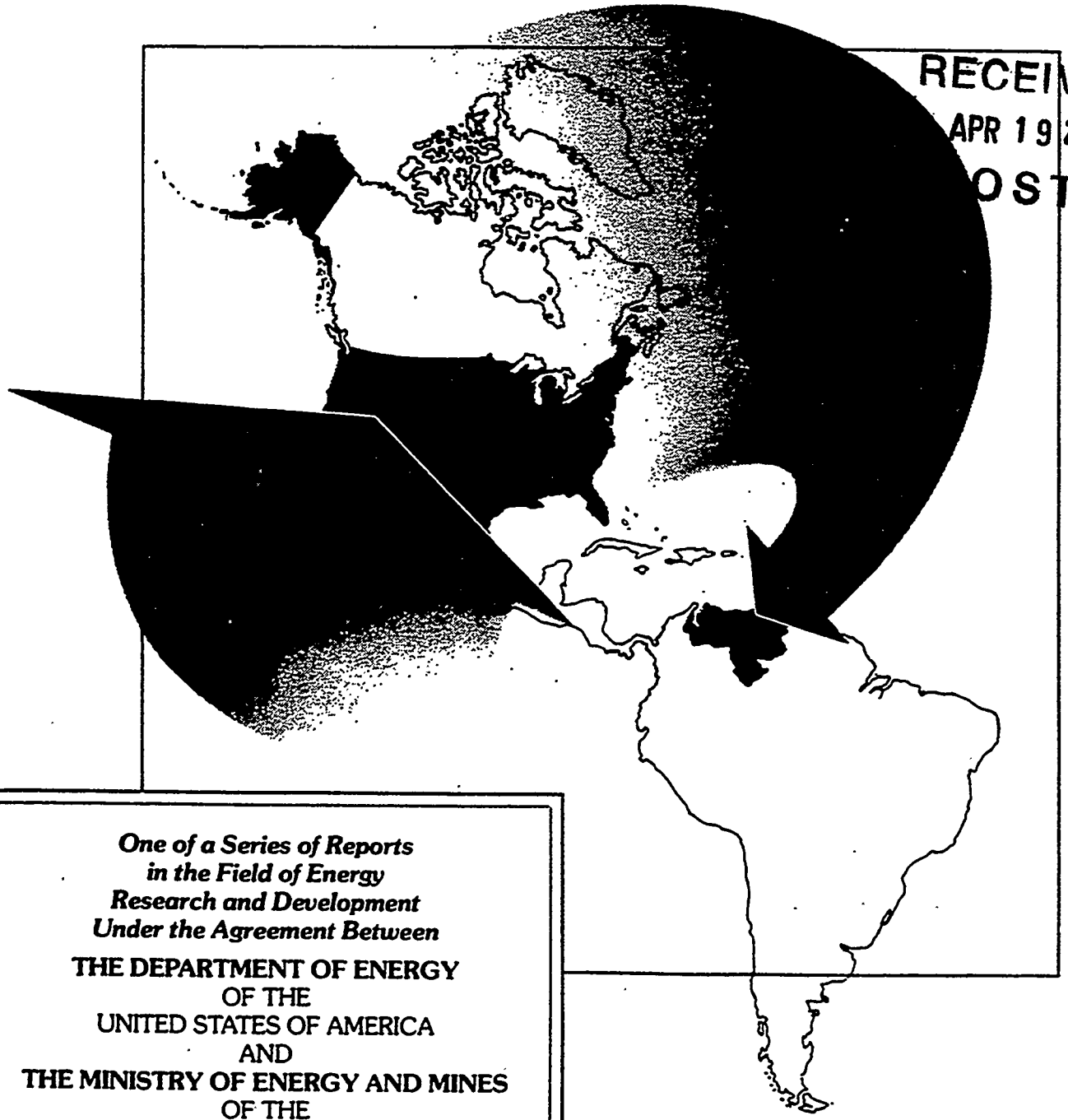

One of a Series of Reports
in the Field of Energy
Research and Development
Under the Agreement Between

THE DEPARTMENT OF ENERGY
OF THE
UNITED STATES OF AMERICA
AND
THE MINISTRY OF ENERGY AND MINES
OF THE
REPUBLIC OF VENEZUELA

DOE/BC-00/2/SP
OSTI ID: 753416
Distribution Category UC-122

ELEVENTH AMENDMENT AND EXTENSION TO

Annex IV-ENHANCED OIL RECOVERY THERMAL PROCESSES

THE DEPARTMENT OF ENERGY OF THE UNITED STATES OF AMERICA

And

THE MINISTRY OF ENERGY AND MINES OF THE REPUBLIC OF VENEZUELA

Submitted By:

Thomas B. Reid, Project Manager
Thermal Recovery/Novel Technology
National Petroleum Technology Office
U.S. Department of Energy

Alexandor Izequeido, Manager
Heavy/Extra Heavy Crude
PDVSA INTEVEP, S.A.
Filial de Petroleos de Venezuela, S.A.

Approved By:

Donald A. Juckett
U.S. Department of Energy
1000 Independence Avenue
Washington, DC 20585

Francisco Simonpietri
Minister of Energy and Mines
Caracas 1010A, Venezuela

United States Department of Energy

PREFACE

An Agreement between the Department of Energy of the United States of America and the Ministry of Energy and Mines of the Republic of Venezuela try cooperate in Energy Research and Development was signed March 6, 1980. The abject of cooperation under the DOE/MEM Agreement was to promote a balanced exchange of energy technologies and to conduct joint projects in the area of Petroleum, Solar Energy, Hydroelectric Energy, and Coal.

This Agreement supported the Agreement for Scientific and Technological Cooperation between the two countries which was signed by the Secretary of State of the U.S.A. and the Minister of Foreign Relations of Venezuela on January 11, 1980.

On October 13, 1997, a second Agreement was signed by the Secretary of Energy of the U.S.A.. and the Minister of Energy and Mines of the Republic of Venezuela to expand the information exchange to include energy efficiency, renewable energy, and policy maters. encompass the original Agreement .

The original DOE/MEM Agreement was supplemented by six annexes to describe specifically the work to be done. Over the past seventeen years, additional annexes have been signed, resulting in a total of seventeen annexes to date. The Agreement has been extended to October 12, 2007. The annexes are:

I. Joint Characterization of Heavy Crude Oils
II. Supporting Research in the Area of Enhanced Oil Recovery
III. Evaluation of Past and Ongoing Enhanced Oil Recovery Projects in the U.S and Venezuela
IV. Enhanced Oil Recovery Thermal Processes
V. Oil Drilling, Coring, and Telemetry
VI. Residual Oil Saturation
VII. Petroleum Products Utilization and Evaluation
VIII. Coal Preparation, Combustion, and Related Technology
IX. Subsidence Due to Fluid Withdrawal
X. On-Site Training of Petroleum Engineers
XI. Energy Conservation
XII. Geochemistry (Oil Generation, Migration, and Accumulation)
XIII. Microbial Enhanced Oil Recovery
XIV. Exchange of Energy Related Personnel
XV. Oil Recovery Information and Technology Transfer
XVI. Oil arid Petrochemical Ecology and Environmental Research
XVII. Drilling Technology

Each of these annexes has a document describing the work to be done as part of the cooperation. Amendments and Extension to the Annexes are provided for in the Agreement

Currently, severs annexes are active (Annexes I, II, X, XIV, XV, XVI, and XVII) and ten annexes have been completed (Annexes I, II, III, V, VI, VII, IX, XI, XII, and XIII). The Agreement is in force until October 12, 2007.

CONTENTS

ABSTRACT

This report contains the results of efforts under the six task of the Tenth Amendment anti Extension of Annex IV, Enhanced Oil Recovery Thermal Processes of the Venezuela/USA Energy Agreement. This report is ;resented in sections (for each of the six Tasks) and each section contains one or more reports that were prepared to describe the results of the effort under each of the Tasks.

A statement of each Task, taken from the Agreement Between Project Managers, is presented on the first page of each section. The Tasks are numbered 68 through 73. The first through tenth report on research performed under Annex IV (Venezuela MEM/USA-DOE Fossil Energy Report Number IV-1. IV-2, IV-3, IV-4, IV-5, IV-6, IV-7, IV-8, IV-9, IV-10 contain the results of the first 67 Tasks. These reports are dated April 1983, August 1984, March 1986, July 1987, November 1988, December 1989, October 1991, February 1993, March 1995, and December 1997, respectively.

Task 68 — DOE shall provide INTEVEP with results from the SUPRI research on heavy oil. This includes flow properties studies, in-situ combustion, foam flow in porous media, and reservoir evaluation methods. In situ upgrading through thermal methods will be part of Task 68.

1.1 EFFECTS OF TEMPERATURE ON MULTIPHASE RELATIVE PERMEABILITY

(S. Akin)

1.1.1 INTRODUCTION

Production of oil from petroleum reservoirs usually involves simultaneous flow of two or more immiscible fluids through a porous rock. Multiphase flow in porous media is a complex process that depends on a number of factors including the absolute permeability, pressure drop, capillary pressure, fluid viscosities, and relative permeabilities of each phase. Of these, the relative permeability is probably the most important parameter determining reservoir performance. For modeling thermal recovery processes for heavy oil recovery, one needs to know not only the relative permeabilities at the original reservoir temperature, but also the changes expected at higher temperatures. Over the past three decades, a number of experimental studies have reported contradictory temperature effects on two phase relative permeabilities in porous media. Most experiments were performed on consolidated rocks, and only a few studies used reservoir cores and crude oils.

The reasons for divergence among experimental multiphase relative permeability data may be summarized as follows:

1. Errors in saturation measurements.
2. Errors caused by neglect of capillary pressure end effects.
3. Wettability variations with differing oils and brines.
4. Assumptions made to develop experimental procedures or calculations.
5. Inadequacy of mathematical models to represent multiphase flow conditions.

It is clear that unless the above problems can be overcome, a better understanding of the effects of temperature on relative permeabilities will not be achieved. Therefore careful, unsteady state, relative permeability experiments at differing temperatures were conducted and reported here. Two phase saturation profiles along an unconsolidated core were measured using computerized tomography (CT) which is a reliable and accurate means of measuring local saturations. A black oil simulator, coupled with a global optimization code was then used to estimate two-phase relative permeabilities. Experimental saturation profiles, differential pressure and recovery data were used in a least squares manner in the numerical model. Heterogeneity effects were considered in the simulations by using CT calculated porosity values along the core.

1.1.2 LITERATURE REVIEW

Relative permeability is the basis used to predict multiphase flow through porous media. It is an empirical concept which allows Darcy's Law to be generalized for multiple phases (Honarpour, 1986). This is done by assuming that the absolute permeability, used in Darcy's Law, may be replaced by a term which contains both the absolute permeability and a "relative permeability" which is a function of the fluid saturation. For a two phase system (oil and water), the flow equations are given as:

$$u_o = -\frac{k k_{or}}{\mu_o}\left(\nabla p_o - \rho_o \frac{g}{g_c}\right) \tag{1}$$

$$u_w = -\frac{k k_{wr}}{\mu_w}\left(\nabla p_w - \rho_w \frac{g}{g_c}\right) \tag{2}$$

where u_i is the flow velocity, k is the absolute permeability, kr_i is the relative permeability, μ_i is the dynamic viscosity, ∇p_i is the gradient of the pressure, ρ_i is the density. In these equations, i represents oil or water, g is the gravitational acceleration, and g_c is the universal constant in Newton's Law. Three differing absolute (base) permeabilities are commonly used: the absolute air permeability, the absolute water permeability, and the permeability to oil at reservoir connate water saturation. Throughout this report water permeability will be used.

Although the concept of relative permeability is simple, the measurement and interpretation of relative permeability versus saturation is not. For example, there is evidence that relative permeability may be a function of many more parameters than fluid saturation (Honarpour, 1986). Temperature, flow velocity, saturation history, wettability changes and the mechanical and chemical behavior of the matrix material may all play roles in changing the functional dependence of relative permeabilities on saturation. The best defined of these dependencies is the variation of relative permeability with saturation history; relative permeability curves show hysteresis between drainage (wetting phase decreasing) and imbibition (wetting phase increasing).

A common use of relative permeability data is in numerical simulators. These data are fundamental parameters necessary in all simulations. However, numerical simulation of thermal recovery processes also requires knowledge of its temperature dependence. Often, relative permeabilities measured at ambient conditions are used to predict performance at higher temperatures, which in turn, may lead to erroneous results.

Over the last three decades, a number of laboratory studies have appeared in the literature on the effects of temperature on relative permeability and residual oil saturation as well as irreducible water saturation. Edmondson (1965) found a reduction in residual oil saturation in Berea cores as the temperature increased. Using refined oils and an unsteady state experimental technique, he noted that the relative permeability ratio of oil to water shifted toward a higher water saturation as the temperature increased.

Poston *et al.* (1970) investigated the effects of temperature on unconsolidated sand using refined oils. They reported that irreducible water saturation increased, and the residual oil saturation decreased with increasing temperature. Moreover, they concluded that relative permeabilities to both oil and water increased with increasing temperature.

Contradicting previous researchers, two studies (Sufi *et al.,* 1982 and Miller and Ramey, 1985) conducted at Stanford University reported temperature independent relative permeability data obtained from unsteady state experiments in unconsolidated and Berea cores using refined oils. Miller and Ramey (1985) noted various artifacts such as; material balance errors, viscous instability, clay migration, wettability alteration by miscible cleaning methods, and capillary pressure end effects, that may have affected former conclusions on the effect of temperature on relative permeability data.

Closmann *et al.* (1985) used the steady state technique to measure altered, unaltered and deasphalted tar and brine relative permeabilities at elevated temperature using frozen Peace River cores. They concluded that at higher temperatures tar and water relative permeability curves shifted toward lower water saturations.

Maini and Batcyky (1985) conducted unsteady state experiments at temperatures ranging from room temperature to 522°F using a frozen core from a heavy-oil reservoir, and stock tank oil and formation brine from the same reservoir. They measured the absolute permeability to formation water using a transient pressure decay test, and used history matching calculations to obtain relative permeabilities. They concluded that, irreducible water saturation increased and residual oil saturation decreased with increasing temperature until an optimum temperature. Moreover, they reported that relative permeability to oil decreased and the relative permeability to water remained unchanged with increasing temperature.

Polikar *et al.* (1986) used the steady state technique to measure the relative permeability of Athabasca bitumen using unconsolidated Ottawa sand as the porous medium. Their results showed no significant effect of temperature on relative permeability and saturation data up to 392°F.

Maini and Okazawa (1987) analyzed unsteady state experiments conducted on an unconsolidated silica sand using Bodo stock tank oil and deionized water. They history matched production and differential pressure data to obtain relative permeability curves. They concluded that the most reliable data they obtained was at residual oil saturation after 3 pore volumes of fluid injected. They observed increasing relative permeability to water with increasing temperature.

Unlike the previous researchers, Watson and Ertekin (1988) studied the effect of temperature gradient on relative permeability measurements using the steady state technique. They found that different temperature gradients caused differences in both the irreducible water saturation and residual oil saturations. This suggested that the fired Berea cores became increasingly water-wet, and unfired cores became increasingly oil wet, during imbibition and drainage. Moreover, they concluded that relative permeabilities to both oil and water decreased with increasing temperature. They also observed that the absolute water permeabilities of fired Berea sandstone cores were unaffected by temperature.

Polikar *et al.* (1990) conducted both steady-state and unsteady-state relative permeability experiments to find out the effects of temperature on relative permeability. Using Athabasca bitumen and deionized water, they used the JBN technique to analyze their results. They observed no significant temperature effects on relative permeability of either phase, nor in the residual oil and irreducible water saturations. They attributed the small changes seen to the heterogeneity effect. Moreover, they reported that steady-state and unsteady-state techniques resulted in similar relative permeability curves with little differences.

More recently, Muqeem *et al.* (1993) conducted steady state two phase and three phase relative permeability experiments at 75°C and 125°C using an unconsolidated silica sand with refined oil, brine and nitrogen gas. The measured relative permeabilities showed no significant temperature effect.

Kumar and Inouye (1994) used the JBN technique to analyze unsteady state relative permeability experiments conducted at differing temperatures. They tried to obtain low temperature analogues to high temperature relative permeability data. They concluded that relative permeability data obtained at ambient conditions can be used for high temperatures as long as the viscosity ratios and the wettabilities are similar. They also reported that residual oil saturation and irreducible water saturation are independent of temperature and are a function of viscosity ratio.

The results obtained from the aforementioned studies are summarized in Table 1. It can be observed that, because of the experimental duration and convenience, most of the researchers preferred to use unsteady-state experiments. The relative permeability data were obtained by interpreting such experiments either with the JBN technique or by one dimensional finite difference computer history matching. Moreover, most experiments were performed on consolidated rocks, and only a few studies used reservoir cores and crude oils.

The reasons for divergence of experimental multiphase relative permeability data may be summarized as follows:

1. Errors in saturation measurements.
2. Errors caused by neglect of capillary pressure end effects.
3. Wettability variations with differing oils, and brines.
4. Assumptions made to develop experimental procedures or calculations.
5. Inadequacy of mathematical models to represent multiphase flow conditions.

It is clear that, unless the problems stated above are overcome, a better understanding of the effects of temperature on relative permeabilities will not be achieved.

1.1.3 APPLICATION OF THE UNSTEADY-STATE RELATIVE PERMEABILITY ESTIMATION TECHNIQUE TO HEAVY OIL SYSTEMS

The principal objective of this section is to examine whether or not a Buckley-Leverett type displacement model could be used describe the megascopic behavior of unstable displacements (and to see if it is possible to do so by adjusting the relative permeability curves to account for viscous instabilities). To achieve this goal, several unstable immiscible displacements were simulated. These were conducted to analyze a possible effect of temperature on relative permeabilitiy curves reported by Sufi *et al.* (1982). It should be noted that the selection is based solely on the availability and the quality of the data. The level of instability in those experiments were quantified by a dimensionless stability number, N_{is} proposed by Peters and Flock (1981).

$$N_{is} = \frac{(M-1)(V-V_c)\mu_w d^2}{N_w k_{wor} \sigma} \qquad (3)$$

Table 1. A Summary of the Recent Experimental Investigations of Temperature Effects on Relative Permeability.

Reference	Experimental Technique	Fluids	Core	Temperature Range	Saturation Measurement	End Point Saturation	Relative Permeability
Edmondson, 1965	Unsteady State (Welge)	Refined Oils (No 5 & 15)	Berea (1382°F)	room-500°F	graduated cylinders	$S_{or}\downarrow$ T↑	shifted
Sufi et al., 1982	Unsteady State (JBN)	Refined Oil	Unconsolidated Ottawa (170-200)	room-250°F	photo cell + frequency counter	independent	independent
Miller & Ramey, 1985	Unsteady State (JBN)	Refined Oil (Blandol)	Unconsolidated Ottawa (100-200) + Berea (932°F)	room-300°F	separator + graduated cylinders	independent	independent
Closmann et al., 1985	Steady State	Altered-unaltered-deasphalted tar	Frozen Peace River Cores	385°F	electrical resistance	np	k_{rw} shifted to lower S_w
Maini & Batcyky, 1985	Unsteady State (History Matching)	Stock Tank Oil	Frozen Core from a Hvy Oil Res	room-522°F	separator + fractional collector	S_{wir}r↑ T↑ $S_{or}\downarrow$ T↑ (until T_{opt} transverse)	$k_{ro}\downarrow$ T↑ $k_{rw}\rightarrow$ T↑
Polikar et al., 1986	Steady State	Athabasca Bitumen	Unconsolidated Ottawa (~200)	room-482°F	material balance	independent	independent below 392°F
Maini & Okazawa, 1987	Unsteady State (History Matching)	Bodo Stock Tank Oil+3.5% ether	Unconsolidated Silica Sand (140-170)	room-392°F	separator + fractional collector	np	k_{rw}↑ T↑ $k_{ro}\downarrow$↑ T↑
Watson & Ertekin, 1988	Steady State	Refined Oil (Soltrol 170)	Berea (1832°F) + unfired	room-300°F	material balance	S_{wir}r↑ T↑	k_{ro}, $k_{rw}\downarrow$ T↑
Polikar et al., 1990	Steady & Unsteady State (JBN)	Athabasca Bitumen	Unconsolidated Silica Sand (170-230)	212°F-482°F	material balance	independent	independent
Muqeem et al. 1993	Steady State	Refined Oil+N2	Unconsolidated Silica Sand (140-200)	167°F&257°F	separator	np	independent
Kumar & Inouye, 1994	Unsteady State (JBN)	Refined Oil-Drakeol 19-G.E. Silicon Oil-San Joaquin Valley Hvy Oil-GulfLight+SJV	Unconsolidated preserved cores + Berea (925°F)	room-300°F	graduated cylinders	independent	shifted

In this equation M refers to end point mobility ratio, V is superficial velocity (m/s or ft/s), V_c is characteristic velocity (m/s or ft/s), μ_w is oil viscosity (m Pa s or cp), d is core diameter (m or ft), N_w is dimensionless wettability number, k_{wor} is the permeability to water at residual oil saturation (m^2 or darcy), and σ is interfacial tension (mN/m or dyne/cm). According to Peters and Flock (1981), a core flood will be stable (no viscous fingering) if the dimensionless stability number is less than 13.56. The stability numbers and the properties of the porous medium and the fluids used in the experiments reported by Sufi *et al.* (1982) are presented in Tables 2 and 3. It can be observed that even at a high temperatures the core floods have high instability numbers. Therefore all the core floods reported should have suffered from significant viscous fingering. However, capillary end effects were found to be minimum as the scaling coefficient proposed by Rapoport and Leas (1953) were higher than the critical (i.e. $Lu\mu_w$,ft-ft/s-cp is greater than 3.5) for all experiments.

Table 2. Properties of Porous Medium and Fluids Used by Sufi *et al* (1982).

Porous Medium	Fluid Properties
Ottawa Sand (mesh 170-	Oil used is Kaydol (equivalent to Chevron
Permeability, k = 5.3	Viscosity at °70 F = 220 cp
Porosity, ϕ = 0.394	Density at °70 F = 0.878 gm/cc
Length, L = 17.8 cm	Water used is distilled and de-mineralized
Diameter, d = 2.54 cm	Viscosity at °70 F = 0.97 cp
	Density at °70 F = 1.00 gm/cc

A black oil simulator, ECLIPSE 100, was used to simulate the experimental conditions given in Table 2. Three dimensional, radial geometry was used to simulate the experiments as shown in Fig 1. To account for viscous fingers center grids have smaller diameter compared to the outer ones* . The first and last grid planes in the z direction had higher transmissibility compared to other grids to reproduce the experimental inlet and outlet lines together with spider-web shaped end plates .

*This type of grid was selected to compare CT images during the experiments which will be seen in the following sections.

Table 3. Stability Numbers for Different Experiments with No Initial Water Saturation as Reported by Sufi *et al.* (1982)

Experiment	1	2	3
Temperature, °F	70	122	150
Stability Number$_s$	40167	6650	3174

Buckley-Leverett type relative permeability estimation techniques use production and pressure differential history across the core collected during displacements in linear core floods. Unsteady-state relative permeability data is then computed by applying the JBN technique (Johnson *et al.*, 1959) or the graphical equivalent proposed by Jones and Roszelle (1978). The JBN technique is based on the solution of the three equations given below:

$$f_o = \frac{1}{1+\frac{k_{rw}\mu_o}{k_{ro}\mu_w}} = \frac{dN_p}{dW_i} \tag{4}$$

$$S_{w2} = S_{wi} + N_p - W_i f_o \tag{5}$$

$$\frac{f_o}{k_{ro}} = \frac{d\left(\frac{1}{W_i I_r}\right)}{d\left(\frac{1}{W_i}\right)} \tag{6}$$

In these equations f is the fractional flow, k_{ro} and k_{rw} are the relative permeabilities to oil and water, S_w is saturation of brine, N_p and W_i are the oil produced and brine injected in terms of pore volumes, and I_r is the relative injectivity. The data required are pressure drop across the core and produced volumes of fluids as functions of volume injected.

Figure 2 gives the comparison of the saturation distributions at 0.193PV of water injected obtained from simulations of three different temperatures (70, 122, and 150°F) at four different locations along the core with a zero initial water saturation. It can be observed that the front is not stable, and moreover, the fingering pattern is visible in the center of the core. It should be noted that the same set of relative permeability curves were used to generate these data.

The relative permeability curves obtained using the JBN analysis are compared to the input curves in Fig 3. It can be observed that although the same relative permeability curves were used to simulate at different temperatures, different apparent relative permeability curves were obtained using the JBN technique. Interestingly, the resulting relative permeability curves show a false temperature dependence. That is to say, there is a considerable increase in relative permeability to oil and a decrease in relative permeability to water at a constant saturation as temperature increases. This false temperature dependence agrees with the general trend that oil and water relative permeability curves shift to the right as reported in studies by Sinnokrot (1969), Weinbrandt et al. (1975), and others. Moreover, these false findings agree with the concept of decreased residual oil saturation with a temperature increase.

Three more hypothetical experiments were simulated to see the effect of initial water saturation. The stability numbers were much smaller compared to the no initial water saturation case, as observed in Table 4. In these cases, the calculated relative permeability curves did not show a false temperature effect, but failed to find the input relative permeability curves as shown in Fig 4. Similar to the previous case, the calculated residual oil saturation decreased with a temperature increase.

Table 4. Stability Numbers for Different Experiments with 10% Initial Water Saturation as Reported by Sufi *et al.* (1982)

Experiment	1	2	3
Temperature, °F	70	122	150
N_{is}	582.3	96.4	46.0

The above findings clearly show that JBN, and like techniques, can not be used to determine heavy oil - water relative permeability curves, and can lead to erroneous results. It seems that the viscous instability effects get smaller if the core is initially saturated with water. Another important finding is that the JBN technique also leads to a false temperature effect.

Another common technique used to estimate relative permeability curves is one dimensional history matching. To estimate relative permeability curves with the history matching or parameter estimation approach, an objective function is constructed as a weighted sum of squared differences between the measured data and calculations from a one dimensional mathematical model of the experiment. For a typical displacement experiment, the measured data might consist of the pressure drops across the core, the recoveries of the displaced phase, and the internal saturation profiles. Then, the objective function, J, can be expressed as:

$$J=\sum_{i=1}^{N} W_{pi}\left(\Delta P_i^{obs}-\Delta P_i^{cal}\right)^2+\sum_{i=1}^{N} W_{qi}\left(Q_{t\,i}^{obs}-Q_{t\,i}^{cal}\right)^2+\sum_{k=1}^{M}\sum_{i=1}^{N} W_{si}\left(S_{i,k}^{obs}-S_{i,k}^{cal}\right)^2 \qquad (7)$$

In the above equation, P is pressure, Q is cumulative production, S is saturation, and the W_i' s are the inverses of the variances of the experimental measurement errors which will give the maximum-likelihood (minimum-variance) estimates of the parameters (Akin, 1997). A single set of data (i.e., pressure profiles) or more than one set of data (pressure, production, saturation profiles) may be used in a history matching procedure.

To see the effects of viscous instability we also used this technique to analyze the hypothetical data generated before. In this study, the numerical reservoir simulator used is the well known black oil simulation code ECLIPSE 100 by Geoquest (1995), and the optimization code is a version of the simulated annealing process developed by Goffe *et al.* (1994). The computer code requires an input data file, and an output data file for execution. The input data file is basically divided into two parts: initialization and recurrent data sections. The initialization data consists of model grid dimensions and geometry, distribution of porosity and permeability, PVT data, and initial pressure and saturation distributions, as well as the solution method and various run parameters. The recurrent data include well data and the time step control information. In this study, the input data file is modified such that relative permeability and capillary pressure data are controlled within the optimization code as unknowns to be found. One other change with the simulator is the usage of extra output files

that produce time dependent pressure and production data as well as saturation profiles. These data files are then used by the optimization code so that Eq. 7 can be used.

By using a one-dimensional radial grid definition, the same hypothetical, aforementioned data were used to generate relative permeability curves by matching the pressure and production response at ambient temperature. Figure 5 compares the estimated relative permeability curves with the input data. Note that the water relative permeability curve agrees with the input curve at low to moderate water saturations but becomes higher at higher water saturations. This is probably due to short duration of the hypothetical experiment, where water saturations never exceeded 0.6. However, the computed oil relative permeability curve is lower then the input curve. Therefore, it can be concluded that one dimensional history matching is not producing correct relative permeability curves when viscous fingering is present. Another history matching was carried out using a two dimensional radial grid to find out whether there would be any improvement. The water relative permeability curve did not change much, but the oil curve seemed to improve as seen in Fig 5. Therefore it was concluded that two dimensional history matching produced better results then the one dimensional history match.

1.1.4 EXPERIMENTAL APPARATUS AND PROCEDURE

High temperature relative permeability experiments require core holders and sleeves that can be used at high temperature and pressure. The SUPRI CT laboratory now has a high temperature and high pressure core holder shown in Fig 6. It consists of an aluminum outer shell with internal adjustable centralizers which hold and centralize a high temperature and pressure, 1 3/4 in ID, and 16 in long aluminum core sleeve. The core sleeve can operate safely up to 482°F and 1000 psi. With its current design the core holder is suitable for CT monitored high temperature experiments using a heating circulator.

Two successful experiments were conducted and analyzed, using South Belridge sand and oil. Table 5 gives the average reservoir properties of the South Belridge field. Oil viscosities, brine viscosities and oil-water viscosity ratios are given in Figs 7 through 9 as functions of temperature.

Table 5. Properties of South Belridge Sand and Fluids Used in the Experiments.

Porous Medium	South Belridge sand Reservoir Temperature ~ 30°C 0.5-10Darcies 30-35% porosity
Oil	South Belridge oil 13 - 15 °API 0.96 - 0.98 gm/cc
Water	De-ionized water + 8%KBr

The same experimental procedure was used in all experiments. After packing the core holder, it is placed on the positioning system and vacuumed to less than 200 mtorr. Following that, a total of 18 reference dry scans were taken using 1 in spacing between slices. The sand pack is then flooded with several pore volumes of South Belridge oil ensuring 100% oil saturation. Reference oil saturated images were taken at the same locations and porosity of the sand pack was calculated. Figure 10 gives a three dimensional reconstruction of the porosity images in Run 1. The average porosity of this sand pack was about 31%. Brine was then injected at a fixed rate of 2ml/min, which was high enough to minimize capillary end effects, as the Rapoport and Leas number was greater than 3.5 CT scans at prescribed locations were taken at different times and these were used to calculate saturation distributions along the sand pack. After a run is finished at ambient temperature, temperature is increased to 122°F and CT scans are again taken at different times. This part of the experiment was continued until oil production ceased. After that, temperature was increased to 150°F and the above procedure is repeated.

1.1.5 METHOD OF SOLUTION

The pressure, saturation and production data collected during the ambient part of the experiment are used to calculate heavy oil - water relative permeability curves using the aforementioned two dimensional history matching procedure. Then, using these relative permeability curves, the rest of the experiment was simulated for the higher temperature data.

There are two possible outcomes of this procedure:

1. Both parts of the data (i.e. cold and hot) are matched by using only one set of relative permeability curves, which would indicate that the flow functions do not depend on temperature.
2. The algorithm fails to represent both parts of the experimental data (i.e. cold and hot) using a single set of relative permeability curves, which would indicate that the flow functions depend on temperature.

A hypothetical heavy oil - water relative permeability run is simulated using the above procedure. A single set of relative permeability curves was used to generate "no temperature effect" pressure, production and saturation profiles. Then, the optimizer-simulator is used to obtain relative permeability curves using the cold part of this hypothetical experiment. Figures 11 - 13 give the pressure, production and saturation profile fits to both cold and hot parts of the hypothetical experiment. Although there are some minor differences between the input and fitted data, a general agreement is observed. There is also good agreement with the input relative permeability curves, as observed in Fig 14. This hypothetical example shows that the proposed technique can be used to find the effect of temperature on flow functions.

1.1.6 RESULTS AND DISCUSSION

The results of two experiments (one with zero initial water saturation, the other with 30% initial water saturation) will be presented in this section. Figure 15 gives saturation images obtained for the experiment with an initial water saturation of 30%. The injection port is on the right and the production port is on the left of these images. There is a 2 cm spacing between successive images. The top two lines correspond to images taken during the ambient part of the experiment whereas the third and fourth line corresponds to images taken at 122°F and 150°F. Viscous fingers are clearly visible as small circular sections. Figure 16 gives the

reconstruction of these saturation images on the x-plane. It can be observed that brine is initially flowing at the bottom of the sand pack for the cold part of the experiment. But as time goes by and the temperature of the system is increased, there is a general brine saturation increase throughout the sand pack. However, brine is still flowing in its own finger structures.

Figures 17 and 18 give the pressure fit and the relative permeability curves used to fit the data using the numerical model. Although the pressure curve is rather noisy a general agreement with the model of the experiment is observed at ambient and at 122°F. Initially, the fit seems to be rather poor. This can be explained with the sensitivity of the least squares minimization process. An alternative may be the use of "the least absolute value" technique which is not sensitive to data outliers. Another interesting point is that, the pressure curve is slightly different for the 150°F part of the experiment. The pressure fit does not seem to be reproducing the experimental trend especially at late time. We do not have an explanation for this problem. So returning to the original hypothesis that states "if both parts of the experimental data (i.e. cold and hot) are matched using only one set of relative permeability curves then the flow functions do not depend on temperature", we can conclude that relative permeability is not a function of temperature for the temperature range studied. However, it is clear that more experiments are needed to clarify this phenomenon accurately.

Another experiment was conducted to see the effect of temperature on heavy oil - water relative permeability curves. Unfortunately, this experiment failed, because of a tubing and core holder failure. In this case, there was no initial water saturation. Probably, the heavy oil plugged the outlet tubing and eventually pressure increased to a level above the burst pressure of the tubing. Figure 19 gives the CT calculated saturation distribution along the core just before the failure. This saturation data is completely different than the previous experiment. Fingering is also present. However, the fingers are larger than the previous experiment. The inlet end seems to be totally swept and the length of the swept area is rather short. There is a main finger structure that continuously decrease in diameter (width) from inlet to the outlet of the sand pack.

1.1.7 NOMENCLATURE

Roman

f	:	Fractional flow
g	:	Gravitational acceleration
k	:	Relative permeability
u	:	Darcy velocity
I	:	Relative injectivity
J	:	Objective function
M	:	Number of grids
N	:	Production or number of data points
Q	:	volume of displaced phase recovered
Δp	:	Pressure differential across the core
∇p	:	Pressure gradient
S	:	Wetting phase saturation, fraction
W	:	Pore volumes injected or weighing factor

Greek

μ	: Viscosity
ρ	: Density

Subscripts and superscripts

cal	:	Calculated
exper	:	Experimental
i, j, k	:	Indices
iter	:	Iteration
model	:	Model
o	:	Oil
obs	:	Observed
p	:	Produced
scale	:	Scale
w	:	Water
w2	:	End point

1.1.8 REFERENCES

1. Akin, S. : "Application of Computerized Tomography to the Determination of Three Phase Relative Permeabilities," Phd dissertation, Middle East Technical University, Ankara, Turkey, Jan 1997.
2. Closmann, P. J., Waxman, M. H., and Deeds, C. T.: "Steady-State Tar/Water Relative Permeabilities in Peace River Cores at Elevated Temperature," paper SPE 14227 presented at 60th Annual Technical Conference and Exhibition of Society of Petroleum Engineers held in Las Vegas, USA, Sept. 22-25, 1985.
3. Edmondson, T. A.: "Effect of Temperature on Waterflooding," J. Cdn. Pet. Tech. (Oct. - Dec. 1965) 236-42.
4. Goffe, Ferrier and Rogers : "Global Optimization of Statistical Functions with Simulated Annealing," Journal of Econometrics, vol. 60, no. 1/2, Jan./Feb. 1994, 65-100.
5. Honarpour, M., Koederitz, L., and Harvey, A. H .:"Relative Permeability of Petroleum Reservoirs," CRC Press, Boca Raton , Florida, 1986.
6. Johnson, E.F., Bossler, D. P., and Naumann, V. O. :"Calculation of Relative Permeability From Displacement Experiments," Trans. AIME (1959) 216, 61-63.
7. Kumar, M., and Inouye, T. A.: "Low-Temperature Analogs of High-Temperature Water/Oil Relative Permeabilities," paper SPE 28616 presented at 69th Annual Technical Conference and Exhibition of Society of Petroleum Engineers held in New Orleans, USA, Sept. 25-28, 1994.
8. Maini, B. B., and Batycky, J. P.: "Effect of Temperature on Heavy-Oil/Water Relative Permeabilities and Vertically Drilled Core Plugs," JPT (Aug. 1985) 1500-1510.
9. Maini, B. B., and Okazawa, T.: "Effect of Temperature on Heavy Oil-Water Relative Permeability of Sand," J. Cdn. Pet. Tech. (May - June 1987) 33-41.
10. Miller, M. A., and Ramey, H. J. Jr.: "Effect of Temperature on Oil/Water Relative Permeabilities of Unconsolidated and Consolidated Sands," JPT (Dec. 1985) 945-953.
11. Muqeem, M., Bentsen, R., and Maini, B.: "Effect of Temperature on Three-Phase Water-Oil-Gas Relative Permeabilities of Unconsolidated Sands," paper 5593-03 presented at the 5th Petroleum Conference of the South Saskatchewan Section, the Petroleum Society of CIM, held in Regina, Canada, Oct. 18-20, 1993.

12. Peters, E.J. and Flock, D.L. :"The Onset of Instability During Two-Phase Immiscible Displacement in Porous Media" Soc. Pet. Eng. J.(April, 1981) 249-258.
13. Polikar, M., Ali, F. S. M., and Puttagunta, V. R.: 'High Temperature Relative Permeabilities for Athabasca Oil Sands," SPE Res. Eng. (Feb. 1990) 25-32.
14. Polikar, M., Ferracuti, F., Decastro, V., Puttagunta, V. R., and Ali, F. S. M.: 'Effect of Temperature on Bitumen-Water End Point Relative Permeabilities and Saturations," J. Cdn. Pet. Tech. (Sep. - Oct. 1986) 44-50.
15. Poston, S. W., Israel, S., Hossain, A. K. M. S., Montgomery III, E. F. and Ramey, H. J. Jr.: "The Effect of Temperature on Irreducible Water Saturation and Relative Permeability of Unconsolidated Sands," Soc. Pet. Eng. J. (June, 1970) 171-180.
16. Rapoport, L. A., and Leas, W. J.: "Properties of Linear Waterfloods," J. Pet. Tech. (May 1953) 139-48.
17. Sinnokrot, A.A., Ramey, H.J.Jr., and Marsden, S.S,Jr. :"Effect of Temperature Level upon Capillary Pressure Curves," Soc. Pet. Eng. J. (March 1971) 13-22.
18. Sufi A. H., Ramey, H. J. Jr., and Brigham, W. E.: "Temperature Effects on Relative Permeabilities of Oil-Water," paper SPE 11071 presented at 57th Annual Fall Technical Conference and Exhibition of Society of Petroleum Engineers held in New Orleans, USA, Sept. 26-29, 1982.
19. Watson, R. W., and Ertekin, T.: "The Effect of Steep Temperature Gradient on Relative Permeability Measurements,' paper SPE 17505 presented at the SPE Rocky Mountain Regional Meeting held in Casper, WY, USA, May 11-13, 1988.
20. Weinbrandt, R.M., Ramey, H.J.Jr., and Casse, F.J. :"The Effect of Temperature on Relative and Absolute Permeability of Sandstones," Soc. Pet. Eng. J. (Oct. 1975) 376-84.

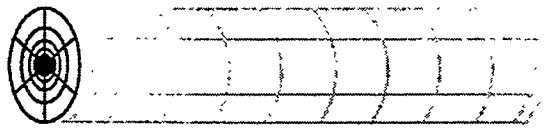

Figure 1. Grid System Used for Simulating Experiments by Sufi et al. (1982).

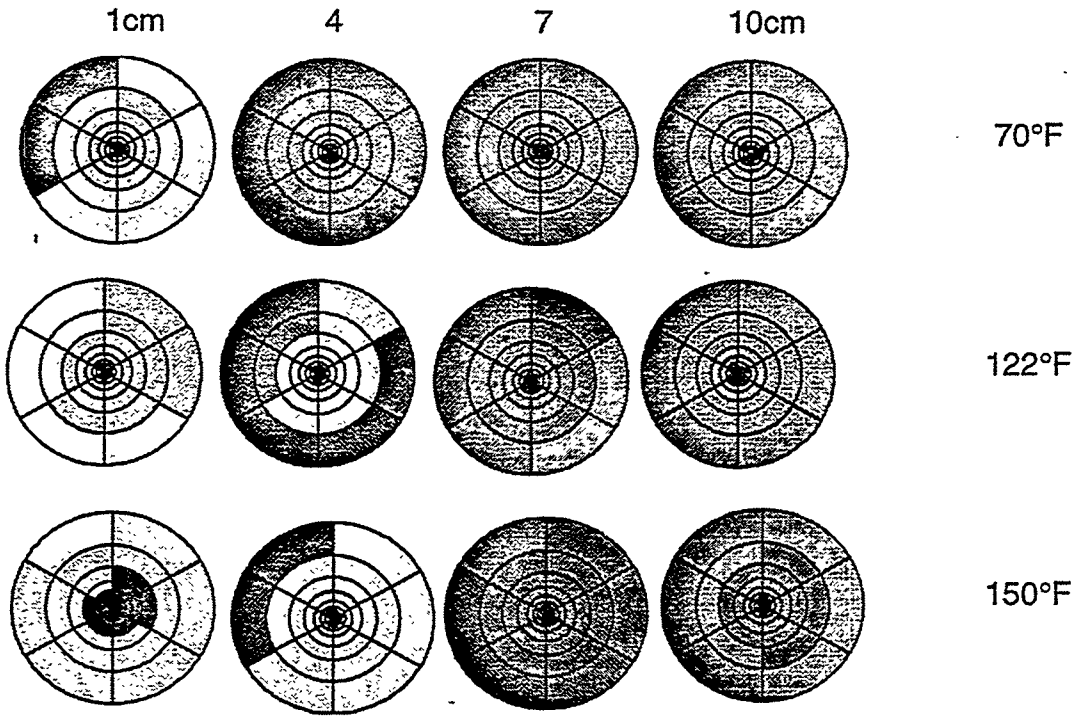

Figure 2.Comparison of Saturation Distributions at Different Temperatures.

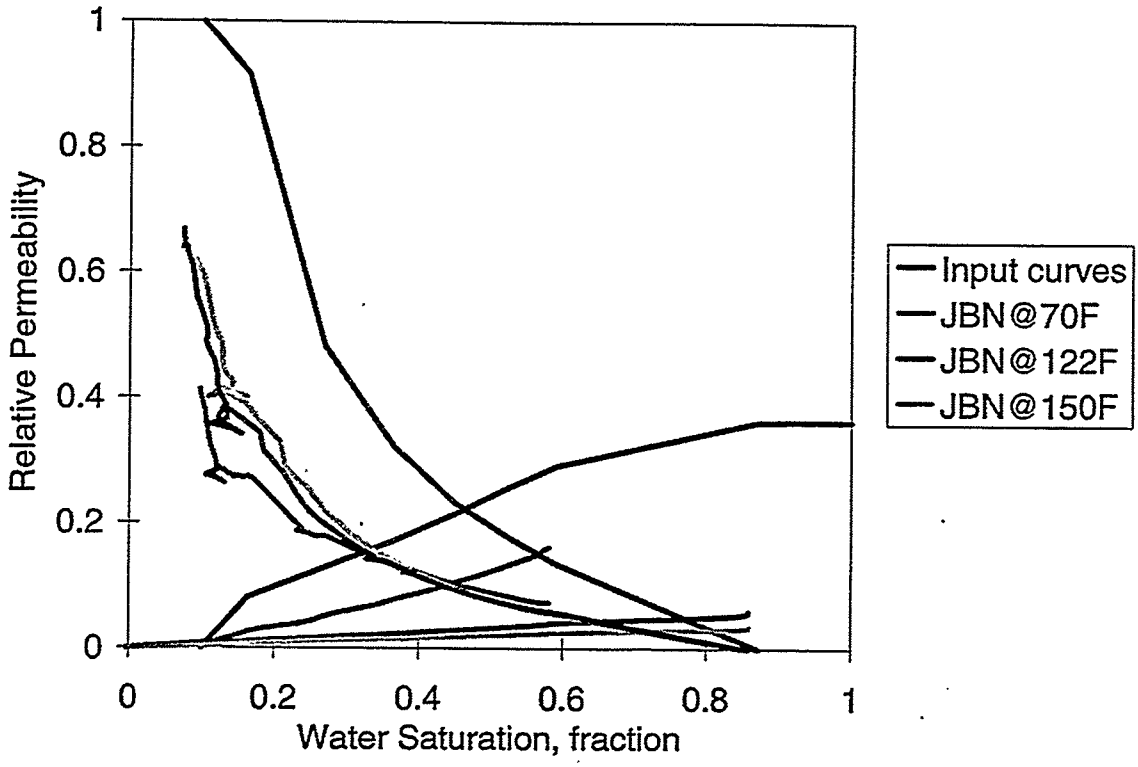

Figure 3. Comparison of JBN Relative Permeability Curves to Input Relative Permeability Data (No Initial Water Saturation).

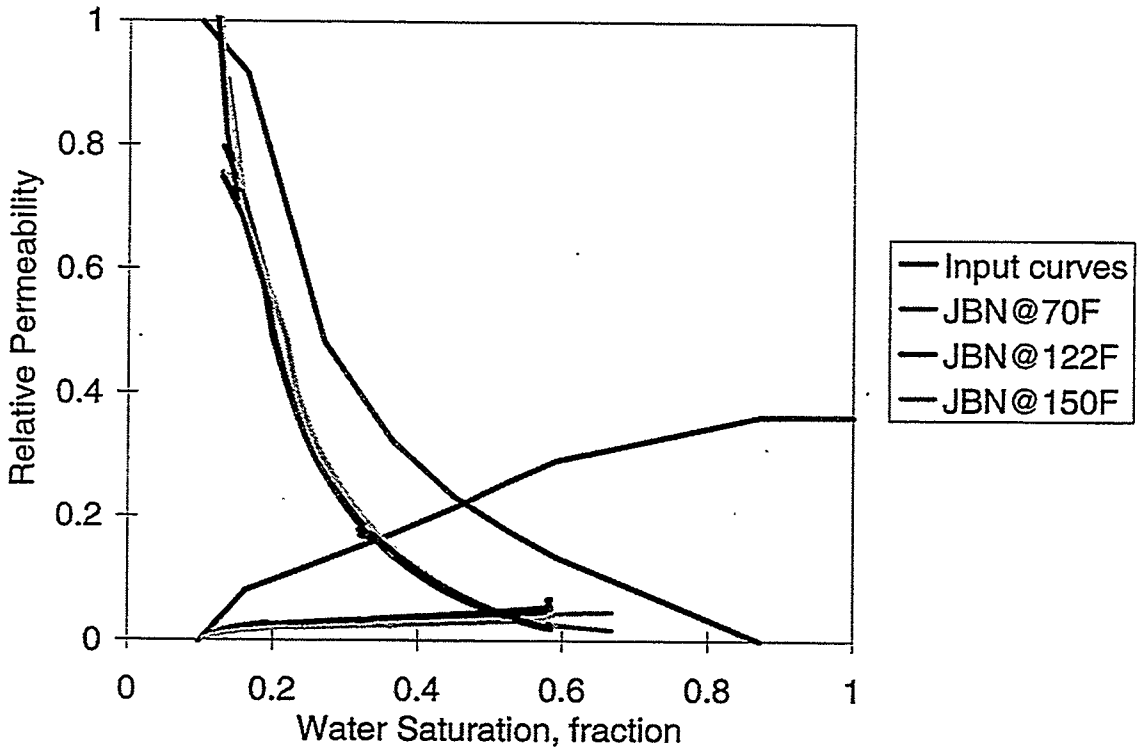

Figure 4. Comparison of JBN Relative Permeability Curves to Input Relative Permeability Data (Initial Water Saturation is 10%).

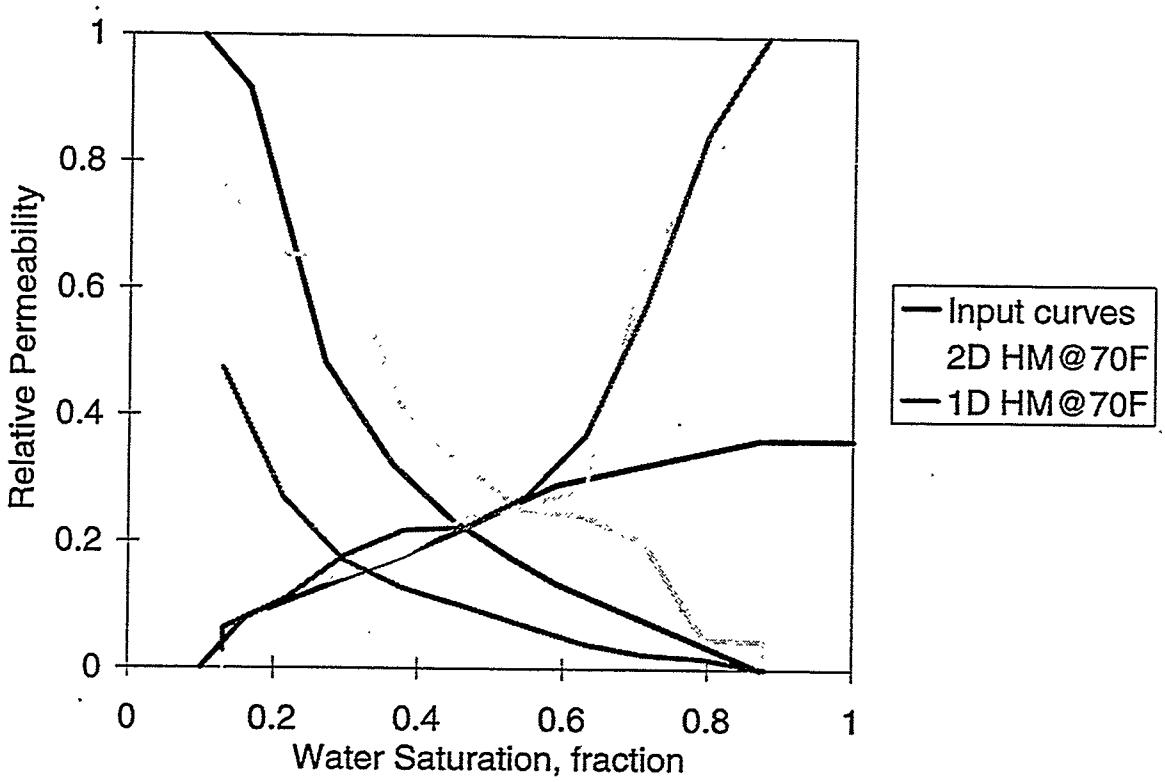

Figure 5. Comparison of 1D and 2D History Matched Relative Permeability Curves to Input Relative Permeability Data (No Initial Water Saturation).

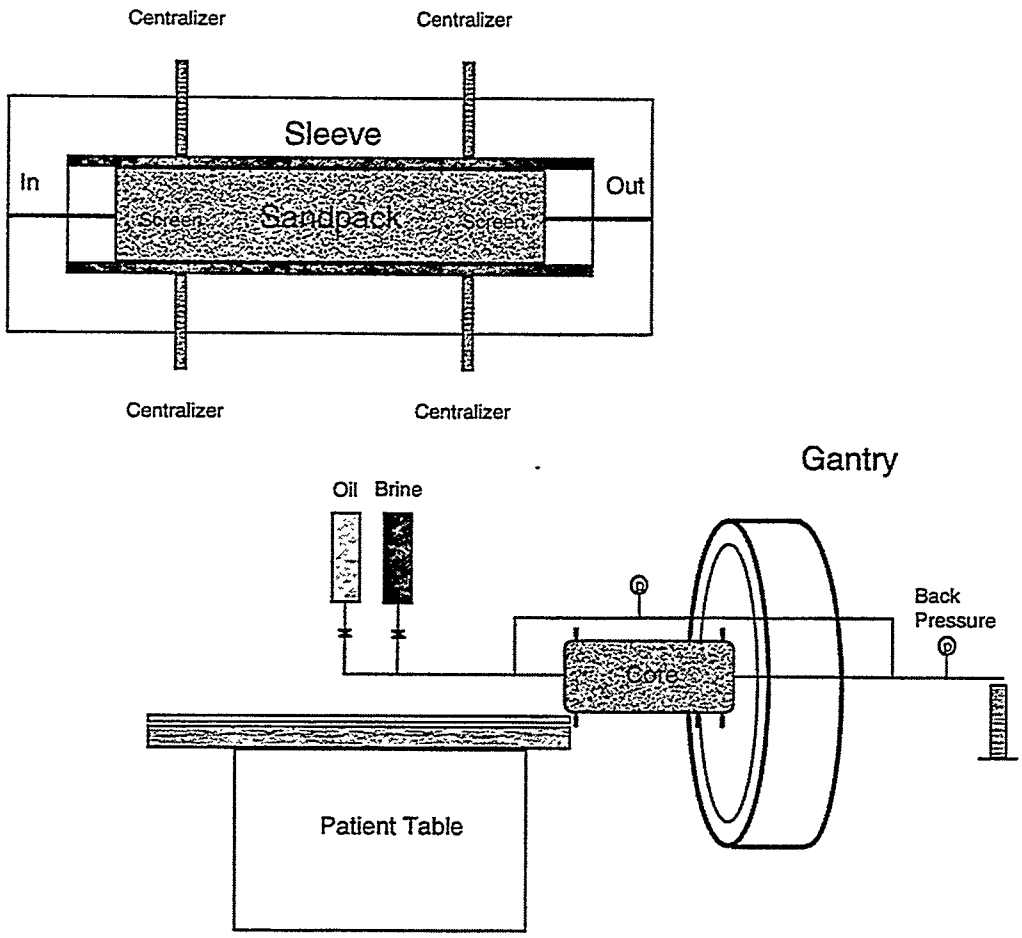

Figure 6. Schematic Diagram of the Experimental Setup.

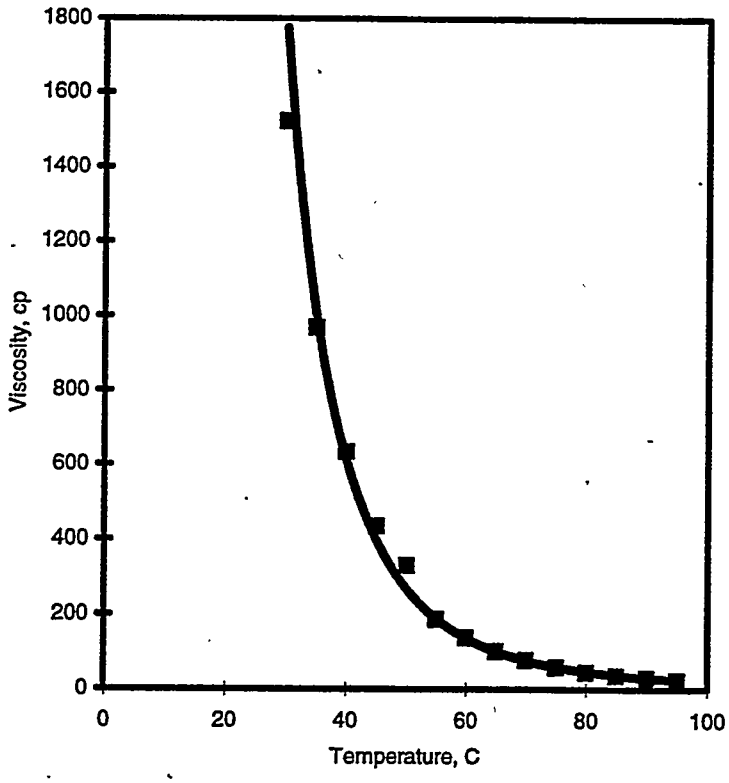

Figure 7. South Belridge Heavy Oil Viscosity Versus Temperature.

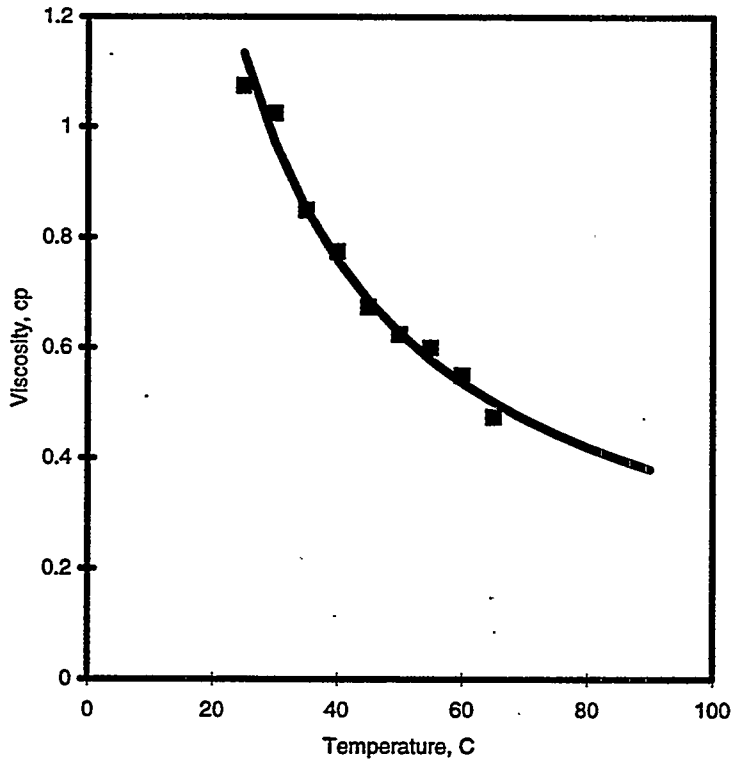

Figure 8. 8% Sodium Bromide Water Viscosity Versus Temperature.

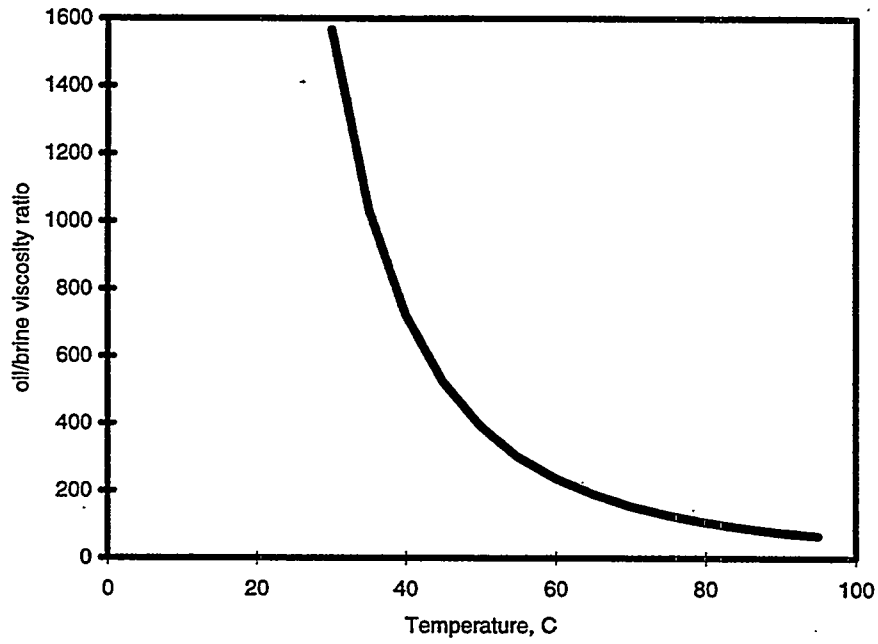

Figure 9. South Belridge Oil - Brine Viscosity Ratio Versus Temperature.

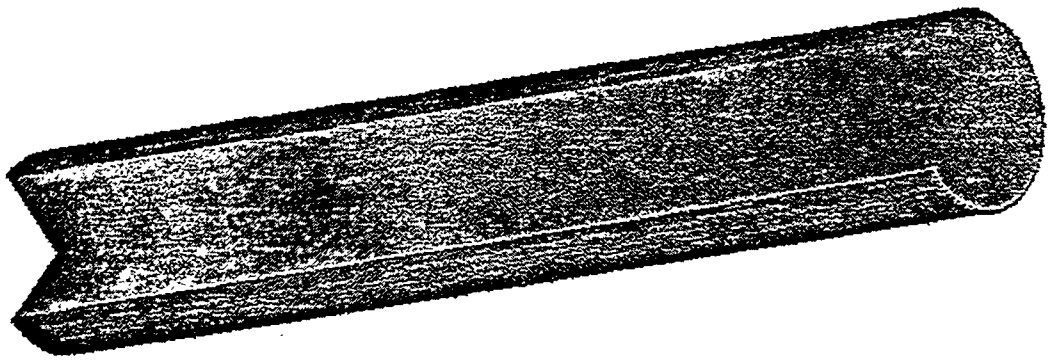

Figure 10. Three Dimensional Reconstruction of Porosity Images in Run 1.

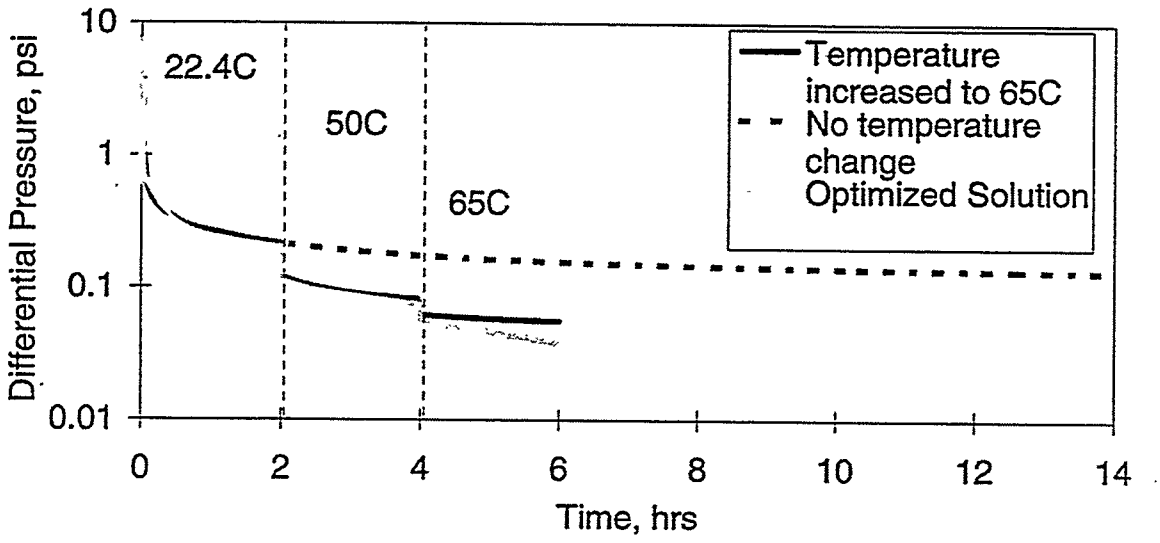

Figure 11. Differential Pressure Fit to Hypothetical "No Temperature Effect" Run.

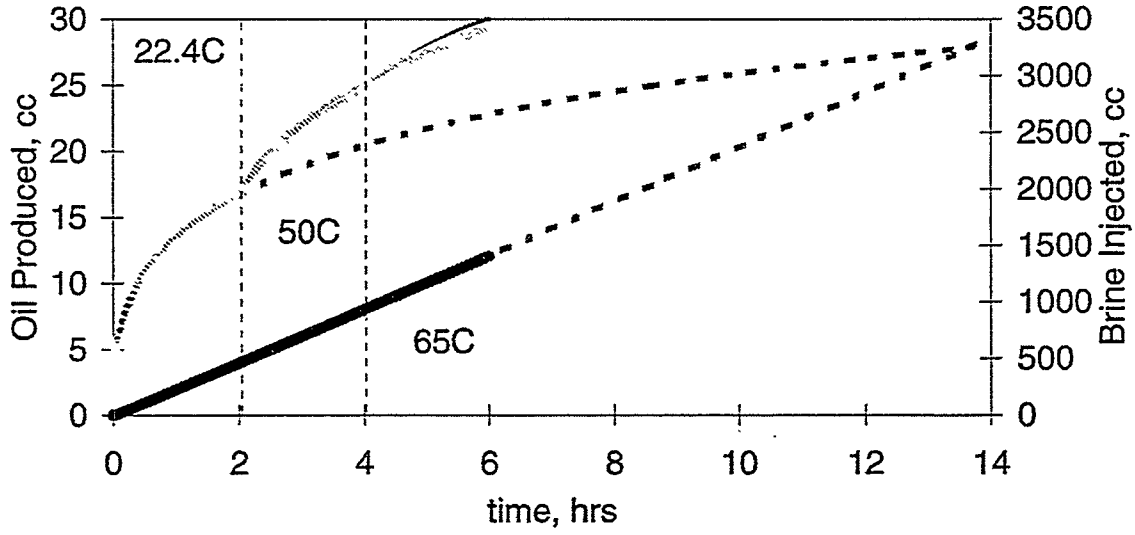

Figure 12. Production Fit to Hypothetical "No Temperature Effect" Run.

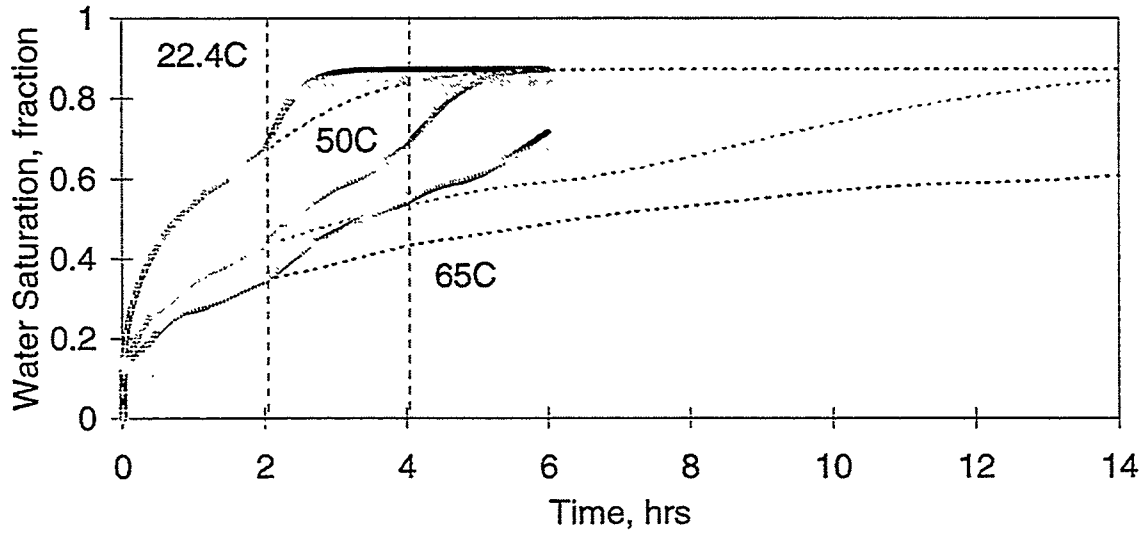

Figure 13. Saturation Fit to Hypothetical "No Temperature Effect" Run.

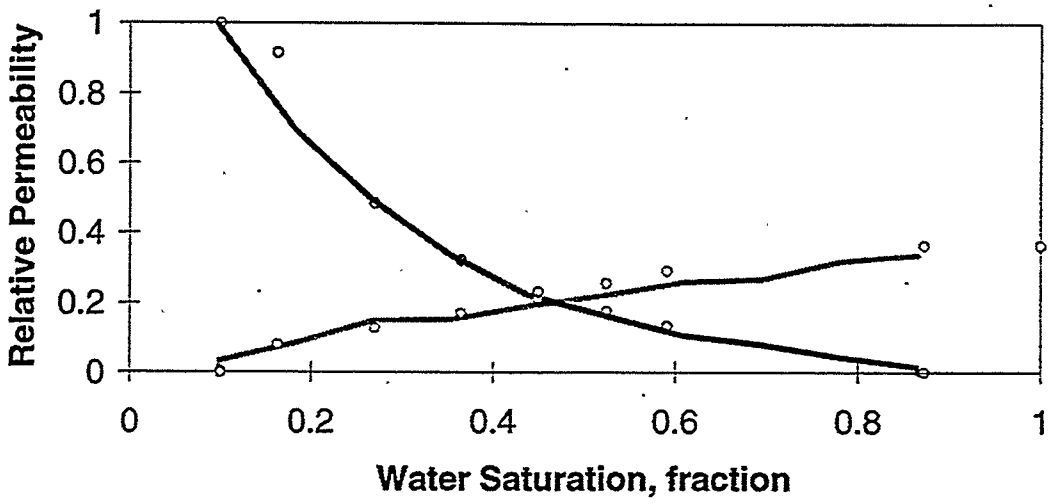

Figure 14. Relative Permeability Fit to Hypothetical "No Temperature Effect" Run.

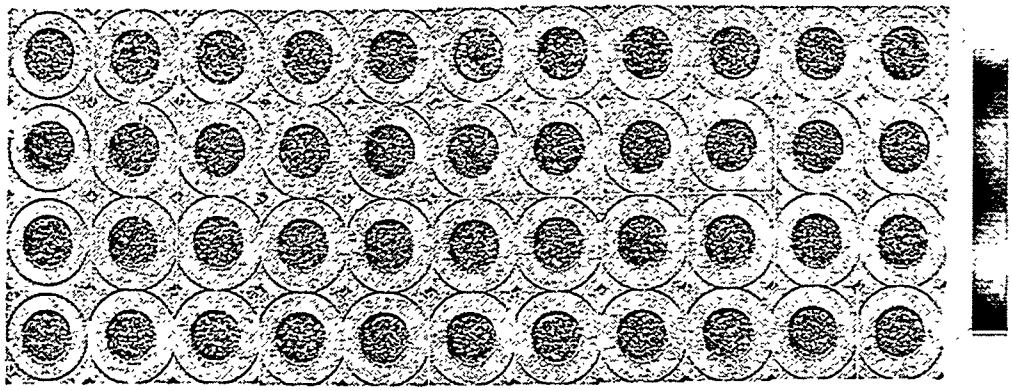

Figure 15. Water Saturation Images in Run 1.

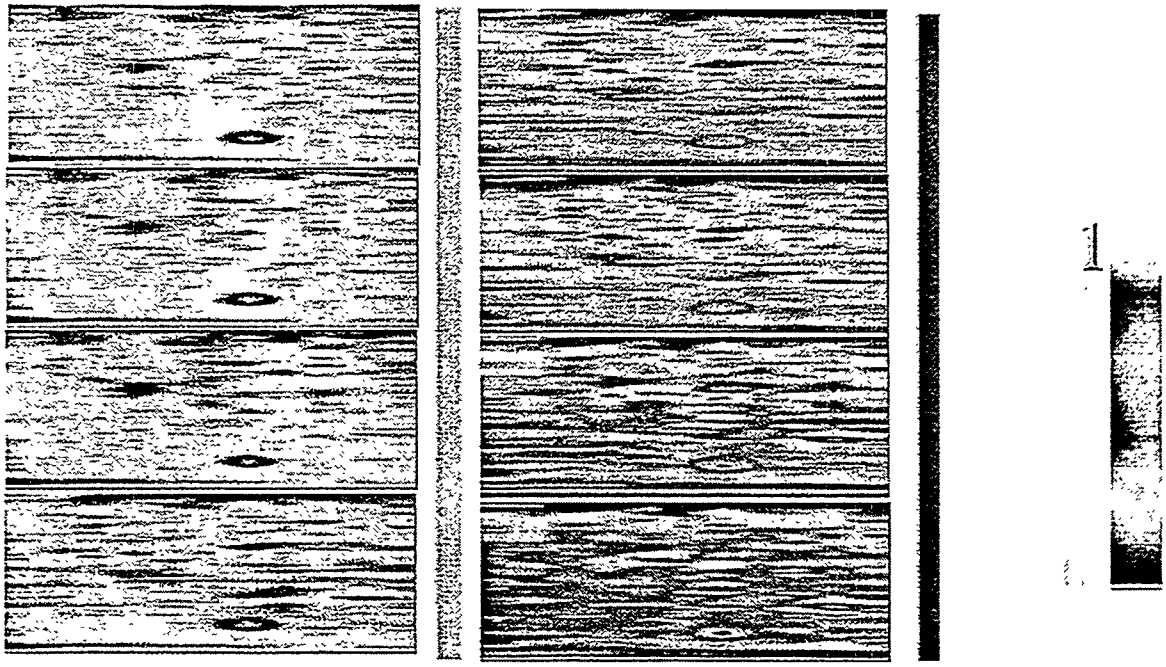

Figure 16. Three Dimensional Water Saturation Images in Run 1.

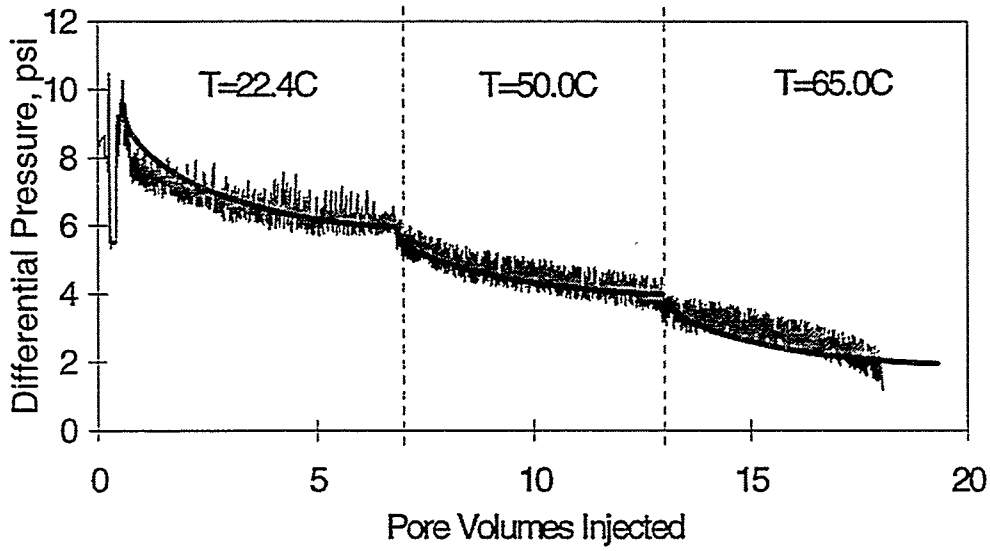

Figure 17. Pressure Fit For Run 1.

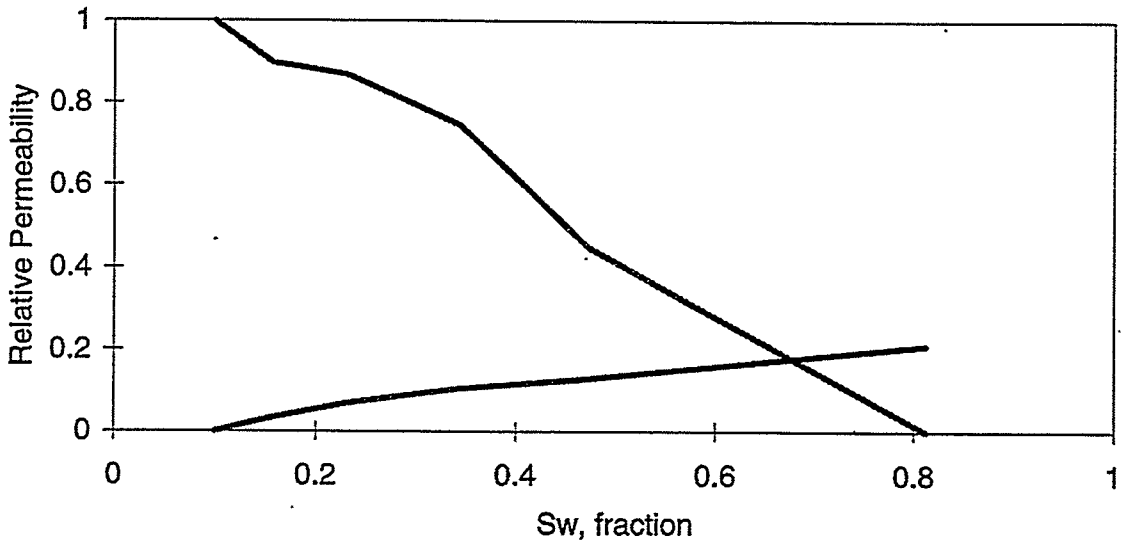

Figure 18. Relative Permeability Curves For Run 1.

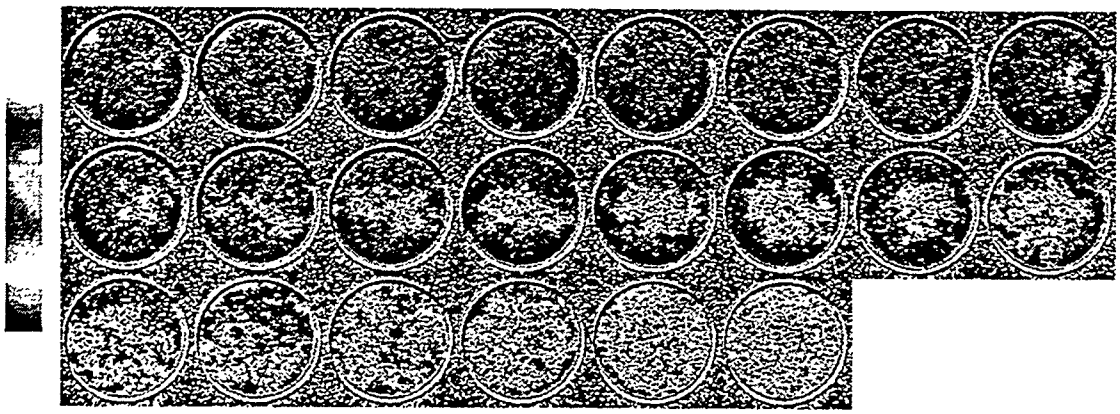

Figure 19. Water Saturation Images in Run 2.

1.2 TWO-PHASE FLOW EXPERIMENTS IN FRACTURED POROUS MEDIA USING CT SCANNER

(E. Rangel-German)

1.2.1 ABSTRACT

The fluid transfer parameters between rock matrix and fracture are not well known. Consequently, simulation of fractured reservoirs uses, in general, very crude and unproved hypotheses such as zero capillary pressure in the fracture and/or relative permeability linear with saturation. In order to improve the understanding of flow in fractured media, an experimental study was conducted and numerical simulation of the experiments were made.

A laboratory flow apparatus was built to obtain data on water-air imbibition and oil-water drainage displacements in horizontal single-fractured block systems. For this purpose, two configurations have been used: a two-block system with a 1mm spacer between the blocks, and a two-block system with no spacer. During the experiments, porosity and saturation measurements along the cores have been made utilizing an X-ray Computerized Tomography (CT) scanner. Saturation images were reconstructed in 3-D to observe how matrix-fracture interactions occurred. Differences on fluid saturations and relative permeabilities caused by changes on fracture width have also been analyzed.

In the case of water-air imbibition, the thin fracture system showed a more stable front and faster breakthrough than the wide fracture system. However, the final water saturation was higher in the blocks near the wide fracture, thus showing that capillary pressure in the narrow fracture has more effect. During oil-water drainage, oil saturations were higher in the blocks near the thin fracture, again showing the effect of fracture capillary pressure. Oil fingering was observed in the wide fracture. Fine grid simulations of the experiments using a commercial reservoir simulator have been started. Relative permeability and capillary pressure curves will be obtained by history matching the experiments. The preliminary results showed that the assumption of fracture relative permeability equal to phase saturation is incorrect. We found that the processes are both capillary and viscous dominated. The matrix capillary pressure obtained by matching an experiment showed lower values than reported in the literature. However, we have yet to complete the simulation study to be sure of these preliminary conclusions.

1.2.2 INTRODUCTION

Fractured porous media are usually divided into two systems: a matrix system that contains most of the fluid storage, and a fracture system where fluids can flow more easily. Under this assumption, flow equations are written considering that recovery is dominated by the transfer of fluid from the matrix to the high conductivity fractures which are also often entirely responsible for flow between blocks and flow to wells. The purpose of this study is to investigate this problem both experimentally and by numerical simulation.

The flow through fractured media depends on some mechanisms (e.g., imbibition, drainage, snap-off, piston like flow) that can be studied by means of both numerical analysis and experimental work. Although some people have already worked on the problem, no one knows exactly which mechanisms occur and how strongly they affect results. We know that a better understanding of the physical mechanisms and the parameters that influence flow through fractured porous media leads to more accurate results from simulator calculations.

To obtain more data on parameters such as capillary pressure, fracture relative permeabilities and/or saturation distributions, we need further experimental work. Most of the first experimental studies tried to represent single block reservoirs with artificial fractured models where the actual fracture distribution was known.

Detailed measurements of pressure, rate and saturation distribution, as the test were being performed, were recorded and attempts to measure phase distribution inside the fracture were also made using a computerized tomography (CT Scanner). This research resulted in a much better handle on the physical processes that occur when two and three phases flow in a fractured system, compared to previous studies such as Guzman and Aziz (1993) or Hughes (1995).

Our first step was reconstructing an apparatus capable of emulating the functions done by that built by Hughes (1995). Thus, we ran similar experiments using two of the coreholders used by him in order to verify that this new experiment gives proper results. Once the apparatus was tested, we ran multiphase flow experiments using an 8% NaBr brine solution as the wetting phase and decane as the nonwetting. Three stages in each experiment were completed: study of water imbibing into a dry core, decane displacing water in a water saturated core; and, water displacing oil.

1.2.3 LITERATURE REVIEW

Most of the early studies focused on the representation of reservoirs by means of single reservoir blocks. Most of the time these studies have relied on the sparse experimental data in the literature (Mattax and Kyte, 1962; Kleppe and Morse, 1974; Kazemi and Merrill, 1979) to verify their models; however those experiments provided rough approximations of the recovery obtained in the actual reservoirs. Later on, experimental work was focused on understanding of mechanisms that control the flow of fluids in porous media (Horie *et al.* 1988; Firoozabadi and Hauge, 1990; Labastie, 1990; Firoozabadi and Markeset, 1992). Hughes (1995) discusses these experiments in detail. From the most recent experiments, we can see that most of them lack an explicit saturation distribution, since its accurate measurement has been one of the biggest difficulties in these kinds of studies. Some of the experimental studies focused on the mechanisms dominant in gravity drainage situations and in small block imbibition displacements, whereas others have emphasized understanding flow through a single fracture with no transfer from the matrix.

In general, several authors (Kazemi and Merrill, 1979), Beckner (1990), Gilman *et al.*, 1994) have assumed that fracture capillary pressures are negligible. Other have shown experimentally capillary continuity becomes important when gravity provides a driving force (Horie *et al.*, 1988; Firoozabadi and Hauge, 1990; Labastie, 1990; Firoozabadi and Markeset, 1992a, 1992b). Kazemi (1990) states his belief that capillary continuity is prevalent in the vertical direction and has suggested that, to reduce the number of equations to solve, fractured reservoir simulations should use the dual permeability formulation for the z direction and the dual porosity formulation for the x and y directions.

1.2.4 REVIEW OF PREVIOUS STANFORD RESULTS

Two of the previous studies are worth mentioning. The first one was a study initiated by Guzman and Aziz (1993), in which an experiment was designed that intended to measure saturation distribution in two cores of identical material, with the final objective of measuring fracture relative permeabilities. Saturations would be measured by means of a CT scanner. Fine grid simulations were performed to help in the design of the

experimental procedure. The experiment was built, but problems at the very beginning did not allow them to obtain results. The second one was developed by Hughes (1995). He redesigned Guzman and Aziz's experimental set-up, improving most of their experiment by building a new apparatus and obtaining some results on water imbibition into a dry system of two fractured blocks. Three core configurations were constructed. The configurations were a compact core, a two-block system with a 1mm spacer between the blocks, and a two-block system with no spacer. The blocks were sealed in epoxy so that saturation measurements could be made throughout the displacement experiments using a CT Scanner. Hughes presented results from a water/air experiment; however, he only presented CT images. These results suggest that it is incorrect to assume negligible capillary continuity between matrix blocks as is often done.

Hughes (1995) evaluated how water imbibed into an unsaturated core. Migration of the water was monitored with the CT scanner. Despite the fact that water was being injected only into the bottom block, capillary imbibition pulled the water across the discontinuity and through the top block such that water from the top block actually broke through before the bottom block.

Three rectangular blocks of Boise sandstone were prepared for this work. The first is a compact (solid) core measuring 3-1/8 x 3-1/16 x 11 inches. The second and third cores consist of two 2-15/16 x 1-1/2 x 11 inch blocks. The second core system has a 1 mm thick spacer fastened in place with Epoxy 907 to provide a separation between the blocks that simulates a fracture. The third core system is constructed similarly but has no spacer between the blocks. The original design of Hughes had two pressure taps on the top and two on the bottom. In addition, a Plexiglas plate that was epoxied to the top surface of the core was removed in the new design. The plate was found to be unnecessary and a potential source for leaks.

1.2.5 EXPERIMENTAL DESIGN

Due to the rectangular shape and the desire to measure in-situ saturations through the use of the CT scanner, conventional core holders could not be used. A core holder similar to the original designed by Guzman and Aziz (1993) was developed for each of the cores used in Hughes' experiments. It consists of an epoxy resin surrounding the core. Plexiglas end plates were constructed for the core holders with a piece of 3/8 inch Viton acting as a gasket

between the core and the Plexiglas end plates. The Viton gaskets were held in place with automotive gasket material and Plexiglas rods. In Hughes' experiments (1995), the Viton was cut for each end face of the core holder, cutting a hole in the Viton so that the core face would be exposed; however following this procedure caused problems in those experiments.

The water injected first dribbled down in the space in between the Plexiglas end plate and the rock (the hole previously cut in the Viton.) To avoid this problem, some material that could fill this space and could guarantee that the injected fluids were in contact with the whole surface at the same time as well was needed. Thus, four sheets of filter paper having all together the same thickness as the Viton, were used. The same automotive gasket material was then used to glue the Viton to the epoxy and the Viton to the Plexiglas end plates as shown in Fig. 1.

Two pumps were calibrated and used. Each calibration curve for these pumps are given in Figs. 2 and 3. Each pump could deliver 0.01 to 9.99 cm^3/min in 0.01 increments. Plumbing downstream of the pumps allows mixing of the fluids being discharged by each pump. This setup allows injection pressure to be monitored with a test gauge and recirculation to measure pump output rates.

All tubing used for the experiment was Paraflex 1/8 inch diameter, with 500 psi working pressure plastic tubing connected with stainless steel Swagelok fittings. This system allows fluids to be directed to any port or combination of ports in the experiment such that, (1) It can be directed to test the calibration of the pressure transducers, (2) inject from one end and produce from the opposite end, (3) inject into one or more if the ports on the top and bottom of the core holder, or (4) to bypass the core holder completely. Figure 4 shows the flow system utilized for this work.

The production measurement system is an adaptation of a design first proposed by engineers at Conoco, Inc that was built by Ameri and Wang (1985) and modified by Qadeer (1994). Figure 5 shows this system.

The tubing labeled with 'from Core outlet' in Fig. 5 carries oil and water from the core. The oil is separated due to density differences and held inside a confining cap in an inner vessel which is suspended from an electronic balance. Water over flows through siphon and is collected in a container (e.g., a beaker) which is on other balance.

The electronic balance attached to the inner vessel measures the bouyant weight of the vessel. The change on the weight corresponds to the variation of total oil accumulated inside the inner vessel. These changes on the cumulative production of oil and water are the

oil and water production rates. These rates should be equal to the injection rates when steady state conditions are reached.

The electronic balances are connected to a serial communication ports of a personal computer (PC) that recorded all the signals coming from their measurements.

1.2.6 EXPERIMENTAL PROCEDURE

The first core used had a fracture with no space in between the blocks. Due to the length of this core (11 inches), and despite the stainless steel fittings that were used for the ports on the top and the bottom of the coreholder, it was decided to choose a regular sequence of scan locations. This was because even when the fitting ports could be avoided it was found that both the previous and the next slices had some artifacts because of the stainless steel fittings, so it was better to find a distribution in which we could scan exactly at those locations and reduce the effects on the previous and next slices as well.

Thus, it was decided to fix the scan location every 2 cm starting from the first two centimeters from the inlet face since any location at less distance could have either effects from the injection stainless steel fitting port or scan the Viton gasket and filter paper.

The total travel distance of the positioning system was then 25.5 cm, resulting in 13 slices including those two located at the fitting ports (fourth and eleventh, for the first experiment; and fourth and tenth, for the second one.) Figure 6 shows the CT scan locations.

To assure the same locations for the next stages of the experiment, the patient table of the CT Scanner was fixed at a proper location, so the positioning system (accuracy ± 0.01mm) would do the rest of the locating process. This provided more accurate results for the porosity and saturation calculations. This was a major improvement compared to Hughes (1995) experiments, since he was using the patient table whose accuracy is ± 1 mm .

The field of view used for this experiment was 24 cm, the image matrix, resolution, voltage, amperage, filter used, and more scanner settings are shown in Table 1. The first step of this experiment was to scan the dry core. This step was very important to verify that the apparatus and all the set-up was working properly. For instance, we could notice some problems with the coreholder in a first trial for the dry scan. We could not keep its position horizontal, because it was quite heavy and held only by one of the sides. Moreover, the

Table 1. CT Scanner Settings

Parameter	Setting
Field of View	24 cm
Image Matrix	512 x 512
Sampling	1024
Scan Speed	3 sec
Slice Thickness	10 mm
Resolution	High
kV	140
mA	65
x-ray filter	3
MAS	341 per slice
Exposure	5.09 sec/slice
Pilot	0.00 sec

gasket makes it harder to hold since it was not rigid. In order to solve this problem, two C clamps were used to strengthen the attachment to positioning system to keep the coreholder in the same position (horizontal) during the experiment. After these improvements, the dry scans were done successfully.

The second step was to evaluate how water imbibed into an unsaturated core. This part of the experiment gave us results that can be compared with the ones obtained by Hughes (1995), and eventually used to evaluate how well the new experiment worked. Starting with a flow rate of 2 cm^3/min, CT images of the core were taken every 5 minutes until the first 20 minutes of water injection; after this, images were taken at 30 min, 45 min, 1 hr., 1hr 30 min, 2 hr, 3 hr, and 4 hours after water injection started. Following that the top and bottom ports were opened since we wanted to fill up the core to the maximum water saturation (Sw = 1). Common to all time steps, we tried to take images up to one location ahead of the possible water front.

After 5 hours of water injection, the flow rate was changed to 0.5 cm^3/min in order to inject water for 14 more hours to reach higher possible water saturations. After 19 hours,

a new set of slices were taken. Then, at 19 hours and 45 min the water rate was changed back to 2 cm^3/min, and the top and bottom ports were closed. At 21 hours a final set of slices was taken to find a possible change in CT numbers. Negligible changes in CT numbers were observed. At 23 hours of water injection, the third step of the experiment started.

The third step of the experiment involved injecting Decane at 2 cm^3/min. The scanning frequency was intended to be the same as the water injection process. Thus, images of the core were taken every five minutes until the first 20 minutes of oil injection; after that, more images were taken at 30 min, 45 min, 1 hr., 1hr 30 min, 2 hr 30 min, and 3 hr 45 min. after oil injection started. Then, the top and bottom ports were opened at 4 hours of starting oil injection since we wanted to fill the core up to the maximum possible point. At 4 hr 30 min of oil injection, one more set of images was taken. After 5 hours of oil injection, the flow rate was changed to 1 cm^3/min for 16 hours to reach higher possible oil saturations (S_{WC}). After 21 hours of oil injection, a new set of slices was taken, and the ports were closed. Then, at 21 hours and 39 min the oil injection was stopped, and water injection at the maximum pump rate (9.99 cm^3/min) was started.

The fourth step of the experiment was the water displacing oil stage. Injecting 9.99 cm^3/min of water, images were taken at 5 min, 15 min, and 30 min. At 1hr 10 min, water injection was stopped, the inlet and outlet lateral ports were also closed, leaving all of the coreholder's ports closed. One more set of images was taken after two days of closing the coreholder to observe if capillary equilibrium had been reached. Table 2 summarizes the flow rates used and the timing of each of them.

The second experiment was done using the coreholder that contained a system with two blocks with a 1 mm thick fracture in between. The same experimental procedure was followed. Essentially, we wanted to obtain CT images, and then saturation values for equivalent times, so we could eventually compare the differences between the two systems. The rates and timing for the case of two blocks with a wider fracture are shown in Table 3.

1.2.7 METHOD OF SOLUTION

The most common way to calculate porosity from CT Scanner images is the following expression (Withjack, 1988):

$$\phi = \frac{CT_{cw} - CT_{cd}}{CT_w - CT_a} \tag{1}$$

where CT_{cw} is the CT number for a water saturated core at a matrix location, CT_{cd} is the CT number for a dry core at a matrix location, CT_w is the CT number for water, and CT_a is the CT number for air. The CT number for water (8%NaBr solution, for this work) is around 360, while the CT number for air is -1000.

We found that the average value for porosity calculated from the scans was 15% which matches with the average value 14.35% reported by Hughes (1995); however, this value differs from the average porosity measurements of 25.4% obtained by Guzman and Aziz (1993) and 29.3% obtained by Sumnu (1995). All of these previous studies have also shown areas in the rocks which have lower permeability.

Table 2. Rates and Timing for the Core with Thin Fracture

Fluid Injected	Time [hr.]	Flow Rate [cm^3/min]	Ports
Water	0.0 - 4.0	2.0	Top and bottom closed, lateral open.
Water	4.0 - 5.0	2.0	Top and bottom open, lateral closed.
Water	5.0 - 19.8	0.5	Top and bottom open, lateral closed.
Water	19.8 - 23.0	2.0	Top and bottom closed, lateral open..
Decane	23.0 - 27.0	2.0	Top and bottom closed, lateral open.
Decane	27.0 - 28.0	2.0	Top and bottom open, lateral closed.
Decane	28.0 - 44.7	1.0	Top and bottom open, lateral closed.
Water	44.7 - 46.0	9.99	Top and bottom closed, lateral open.
	46		Shut down everything

Table 3. Rates and Timing for the Core with Wider Fracture

Fluid Injected	Time [hr.]	Flow Rate [cm^3/min]	Ports
Water	0.0 - 5.0	2.0	Top and bottom closed, lateral open.
	5.0 - 21.0	0.0	Top and bottom closed, lateral closed.
Water	21.0 - 22.5	2.0	Top and bottom open, lateral closed.
Water	22.5 - 25.6	2.0	Top open, bottom closed, and lateral closed..
	25.6 - 45.0	0.0	Top and bottom closed, lateral closed.
Decane	45.0 - 48.0	2.0	Top and bottom closed, lateral open.
Decane	48.0 - 49.2	4.0	Top and bottom closed, lateral open.
Decane	49.2 - 51.0	4.0	Top and bottom open, lateral closed.
	51.0 - 52.0	0.0	Top and bottom closed, lateral closed.
Water	52.0 - 54.3	4.0	Top and bottom closed, lateral open.
Water	54.3 - 68.8	0.5	Top and bottom closed, lateral open.
Water	68.8 - 71.0	4.0	Top and bottom open, lateral closed.
	71		Shut down everything

The water and oil saturations were also calculated from the CT images. The following equations show the way to evaluate water saturation for the air displacing air case, and for the case oil displacing water or water displacing oil.

$$Sw = \frac{CT_{aw} - CT_{cd}}{CT_{cw} - CT_{cd}} \tag{2}$$

where CT_{aw} is the CT number for a water and air saturated core at a matrix location. Similarly, for the case of oil-water systems

$$Sw = \frac{CT_{ow} - CT_{cw}}{\phi\,(CT_o - CT_w)} \tag{3}$$

where CT_{ow} is the CT number for a water and oil saturated core at a matrix location, and CT_o is the CT number for oil. The CT number for oil (decane, for this work) is around -272.

All the saturation values are shown in the following section, as well as the way to read them in the corresponding figures.

1.2.8 RESULTS

Guzman and Aziz (1993) presented a CT image from which it can be seen that CT numbers can indicate differences in fluid saturations Later on, Hughes (1995) presented images showing how water imbibes into an unsaturated core. As we stated previously, his coreholder contained a gap between the core and the Plexiglas plate, so the CT images show the water going down, filling first the gap and then imbibing the core. It can be easily concluded, that his results showed the water imbibing first the bottom block. After some time water filled the gap, but it was late because the water had imbibed a good portion of the bottom block, and finally much time had passed before water reach the fracture level. Hughes' (1995) results are good in the sense that he conducted a reasonably controlled experiment, he showed that CT images for different times could be obtained, and that his shortcuts could be improved. Thus, his results started the motivation for this work; considering the development of more sophisticated software as well as better computers, we

thought experiments like those presented in this work could be done. Improving previous designs, following carefully the procedure planned and trying to obtain the data as accurately as possible, we would be able to complete a multiphase flow experiment in fractured porous media. We also could obtain images of theporosity distribution, as well as the saturation images.

The following sections present a set of images, each square shows a scan location, with the distribution shown in Fig. 6. First of all, we computed the values of porosity at each location, so we could obtain the best approximation of the porosity distribution of the two systems. The different porosity images for both systems are shown in Fig. 7, the values below each square correspond to the mean and the standard deviation respectively of the porosity values obtained from CT numbers. This step was essential for both experiments because from these images and their corresponding values we could differentiate the regions with higher or lower porosity. Thus, in those images, the range of values are shown in the color bar in the right hand side in Fig. 7. There, we can also see that the system with the thin fracture has a little higher porosity than the system with the wide fracture, specially in the top block, where values up to 0.13 were observed.

1.2.8.1 Results for the Thin Fracture System

Following the procedure explained above, and the flow rates, times and injection/production conditions shown in Table 1, we ran the first experiment. Figures 8, 9 and 10 show the sets of images corresponding to 1 hour, 1.5 hours, and 2 hours of water injection. Similarly as the porosity images, each square correspond to one location, but now the water saturation distributions are shown. The pairs of values presented below each square correspond to the mean and standard deviation (separated by commas) of the top, bottom and both blocks respectively. Colors for each saturation value were also assigned. The color bar on the right hand side show the range of values and their corresponding lightness or darkness. In all the images shown in Figs. 8-10, darker shades indicate lower water saturation. For instance, black means zero water saturation, and white means water saturation equal to 1. Those figures also include plots of the water saturation profiles. The left hand side ones correspond to the average values (the last mean of each square); and the right hand side ones, correspond to the values of the top and bottom blocks (first and second means of each square respectively). Different profiles, corresponding to different pore

volumes of water injected are shown in Fig. 11. There we can see that the profiles are stable and they appear to follow Buckley-Leveret theory.

Similar images were obtained for the second stage of the first experiment (oil injection). Figures 12 and 13 show sets of images corresponding to 2.5 hours and 3.75 hours of oil injection. Here, the pairs of values below each square indicate the mean and the standard deviation of oil saturations, respectively. Colors were also assigned to the oil saturation values; thus, the color bar on the right hand side show the range of values and their corresponding lightness or darkness. In all the images shown in Figs. 12 and 13, darker shades indicate lower oil saturation. For instance, black means zero oil saturation. Figure 14 shows oil saturation profiles for different times. There, one can see some special behavior up to 3.75 hours; however, we could not follow it because we opened the lateral ports of the coreholder at 4 hours in order to fill up the core at the maximum possible point (Sw =1.)

Images for the third stage of the experiment (water displacing oil) were also obtained; however, due to problems with one of the pumps, we could not analyze properly the rest of the data.

1.2.8.2 Results for the Wide Fracture System

Following the procedure explained above, and the flow rates, times and injection/production conditions shown in Table 2, we ran the second experiment. Figures 15-17 show the sets of images corresponding to 1 hour, 1.5 hours, and 2 hours of water injection for the wider fracture system. Similarly as the images obtained in the case for thin fracture system, each square corresponds to one location, and also the water saturation distributions are shown. The pairs of values presented below each square also correspond to the mean and standard deviation (separated by commas) of the top, bottom and both blocks respectively. In all the images shown in Figs. 15-17 darker shades indicate lower water saturation. For instance, black means zero water saturation, and white means water saturation equal to 1. Different profiles, corresponding to different pore volumes injected are shown in Fig. 18. There we can see that the profiles are less stable than those for the thin fracture system.

Figures 19 and 20 show sets of images corresponding to 2.5 hours and 3.75 hours of the second stage of the second experiment (oil injection). Similar to the sets of images of oil injection of the first experiment, the pairs of values below each square indicate the mean

and the standard deviation of oil saturations, respectively. Colors were also assigned to the oil saturation values. In all the images shown in Figs. 19 and 20 darker shades indicate lower oil saturation. For instance, black means zero oil saturation. Figure 21 shows the profiles for different times. Nothing special can be seen due to some leaks during this stage. Although, we could observe very low saturation values in zones far from the leaking point.

Images for the third stage of the second experiment (water displacing oil) were also obtained. The most interesting sets are shown in Figs. 22 and 23, where one can see how the displacement of oil is completed almost perfectly. Some oil is in the core at 16 hours, and after 17 hours of water injection the oil is totally swept from the core. See the differences between Figs. 22 and 23.

1.2.8.3 Comparison of the Results for Both Systems

Due to the fact that the experiments ended in different ways, we were able to compare the results up to the second stage of both experiment. This section show graphically how they can be compared.

Three-dimensional (3-D) reconstructions of the sets of images were done. These 3-D images show more clearly how the fluids actually flow through fractured porous media. This work was intended to show the differences in the flow patterns for different fractures thicknesses. The reconstructed images are shown in Figs. 24- 27. Each image corresponds to a specific time; thus, the first image of Fig. 24 is compared to the first one of Fig. 26, the second image of Fig. 24 was done for the same time as the second image on Fig. 26, and so on. There, we can see how the water front for the wider fracture system goes almost at the same speed as the water front for the thinner fracture system does for the same time. For instance, one can see that after 1.5 hours of water injection, the water front of the thin fracture system seems to be ahead of the front for the wide fracture system; however, after two hours of water injection water has filled up both systems.

Similarly, 3-D reconstructions for the second stage (oil injection) were done. Since the oil saturations were low for both cases, it is a bit harder to see the differences; however, it is possible to see that the thinner fracture system had higher oil saturation close to the fracture. This is shown in Figs. 28 and 29. One can see that the thin fracture system had lighter colors close to the injection surface. We can also see that for the case of a wide fracture system, the oil do not penetrate; furthermore, it flows almost completely through the fracture; this is shown in Fig. 29 by the almost white horizontal line, which correspond to

the fracture. Remember that for the case of oil injection stages, darker means lower oil saturation.

1.2.9 PRELIMINARY CONCLUSIONS

The results of the experiments we made in this work showed that:

a. Using this apparatus as well as the procedure explained here, one can identify areas with lower permeability and porosity.
b. Thin fracture systems show more stable fronts and faster breakthrough than wide fracture systems.
c. Capillary pressure has more effect in thin fractures.
d. Multiphase flow through the fracture was observed.
e. Larger recoveries can be obtained when the fracture are wider.

1.2.10 FUTURE WORK

Fine grid simulations of the experiments using a commercial reservoir simulator have been started. Relative permeabilities and capillary pressure curves will obtained by history matching the experiments.

After the simulation work is done we will try to obtain complete conclusions on mutiphase flow in fractured porous media. This will allow us to establish a procedure for looking at both the transmissibilities and the transfer terms that appear on the flow equations for any reservoir simulator.

1.2.11 REFERENCES

1. Beckner, B.L.: "Improved Modeling of Imbibition Matrix/Fracture Fluid Transfer in Double Porosity Simulators," PhD dissertation, Stanford University (July 1990).
2. Firoozabadi, A. and Hauge, J.: "Capillary Pressure in Fractured Porous Media," *JPT* (June 1990) 784-791.

3. Firoozabadi, A. and Markeset, T.: "An Experimental Study of Capillary and Gravity Crossflow in Fractured Porous Media," SPE 24918, presented at the 67th SPE Annueal Technical Conference and Exhibition, Washington, D.C. (October 4-7, 1992).
4. Firoozabadi, A. and Markeset, T.: "An Experimental Study of Gas-Liquid Transmissibility in Fractured Porous Media," SPE 24919, presented at th 67th SPE Annual Technical Conference and Exhibition, Washington, D.C. (October 4-7, 1992).
5. Gilman, J.R., Bowzer, J.L. and Rothkopf, B.W.: "Application of Short-Radius Horizontal Boreholes in the Naturally Fractured Yates Field," SPE 28568, presented at the 69th SPE Annual Technical Conference and Exhibition, New Orleans, LA (September 25-28, 1994).
6. Guzman, R.E. and Aziz, K.: "Design and Construction of an Experiment For Two-Phase Flow in Fracuted Porous Media," SUPRI TR-95, Stanford Petroleum Research Institute, Stanford, CA (June 1993).
7. Horie, T., Firoozabadi, A. and Ishimoto, K.: "Capillary Continuity in Fractured Reservoirs," SPE 18282, presented at the 63rd SPE Annual Technical Conference and Exhibition, Houston, TX (October 2-5, 1988).
8. Hughes, R.G.: "CT Measurements of Two-Phase Flow in Fractured Porous Media," Masters Report, Stanford University (December 1995).
9. Kazemi, H. and Merrill, L.S.: "Numerical Simulation of Water Imbition in Fractured Cores," *SPEJ* (June 1979) 175-182.
10. Kazemi, H.: "Naturally Fractured Reservoirs," Third International Forum on Reservoir Simulation, Baden, Austria (1990).
11. Kleppe, J. and Morse, R.A.: "Oil Production from Fractured Reservoirs by Water Displacement," SPE 5084 presented at the 49th Annual Meeting of the Society of Petroleum Engineers, Houston, TX (October 6-9, 1974).
12. Labastie, A.: "Capillary Continuity Between Blocks of a Fractured Reservoir," SPE 20515 presented at the 65th SPE Annual Technical Conference and Exhibition, New Orleans, LA (September 23-26, 1990).
13. Mattax, C.C. and Kyte, J.R.: "Imbibition Oil Recovery from Fractured, Water-Drive Reservoir," *SPEJ* (June 1962), 177-184.
14. Operator's Guide, Synerview 600s/1200SX, C85:f, REV1, Picker International (January 1983).
15. Qadeer, S.: Techniques to Handle Limitations in Dynamic Relative Permeability Measurements, PhD dissertation, Stanford University (to be completed).
16. Withjack, E.M: "Computed Tomography for Rock-Property Determination and Fluid-Flow Visualization," *SPEFE* (December, 1988) 696-704.

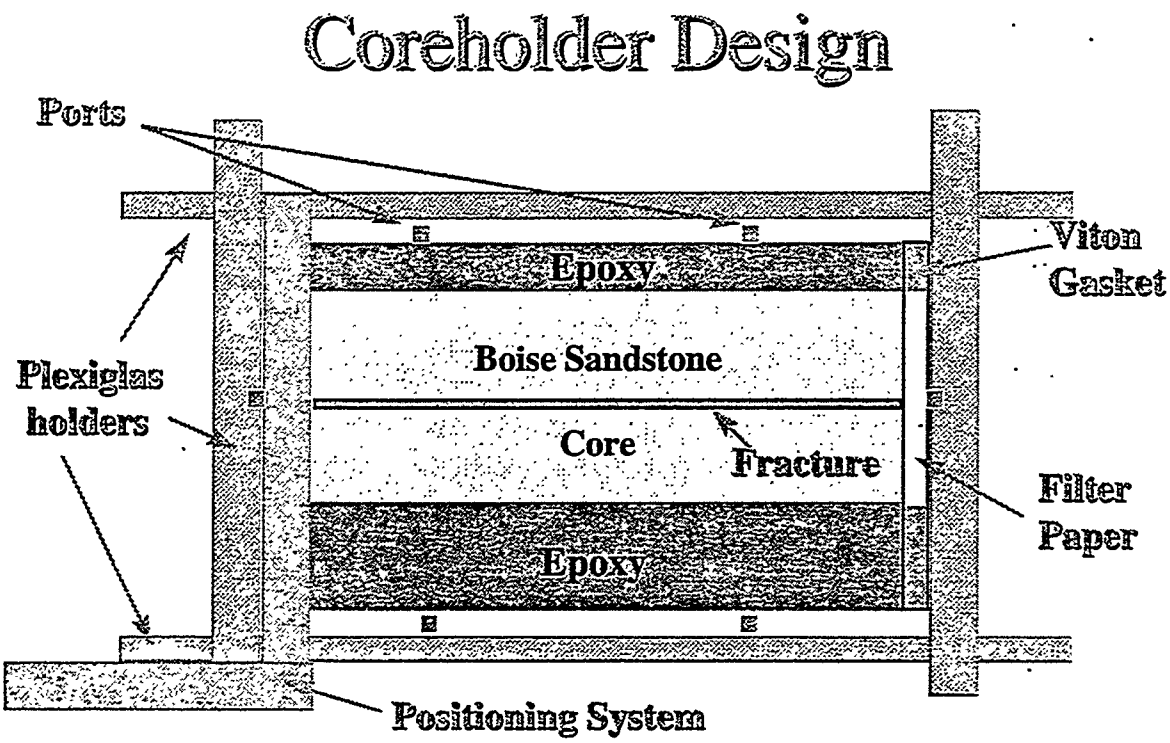

Figure 1. The core holder.

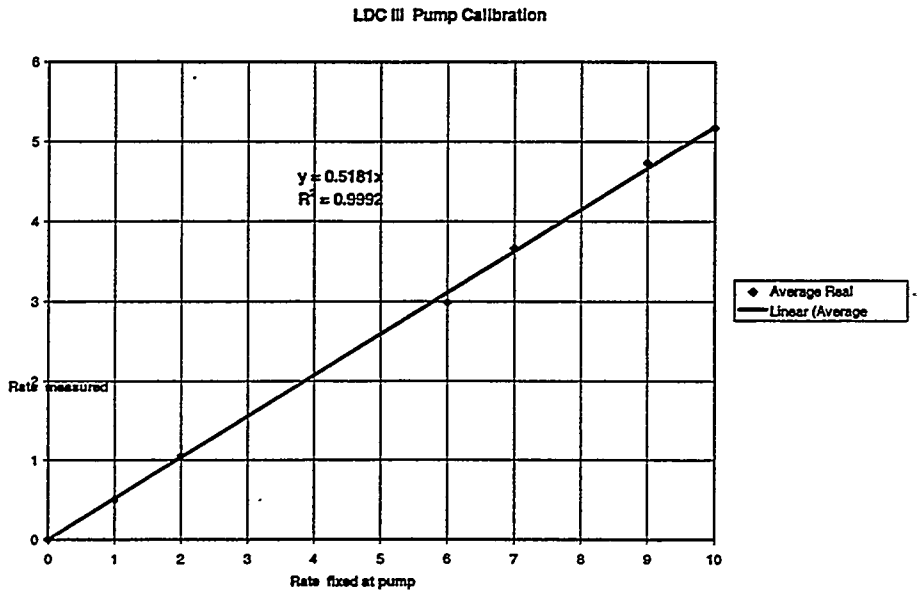

Figure 2. LDC III Pump Calibration Curve.

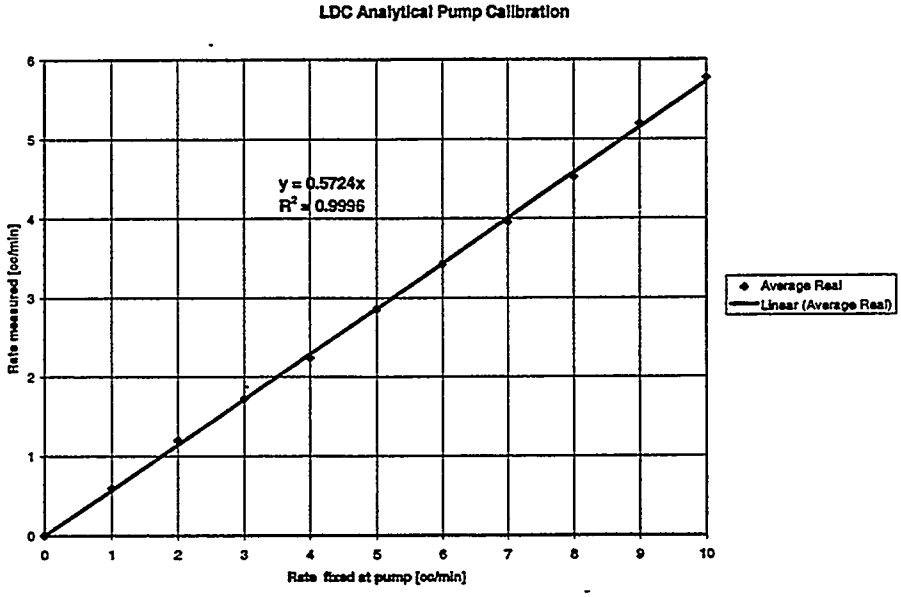

Figure 3. LDC Analytical Pump Calibration Curve.

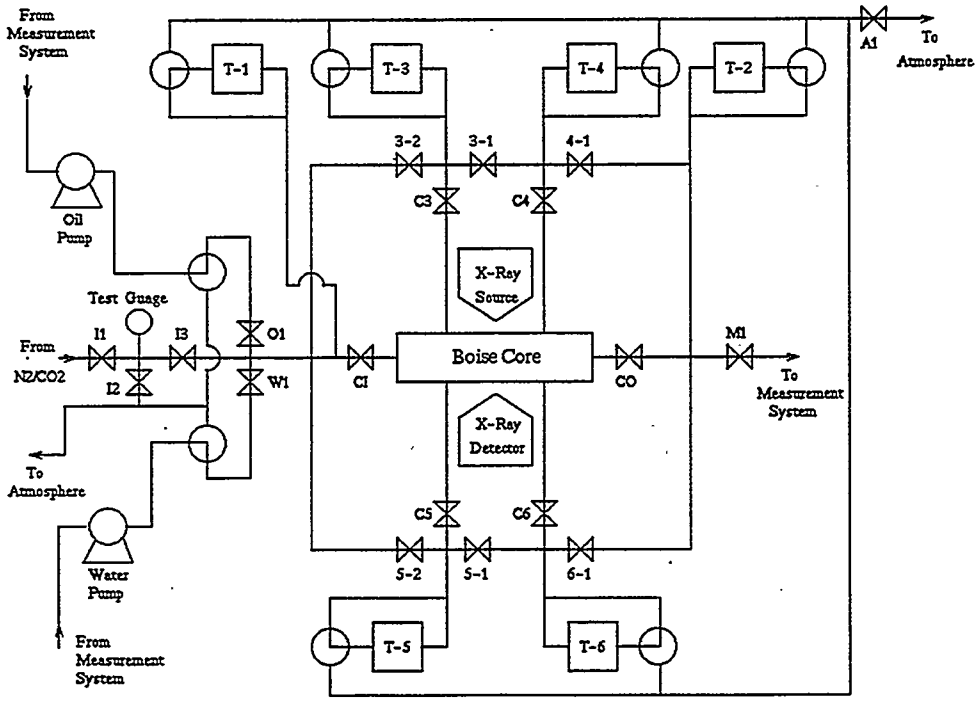

Figure 4. Flow System (Hughes, 1995.)

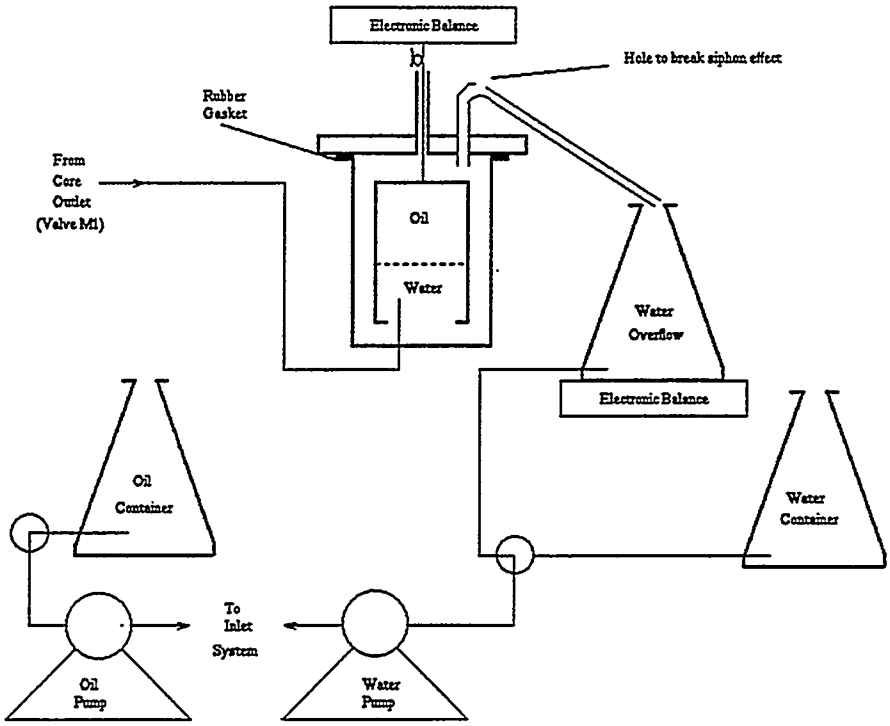

Figure 5. Production System (After Hughes, 1995)

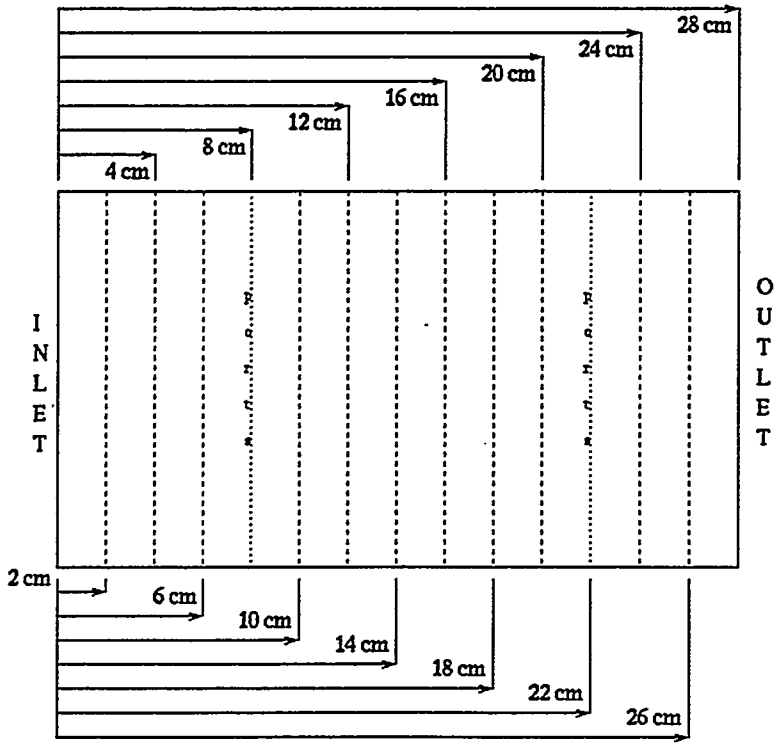

Figure 6. CT Scan Locations.

Porosity Distribution

Blocks with no space in between.

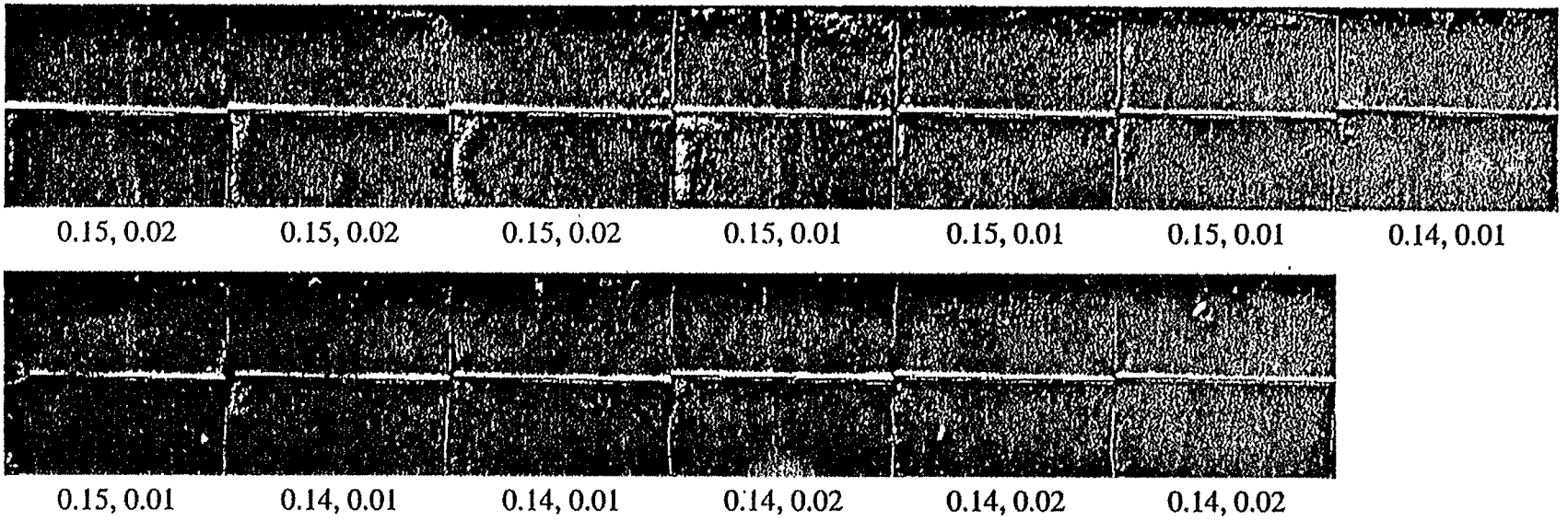

Blocks with 1mm space in between.

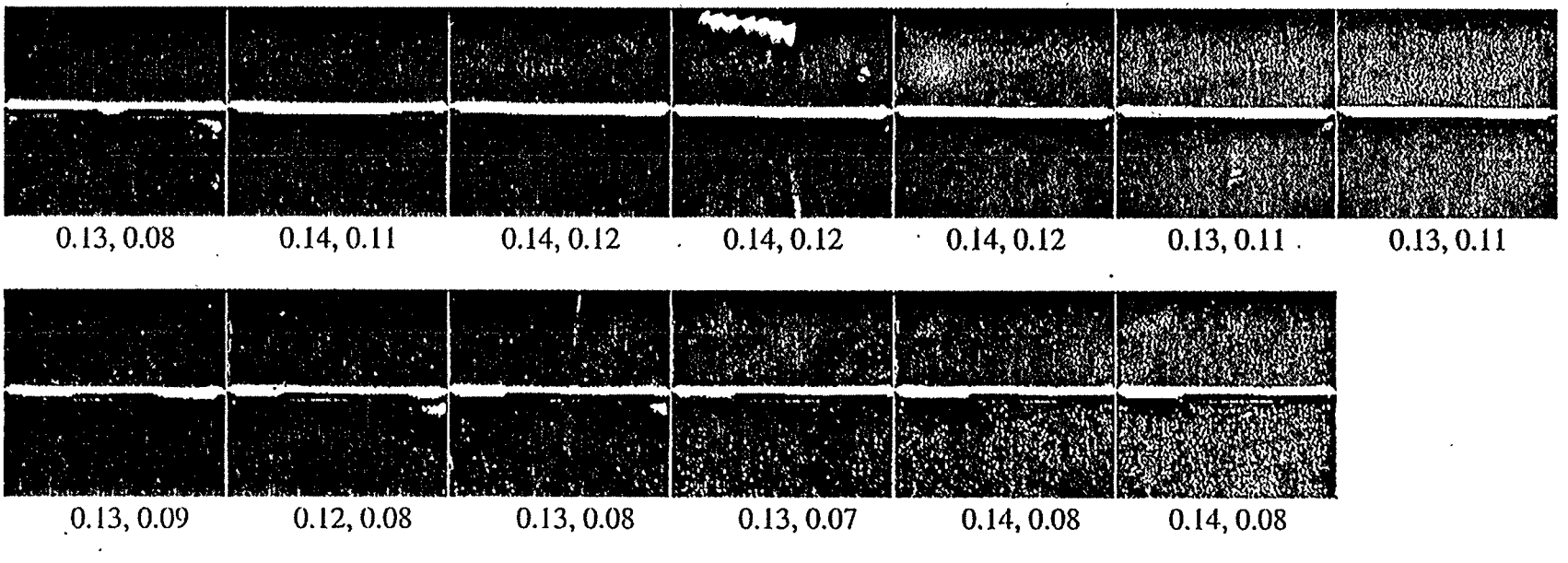

Figure 7. Porosity Distribution for the experimental system

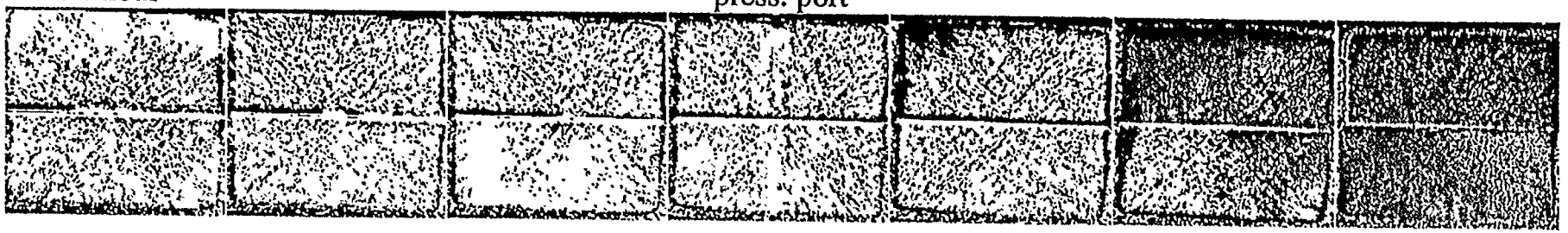

0.98, 0.05	0.96, 0.04	0.96, 0.04	0.97, 0.04	0.94, 0.05	0.75, 0.09	-0.01, 0.04
0.96, 0.04	0.98, 0.04	0.99, 0.05	0.98, 0.04	0.97, 0.04	0.91, 0.06	0.50, 0.19
0.98, 3.72	*1.00, 1.81*	*1.00, 1.47*	*0.98, 1.14*	*0.96, 0.10*	*0.83, 0.13*	*0.23, 0.27*

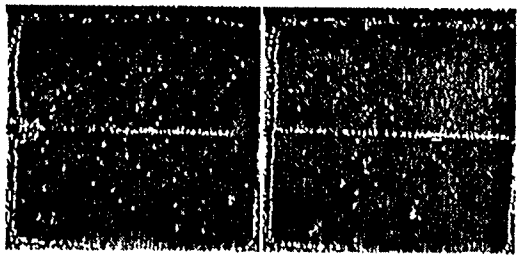

-0.01, 0.04	-0.01, 0.03
-0.01, 0.04	-0.01, 0.04
-0.01, 0.09	*-0.01, 0.36*

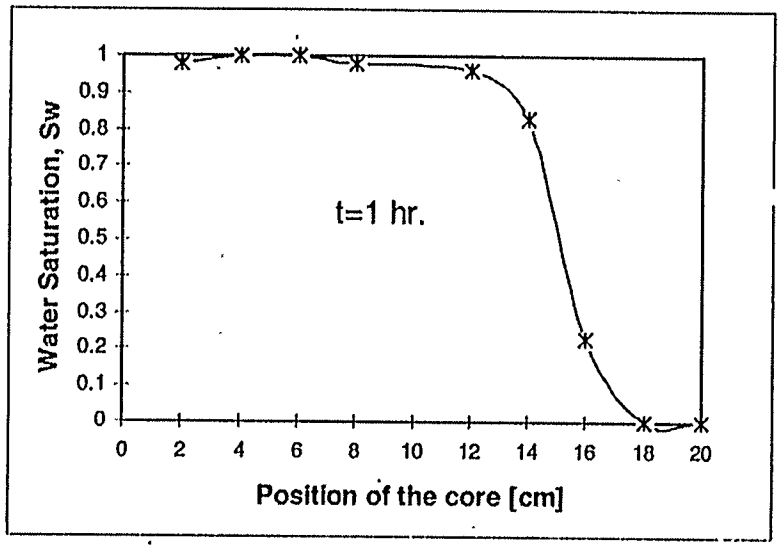

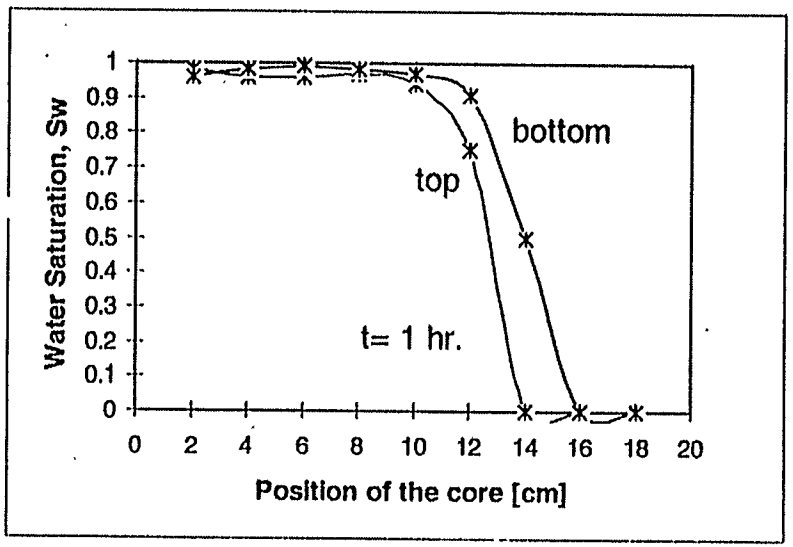

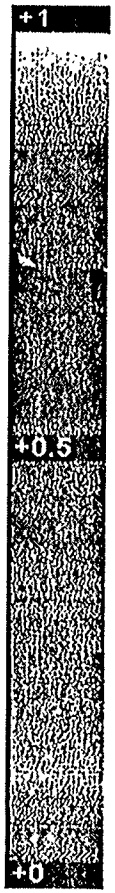

Figure 8. CT Saturation images for the Thin Fracture System after 1 hr of Water injection (0.45 PV)

after 1 hr. 30 min.

press. port

0.98, 0.05	0.96, 0.04	0.96, 0.04	0.97, 0.04	0.96, 0.04	0.96, 0.04	0.97, 0.04
0.96, 0.04	0.98, 0.04	0.99, 0.05	0.98, 0.04	0.97, 0.04	0.97, 0.04	0.97, 0.04
0.98, 4.46	*1.04, 3.40*	*1.04, 3.33*	*1.02, 0.35*	*1.00, 0.26*	*1.00, 0.26*	*1.00, 0.22*

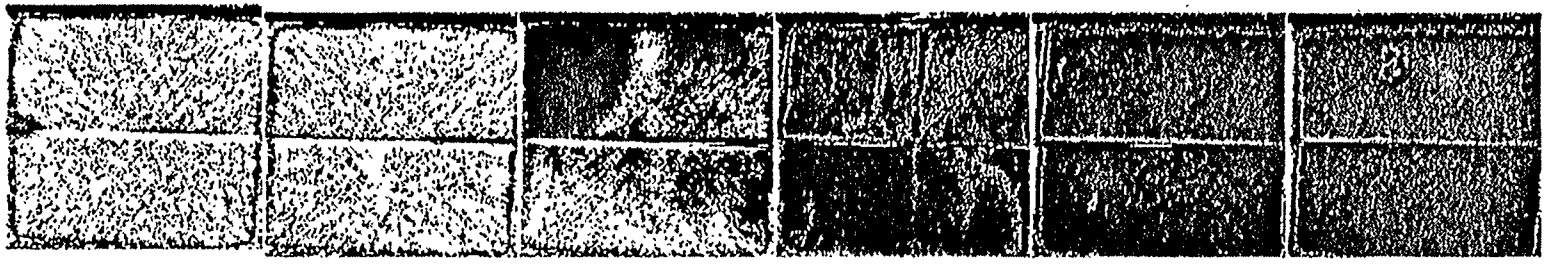

0.97, 0.03	0.97, 0.04	0.85, 0.10	0.16, 0.12	-0.01, 0.04	-0.01, 0.54
0.97, 0.04	0.97, 0.04	0.93, 0.05	0.52, 0.19	-0.01, 0.04	-0.01, 0.04
0.99, 0.20	*0.98, 0.60*	*0.88, 1.25*	*0.32, 0.53*	*-0.02, 0.74*	*-0.02, 0.62*

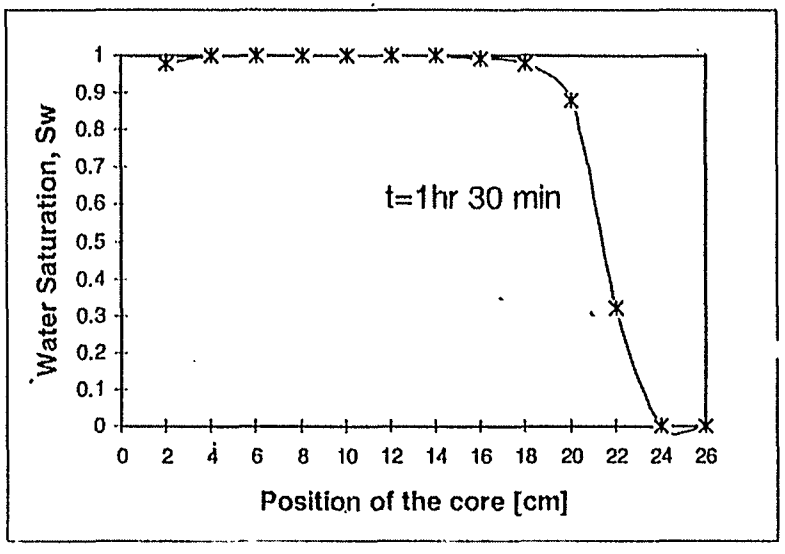

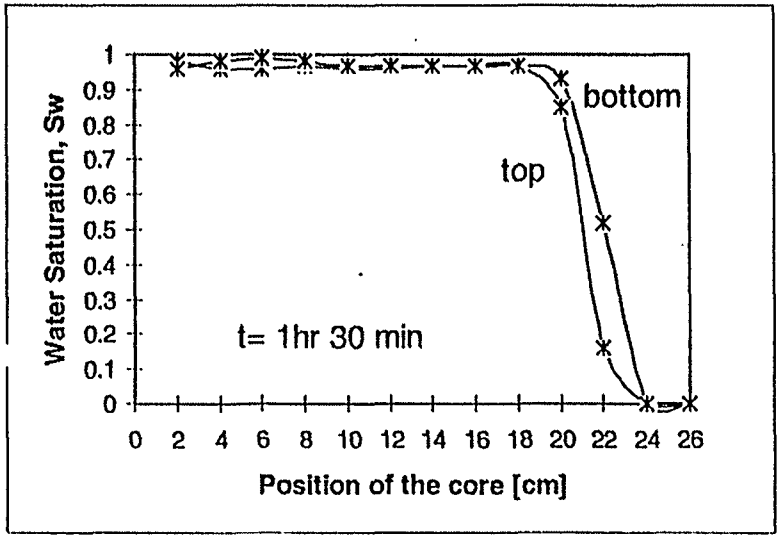

Figure 9. CT Saturation images for the Thin Fracture System after 1 hr 30 min of Water injection (0.67 PV)

after 2 hour

press. port

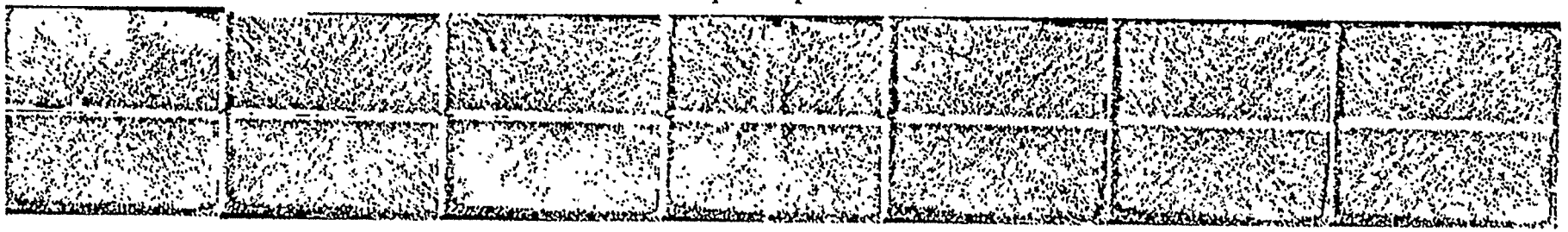

0.98, 0.06	0.96, 0.03	0.96, 0.04	0.97, 0.04	0.96, 0.04	0.96, 0.04	0.97, 0.04
0.96, 0.04	0.98, 0.04	0.99, 0.05	0.98, 0.04	0.97, 0.04	0.97, 0.04	0.97, 0.04
0.98, 4.15	*1.04, 4.07*	*1.05, 3.33*	*1.02, 0.34*	*1.00, 0.25*	*1.00, 0.25*	*1.00, 0.31*

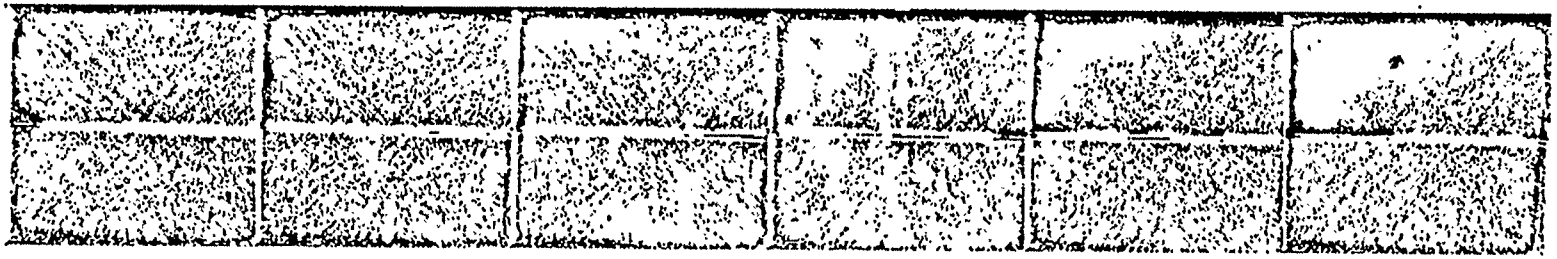

0.97, 0.04	0.97, 0.04	0.97, 0.04	1.01, 0.08	0.99, 0.06	1.07, 0.36
0.97, 0.04	0.97, 0.04	0.99, 0.05	0.99, 0.05	0.99, 0.04	0.98, 0.04
1.00, 0.50	*1.02, 2.31*	*0.95, 4.71*	*1.05, 6.10*	*1.06, 2.67*	*1.07, 1.17*

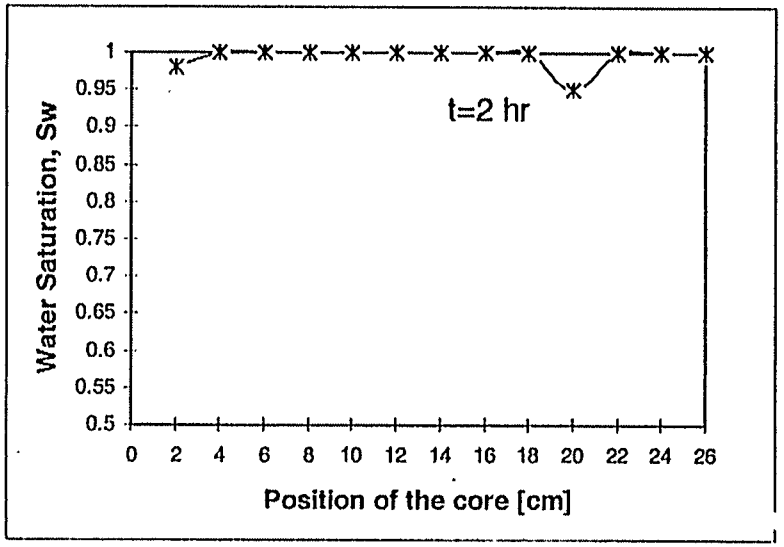

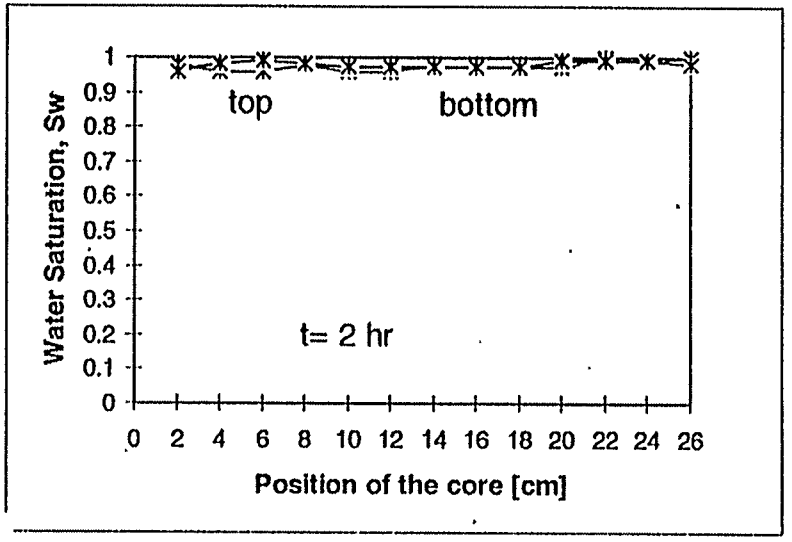

Figure 10. CT Saturation images for the Thin Fracture System after 2 hr of Water injection (0.89 PV)

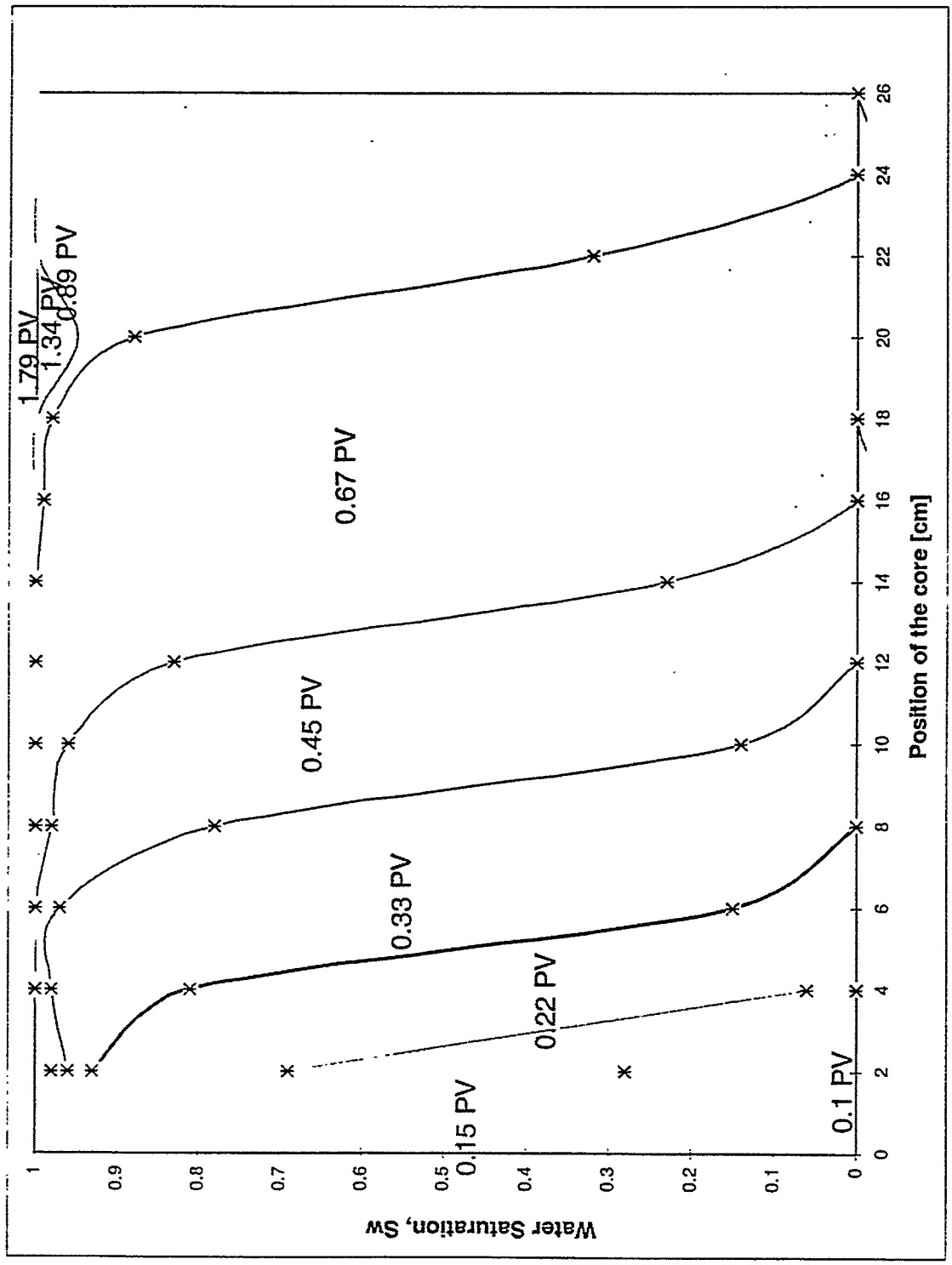

Figure 11. Water Saturation Profiles for Thin Fracture sytem for different PV of Water injection

after 2 hr. 30 min.

press. port

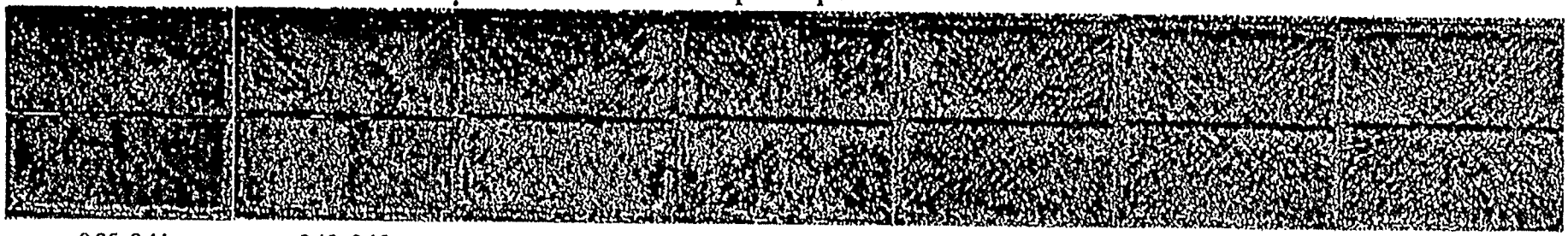

0.25, 0.11	0.13, 0.13	0.05, 0.11	0.06, 0.12	0.01, 0.09	0.00, 0.09	0.00, 0.09
0.32, 0.11	0.24, 0.12	0.15, 0.10	0.06, 0.11	0.01, 0.09	0.00, 0.09	0.00, 0.10
0.28, 3.82	*0.08, 3.95*	*0.04, 3.19*	*0.02, 0.36*	*-0.02, 0.26*	*-0.02, 0.24*	*-0.03, 0.32*

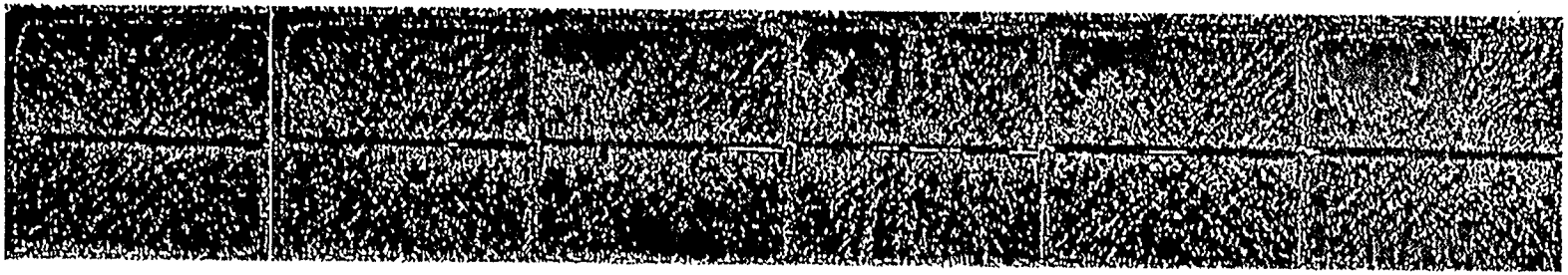

-0.01, 0.08	0.01, 0.09	0.02, 0.12	0.02, 0.12	0.01, 0.13	-0.03, 0.46
0.00, 0.09	0.01, 0.10	0.00, 0.11	0.01, 0.12	0.00, 0.10	0.00, 0.10
-0.05, 0.81	*-0.04, 2.37*	*0.02, 2.63*	*-0.03, 6.17*	*-0.10, 4.14*	*-0.01, 0.10*

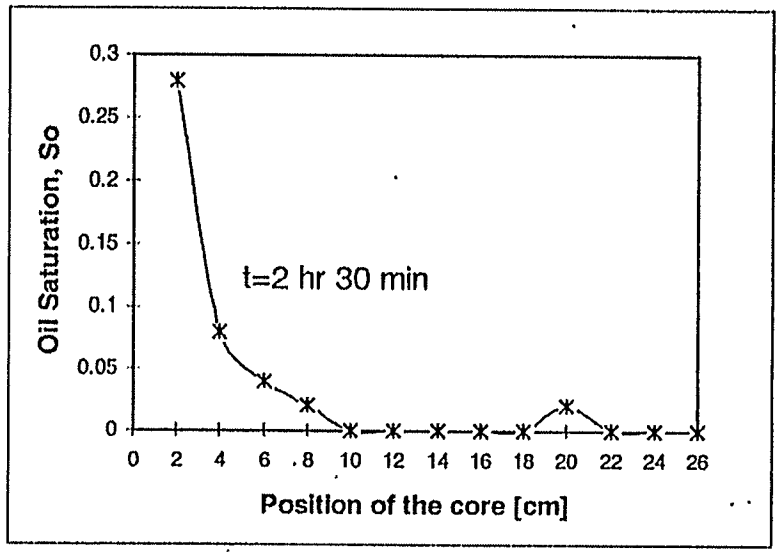

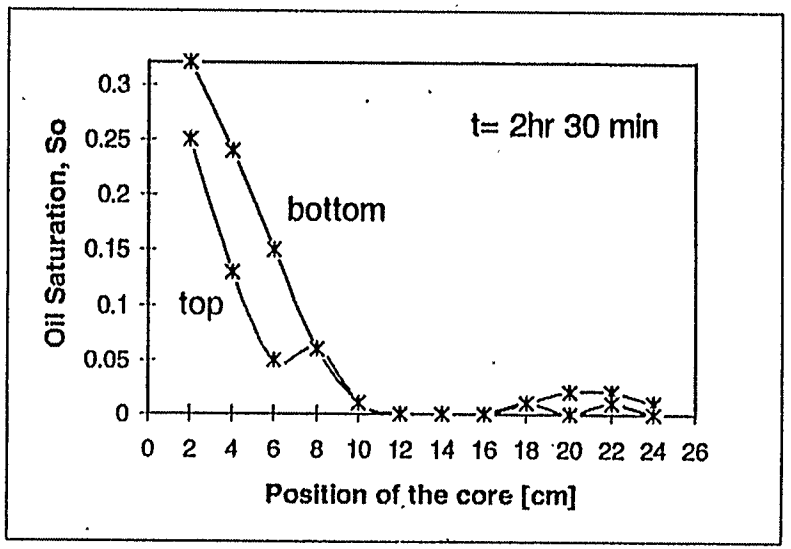

Figure 12. CT Saturation images for the Thin Fracture System after 2 hr 30 min of Oil injection (1.11 PV)

Figure 13. CT Saturation images for the Thin Fracture System after 3 hr 45 min of Oil injection (1.67 PV)

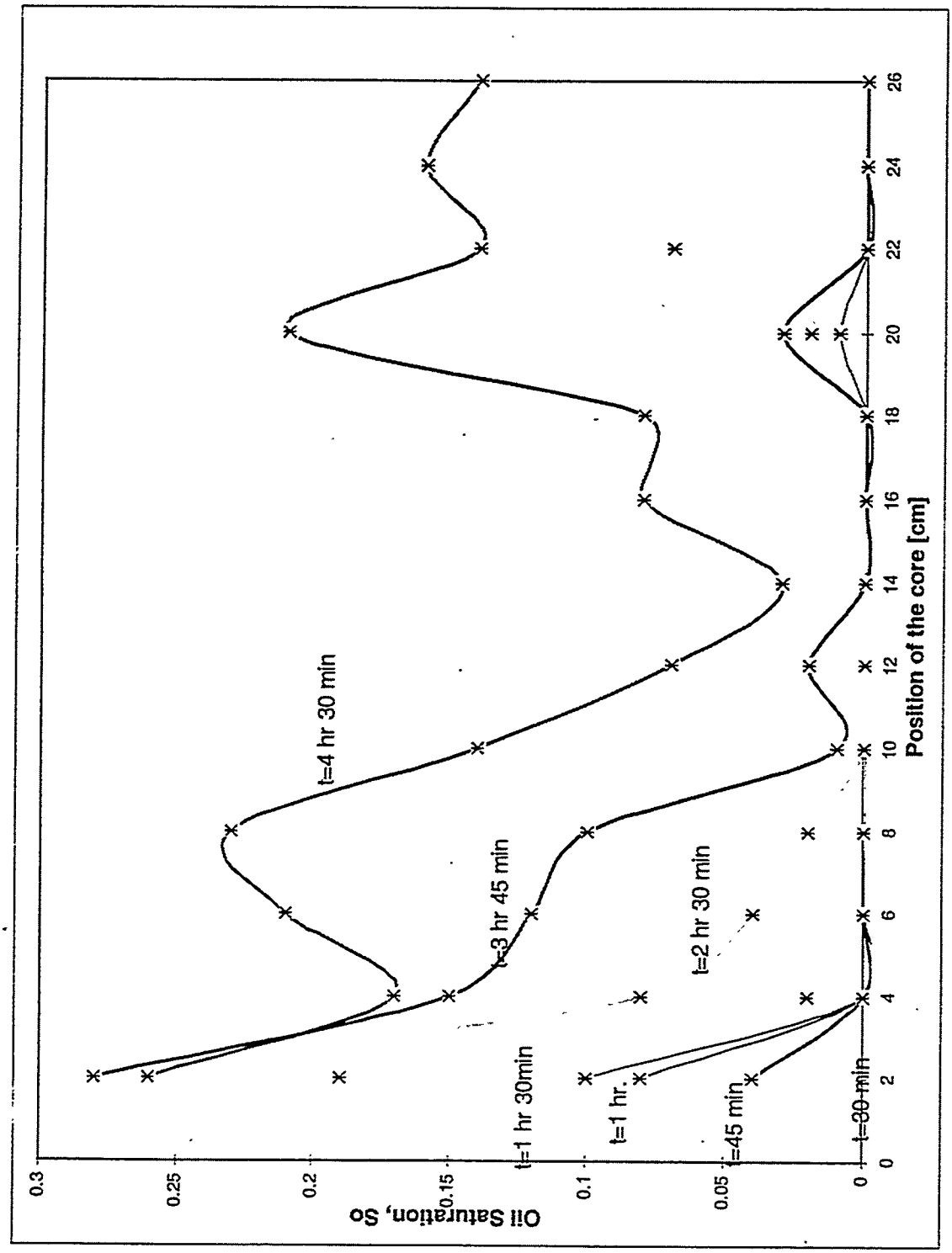

Figure 14. Oil Saturation Profiles for Thin Fracture sytem for diferent time of Oil injection

after 1 hour

press. port

0.99, 0.05	0.98, 0.04	0.98, 0.06	0.96, 0.15	0.57, 0.50	0.46, 0.53	0.11, 0.31
1.00, 0.04	0.99, 0.04	1.00, 0.04	0.99, 0.06	1.00, 0.07	0.99, 0.08	0.90, 0.09
0.96, 2.18	*0.99, 2.08*	*1.00, 0.10*	*0.98, 0.44*	*0.78, 0.44*	*0.71, 0.48*	*0.48, 0.53*

press. port

-0.01, 0.04	-0.01, 0.03	0.02, 0.07	-0.01, 0.03	-0.01, 0.04	-0.01, 0.03
0.48, 0.31	0.00, 0.05	0.02, 0.05	-0.01, 0.03	-0.01, 0.03	-0.01, 0.03
0.20, 1.41	*0.00 0.83*	*0.03, 0.55*	*0.00, 0.91*	*0.00, 0.48*	*0.01, 0.06*

Figure 15. CT Saturation images for the Wide Fracture System after 1 hr of Water injection (0.45 PV)

after 1 hr. 30 min.

press. port

0.99, 0.05	0.98, 0.05	0.98, 0.05	0.98, 0.13	0.97, 0.04	0.99, 0.06	0.95, 0.07
0.99, 0.04	0.99, 0.04	0.99, 0.05	0.97, 0.04	0.99, 0.04	0.99, 0.06	0.98, 0.04
0.95, 2.27	*0.98, 2.06*	*1.00, 0.10*	*0.99, 0.13*	*0.99, 0.11*	*0.99, 0.10*	*0.97, 0.10*

press. port

0.75, 0.29	0.64, 0.39	0.50, 0.41	0.16, 0.26	-0.01, 0.04	-0.01, 0.03
0.99, 0.04	0.96, 0.04	0.93, 0.05	0.74, 0.15	0.20, 0.19	-0.01, 0.04
0.83, 1.09	*0.77, 0.86*	*0.68, 0.55*	*0.41, 0.78*	*0.09, 0.57*	*0.01, 0.60*

Figure 16. CT Saturation images for the Wide Fracture System after 1 hr 30 m of Water injection (0.67 PV)

after 2 hour

press. port

0.98, 0.06	0.98, 0.05	0.98, 0.04	0.98, 0.12	0.98, 0.04	0.97, 0.06	0.97, 0.04
0.99, 0.04	0.99, 0.04	0.99, 0.05	0.97, 0.05	0.99, 0.04	0.98, 0.04	0.98, 0.04
0.96, 1.29	*0.98, 1.97*	*1.00, 0.12*	*0.98, 0.40*	*0.99, 0.10*	*0.99, 0.10*	*0.98, 0.09*

press. port

0.97, 0.04	0.98, 0.04	0.99, 0.10	0.95, 0.08	0.96, 0.06	0.85, 0.20
0.98, 0.04	0.98, 0.04	1.00, 0.05	0.98, 0.04	0.98, 0.04	0.98, 0.04
0.96, 1.50	*0.95, 1.12*	*0.96, 0.72*	*0.95, 1.57*	*0.93, 0.70*	*0.88, 1.31*

Figure 17. CT Saturation images for the Wide Fracture System after 2 hr of Water injection (0.89 PV)

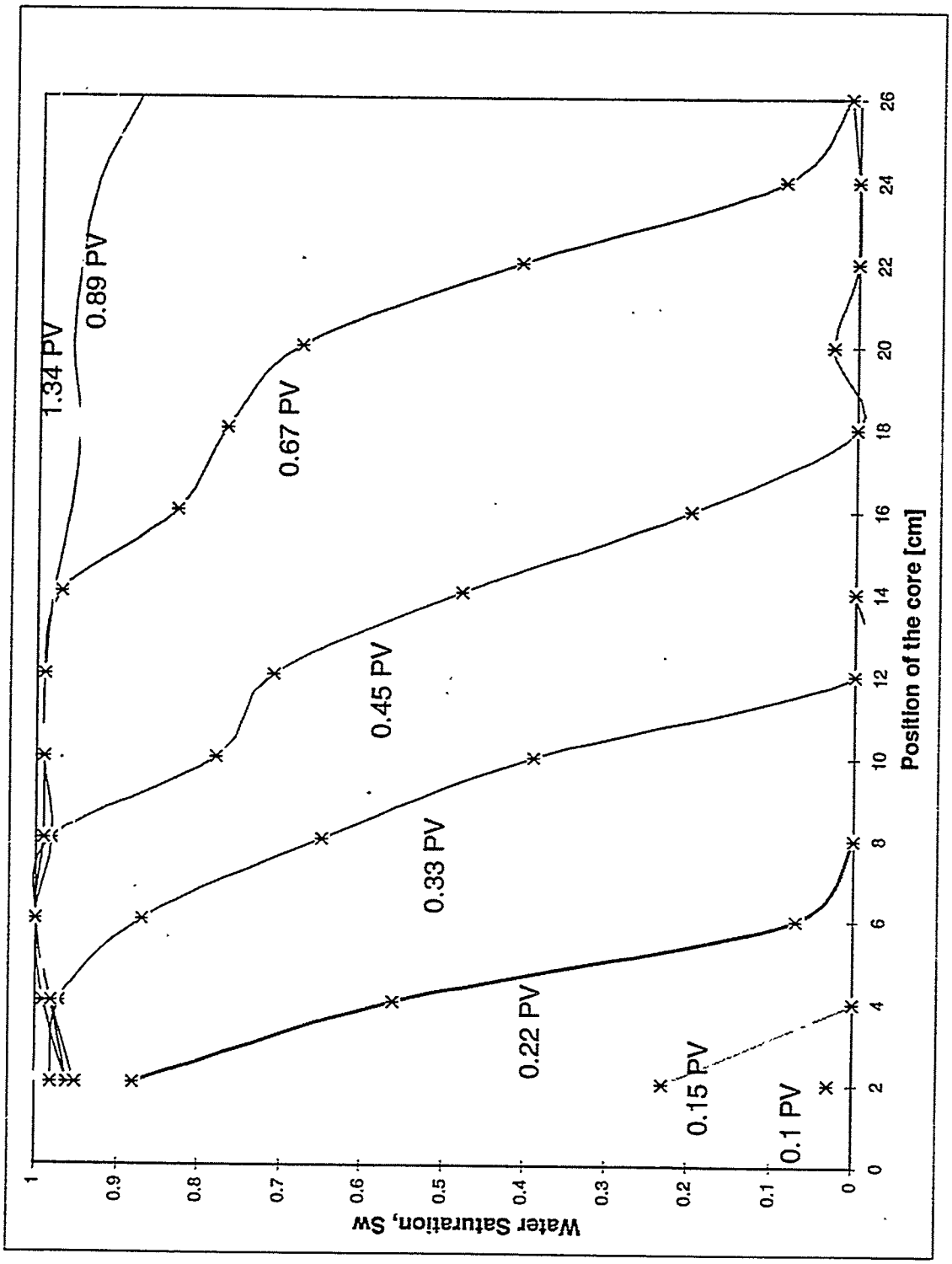

Figure 18. Water Saturation Profiles for Wide Fracture sytem for different PV of Water injection

after 2 hr. 30 min.

press. port

0.02, 0.11	-0.06, 0.13	-0.07, 0.11	0.01, 0.23	-0.04, 0.12	-0.05, 0.12	-0.06, 0.13
0.02, 0.09	-0.05, 0.09	-0.05, 0.10	0.11, 0.23	-0.03, 0.11	-0.03, 0.14	-0.03, 0.10
0.17,10.15	-0.02, 0.92	*-0.02, 0.45*	*0.10, 0.43*	*-0.02, 0.25*	*-0.02, 0.26*	*-0.04, 0.25*

press. port

-0.03, 0.12	0.01, 0.12	-0.06, 0.18	0.02, 0.12	0.02, 0.10
-0.01, 0.09	0.00, 0.10	-0.05, 0.14	0.01, 0.12	0.01, 0.09
-0.12, 8.15	*0.02, 4.61*	*-0.06, 9.22*	*0.10,14.12*	*-0.01,12.20*

Figure 19. CT Saturation images for the Wide Fracture System after 2 hr 30 m of Oil injection (1.11 PV)

after 3 hr. 45 min.

press. port

0.04, 0.13	-0.02, 0.13	0.00, 0.11	0.01, 0.21	0.04, 0.12	0.03, 0.11	0.01, 0.13
0.02, 0.09	-0.02, 0.09	0.01, 0.10	0.19, 0.22	0.05, 0.11	0.03, 0.14	0.02, 0.10
0.21, 9.91	0.04, 1.10	*0.04, 0.36*	*0.16, 0.32*	*0.05, 0.17*	*0.04, 0.19*	*0.03, 0.86*

press. port

0.03, 0.09	0.06, 0.12	-0.01, 0.21	0.07, 0.12	0.08, 0.12	0.07, 0.11
0.03, 0.10	0.04, 0.11	-0.02, 0.14	0.02, 0.09	0.06, 0.11	0.04, 0.09
-0.12,10.72	*0.06, 5.24*	*0.00, 9.30*	*0.13,14.61*	*0.01,14.06*	*0.14, 7.90*

Figure 20. CT Saturation images for the Wide Fracture System after 3 hr 45 m of Oil injection (1.67 PV)

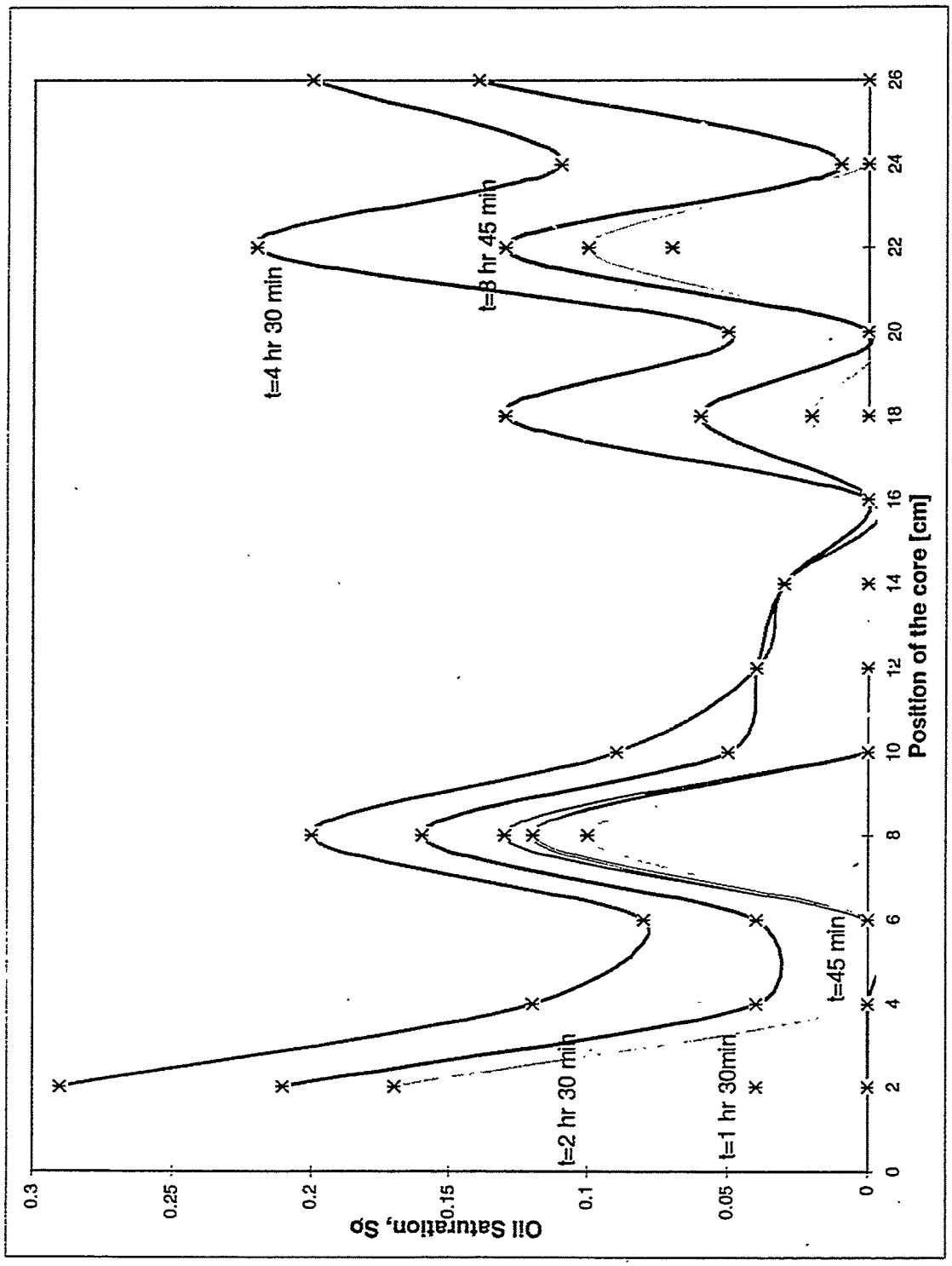

Figure 21. Oil Saturation Profiles for Wide Fracture sytem for diferent time of Oil injection

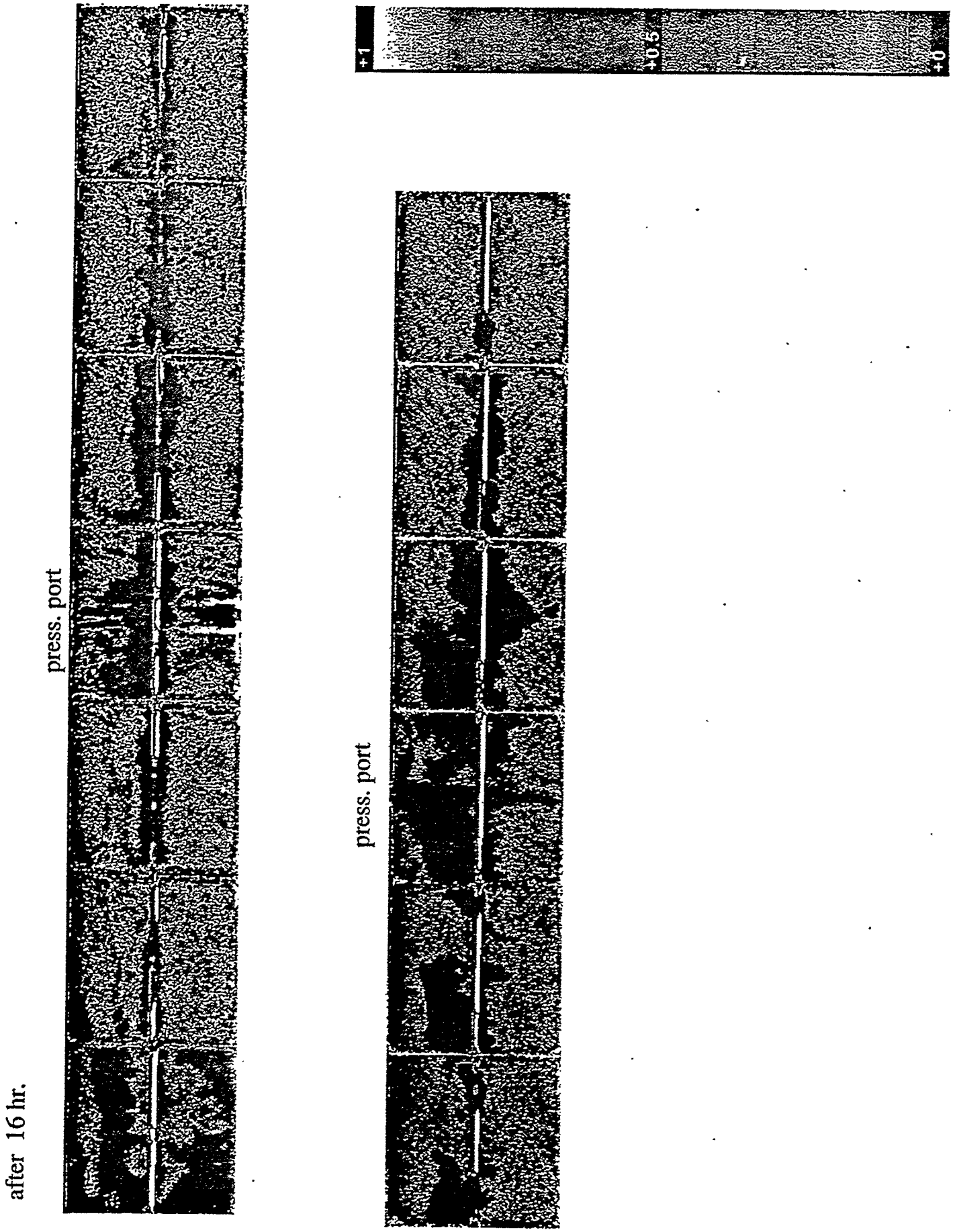

Figure 22. CT Saturation images for the Wide Fracture System after 16 hr of Water injection (7.11 PV)

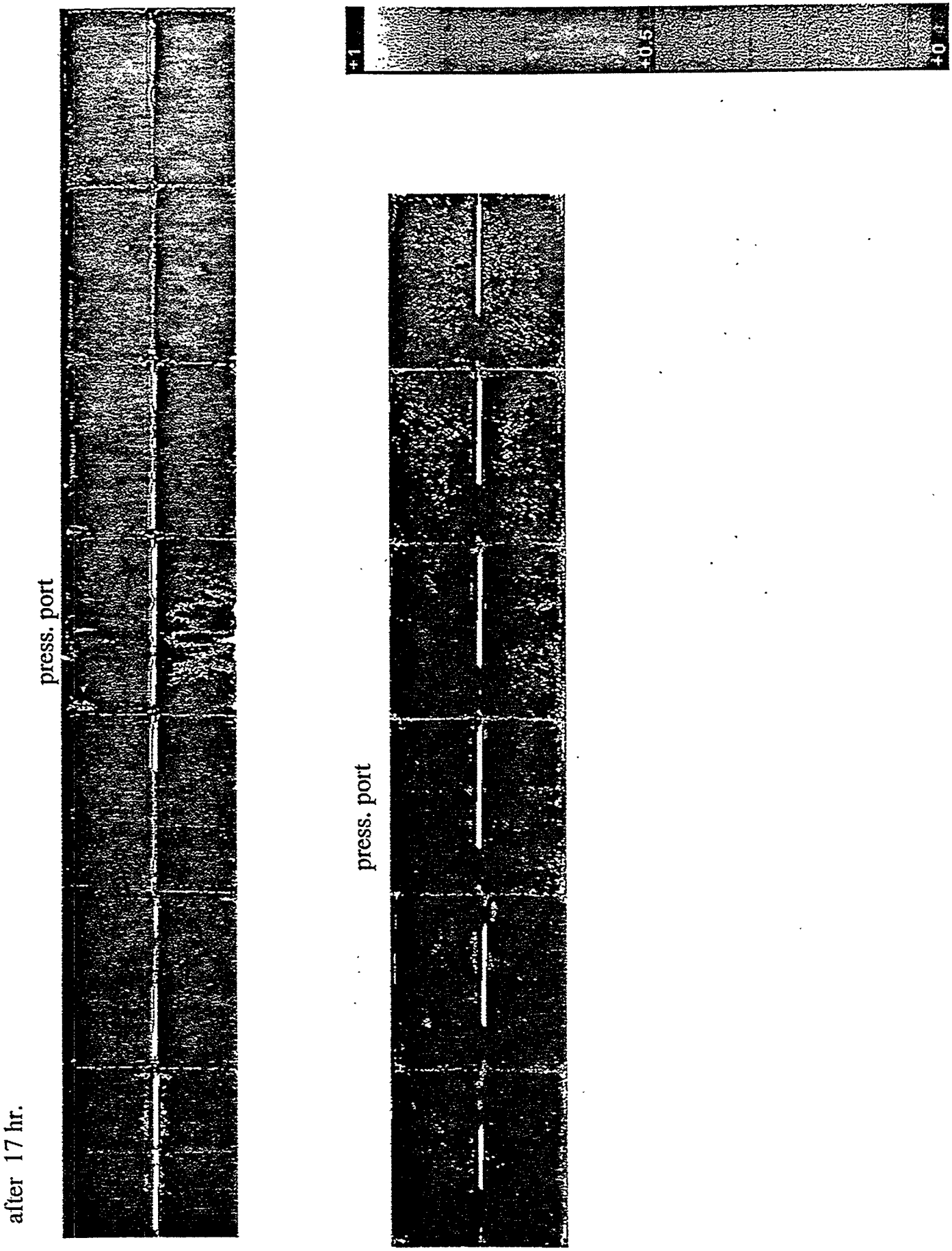

Figure 23. CT Saturation images for the Wide Fracture System after 17 hr of Water injection (7.56 PV)

Water Injection (thinner fracture)

0.22 PV (30 min)

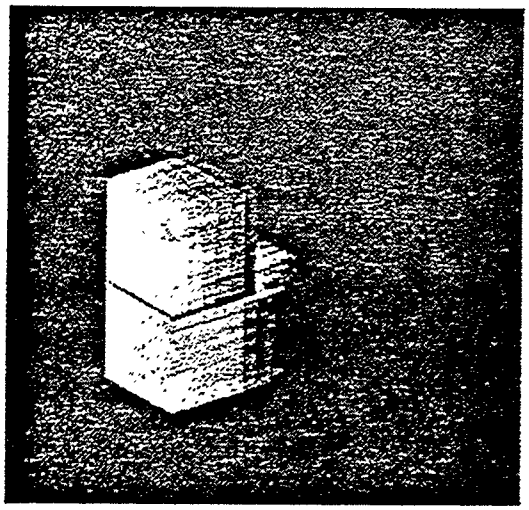

0.33 PV (45 min)

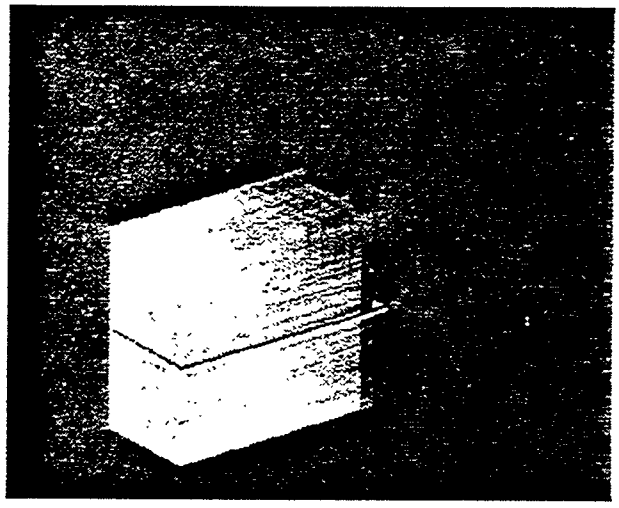

Figure 24. 3-D Reconstructions for the Thin Fracture system

0.45 PV (1hr.)

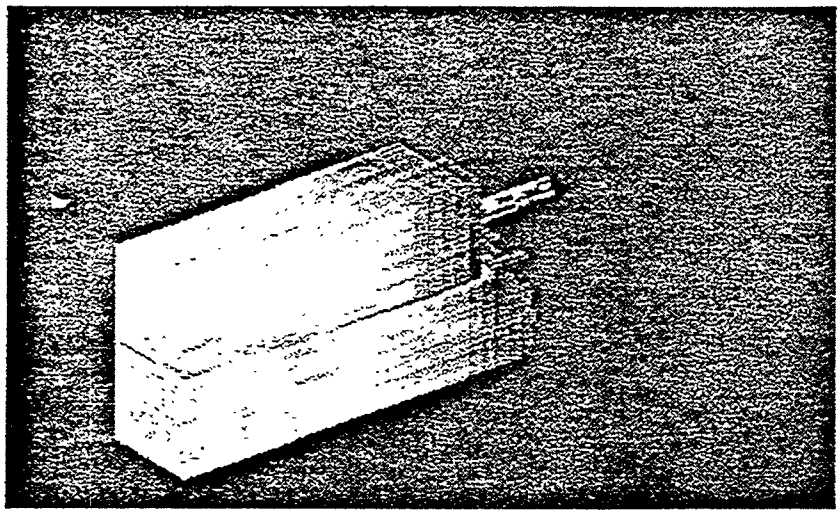

0.67 PV (1hr. 30 min)

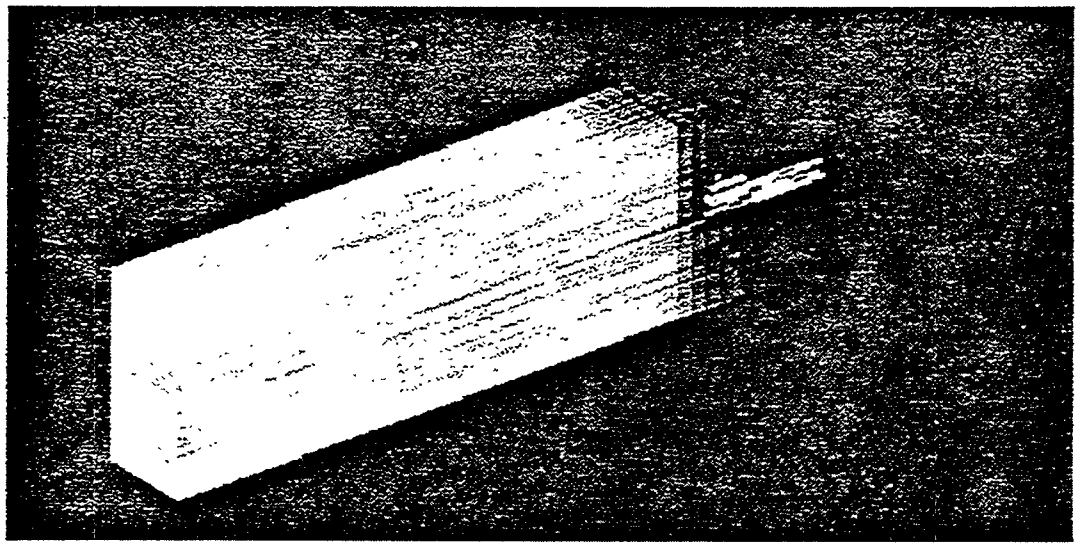

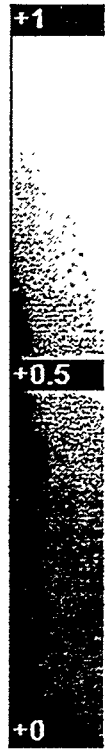

0.89 PV (2 hr.)

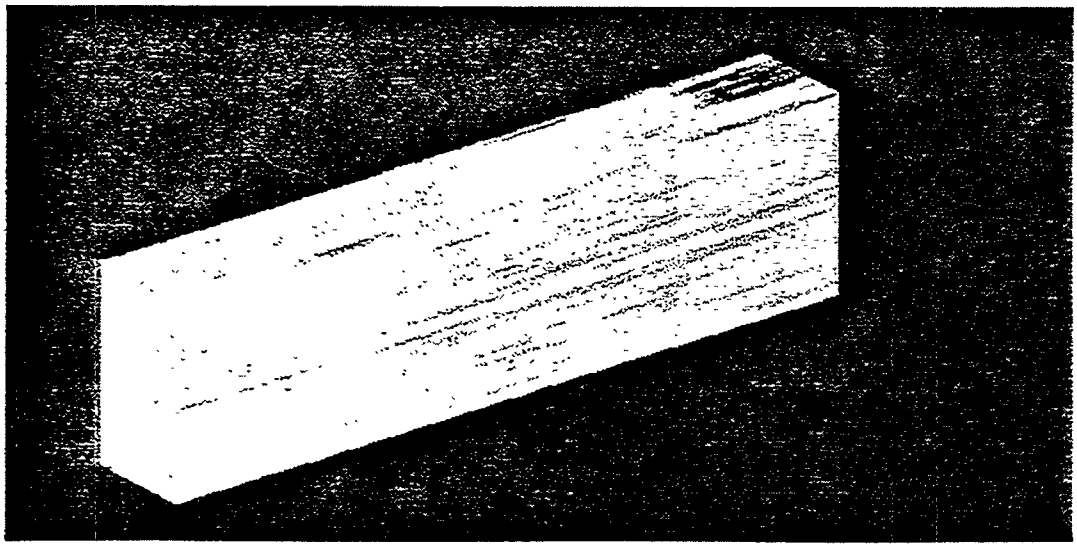

Figure 25. 3-D Reconstructions for the Thin Fracture system

Water Injection (wider fracture)

0.22 PV (30 min)

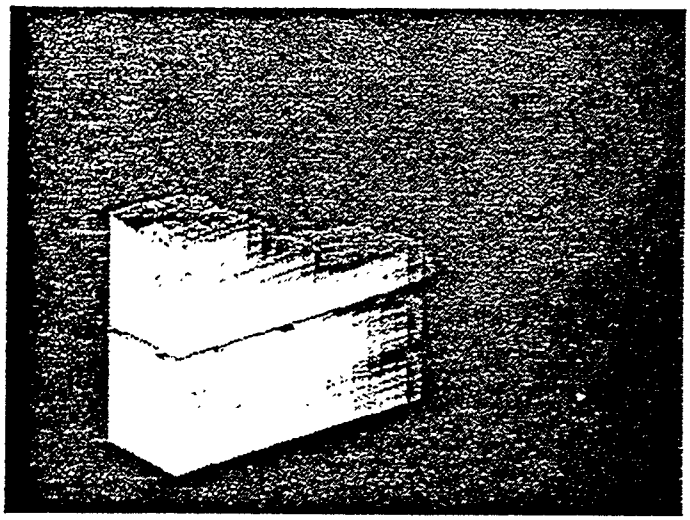

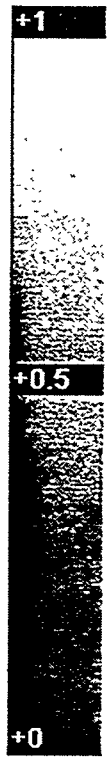

0.33 PV (45 min)

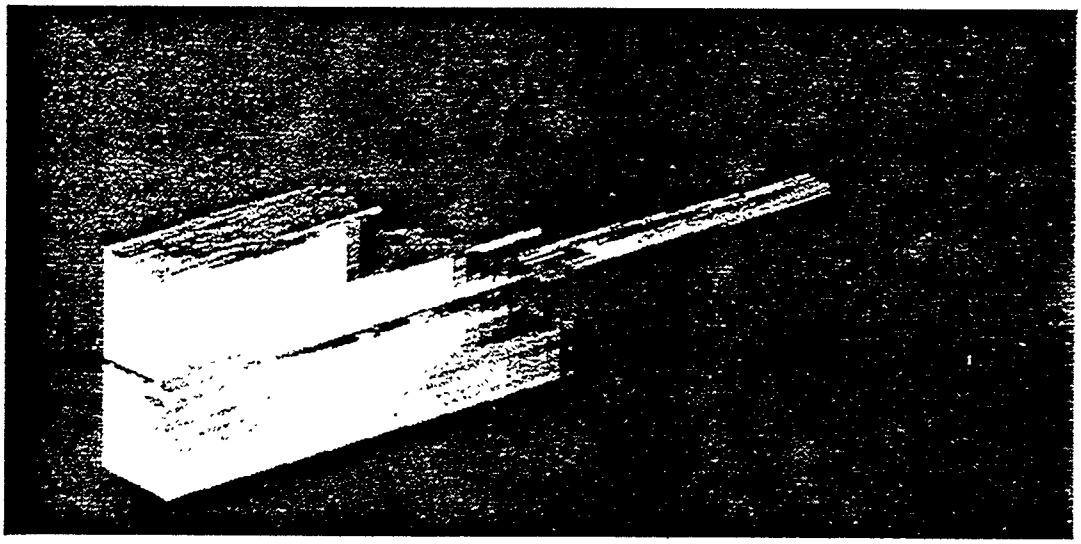

Figure 26. 3-D Reconstructions for the Wide Fracture system

0.45 PV (1hr.)

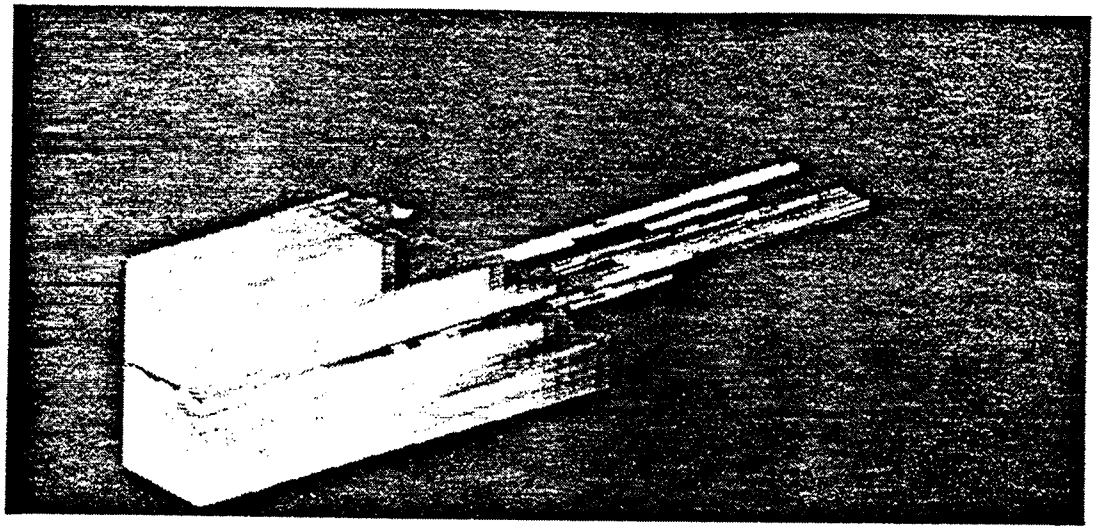

0.67 PV (1hr. 30 min)

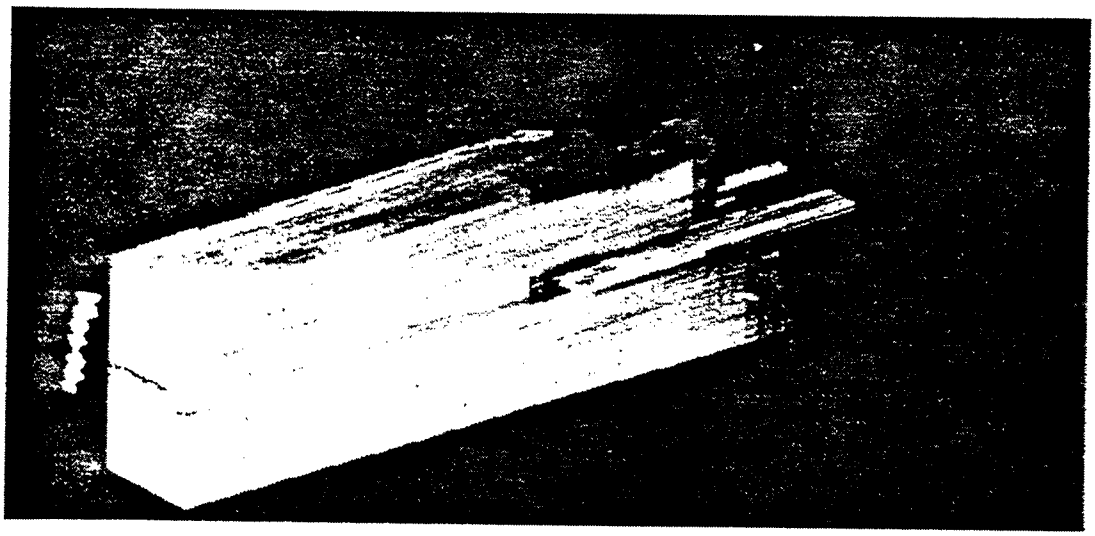

0.89 PV (2 hr.)

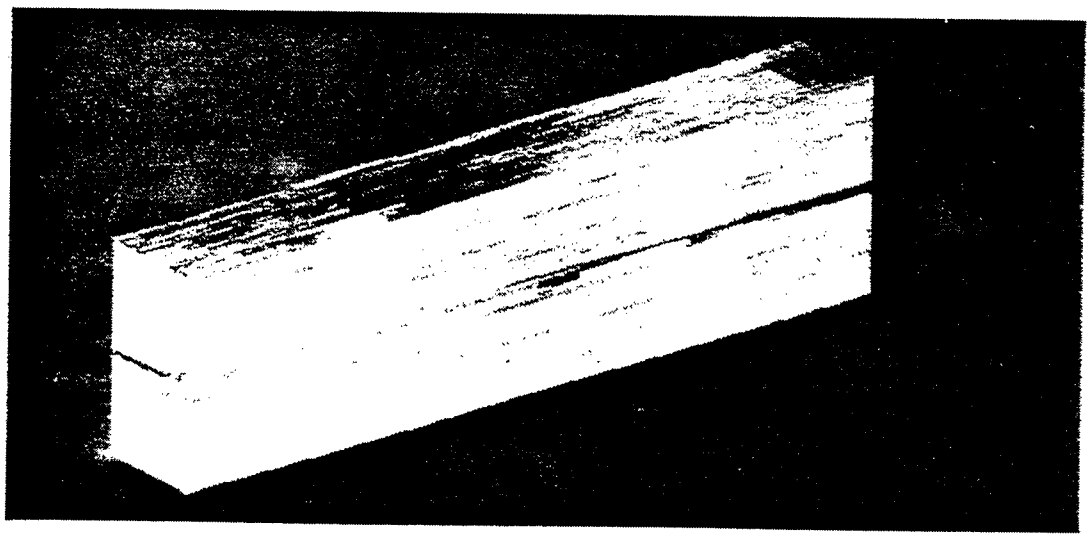

Figure 27. 3-D Reconstructions for the Wide Fracture system

Oil Injection *(thinner fracture)*

1 hr. 30 min

2 hr. 30 min

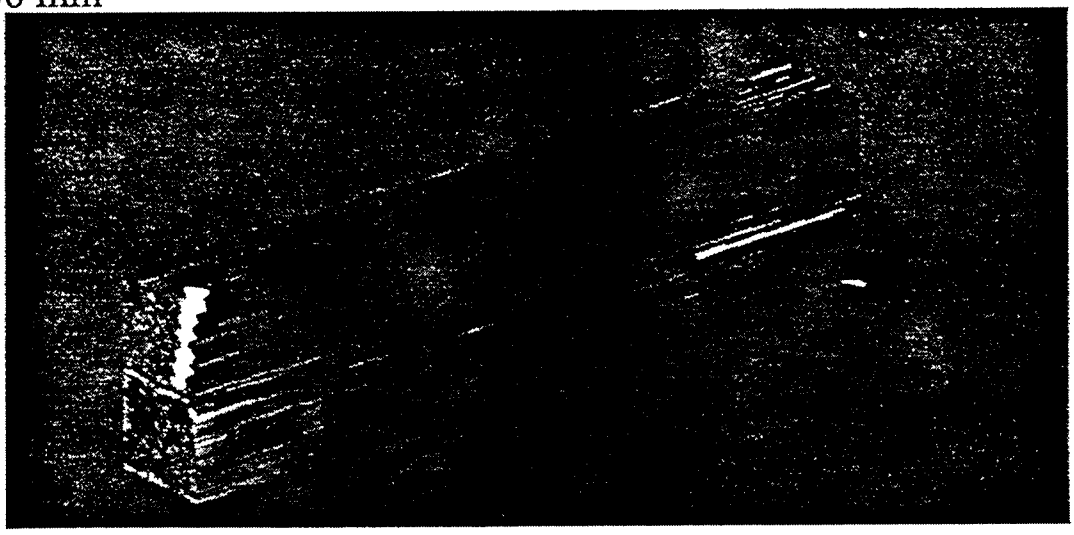

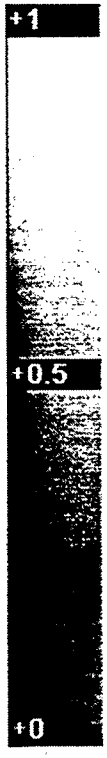

3 hr. 45 min

Figure 28. 3-D Reconstructions for the Wide Fracture system

1 hr. 30 min

Oil Injection (wider fracture)

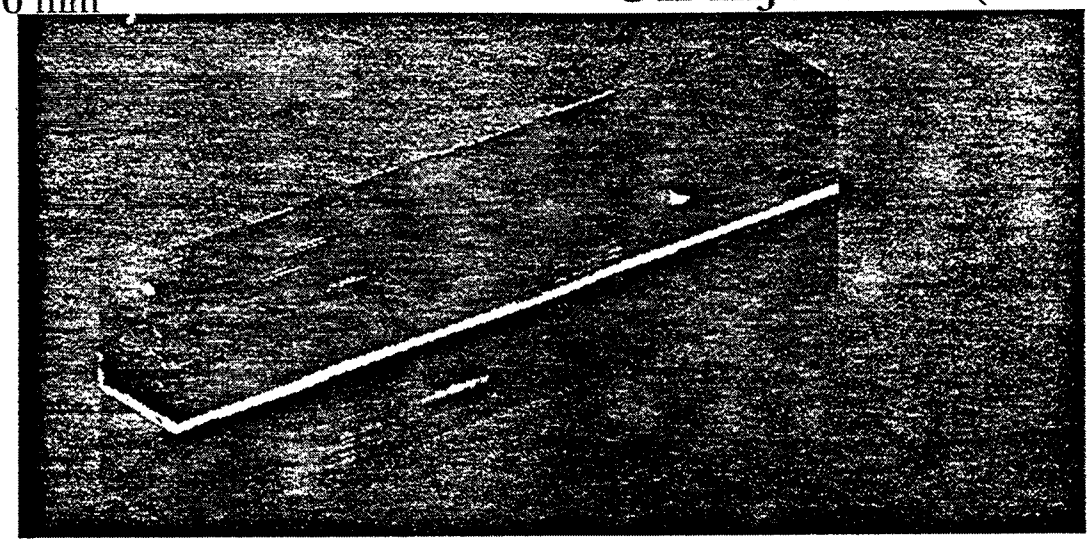

2 hr. 30 min

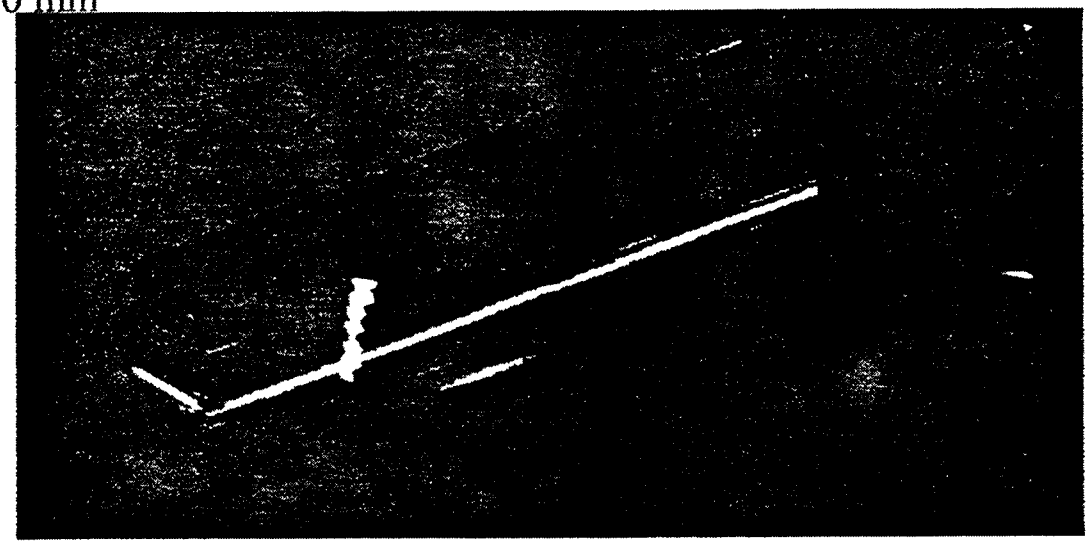

3 hr. 45 min

Figure 29. 3-D Reconstructions for the Wide Fracture system

2.1 IN-SITU COMBUSTION USING WATER SOLUBLE METALLIC ADDITIVES

(U. Diwan)

2.1.1 INTRODUCTION

Crude oils are often grouped into three categories based on specific gravity range:

1. Heavy Oil (10°-20°API)
2. Intermediate Oil (20°-30°API)
3. Light Oil (greater than 30°API)

Heavy oils consist mainly of high density naphthenes, aromatics and heteroatoms that are poor in alkanes, while light oils consist mainly of alkanes (Boduszynski, 1987; Boduszynski, 1988). Bitumen or tar are extremely dense hydrocarbons (about 10°API or less), and are non-volatile liquids, semi-solids or solids.The deposits are often referred to as oil sands or tar sands.

2.1.2 IN-SITU COMBUSTION

In-situ combustion is a thermal recovery technique in which a part of the heavy oil in place is burned to generate heat. This heat brings about a reduction in viscosity of the crude oil to get improved mobility and hence oil production rate and recovery. In a laboratory the process of ignition is initiated by using electric heaters while a stream of air is injected into a combustion tube to initiate and sustain combustion. Pure oxygen may also be used, but for economy sake air is popular. The fuel that is burned is the unrecoverable carbon rich residue of that is left on the reservoir matrix behind the steam front as a result of steam distillation, thermal cracking and some catalytic cracking. The heat that is generated partially distills the crude oil. The lighter ends are distilled off, and they condense in the cooler regions ahead of the combustion front along with the vaporized connate water and water produced as a combustion byproduct. The region ahead of the combustion front is heated by conduction, by convection of combustion gases, and by the condensation of volatiles (light ends) and steam. The oil ahead of the combustion front is displaced toward the production well by gas drive

provided by the combustion gases, by hot water and steam steam drive, and by miscible drive provided by the condensed light hydrocarbons (Alexander *et al.*, 1962; Holt, 1992).

A typical combustion front moves through the reservoir matrix by consuming the fuel as it moves ahead, thereby leaving no oil behind the burning front. Figure 1 (Shallcross, 1989) shows the typical combustion zones and a temperature profile of the in-situ combustion process. As the combustion front approaches the volume element, the temperature of the element rises and water and light ends are vaporized. These vapors are carried in the gas stream and condense in the cooler regions ahead of the combustion front. The water vapors condense to form a water bank (E), following a bank of light hydrocarbons (F). A steam plateau (D) comprises of the steam-liquid, two-phase region. As the temperature in the volume element exceeds 350°*C* the oil undergoes thermal cracking to form a volatile fraction and a low volatility heavy residue (represented by C). The volatile fraction gets carried in the gas stream and the heavy residue constitutes the fuel which gets burned in the combustion zone (B). The heat generated in the combustion zone gets transported ahead of the front by conduction and convection by the vapors and liquids. The combustion zone is often only a few inches in thickness and has a temperature in the range 350° - 650°*C*. As the combustion front moves past this volume element it leaves behind a zone of clean sand (A) which serves as a preheater for the incoming air.

2.1.2.1 Applicability, Merits and Demerits of In-situ Combustion

In-situ combustion is applicable to a wide range of reservoir fluid characteristics. The absence of well bore heat losses in the injection well allows in-situ combustion to be carried out in deeper reservoirs having thinner, tighter sand sections which are not amenable to steam injection. The oil that is produced is also lighter than the oil in place as a result of cracking and distillation.

This technique is amongst the most energy efficient of improved oil recovery methods available today for heavy oils. However, one major constraint that limits its practical application is the amount of fuel formation in the matrix. If a sufficient amount of fuel is not deposited, as is often the case for light oils, the combustion front will not sustain itself. Conversely, if the quantity of fuel deposited is large, as is often the case with very heavy oils, the rate of advance of the front tends to be slower, with an uneconomically high demand for compressed air to sustain combustion (Alexander *et al.*, 1962).

As a result it would be desirable to find substances that alter the reaction kinetics of oil oxidation during in-situ combustion. There are a number of factors affecting the rates of these reactions, among which are the composition and concentration of the catalyst, surface of the catalyst available for reaction temperature. Combustion tube studies with metallic additives (Baena *et al.*, 1990; Castanier *et al.*, 1992; Holt, 1992) have shown that the addition of water soluble metallic salts can change the reaction kinetics of combustion. These indicate an increased fuel deposition in runs which carried salts of iron or tin. It has not been established for certain how the presence of theses substances affect the fuel deposition mechanism, but it may be due to the reduction in the temperature required for cracking reactions.

Kinetic tube studies with metallic additives (de los Rios *et al.*, 1988; Shallcross, 1989) indicate that aqueous solutions of certain metallic salts like zinc, iron and tin increased the fuel concentrations. All these studies indicate that the overall oxidation mechanism of crude oils in porous media is the result of an overlap of several reactions that occur at different ranges of temperature. These have been classified as low temperature, medium temperature and high temperature reactions.

In a properly designed combustion process there should be minimal amount of low temperature oxidation (Agrawal and Sidqi, 1996). Therefore, the presence of metallic additives, which affect reaction kinetics, would affect the overall performance of the combustion process. It is believed that low temperature oxidation reactions affect fuel formation, therefore the alteration of this reaction would affect fuel deposition characteristics.

Earlier work done by De Los Rios (1987), has shown, on a quantitative basis, that the use of metallic additives affects the nature of the fuel formed; this, in turn, will affect the heat of combustion, the air-oil ratio, the air requirements, the front velocity and the oil recovery rate.

2.1.2.2 Metallic Additives in In-situ Combustion

Studies on the effect of metallic additives (salts) on in-situ combustion date back to the early nineteen seventies. It was observed that reservoirs having mineral contents with high metallic content in the rock matrix had increased fuel deposition (Burger and Sahuquet, 1972). Early attempts at understanding the mechanics of oil oxidation reactions was done through kinetic tube experiments in the presence of metallic additives.

A brief description to explain how the oxidation reactions take place is given on the following page.

2.1.2.3 Kinetic Studies with Metals and Metallic Additives

Several studies have been performed to determine the influence of metals and metallic additives on the oxidation characteristics of crude oils. The work performed and observations made during these experiments are described below.

1. Of particular importance to the current study are the kinetic studies performed by De Los Rios (1988) and Shallcross (1989) at Stanford University. De Los Rios performed kinetic experiments on Huntington Beach Oil and various metallic additives. Shallcross performed kinetic experiments on Huntington Beach and Venezuelan oils with various metallic additives. Both studies analyzed oxygen consumption data by decoupling the total oxygen consumption data into three parts. This was done to represent the oxygen consumed by the three competing groups of reactions. The found that metallic additives iron and tin increased oxygen consumption. They also reported that iron and tin increased the reaction rates for the oxidation reactions. They found that zinc did not produce the effects reported for iron and tin. From the results of these studies it was expected that iron and tin may be useful agents in catalyzing combustion reactions (Mamora, 1993).
2. Burger and Sahuquet (1981) report on two kinetic runs using 2000 ppm copper performed on a 27°API oil. The activation energy for the LTO was found to be lowered due to the copper additive (Holt, 1992).
3. Fassihi *et al.* (1981) report on kinetic experiments with 2000 ppm copper says that the activation energy of the LTO was unaffected, but it's reaction rate was increased. Fassihi also reported that the activation energy for the high temperature portion of the reaction was reduced (Baena *et al.*, 1990; Mamora, 1993).

Reactions taking place:

1. Low temperature oxidation (LTO)	Result in formation of peroxides, hydroperoxides, aldehydes, ketones, carboxylic acids and alcohols (Burger and Sahuquet, 1972). Alexander *et al.*(1962) and Al-Saadon (1970) showed that fuel availability was increased when LTO of crude oil took place. Dabbous and Fulton (1974) corroborated this and also found that LTO causes a substantial decline in recoverable oil from the distillation and cracking zones, an increase in the fuel deposition and marked changes in the fuel characteristics and coked sand properties. Weijdema (1968) and Fassihi (1981) found that the order for the LTO reaction, in terms of the partial pressure of oxygen, was close to unity.
2. Medium temperature oxidation (MTO)	Involve distillation, visbreaking and coking of the fuel along with partial oxidation of the products formed (Bardon and Gadelle, 1977; Fassihi, 1981; Sidqi *et al.*, 1985). The amount of coking and atomic H/C ratio of the fuel were found to decrease with increasing coking temperature (Bousaid, 1967). Increasing pressure was found to increase the amount of hydrocarbon residue formed; but the fuel deposited has a lesser hydrogen content (Sidqi *et al.*, 1985).
3. High temperature oxidation (HTO)	Involve oxidation of the cracked hydrocarbon residue. HTO takes place according to the following equation:

$$CH_n + \left(\frac{2m+1}{2m+2} + \frac{n}{4}\right) O_2 \rightarrow \left(\frac{m}{m+1}\right) CO_2 + \left(\frac{1}{m+1}\right) CO + \left(\frac{n}{2}\right) H_2O$$

m: ratio of carbon dioxide to carbon monoxide formed upon oxidation of the fuel

n: atomic hydrogen to carbon ratio of fuel burned

The reaction rate has been found to be first order with respect to the fuel concentration and was found to have an order of 0.5 to 1.0 with respect to the oxygen partial pressure (Dabbous and Fulton, 1974).

To recap:

- It has been found by previous researchers that the presence of certain metals can affect the kinetic parameters used to model combustion reactions.
- These kinetic experiments can give estimates of activation energies and reaction rates for combustion reactions.

2.1.2.4 Tube Studies with Metallic Additives

Observations that the physical and chemical properties of the core material can affect the combustion performance in tube runs was made by several researchers. Some of them are mentioned below.

1. Vossoughi *et al.*, 1982, Hardy *et al.*, 1972, Alexander *et al.*, 1962 observed that, for a particular oil, more fuel can be expected from a native core than from a clean sand pack. This is believed to result from both physical and chemical processes. Fine grained material in native cores provides more surface area for combustion reactions while metals in natural minerals act as catalysts (Baena *et al.*, 1990; Bardon and Gadelle, 1977).
2. Baena *et al.*, 1990 report on experiments with 22°API Huntington Beach Oil. They observed that tin and iron additives increased oxygen utilization efficiency, burning front velocity, and fuel concentration. The zinc additive showed lesser effect (Baena *et al.*, 1990).
3. Castanier *et al.*, 1992 report on thirteen metallic additive combustion tube runs. The runs made with 10°API Hamaca oil show that tin and iron increased the fuel deposition, oxygen utilization efficiency, and front velocity while zinc was less effective (Bardon and Gadelle, 1977).

2.1.3 PRESENT STUDY

The present study shall involve a series of combustion tube experiments performed with the Wilmington Oil (~15°API) and a couple of aqueous metallic additives.

2.1.4 WORK COMPLETED

- Thermocouple testing
- Calibration of mass flow meter
- Calibration of mass flow controller
- Calibration of carbon monoxide gas analyzer
- Calibration of carbon dioxide gas analyzer

2.1.5 FUTURE WORK

- Calibration of oxygen analyzer
- Checking apparatus for leakages
- Checking data logger
- Transducer calibration to measure pressure drop along tube
- Conduct a trial run using no packing, just air
- Observe temperature profiles
- Pack the combustion tube with the crude oil
- Perform runs

2.1.6 REFERENCES

1. Agrawal, V.K. and Sidqi, A.: "A Study of In-situ Combustion on Saudi Tar," Stanford University Petroleum Research Institute, SUPRI-TR-105 [DE-FG22-93BC14899], Stanford University, Stanford (April 1996).
2. Alexander, J.D., Martin, W.L., and Dew, J.N.: "Factors Affecting Fuel Availability and Composition During In-Situ Combustion," *J. Pet. Tech.* (October 1962) 1154-1162.
3. Baena, C.J., Brigham, W.E., and Castanier, L. M.: "Effect of Metallic Additives on In-Situ Combustion of Huntington Beach Crude Experiments," Stanford University Petroleum Research Institute, SUPRI-TR-78 [DE-FG19-87BC14126], Stanford University, Stanford (August 1990).

4. Boduszynski, M. M.,: "Composition of Heavy Petroleums. 1. Molecular Weight, Hydrogfen Deficiency, and Heteroatom Concentration as a Function of Atmospheric Equivalent Boiling Point upto 1400°F (760°C)," *Energy & Fuels* (1987) **1**.
5. Boduszynski, M. M.,: "Composition of Heavy Petroleums. 2.Molecular Characterization," *Energy & Fuels* (1988) **2**.
6. Bardon, C. And Gadelle, C.: "Essai de Laboratoire Pour L'Etude de la Combustion In-Situ," Institute Francais du Petrole, Paris (May 1977).
7. Bousaid, I.S. and Ramey, H.J. Jr.: "Oxidation of Crude Oil in Porous Media," *Soc. Of Pet. Eng. J.* (June 1968) 137-148.
8. Combustion Kinetics," *Soc. Pet. Eng. J.* (October 1972) 410-420.
9. Castanier, L. M., Baena, C.J., Tavares, C., Holt, R. J., and Brigham, W.E.: "In-Situ Combustion with Metallic additives," No. SPE 23708, paper presented at the SPE-AIME Latin merican Petroleum Engineering Conference, Caracas (March 1992).
10. Dabbous M.K. and Fulton, P.F.: "Low-Temperature Oxidation Reaction Kinetics and Effects on the In-Situ Combustion Process," *Soc. of Pet. Eng. J.* (June 1974) 253-262.
11. De Los Rios, C. F., Brigham, W. E., and Castanier, L. M.: "The Effect of Metallic Additives on the kinetics of Oil Oxidation Reactions in In-Situ Combustion," Stanford University Petroelum Research Institute, SUPRI-TR-63 [DE-FG19-87BC14126] Stanford University, Stanford, (November 1988).
12. Fassihi, M. R.: "Analysis of Fuel Oxidation in In-Situ Combustion Oil Recovery," PhD disertation, Stanford University, Stanford (May 1981).
13. Gureyev, A. A., and Sablena, Z. A.: "The Role of Metals in Oxidation of Hydrocarbon Fuels in the Liquid Phase," Scientific Research Institute of Fuel and Lubricating Materials, Pergamon Press (1965).
14. Holt, R. J.: "In-Situ Combustion with Metallic Additives," Stanford University Petroleum Research Institute, SUPRI-TR-87 [DE-FG22-90BC14600], Stanford University, Stanford (July 1992).
15. Mamora, D. D.: "Kinetics of In-Situ Combustion," PhD dissertation, Stanford University, Stanford, California (May 1993).
16. Shallcross, D. C.: "Modifying In-Situ Combustion Performance by the use of Water-Soluble Metallic Additives," No. SPE 19485, paper presented at the SPE-AIME Aia-Pacific Conference, Sydney, Australia (September 1989).
17. Sidqi, A., Ramey, H. J. Jr.,Pettit, P., and Brigham, W. E.: "The Reaction Kinetics of Fuel Formation for In-Situ Combustion," Stanford University Petroleum Research Institute, Stanford, CA, SUPRI-TR-46 [DE-AC03-81SF 11564] (May 1985).

18. Weijdema, J.: "Determination of the Oxidation Kinetics of the in-Situ Combustion Process," Report from Koninklijke/Shell Exploratie En Producktie Laboratorium, Rijswijk, The Netherlands (1968).

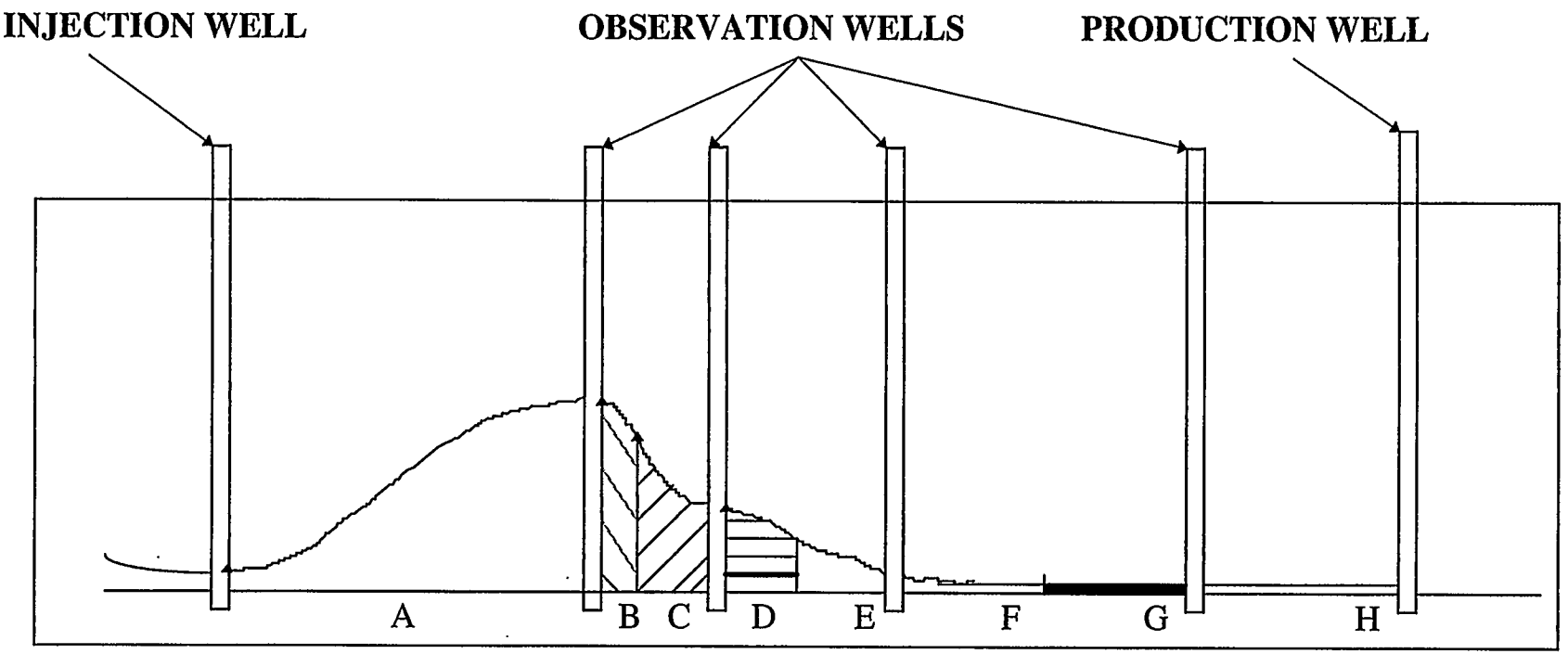

A : BURNED ZONE
B : COMBUSTION ZONE
C : CRACKING ZONE
D : STEAM PLATEAU
E : WATER BANK
F : LIGHT HYDROCARBONS
G : OIL BANK
H : INITIAL ZONE

Fig 1 ! TEMPERATURE PROFILES AND CORRESPONDING COMBUSTION ZONES

3.3 VISUALIZATION OF MULTIPHASE FLOW THROUGH POROUS MEDIA AT HIGH PRESSURE

(D. George)

3.3.1 INTRODUCTION

Much research has been performed using micromodels to study foam flow through porous media (Chambers and Radke, 1989). Observations of oil-foam interactions in micromodels have also been made (Sagar, 1997). Because micromodels are not typically constructed to contain fluids at high pressure or elevated temperature, little research has been performed in which multiphase flow through porous media at high pressure conditions has been observed.

The goal of this project is to observe foam flow and oil-foam interactions in a micromodel at high pressures (greater than 100 psi). In order to achieve this goal, a pressure vessel is being constructed in which a micromodel will be housed. A confining liquid in the vessel will allow pressure within the micromodel to be increased without developing a pressure differential between the inside and the outside of the micromodel great enough to cause mechanical failure of the micromodel. A window in the pressure vessel will permit direct observation of the micromodel.

3.3.2 MICROMODELS

Micromodels are produced with the objective of directly observing fluid flow through porous media. Micromodels contain an etched flow pattern that can be viewed with a microscope. The flow pattern can be a lattice of straight or constricted channels, or the pore network can be modeled after the pores found in naturally occurring rock. Fluid enters a micromodel, flows through the porous medium, and exits the micromodel. Several studies have been performed using etched glass micromodels. Attempts were made to replicate naturally occurring pore patterns with etched glass micromodels, but the necessary etching and annealing processes resulted in a loss of surface roughness and an enlargement of pore size.

The micromodels developed by Hornbrook, *et. al.* (1992), are superior to etched glass micromodels. An almost exact replica of a thin section of Berea sandstone is reproduced on a silicon wafer. The silicon wafer is oxidized to reproduce a water-wet porous medium, and then the silicon wafer is bonded to a glass plate. These micromodels possess roughness and wettability characteristics that are approximately equal to those of the original sandstone. Futhermore, when the micromodels are produced the depth of the pore and channel network can be controlled with great accuracy.

3.3.3 PRESSURE VESSEL

An assessment of the typical conditions for an experiment was made. This led to the selection of expected operating parameters, design guidelines, and concerns about safety.

3.3.3.1 Operating Parameters

The pressure vessel should be able to operate at pressures up to 1000 psi. The temperature of the vessel should be controlled, ranging from 15°C to 50°C. Because the surface of the silicon micromodel is oxidized, higher operating temperatures demand some reconsideration of the use of silicon micromodels. Silicon dioxide (SiO_2) is appreciably soluble in water.

3.3.3.2 Design

A pressure vessel will be constructed to accommodate the micromodels. The micromodel sits inside of the body of the pressure vessel. Holes to serve as fluid inlet/outlet ports are drilled in the bottom of the micromodel. These holes rest directly above tubes that carry fluid to and from the micromodel. O-rings are used to create a seal where the tubes meet the inlet/outlet ports of the micromodel. Figure 1 details the inlet and outlet ports through which fluid will enter and exit the micromodel. Confining liquid circulates through the interior of the pressure vessel, entering and exiting through tubes that are located on opposite sides of the vessel. The confining liquid is used to control the temperature of the micromodel and provide pressure support. A 4.7 mm thick sapphire window is located directly above the

micromodel. Sapphire was selected because of its superior mechanical and optical qualities. The window will be held between the micromodel and the pressure vessel lid in a manner such that its edges are considered to be fixed. This leads to maximum mechanical strength. An O-ring between the lid and the window seals the space. The pressure vessel lid is shaped like an annular ring. The lid fits over both the body of the pressure vessel and the window, such that the window, and thus the micromodel, is viewed in the center of the annular ring, as shown in Figure 2. The lid will be held to the pressure vessel by six 1/2 inch bolts, and a seal will be provided by an o-ring located between the lid and the pressure vessel. Figure 2 displays the cross-section of each of the components of the pressure vessel and indicates the proper assembly of these components.

3.3.3.3 Safety Features

In order to prevent failure of the pressure vessel and to protect users, several safety features are designed into the pressure system. A confining liquid will be used. Liquid will not expand nearly as much as gas in the event of failure. A pressure release valve will be located in the pressure system, and set to release pressure at 1100 psi. A burst disk that will break at 1200 psi will be incorporated into the design of the pressure vessel. The pressure system will be designed for 1500 psi, even though the maximum operating pressure of the system will be 1000 psi, a factor of safety of 1.5. A shield made of Lexan (a highly impact resistant material) may surround the pressure vessel to provide an additional measure of safety to the users.

3.3.4 PROGRESS TO DATE AND A PLAN FOR CONTINUED PROGRESS

I am currently working on a literature review for the project. Marsden (1986) exhaustively describes literature relative to the topic that was generated before 1986. Sagar (1997) gives a thorough review of literature generated after 1986, and particularly literature pertaining to the observation of oil-foam interactions in micromodels. What remains to be reviewed is the most current literature and literature related to micromodel studies performed at high pressure conditions.

The design of the pressure vessel is almost complete. A final design will be produced by late January, and parts will be ordered at that time. All parts should be received by the beginning of February. The optical system that will be used to observe the micromodel from

outside of the sapphire window must be selected. To have this done by the time the parts for the pressure vessel arrive is a goal. The construction of the pressure vessel, along with the construction of the rest of the experimental apparatus (including pipes, valves, pumps, vacuums, etc.) should be completed by the end of February or the beginning of March. At this time, the system will be tested. As soon as the system is operable, safe, and effective, data collection will begin.

3.3.5 REFERENCES

1. Chambers, K.T. and C.J. Radke "Capillary Phenomena in Foam Flow Through Porous Media." in Interfacial Phenomena in Petroleum Recovery, N.R. Morrow, Editor. Surfactant Science Series. Marcel Dekker, Inc. New York, pp 191-255, 1991.
2. Hornbrook, J.W., L.M. Castanier, and P.A. Pettit "Visualization of Foam/Oil in a New High Resolution Sandstone Replica Micromodel." Report SUPRI TR-86, Stanford University, 1992.
3. Marsden, S.S. "Foams in Porous Media", SUPRI TR-37, Stanford University, 1986.
4. Sagar, N. "Oil-Foam Interactions in a Micromodel." Stanford University, 1997.

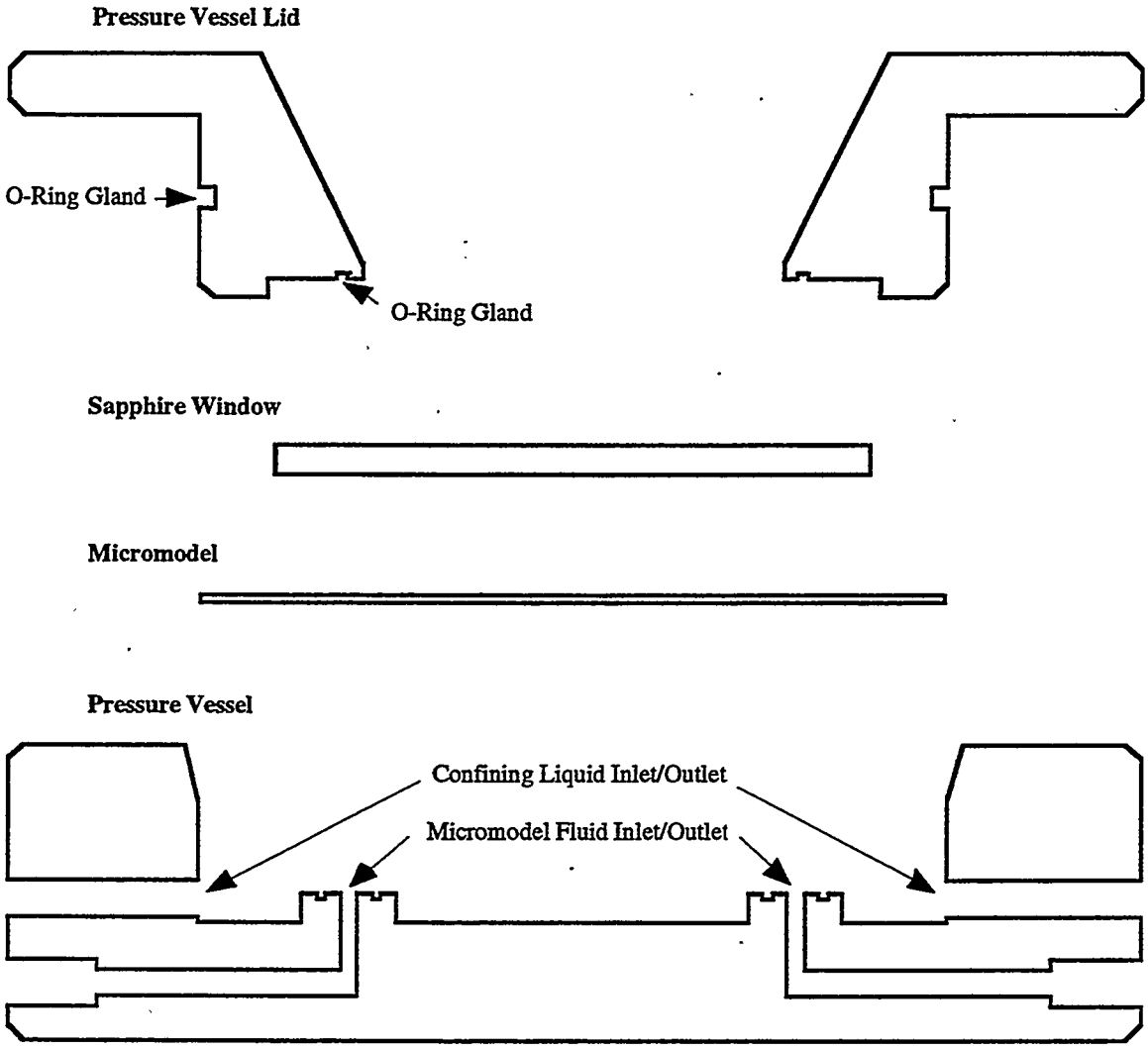

Figure 1: Exploded Cross-Sectional Diagram of the Pressure Vessel

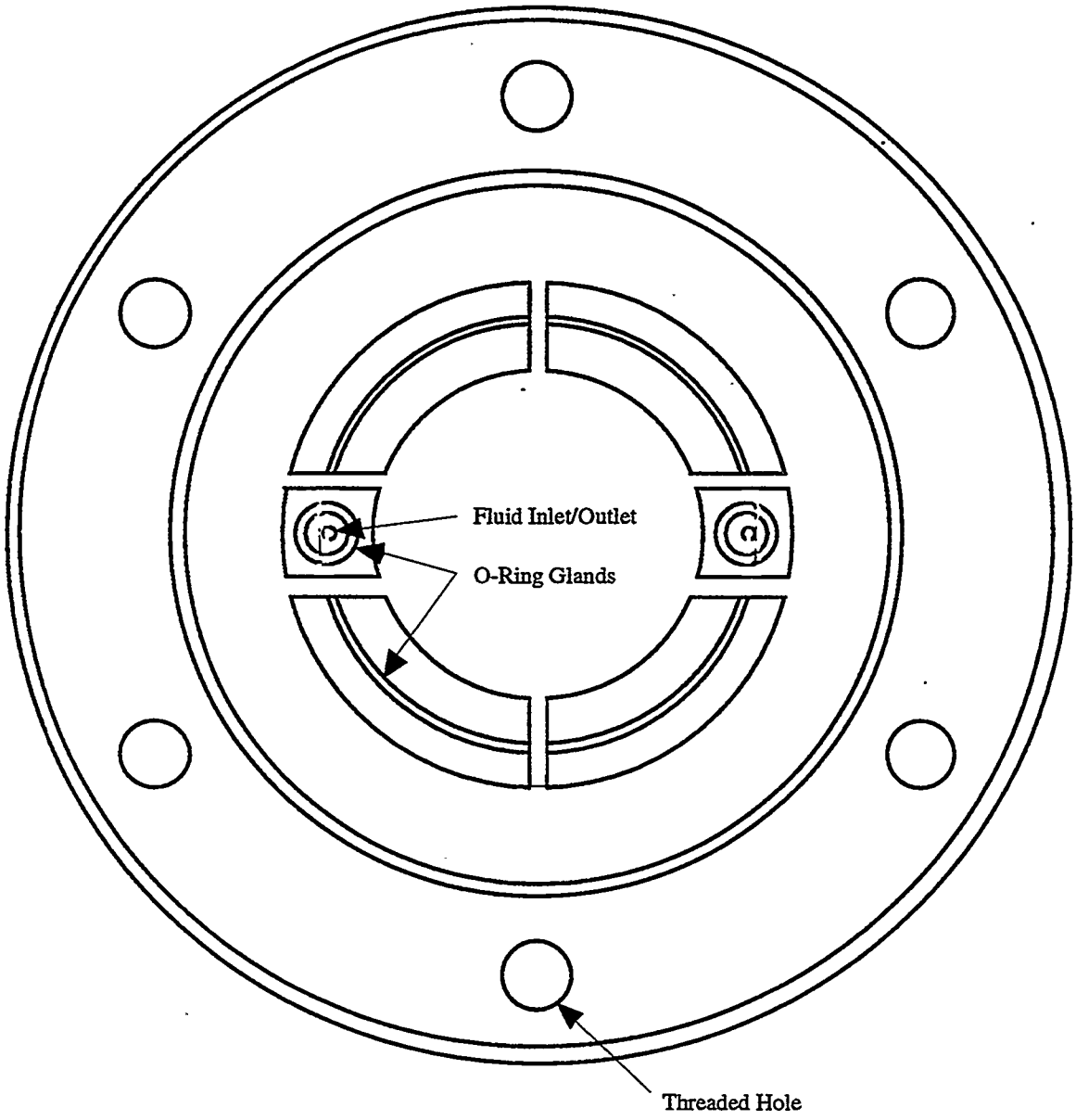

Figure 2: Top View of the Interior of the Pressure Vessel

4.2 EFFECT OF MOBILITY RATIO ON PATTERN BEHAVIOR OF A HOMOGENEOUS POROUS MEDIUM

(Y. Wang)

4.2.1 ABSTRACT

It is well known, for unit mobility ratio, that the areal sweep efficiency of a staggered line drive pattern is always better than a five spot pattern. However, this observation does not hold for very favorable mobility ratios. We present simulation results and, with the help of streamline and saturation distributions, explain the differences between unit and favorable mobility ratios. Simulations compare well with experiments conducted elsewhere. Accurate definition of breakthrough time is also discussed for multiphase, streamline, simulation results. The exact definition of breakthrough is difficult due to physical dispersion in experiments and numerical dispersion in simulations.

4.2.2 INTRODUCTION

Pattern geometry plays a major role in determining oil recovery during secondary and enhanced oil recovery operations. Although simulation is an important tool for design and evaluation, the first step often involves rough calculations based upon areal sweep efficiencies of displacements in homogeneous, two-dimensional, scaled, physical models (c.f., Dyes *et al* , 1954; Craig, 1971; Lake, 1989). These results are available as a function of the displacement pattern and the mobility ratio, M. The mobility ratio is simply the mobility of the displacing phase over that of the displaced, or resident, phase. Because it is possible to compute sweep efficiency when the displacing and displaced phase have the same mobility (Morel-Seytoux, 1966), scaled physical model results have been verified for unit mobility ratios.

Convincing verification of the non-unit mobility ratio cases does not appear in the literature. Typical finite difference solution of the reservoir flow equations suffers from numerical dispersion, the effects of which are hard to evaluate. Furthermore, the scaled physical model results at low mobility ratios ($M \ll 1$) are provocative. For instance, Fig. 1a

shows that recovery from a five spot pattern at breakthrough for 1/M greater than about 6 is virtually 100%, whereas recovery at breakthrough in Fig. 1b for a staggered line drive pattern at an 1/M of 6 is only 88%. This contradicts the common notion that areal sweep efficiency from a staggered line drive pattern is always better than that from a five spot pattern.

We use a 3D streamline simulator (Batycky *et al*, 1997) to analyze displacements in five spot and staggered line drive patterns for stable displacements, that is M less than 1. In the following sections, we present streamline distributions, saturation distributions, and fractional flow versus dimensionless time, t_D, at the producer. The dimensionless time is the pore volumes of displacing fluid injected. With the streamline and saturation distributions at different times, we explain why and at what mobility ratio the five spot pattern can recover more oil than a staggered line drive pattern.

The streamline calculation method is advantageous in that the results suffer from much less numerical dispersion than typical finite difference approximations, but some dispersion in simulation results is evident. Therefore, we discuss how to treat the numerical dispersion to obtain accurate estimates of breakthrough time. We discuss the proper way to calculate fractional flow based on the flow rates at the producer. In comparing the simulation results with the experimental results of Dyes *et al*, physical dispersion in the experiments is found even though a piston-like displacement was assumed.

4.2.3 SWEEP EFFICIENCY

Before proceeding, it is useful to recall the representation of experimental data in Fig. 1 and the meaning of sweep efficiency. Dyes *et al.* (1954) used various oils as both the injected and displaced phases. These hydrocarbons were miscible and they assumed piston-like displacement. An X-ray shadowgraph technique was used to observe the position of the displacing front. Areal sweep efficiencies are plotted versus displacable pore volumes injected for different mobility ratios. In the figure, the x axis is the reciprocal of mobility ratio. Each curve in the graphs corresponds to a specific $t_D / \Delta S$. That is, displacable pore volume injected. The bottom curves show sweep efficiency at breakthrough. It is assumed that the displacement has a piston-like front and there is no physical dispersion. Likewise, the porous medium is assumed to be perfectly homogeneous.

For piston-like displacement, the areal sweep efficiency is

$$E_A = A_S / A_T \tag{1}$$

where A_S is the swept area and A_T is the total area. Before and at breakthrough, the amount of displacing fluid injected is equal to the displaced fluid produced, disregarding compressibility. Assuming piston-like displacement, injected volume is related to area swept

$$V_I = A_S h \phi \Delta S \tag{2}$$

where V_I is the volume of displacing fluid injected, h is the thickness of the formation, and ϕ is porosity. Hence,

$$E_A = A_S / A_T = V_I / (A_T h \phi \Delta S) = t_D / \Delta S \tag{3}$$

where $t_D = V_I / (A_T h \phi)$ is the pore volume of fluid injected, also commonly called dimensionless time. For $\Delta S = 1$, $E_A = t_D$ before and at breakthrough.

After breakthrough,

$$E_A = (V_I - V_P) / (A_T h \phi \Delta S) \tag{4}$$

where V_P is volume of displacing fluid produced.

5.2.4 SIMULATION RESULTS

We use a three-dimensional streamline simulator, called 3DSL, written by Batycky *et al* (1996-7) to simulate the displacement for the five spot and staggered line drive patterns. In the simulations, we set the conditions identical to those in the experiments and choose relative permeability curves that ensure a piston-like displacement. The conditions:

1. Homogeneous permeability field, *i.e.,* k is constant.
2. Straight line relative permeability curves with end point relative permeability of 1, i.e.,

$$k_{rw} = S_w, \qquad k_{ro} = S_w \tag{5}$$

3. Therefore, $k_{rw} + k_{ro} = 1$ for any S_w.

4. Mobility is altered by changing viscosity, and the mobility ratio is the reciprocal of viscosity ratio.
5. We set $\Delta S = 1$ which means that ahead of the displacing front, the displacing phase saturation is zero, and behind the front, the saturation is unity.

3DSL is very fast compared to conventional finite difference simulators and exhibits much less numerical dispersion (Batycky *et al*, 1996, Thiele *et al*, 1996). For our problem, it offers us the streamline distribution which facilitates explanation of displacement behavior.

We use many pressure solves (time steps) and very fine grids (100 by 100 cells for five-spot and 140 by 70 cells for the staggered line drive) to ensure converged simulation results. A grid refinement study showed these grids to be optimal in that further refinement of the grid did not yield noticeable changes in breakthrough time, the oil production curve, or displacement patterns. For unit mobility ratio (M = 1), we actually only need one pressure solve. But for mobility ratios far from 1, we need many pressure solves. For 1/M = 20, we used up to 1000 pressure solves to ensure that the results were converged. In the streamline approach, a pressure solve is accompanied by a re-determination of streamline paths; hence, the flow field.

Figure 2 displays areal sweep efficiencies as a function of pore volume injected for differing mobility ratios, and compares simulation and experimental results (Dyes *et al.*, 1954). The solid circles are experimental results, solid lines simulation results, and the experimental breakthrough curve is connected by dashed lines for ease of viewing. In this figure, we concentrate on only the favorable mobility ratios, M < 1. We noticed more numerical dispersion for unfavorable mobility ratio cases, not reported here.

Figure 3 shows the displacing fluid fractional flow as a function of dimensionless time at the producer for several mobility ratios. To compute fractional flow from the numerical data, we use a central finite difference formula rather than backward differences. The shapes of the fractional flow curves at breakthrough (t_D from roughly 0.7 to 1) indicate some numerical dispersion. We expect the fractional flow to increase sharply rather than gradually at water breakthrough. As expected, the numerical dispersion decreases as M becomes more favorable. The most numerical dispersion occurs for unit mobility ratio, as shown in Fig. 3. We modify the breakthrough time by trimming the numerical dispersion as will be described next.

4.2.5 BREAKTHROUGH DETERMINATION

Due to numerical dispersion, injected fluid breaks through earlier at the producer than it should. However the numerical dispersion does not have much effect on the late-time displacing fluid production. The fractional flow versus t_D plots (Fig. 3) show the earlier breakthrough caused by numerical dispersion.

To correct for numerical dispersion in breakthrough times and approximate the breakthrough time more accurately, we use fractional flow data after breakthrough and extrapolate back to breakthrough time. A least squares method with second order polynomials is used:

$$t_D = a + bf_w + cf_w^2 \tag{6}$$

The data are points between $0.1 < f_w < 0.5$. The dashed lines in Fig. 3 illustrate this procedure. All the breakthrough times in Fig.2 are modified using this method.

Numerical dispersion is also related to the number of time steps (*i.e.,* pressure solves). In the streamline approach applied here, dispersion can be introduced through the process of mapping the streamline saturation distribution onto the underlying Cartesian grid used to compute the pressure field (Batycky *et al*, 1996). Hence, for a unit mobility ratio where the pressure field does not change, the most accurate results are obtained when a single time step is used. By performing various single time step simulations, we determine a breakthrough time of 0.7178 for the five spot with M equal to 1. This is in good agreement with the analytical solution of t_D equal to 0.7177. Likewise, analytically (Morel-Seytoux, 1966) and numerically determined breakthrough times for a staggered line drive pattern are both equal to 0.785. With multiple time steps (50) and the quadratic curve-fitting method above, we obtain the same values for the breakthrough times, at $M = 1$.

4.2.6 DISCUSSION OF THE EXPERIMENTAL AND SIMULATION RESULTS

Comparing simulation results and experimental results in Fig. 2, we notice that breakthrough occurs earlier in the experiments than predicted by the simulations. For the staggered line drive pattern in Fig 2(b), experimental data indicates that E_A at breakthrough is

roughly 0.75 for M equal to 1. In the experiments, there is physical dispersion even though a piston-like displacement front is assumed.

After breakthrough, the differences in areal sweep efficiencies between the experiments and simulations become much smaller (Fig. 2). After breakthrough, the numerical dispersion consists of only a portion of the displacing fluid produced. As time increases, this portion decreases and the dispersion has less effect on areal sweep efficiency. However, the differences between the experimental results and the simulation results are consistent, i.e. the areal sweep efficiencies of the simulations are generally higher than those of the experiments. As shown in Fig. 2(a), the simulated breakthrough curve levels off at large $1/M$ with zero slope and does not exceed 1. However, the experimental curve shows E_A equal to 1 at $1/M$ equal to 7. We note that in the plot drawn by Dyes *et al*, the point where the breakthrough curve hits the E_A equal to 1 line is only an extrapolation from other data points.

4.2.7 MOBILITY RATIO VS. PATTERN ON AREAL SWEEP EFFICIENCY

Figure 4 plots computed breakthrough, t_D, versus the conventional shape factor d/a for various mobility ratios. The analytical solution for the unit mobility ratio (Morel-Seytoux, 1966) is also plotted on the same figure for comparison. We find a good match of the sweep efficiency at breakthrough between the analytical solution and simulation results.

For unit mobility ratio, Fig. 4 teaches that a staggered line drive pattern always has better areal sweep efficiency than a five-spot pattern. As the staggered line drive pattern becomes longer relative to its width, the displacement pattern approaches linear flow. High sweep efficiency results.

As the mobility ratio becomes more favorable, the advantage of staggered line drive on sweep efficiency diminishes. When the mobility ratio decreases to 0.2, the five spot pattern becomes better than the staggered line drive pattern with $d/a=1$. However, if d/a is increased, the staggered line drive recovery is better than the five spot pattern for this mobility ratio.

When the mobility ratio decreases to 0.1 or lower (very favorable), the areal sweep efficiency for the five spot pattern is essentially 1 at breakthrough. That is, sweep out is complete at breakthrough. At this mobility ratio, the five spot pattern is as good as a very long staggered line drive ($d/a=25$, almost linear flow), and much better than the common

staggered line drive ($d/a=1$). The transition point for five spot sweep efficiency exceeding that from a staggered line drive is around a mobility ratio of 0.3. That is to say, if the mobility ratio is higher than 0.3, a staggered line drive is always better than a five spot. If mobility ratio is lower than 0.3, then the five spot can be higher in sweep efficiency than a staggered line drive. The excellent displacement from a five spot pattern is discussed below.

4.2.8 DISCUSSION OF PATTERN BEHAVIOR

In this section, we explain, with the help of streamline distributions, how a five spot pattern can exhibit higher areal sweep efficiency than a staggered line drive pattern for very favorable mobility ratios.

4.2.8.1 Unit Mobility Ratio

For the unit mobility ratio, the pressure field remains unchanged throughout the displacement, and so do the streamlines. The streamline distributions at $M=1$ for the five spot and staggered line drive ($d/a=1$) patterns are shown in Fig. 5. Every pair of streamlines forms a stream tube, and the volumetric flow rate is the same in all the stream tubes. All of the stream tubes connect with the same injector and producer, and the pressure drop for all the streamtubes is the same. With the same pressure drop and the same volumetric flow rate, the flow resistance is the same for all the streamtubes.

For our straight-line relative permeability assumption ($k_{rw}+k_{ro}=1$), we have

$$R_i=-\Delta p/q=\int_0^{L_i}\frac{\mu}{kA}dl \tag{7}$$

where R_i and L_i are the resistance and length of streamtube i, respectively; k is the permeability, for our study, k is uniform throughout the field; A is the cross sectional area of the streamtube along the streamtube.

$$A=hw$$

where h is the thickness of the layer and is the same for all streamtubes, and w is the width of the streamtube.

Resistance in streamtube i is the same as that in streamtube j, which leads to

$$\int_0^{L_i} \frac{\mu}{kA} dl = C \tag{8}$$

for all the streamtubes at a given time, where C is constant. Move the constant parameters k and h to the right hand side and we have

$$\int_0^{L_i} \frac{\mu}{w} dl = C \tag{9}$$

For a piston-like displacing front, we have

$$\mu_1 \int_0^{l_{fi}} \frac{1}{w} dl + \mu_2 = C \int_0^{L_i} \frac{1}{w} dl = C \tag{10}$$

where μ_1 and μ_2 are the viscosity of the displacing and displaced fluids, respectively, and l_f is the distance from the injector to the displacing front.

For unit mobility ratio,

$$\int_0^{L_i} \frac{1}{w} dl = C \tag{11}$$

From Eq. 11, we know that, if the ith streamtube is longer than the jth streamtube, then the average width of the ith streamtube w_i is greater to keep the same resistance or flow rate. Therefore, the volume of the ith streamtube is larger than the jth streamtube. The greater the difference in streamtube length, the bigger the difference in streamtube width, and, when breakthrough happens in the jth streamtube, the front has not progressed as far in the ith streamtube.

For a five spot pattern, the longest streamline is that along the boundary, which is 2a. The shortest streamline is the one along the diagonal, at a length of $\sqrt{2}\,a$. The ratio of the

longest streamtube length over the shortest is $\sqrt{2}$. Since the width of the longest streamtube is also $\sqrt{2}$ times as great as the shortest streamtube, the volume of the longest streamtube is twice that of the shortest.

However, for a staggered line drive pattern, the ratio of the length along the boundary $(d+a=3a)$ over the diagonal $(\sqrt{d^2+a^2}=\sqrt{5}a)$ is $3/\sqrt{5}\approx 1.34$. From the streamline distribution in Fig. 5, we know that the shortest streamline is longer than diagonal, and therefore the ratio of the longest streamline over the shortest is less than 1.34. This ratio is about 1.3 and, therefore, less than that ratio for a five spot pattern which is 1.41. That is to say, the streamlines are more evenly distributed in the staggered line drive than in the five spot pattern. Therefore, when the shortest streamtube breaks through, a larger portion of the other streamtubes have been swept in a staggered line drive than in a five spot pattern. When d/a increases, the streamtube length ratio (longest to shortest) decreases. When breakthrough happens in the shortest streamtube, a greater portion is swept in the longest streamtube, and therefore results in higher sweep efficiency at breakthrough.

4.2.8.2 Five-spot Pattern, Very Favorable Mobility Ratio

For a favorable mobility ratio ($M<1$), the displacement is stable. For equal volumetric flow rate streamtubes, Eq. 10 holds

$$\mu_1 \int_0^{l_{fi}} \frac{1}{w} dl = \mu_2 \int_{l_{fi}}^{L_i} \frac{1}{w} dl = C$$

Here, we consider the case of very favorable mobility ratio, i.e., the displacing fluid viscosity is much higher than that of the displaced fluid. When the front moves a portion of the way down the streamtube, the pressure drop is mainly in the displacing phase. That is to say, after a short time(compared to breakthrough) of injecting displacing phase, the pressure drop in the displaced phase is negligible. Therefore, Eqn. 10 can be simplified to the following form

$$\int_0^{l_{fi}} \frac{1}{w} dl = C \qquad (12)$$

In this extreme case, the displacing phase does not feel the producer until it is very close to it because the pressure drop between the front and the well plays a negligible role in displacement. Initially, flow around the injector is radial, because the pattern appears to be infinite at short times. For example, examine Fig. 6b for $t_D = 0.204$ and 0.408.

However, after the front passes the corner of a pattern without a well, the no-flow boundary condition along pattern borders alters the radial flow pattern. Pressure isobars must intersect the no-flow boundaries at 90°. This constrains the streamlines in the region adjacent to a boundary to be parallel to it. Because the fluids are incompressible, streamlines cannot terminate. The flow field in the region near the front transitions from radial to quasi-radial. From the figure, we also see that streamtubes ahead of the front are narrower along the boundary than those in the center, which makes the front in the boundary streamtubes move faster than in the central streamtubes. Before the front reaches the no-flow corners of the pattern, the flow is radial around the producer, as we can see in Fig. 6b. Little area is unswept and the sweep efficiency at breakthrough approaches unity.

Similar to before, if the path of displacing fluid in the ith streamtube is longer than that in the jth streamtube, then the ith streamtube should be wider in displacing fluid to keep the same resistance(same flow rate and pressure). Therefore, the streamtubes along the boundary become wider near the corner where the streamtube changes direction. Streamlines remain smooth. This streamline distribution trend is apparent in Fig. 6.

In summary, the very favorable mobility ratio conspires with boundary conditions to determine the way that streamlines evolve, and makes the sweep efficiency at breakthrough near unity. If the mobility ratio is very favorable, the pressure drop is mainly in the displacing phase, and it does not feel the well, but is affected by the boundary.

4.2.8.3 Staggered Line Drive, Very Favorable Mobility Ratio

For the staggered line drive pattern, the displacement at the beginning is similar to that in the five spot pattern. That is, the displacement pattern is radial around the injector before the front reaches the no-flow corner. The differences in displacement behavior between the two patterns occur after the front reaches the corner. For a five spot, because of the symmetry, the front reaches the two no-flow corners at the same time. However, for a staggered line drive, the front reaches the nearest no-flow corner first.

After the front passes the near corner, the streamlines evolve in a way similar to the five spot. The streamtubes along the boundary are wide near the corner but narrow near the

front. This makes the front near the boundary move faster because the streamtubes are narrower than those in the center of the pattern. Therefore, the front near the boundary on the near no-flow corner side catches up, and the displacement approaches linear flow (see the relevant streamline distribution in Fig. 7). If the aspect ratio is large, flow in the center of the pattern must become nearly linear because the pressure isobars are nearly straight and intersect the pattern boundary at 90°.

Similar to the discussion above for a five-spot pattern, for a very favorable mobility ratio, the displacing front is perpendicular to the borders of the pattern both before and after the front passes the no-flow corner. As a result, we see linear displacement for some time until the front on the near-corner side approaches the producer. We see these front shapes in Fig. 7.

When the front approaches the producer, the streamtubes narrow due to the confinement of the pattern boundary and the well. And therefore, with the same flow rate, the displacing fluid will break through relatively quickly in these streamtubes. However, the front on the far no-flow side progresses more slowly. This streamline distribution does not change greatly as the mobility ratio becomes more favorable for staggered line drive patterns. Sweepout of the pattern is not complete at breakthrough. For instance, a small amount of the resident fluid remains along the right hand boundary as shown in Fig 7a at $t_D = 0.940$.

If the length of staggered line drive is increased (increasing d/a), then the displacement will approach linear flow and the sweep efficiency will approach unity. The proportion of unswept area decreases as d/a increases.

4.2.9 CONCLUSIONS

Pattern performance changes with mobility ratio. For unit mobility ratio, unfavorable mobility ratios and some favorable mobility ratios ($M > 0.3$), a staggered line drive pattern has higher areal sweep efficiency than a five spot pattern. However, for very favorable mobility ratios ($M < 0.3$), a five spot pattern has better sweep efficiency than a staggered line drive.

The reason for this behavior is the change of streamline and pressure distributions with mobility ratios. For very favorable mobility ratios, the displacing front is near an isobar and intersects the pattern boundary at 90°. This causes the fronts at late times near breakthrough to become circles around the producer for a five spot pattern. This displacing front shape is due to the symmetry of the five spot pattern.

For a staggered line drive, the displacing front is also perpendicular to the border of the pattern. However, because the pattern is not symmetric, when the displacing front on one side reaches the producer, it has only moved partially along the other side border.

The simulation results are quite close to the analytical solutions for unit mobility ratio. The results are also very close to the experimental data, Dyes *et al* (1954), after breakthrough at various mobility ratios. We find physical dispersion in the Dyes experimental results that cause earlier breakthrough time.

We observed some numerical dispersion in our simulation results. For very favorable mobility ratios, the dispersion is small. We corrected the simulation results by fitting the fractional flow curve with a second order polynomial to estimate breakthrough time.

4.2.10 NOMENCLATURE

A area

A_S area swept

A_T total area of the pattern

a distance between like wells (injection or production) in a row

d distance between adjacent rows of injection and production wells

E_A areal sweep efficiency

f_w fractional flow of water

h bed thickness

k permeability

k_{ro} relative permeability of oil

k_{rw} relative permeability of water

l length

L_i length of stream tube i

l_{fi} distance (length) of the displacing front from the injector in stream tube i

M mobility ratio

p pressure

q flow rate

R_i flow resistance of stream tube i

S saturation

S_w water saturation

t_D dimensionless time

V_I volume of displacing phase injected

w width of a stream tube

ϕ porosity

μ viscosity

4.2.11 REFERENCES

1. Abbaszadeh-Dehghani, M. And Brigham, W. E.: "Analysis of Unit Mobility Ratio Well-to-Well Tracer Flow to Determine Reservoir Heterogeneity," SUPRI-TR 36, Stanford University, Stanford (August 1982),.
2. Batycky, R. P., Blunt, M. J., and Thiele, M. R.: "A 3D Field Scale Streamline Simulator with Gravity and Changing Well Conditions," SPE (October 1996).
3. Craig, F. F. Jr.: "The Reservoir Engineering Aspect of Water Flooding," Henry L. Doherty Memorial Fund of AIME, 1971.
4. Dyes, A. B., Caudle, B. H., and Erickson, R. A.: "Oil Production after Breakthrough—as Influenced by Mobility Ratio", Petroleum Transactions, *AIME* (1954) 27-32.
5. Lake, L. W.: Enhanced Oil Recovery, Prentice Hall Inc., New Jersey (1989).
6. Morel-Seytoux, Hubert J.: "Unit Mobility Ratio Displacement Calculations for Pattern Floods in Homogeneous Medium," SPE 1359 (September 1966) 217-226.
7. Thiele, M. R., Batycky, R. P., Blunt, M. J. and Orr Jr, F. M.: "Simulating Flow in Heterogeneous Systems Using Streamtubes and Streamlines," *SPERE* (February 1996), 5-12.

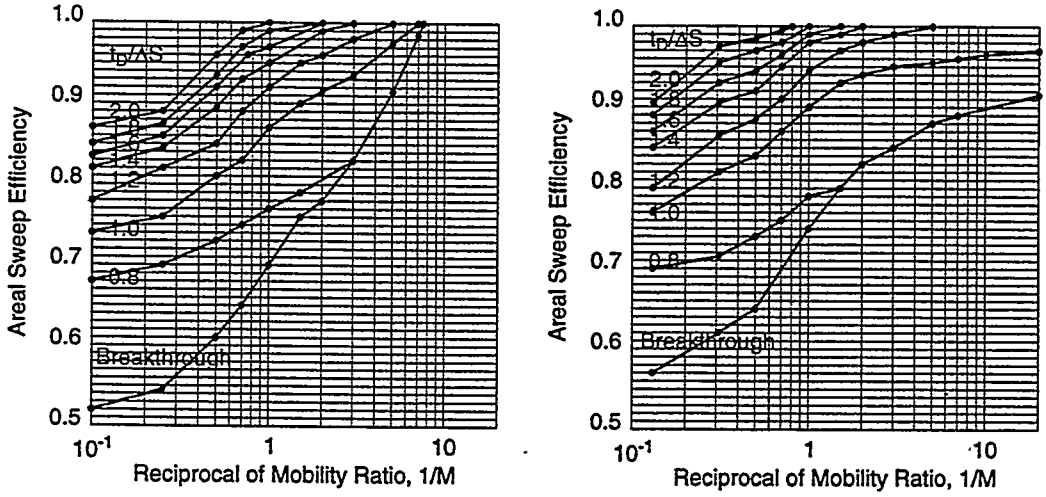

(a) Five Spot Pattern (b) Staggered Line Drive, d/a = 1

Fig 1 Dyes et al(1954) Experimental Results

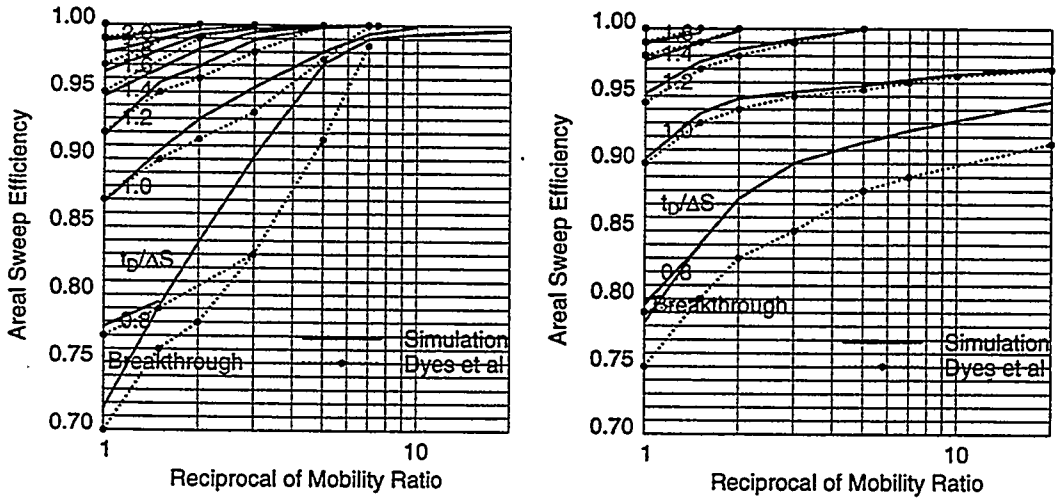

(a) Five Spot Pattern (b) Staggered Line Drive, d/a = 1

Fig 2 Comparison of Simulation and Experimental Results by Dyes et al(1954)

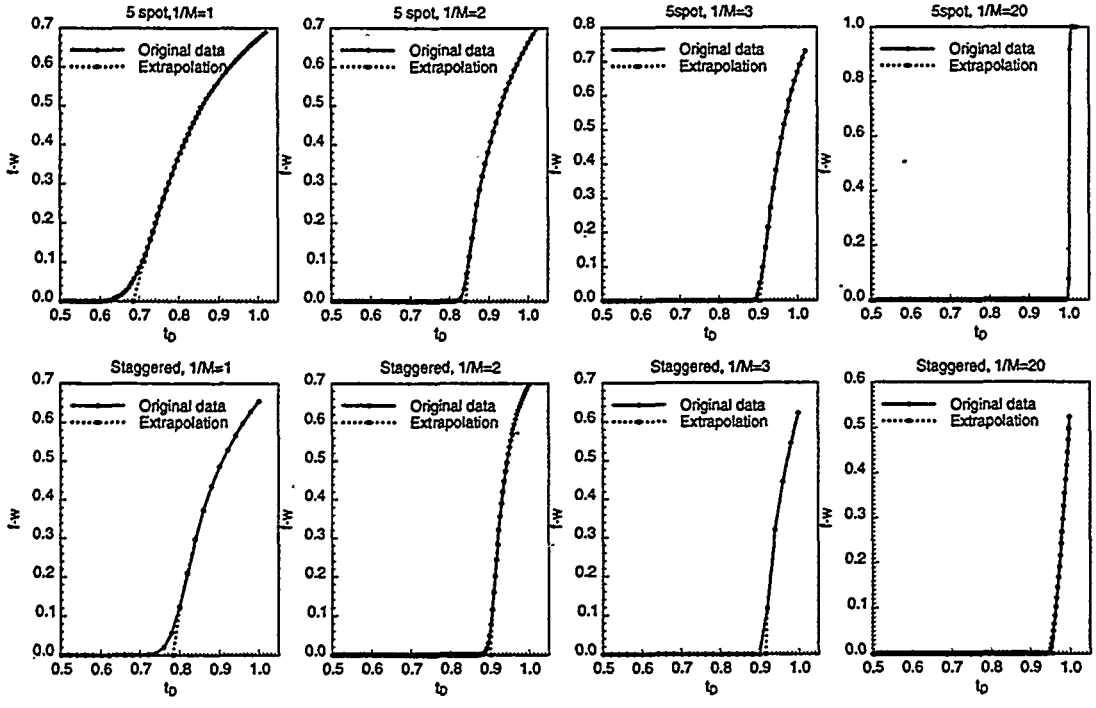

Fig 3 Fractional Flow(f_W) vs t_D at Producer

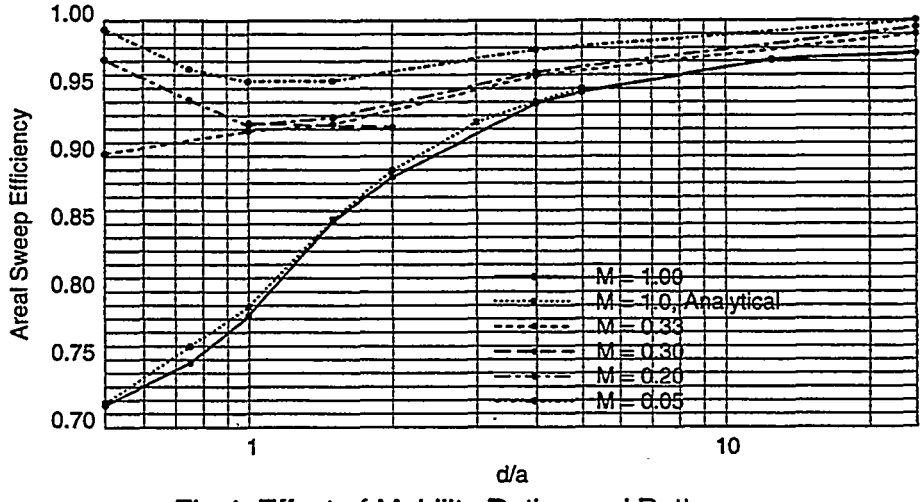

Fig 4 Effect of Mobility Ratios and Patterns
On Areal Sweep Efficiency

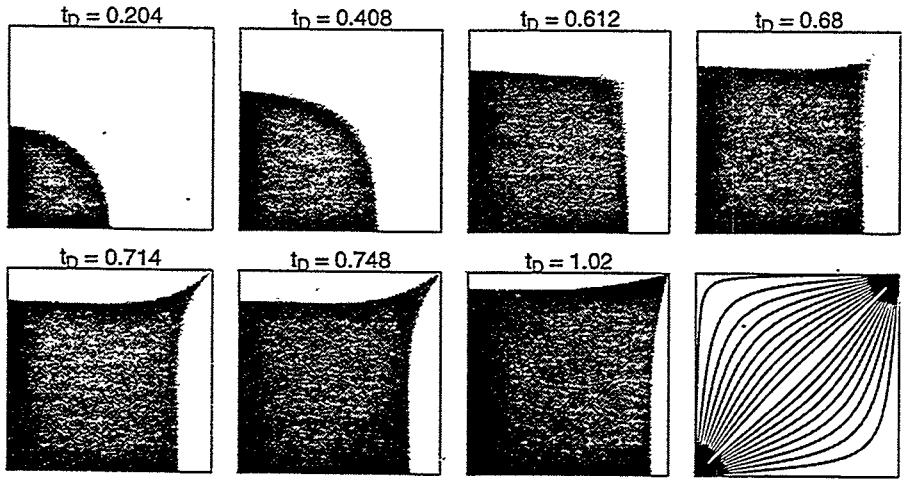

(a) Saturation Distribution

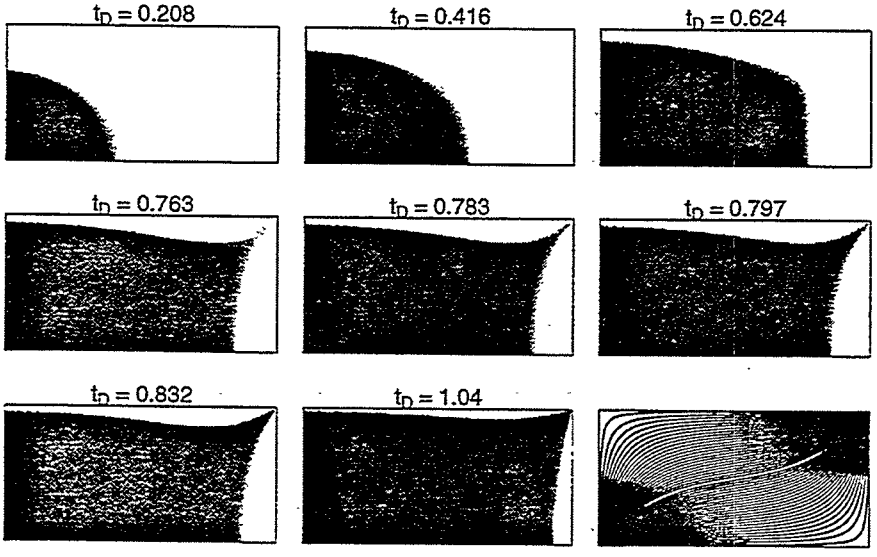

(b) Streamline Distribution

Fig 5 Five Spot and Staggered Line Drive, Unit Mobility Ratio

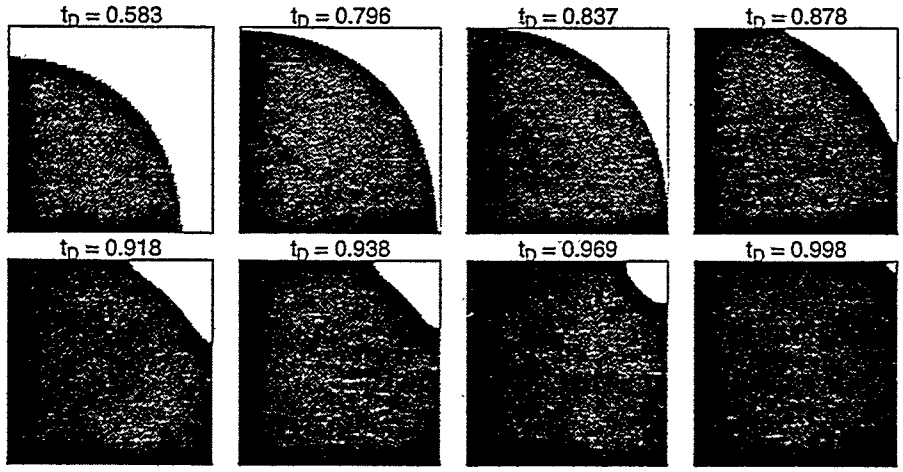

(a) Saturation Distribution

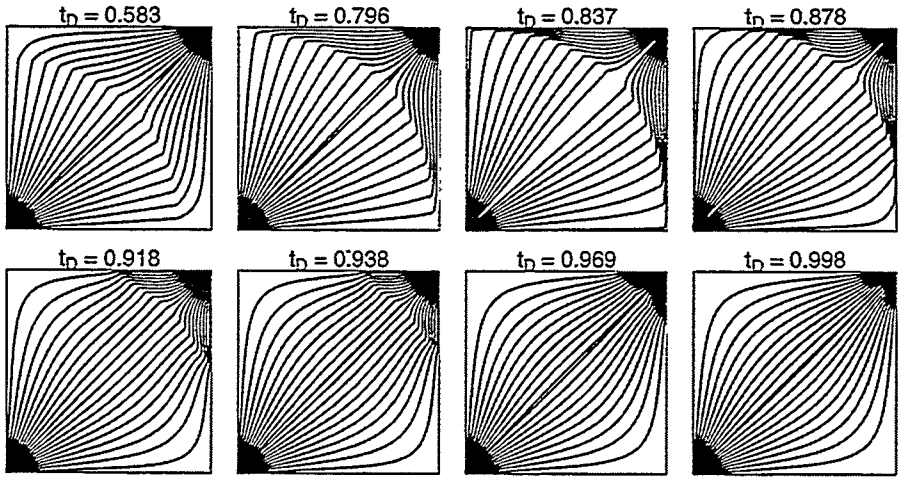

(b) Streamline Distribution

Fig 6 Five Spot Pattern, Very Favorable Mobility Ratio(1/M=20)

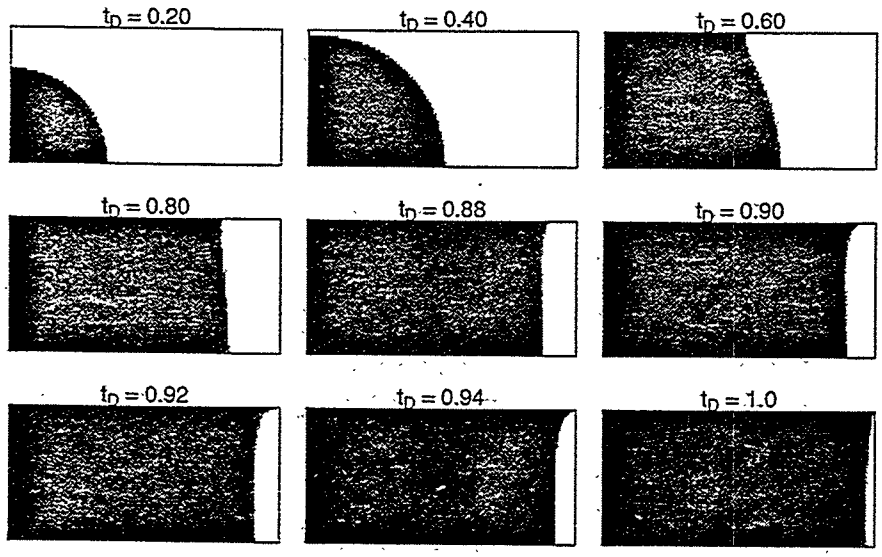

(a) Saturation Distribution

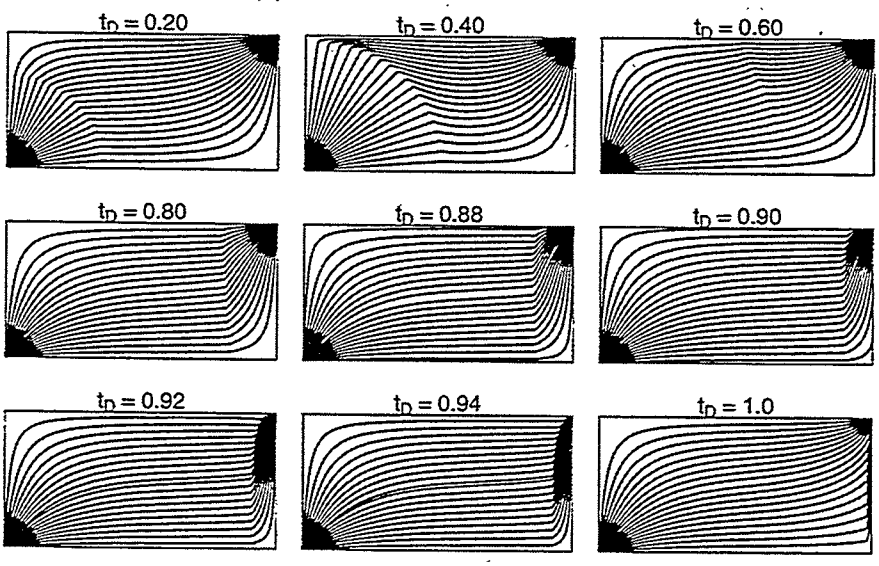

(b) Streamline Distribution

Fig 7 Staggered Line Drive, Very Favorable Mobility Ratio(1/M=20)

Task 69 — INTEVEP shall provide DOE with information on Geomechanical Modeling of unconsolidated formations. This includes studies on borehole stability in vertical and horizontal wells.

STRESS FIELD DETERMINATION
AN INTEGRATED METHODOLOGY THROUGH A CASE HISTORY

Presented by:
Alberto Munoz – PDVSA Intevep

TABLE OF CONTENTS

LIST OF FIGURES

LIST OF TABLES

SUMMARY

A detailed description of tests and field information used for determination of *in situ* conditions in deep reservoir and highly compressive rocks are presented. This report specifies parameters determined in field for well trajectory planning, hole stability calculations, and shotted cavities in order to reduce drilling costs, control sand, and plan fracture. Also, information on *in situ* stress direction provides technical fundament for applying perforation techniques to reduce rupture pressure during hydraulic fracturing, and planning, from the stability point of view, of horizontal well trajectory and highly deviated wells.

The study reveals that stress field in reservoir analyzed presents particular characteristics, not reported before in Venezuelan oil reservoirs. Stress regime is characterized by a low contrast between vertical stress (calculated by integrating density logs), and minimum horizontal stress, estimated in microfracturing and leak-off tests in open or cased holes. Maximum horizontal stress is estimated in 1.35 psi/ft. Reservoir minimum stress is N 50° E for regions away from reservoir limit faults. This is consistent with direction estimated by interpretration with other techniques applied in the region, namely: focal mechanisms and ovalization analysis of other reservoirs distributed throughout the basin. Preliminary interpretation of microfracturing and leak-off tests suggests that stress field tensor is deviated with respect to vertical extension. This fact limits the thickness being shotted, when performing FracPac or hydraulic fracturing. Main recommendations for the reservoir studied are:

If oriented perforation is applied, direction should be N 40° W, specially in those wells away from North-South reservoir limit fault, due to uncertainty of maximum stress direction of near wells.

For FracPac technique application, height of zone being shotted should be maximum sand thickness in wells subject to this sand control method. This recommendation is supported on the limited vertical extension of fractures, given the stress regime characteristics. Objective is to effectively control facture location and optimize use of FracPack to control sand. Horizontal wells of the area, according to stipulations in this report, shall be oriented in the same direction of the maximum horizontal stress.

1. INTRODUCTION

The area analyzed in this study is located southeast of Lake Maracaibo, Eastern Venezuela (Figure 1).

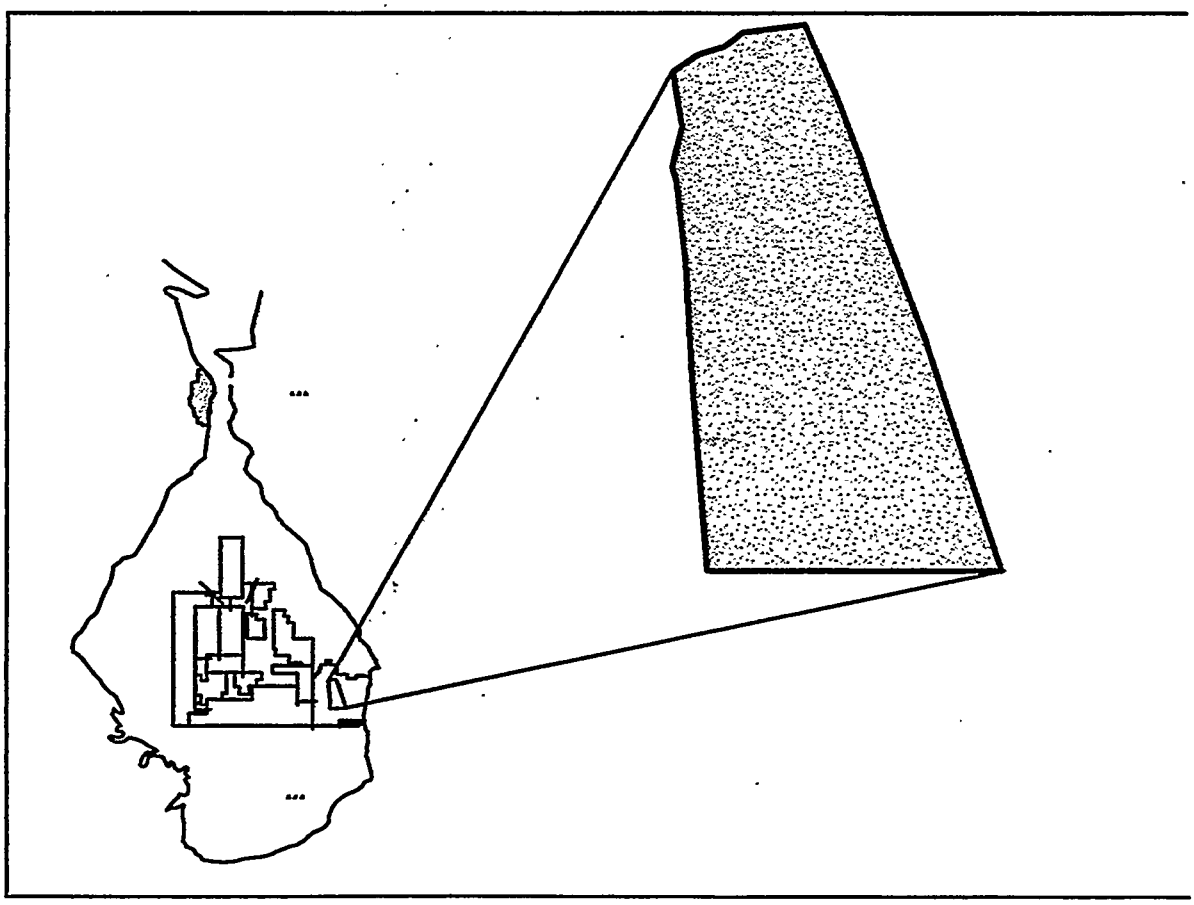

Figure 1 Location map of reservoir studied.

Eocene sands located between 14,000 and 18,000 ft TVD deep (4,300 m and 5,450 mTVD) are zones of interest for the study. Main problem found in these reservoirs is the high sand production (higher than 10 lbs/MBD), which increases operational costs of frequent cleaning of wells and facilities.

Sand problem is fundamentally a geomechanical question, and consists in rock breaking in the well drainage area. Rock breaking begins when equilibrium between internal resistance and cohesion forces, and thrust and cut external forces imposed by oil flow around well is broken. This force disbalance is caused by different factors:

- Mechanical properties of reservoir rock (resistence and deformability)

- *In situ* condition (stress field, pore pressure, natural fractures)
- Operational practices (well integrity, completion type, perforation type and density, formation damage, pressure differential, etc.)

To determine factors involved in reservoir process, and since one of the main aspects involved sand production is the mechanical characteristics of reservoir rock, a strategy to study sand problem in the area selected was developed. The strategy was described in the geomechanical information-gathering plan designed to determine both rock resistance and deformability properties, and *in situ* conditions to which rock is subject to in reservoir.

In general, information-gathering plan includes: i) core sampling of at least 60 ft from production sands, adjacent to stratigraphic cores of the area, and ii) performance of 60 geomechanical tests in laboratories of TerraTek and Intevep. Additionally, complete wave and dipolar sonic logs were performed in new wells in order to elaborate resistance profiles. Using this information, a core-profile correlation [1] was developed to estimate mechanical resistance characteristics in those wells, for which only log information was available.

For establishing *in situ* conditions of reservoir rock, several logs, including density and sonic logs from intermediate hole in a given well, and field tests, such as extended integrity and microfrac, were programmed to estimate *in situ* stress field magnitude.

Using this information, pore pressure profiles and horizontal stress variation were established for critical flowing pressure calculations, in order to obtain optimum reduction values in each well for initial well opening. This information constitutes the initial control measurement within the global sand control strategy, as long as permanent contention measurements, such as sand exclusion or *in situ* consolidation through hydraulic fracturing are implemented.

Objective of this study is to present results of reservoir stress field estimation, and compare different techniques to establish a guideline for similar studies in other regions or reservoirs.

In general, stress field involves five fundamental parameters; namely: overloading stress, σ_V, maximum horizontal stress, σ_H, minimum horizontal stress, σ_h, direction of minimum stress or maximum horizontal stress, and pore or formation pressure, P_0. For an effective use in typical reservoir development activities, a stress field study shall include space variations (3D model), and depth of each of these variables (2D model). Also, equations and correlations, involved in reservoir development activities, and used in the different geomechanical aspects of the study, shall be considered. Since reservoir analyzed presented a particular situation, this report was

structured in two main sections. First, a section describing magnitudes found in stress field, and second, a section including information on areal variation stress field direction. Finally, conclusions and recommendations about relative importance of techniques used are given.

2. DETERMINATION OF STRESS FIELD

Below, a detailed description of tests and field information used for determination of rock *in situ* conditions in the area studied. Bases of methodology applied are described in [2], whose main objetive is to provide correlations and parameters determined in field and used in well evaluations, well stability and perforation cavity calculations, in order to reduce drilling and sand control costs. Additionally, information of *in situ* stress direction provides the technical support to implement perforation method, oriented to reduce rupture pressure during hydraulic fracturing and planning operations from the point of view of well stability of horizontal wells.

2.1 OVERLOADING STRESS σ_v

Overloading stress estimation was obtained by integrating density log, taken at intermediate well, and production log of a well located in central zone of reservoir. In Figure 2, a set of profiles used in stress field determination (dipolar sonic (P and S waves)), density, neutron porosity, resistivity, gamma ray and caliper) is shown.

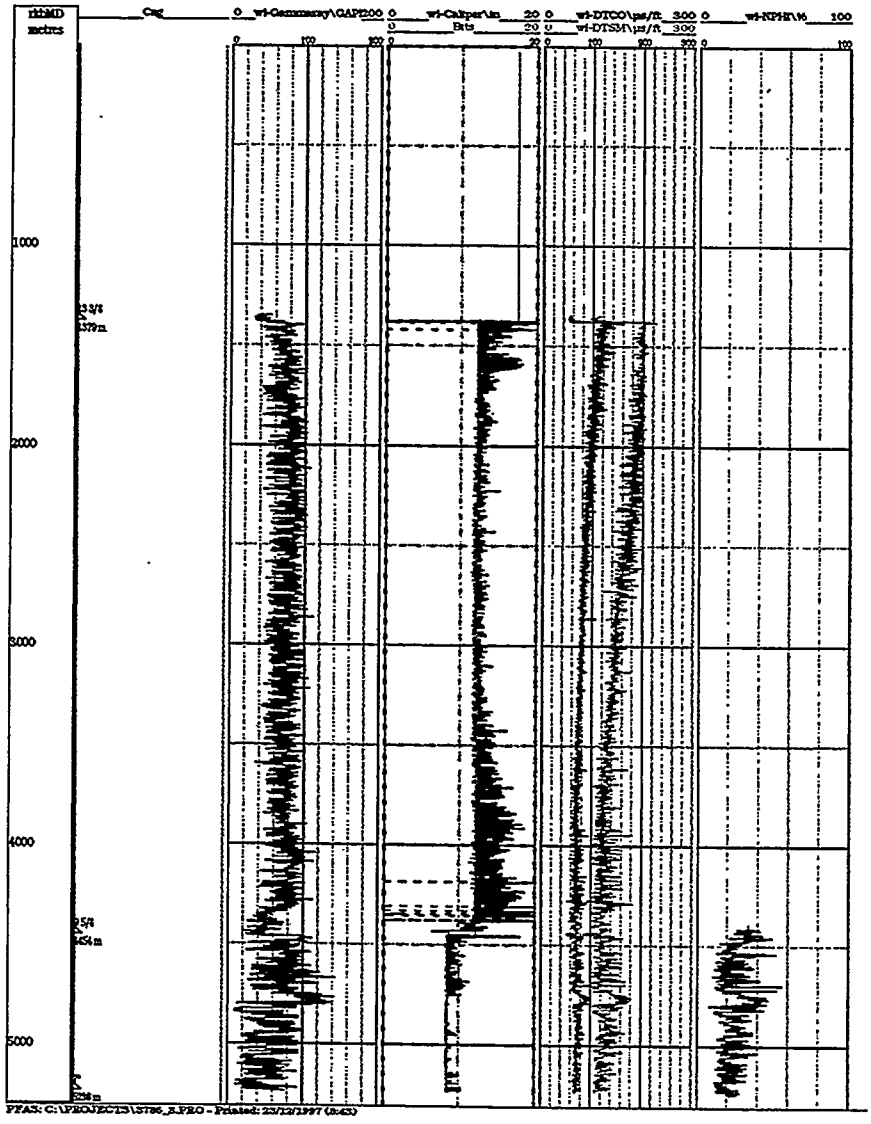

Figure 2 Density, gamma ray, caliper, compressional sonic and reference well cut profiles, used in stress field estimation, and core-profile correlation for the area of study.

As shown, density log covers from 4,543.0 ft to 17,220.0 ft deep. The log indicates that caliper shows an excellent hole quality, compared with drill size, in the part of the registered section. Therefore, the quality is considered acceptable to its integration and obtention of overloading stress using equation:

$$\sigma_v(D) = 0.433 * [\rho_w * WD + 2{,}430 * (4{,}543.0 - WD) + \sum_{4543.5-WD}^{D} \rho_i * \Delta h\ ]\ [psi] \qquad \text{(Eq. 1)}$$

where:

Δh = 3.28 ft (MD) = 1 m
ρ_i = density values, according to log [g/cc^3]
ρ_w = water density ≈ 1,0000 g/cc^3
WD = lake depth rkb
D = depth in ft (MDrkb)

For formation section for which no density information is available, a lithostatic density equivalent to average of all values registered [ρ = 2.43 g/cc^3] was estimated as first approximation. Although this approximation constitutes an overestimation, the parameter will be used as main variable to perform error sensitivities in overloading stress estimation (see Table 1).

As a result of previous integration, a linear correlation was generated to estimate overloading stress in reservoir studied. The correlation is expressed as follows:

$$\sigma_v(D) = [1{,}057 \pm 0.011] * D - [72.58 \pm 1.16]\ [psi] \qquad \text{(Eq. 2)}$$

Since depth of lake in reservoir studied is approx. constant to 100 ft deep, intercept of Eq. 2 includes correction of lake depth:

From this equation, overloading gradient corresponds to value of:

$$\frac{\partial \sigma_v}{\partial D} = 1{,}057 \pm 0.011\ [psi/ft] \qquad \text{(Eq. 3)}$$

Considering approximation employed in density estimation for the first 4,543.5 ft, value of gradient shall be calculated based on a higher value for vertical stress. Results of sensitivity analysis for gradient value at reservoir depth are given in Table 1. As seen, value of σ_v corresponds to a value typically used of 1.05 psi/ft.

Table 1 Sensitivity analysis for overloading gradient at reservoir depth @ 17,184.0 ft.

ρ (g/cm^3)	$\frac{\partial \sigma_v}{\partial D}$ (psi/ft)
1.90	1,000
2.05	1,019
2.20	1,030
2.25	1,035
2.35	1,046

2.2 ESTIMATION OF PORE PRESSURE

Pore pressure estimation in function of depth was performed with Eaton method [3], applied to compressional wave of sonic profile ($\Delta\tau_C$). This method is based on the hypothesis that different formations with the same porosity value, or a value of a property dependent on porosity (such as compressional transit time), are subject to the same value of the effective stress value. With this hypothesis, following equation is obtained:

$$\sigma_z(D) = \sigma_{zn}(D_n) = \sigma_{vn} - P_n \qquad \text{(Eq. 4)}$$

where D is depth, σ_z is effective stress, P_n is pore pressure, and σ_{vn} is evaluated at depth of D_n of equivalent porosity. So, pore pressure at depth D is obtained with equation:

$$P_D = \sigma_v(D) - \sigma_z(D_n) \qquad \text{(Eq. 5)}$$

Noteworthy is that Eq. 4 is generically known as Terzaghi criterium [4], which expresses the effective stress acting on porous material as the difference between total stress and pore pressure. In general, this criterium is only valid for zones in which value of Biot constant (α) is close to 1.0. Therefore, this methodology requires the identification of zones rich in lutites from several formations, intercepting each other when drilling a well.

In the practice, the method described is implanted developing empirical correlations, in which porosity-dependant value is determined from a curve property-depth, in which normal gradient of pore pressure (X_a) and real value of parameter selected at the same depth X_b have been

1. performing a petrophysical analysis, in which gamma ray index, I, is used as direct indicator of clay content, according to equation:

$$I = V_{shale} = \frac{Gr - Gr_{min}}{Gr_{max} - Gr_{min}} \quad \text{(Eq. 6)}$$

where Gr, Gr_{max} and Gr_{min} are gamma ray values at depth of interest. Gr_{max} and Gr_{min} represent maximum and minimum values detected in the log, respectively. Although there are other relations, in this study this indicator was considered sufficient. However, a better correlation than the one applied in this study is required for the petrophysical evaluation of wells [5].

2. Once clay volume is obtained, performing a frequency analysis of parameter V_{shale} was peformed, in order to identify "sands" and "lutites" zones. When cut point was established, values of $\Delta\tau_C$, identified as coming from lutites, were selected from compressional wave log.

3. Using values obtained from previous procedure, a depth graph was performed, and so, equation corresponding to normal trend of pressure gadient was established.

4. Then, criterium expressed in Eqs.4 and 5 was applied, to estimate pore pressure in function of depth.

As a result of applying this procedure, following expressions to calculate pore pressure in area of study were obtained. Equivalent depth (D_n) to estimate P_o is obtained with Eq 7:

$$D_n = \frac{29{,}005.6}{(\Delta\tau_c)^{0.5901}} \quad \text{(Eq. 7)}$$

where $\Delta\tau_C$ is expressed in µs/ft and D_n in ft.

Once equivalent depth for the area of study is obtained, pore pressure is evaluated with following equation:

$$P_o(D) = \sigma_v(D) - [\sigma_v(D_n) - K^*D] \text{ [psi]} \quad \text{(Eq. 8)}$$

where constant K represents normal gradient of reservoir hydrostatic pressure. In general, for calculations, K is fixed with data of known pore pressure. Initial value used for K is 0.433 psi/ft.

2.2.1 EVALUATION OF RESERVOIR PORE PRESSURE

In Figure 3, result of pore pressure evaluation by combining Eqs. 4, 7, and 8 in the area of study is shown. For comparison, results of assays Repeat Formation Tester (RFT), performed to determine reservoir pressure in reference well, are given. As shown and despite it is not strictly valid for sands, an excellent correspondence between pressure values estimated from correlation here presented, and values obtained with direct evaluation in well is observed.

Agreement obtained between correlation here presented and field results in reservoir sands might be attributed to the high values reported from geomechanical tests for values of Biot constant [6]. Indeed, as previously explained, methodology used in this study to estimate P_o is only applicable to clay-rich formations, because in these formations higher value of Biot coefficient are expected. As α approaches the unit, a better scenario to fulfill Terzaghi criterium, which is the base of hypothesis for P_o estimation, is expected.

In reservoir studied, many geomechanical assays [1,2,9] have established that Biot coefficient presents a value near 0.95.

Considering alterations usually found in core sampling and handling operations, it is expected that under reservoir conditions, these values constitute a lower limit for α value in production sands. Agreement observed between pore pressure obtained with Terzaghi approximation and RTF field measurements is then explained.

As observed in Figure 3, pore pressure estimation presents an overpressurized zone at 12,000 ft TVD (3,630 mTVD) at Miocene-Eocene transition formation depth. The zone is consistent with a field experience in which a high pressure zone is present, which causes intermediate casing to set at the depth of this formational top. It is worth mentioning that correlation here proposed for P_o estimation is fundamentally an indicator of reservoir initial pressure, when drilling the well.

2.3 MAGNITUDE OF HORIZONTAL STRESS

Ideally, magnitude of horizontal stress (both maximum and minimum) shall be directly calculated from extended integrity tests (leak-off test, LOT) or microfrac tests performed in each casing shoe of oil well. LOT is usually carried out in fresh formation, once surface or intermediate casing has been installed fracturing formation. Data of this test (surface pressure and pumping rate) are registered in function of time, and are intrepreted to obtain formation closing pressure, which is

equivalent to σ_3 (lowest value of main *in situ* stresses), corresponding to minimum horizontal stress.

As part of stress field study, several measurements to establish σ_3 magnitude have been performed. Below, results in chronological order of each leak-off test or microfrac carried out for this study

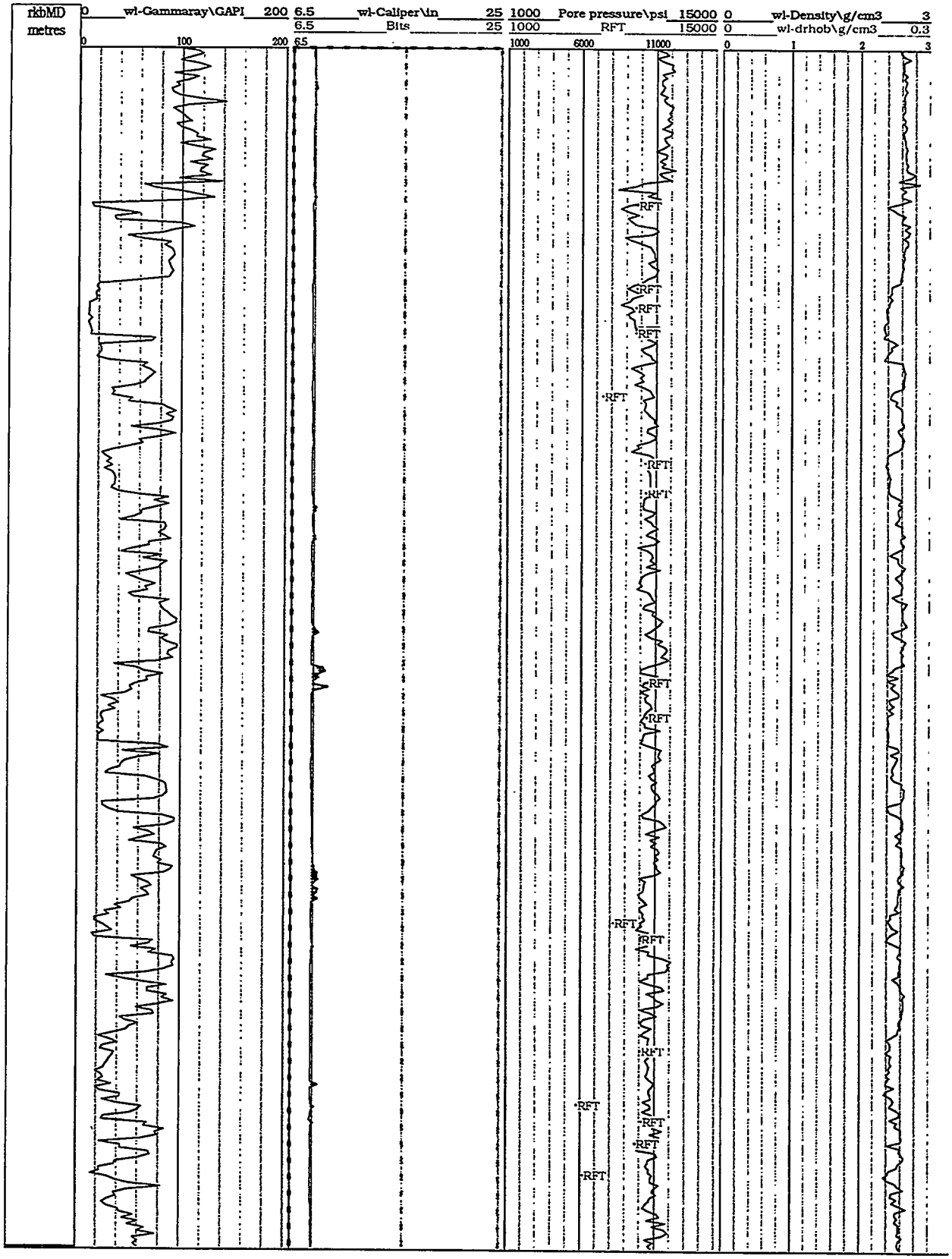

Figure 3 Variation of pore pressure in function of depth in the area of study.

2.3.1 LEAK-OFF TEST(LOT) IN WELL #1

First test performed to estimate smallest component of main stress triad was carried out in the shoe of intermediate hole in well #1. Test corresponds to an extended leak-off (two cycles) carried out in Lagunillas Formation, using an open hole section between 14,751'-14,772' TVD (4,466 mTVD). In Figure 4, a graph with data obtained during tests is given. Although problems of pumping rate control are detected, rupture pressure, closing pressure, formation reopening pressure, are clearly seen, which are parameters necessary to estimate stress magnitude.

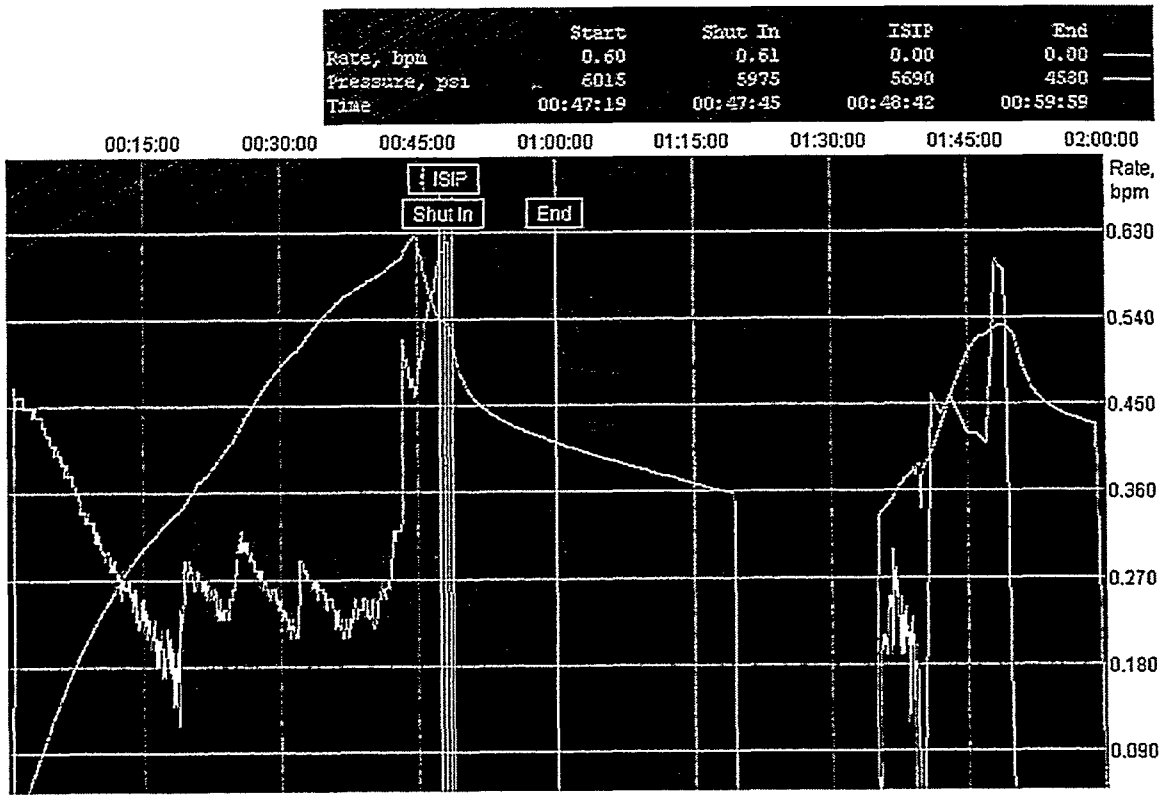

Figure 4 Curve of pressure (------) versus time and pumping rate ( ) versus leak-off time of well #1.

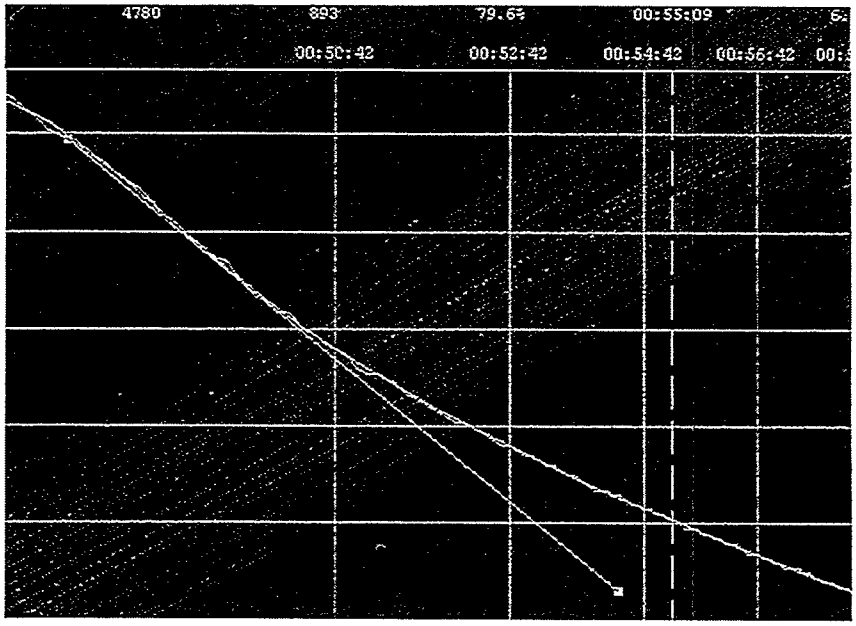

Figure 5 Microfracture analysis for minimum main stress σ_3 determination.

Microfrac analysis of curves presented in Figure 4 was performed with Microfrac Analysis© program of the company Halliburton. In Figure 5, result of magnitude analysis of main minimum stress, σ_3, is presented using an specialized graph of pressure *vs.* time square root (P *vs* $\sqrt{t}$). Value of σ_3 is considered the one corresponding to transition from a linear flow regime to a radial regime, expressed as deviation of straight line in graph P *vs* $\sqrt{t}$. This value and parameters obtained with LOT, concerning reopening pressure, pore pressure calculated with procedure described in Section 2.2, and following equation for rupture pressure of a fracture in elastic regime, viz.

$$P_b = 3\,\sigma_h - \sigma_H - P_0 + T_0 \qquad \text{(Eq. 9)}$$

allows obtaining a first approximation of main stress magnitude in the area studied.

Table 2 Summary of results of LOT analysis of well #1.

Rupture pressure (P_b)	16,695 psi
Minimum main stress (σ_3)	14,530 psi
Resistence to tension (T_0)	1,150 psi
Pore pressure (P_0)	8,430 psi
Maximum main stress (σ_1)	19,615 psi
Stress relation $\frac{\sigma_1}{\sigma_3}$	1.35
Stress gradient $\frac{\partial \sigma_3}{\partial D}$	0.98 psi/ft

A preliminary discussion of implications on stress regime of results presented in Table 2, indicates a high value of minimum main stress. Indeed, a comparison of $\frac{\partial \sigma_3}{\partial D}$ value obtained in this well and typical values from other basins ($\approx$ 0.7 psi/ft) for this gradient, which in the area studied is subject to a high tectonism. This preliminary conclusion will be extended as additional information on microfracturing and *in situ* stress direction, considering practical implications on well orientation, height of shotted section for hydraulic fracturing, among other operational recommendations, is introduced.

2.3.2 CASED HOLE MICROFRACTURING IN WELL #2

Considering previous results and in order to verify the value obtained, a second microfracturing test was proposed, this time, in reservoir production sands. To minimize operational risks and ensure well integrity, tests were performed after cementing production casing (7"), through perforation holes TCP 30°, phases of 2" of formation in production sands near 16,307 ft deep (top of drillings).

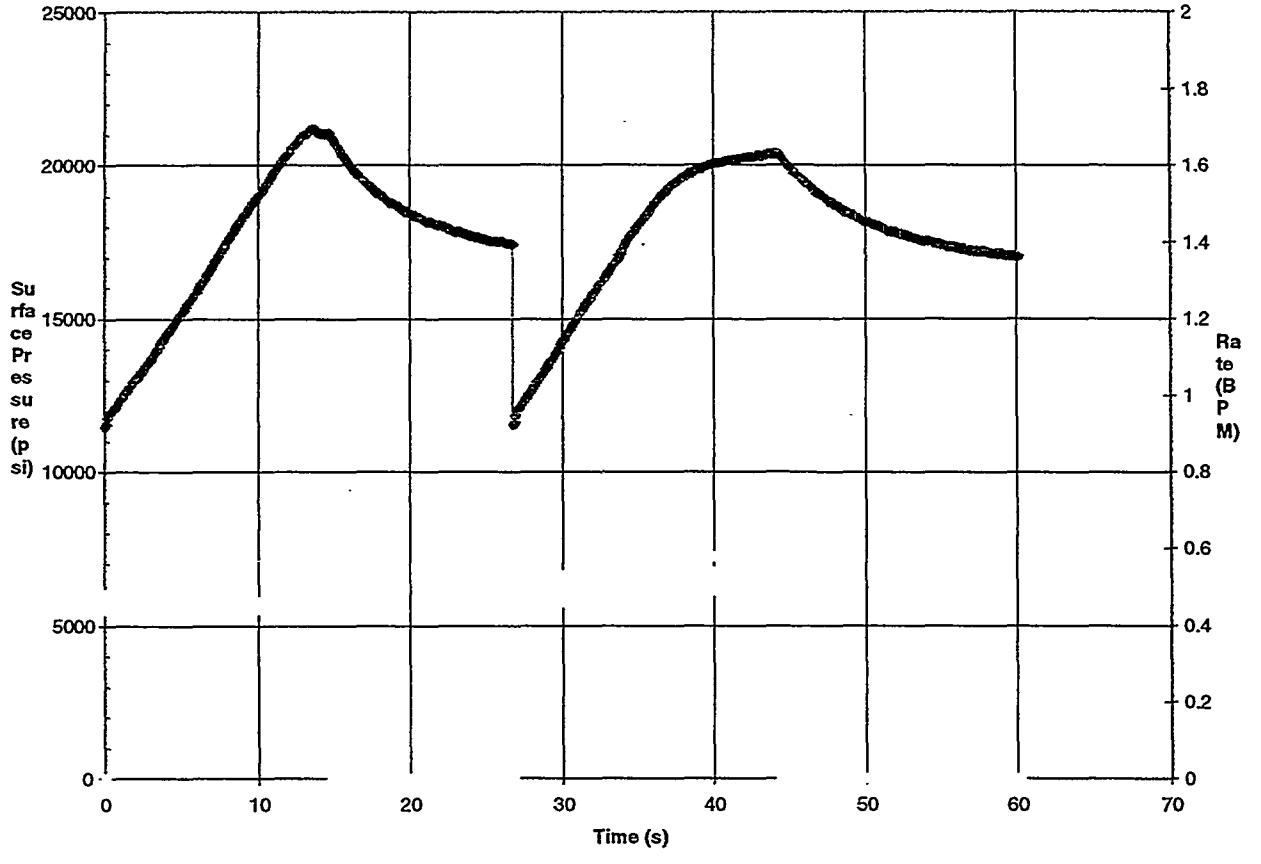

Figure 6 Curve of pressure/pumping rate *vs.* microfrac time in well #2.

In Table 3, results of microfracturing analysis are presented. As in formation integrity test performed in open hole, a high value of minimum stress gradient is obtained. On this ocassion, a higher gradient value was registered, which in principle is attributed to misalignment effect of drilling with stress field [10]. As it is known, this misalignment leads to an initial winding, while fracture propagates, and aligns with maximum stress, according to stress field orientation.

Table 3 Summary of results of microfracturing analysis in well #2.

Rupture pressure (P_b)	16,046 psi
Minimum main stress (σ_3)	19,537 psi

Table 3 Summary of results of microfracturing analysis in well #2.

Rupture pressure (P_b)	16,046 psi
Minimum main stress (σ_3)	19,537 psi
Resistence to tension (T_0)	809. psi
Pore pressure (P_0)	10,595 psi
Maximum main stress (σ_1)	28,047.0 psi
Stress relation $\frac{\sigma_1}{\sigma_3}$	1.35
Stress gradient $\frac{\partial \sigma_3}{\partial D}$	1.22 psi/ft

2.3.3 MICROFRAC ANALYSIS DURING FRACPACK

With the application of FracPac technique as control method of sand production control, additional minifrac tests were performed in wells #3, #4, #5, #6 and #7. Results obtained in each of these tests confirmed the need to use higher pressure to achieve formation rupture and extension of fracture, which is a direct evidence of this particular situation in reservoir studied.

2.3.4 OPEN HOLE MICROFRACTURING IN WELL # 8

As complement of magnitude and orientation of stress field, a open hole microfracturing was executed, followed by an orientated core sampling and image logging. Application of this technique provides the most reliable information to establish stress magnitude and fracture orientation (vertical and horizontal) in the area studied. Additionally, the technique might allow to corroborate of stress direction and stress variation in depth.

As the most relevant operational result, an orientation fracture was intended, in order to post recommendations on optimum thickness to shot in hydraulic fracturing.

Figure 7 shows graph pressure *vs.* square root of well # 8. Microfracturing analysis indicates the presence of closing of at least two fractures, evident by the double change of slope observed. Slope changes correspond to a linear to radial change of flow regime, after fracture is closed. Behaviour of curve pressure *vs.* time has been observed in test of large blocks performed by Abass *et al.* [11].

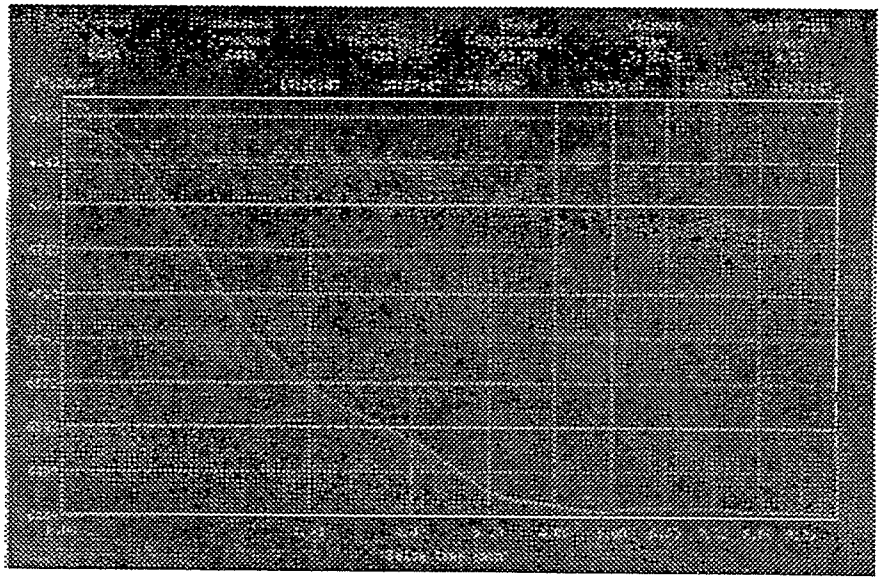

Figure 7 Microfracture analysis of microfrac first cycle of well #8.

Quantitative analysis of pressure curve is shown in Table 4. As seen, closing of two fractures implies a difference in closing pressures of 429 psi. This type of multiple fractures is commonly associated to fracturings in directional wells; due to misalignment between stress field and well axes, as a consequence of well geometry.

Table 4 Results of open hole microfracturing in well #8 (La Rosa Formation).

Closing pressure 1	6,570 psi (surface)
Closing pressure 2	6,141 psi (surface)
Rupture pressure (P_b)	8,076 psi
Resistence to tensión (P_0)	1,076 psi
Stress gradient $\frac{\partial \sigma_3}{\partial D}$	1,000 psi/ft

In deep vertical wells, as in hydraulic fracturing of the area studied, presence of multiple fractures can be attributed to two main reasons.

a) Presence of a stress field, whose main axes system is deviated with respect to vertical line (probably well axis).

b) A stress regime, whose contrast between vertical stress and minimum horizontal stress is low, *i.e.* $\sigma_H > \sigma_h \approx \sigma_v$ o $\sigma_H > \sigma_v \approx \sigma_h$.

As seen in Table 5, information currently available about the area studied allows considering at least two main possibilities in function of vertical stress gradient. Main observation about this example is that in case that vertical stress gradient corresponds to a value of 1.00 psi/ft, order of main stresses implies the feasibility of generating horizontal fractures.

Table 5 Order of stress tensor in function of vertical stress gradient.

Vertical stress gradient (psi/ft)	σ_H (psi)	σ_h (psi)	σ_v (psi)
1.00	21,675	16,375	15,640
1.10	21,657	17,204	16,375

This possibility substantially affects perforation strategy of fractures in the area of study, because then it will be peremptory to reduce intervals to be shotted from current 100 ft to 5 ft, in order to better use sand control fracture. First, because interval to be shotted is controlled, and at the same time, creation of multiple fractures is avoided, which negatively affect formation of broad fractures that cannot be effectively packed, as required in FracPack. In any of both scenarios considered, *i.e.* stress tensor deviated with respect to well vertical axis, or horizontal fractures, reduction of shotted thickness constitutes an optimum strategy from a technical point of view for both situations. Additionally, this regime implies that most favorable orientation of a horizontal well is σ_H direction.

When this report was prepared, no paleomagnetism orientation analysis of cores from Formations La Rosa and Misoa was available. Preliminary inspection performed by PDVSA staff revealed no fracture with vertical extension, which indirectly makes evident the propagation of a deviated stress tensor or horizontal fractures.

3. ORIENTATION OF STRESS FIELD

Additionally, considering stress magnitude, a very important aspect to be studied when determining *in situ* forces acting on formation, is the orientation of maximum or minimum stress Azi_σ_3. Knowing Azi_σ_3 parameter allows, among other aspects, implementing the techniques, such as oriented perforation for sand production control, and establishment of optimum direction of a deviated or horizontal well to reduce stress concentration, and minimize sand production.

Direction determination of stress field in the area analyzed was carried out by combining several methods from core orientation measurements to orientation direct measurements using microfracturing followed by overcoring. Below, a summary of orientation measurements performed in reservoir studied. Results here presented have been regionally compared, and validated with information from focal mechanisms applied in Intevep [12].

3.1 STRESS FIELD ORIENTATION IN BASIN STUDIED

In order to establish the regional situation as reference for further discussion on stress field orientation in the area analyzed, focal mechanism study of G. Malavé [2] is here described. This study, Lake Maracaibo basin tectonics is characterized by tectonic plates of the Caribbean Sea and South America. Maracaibo basin is delimited by three systems of dextral transcurrent faults, namely: Morón, Boconó and Oca-Ancón (see Figure 8).

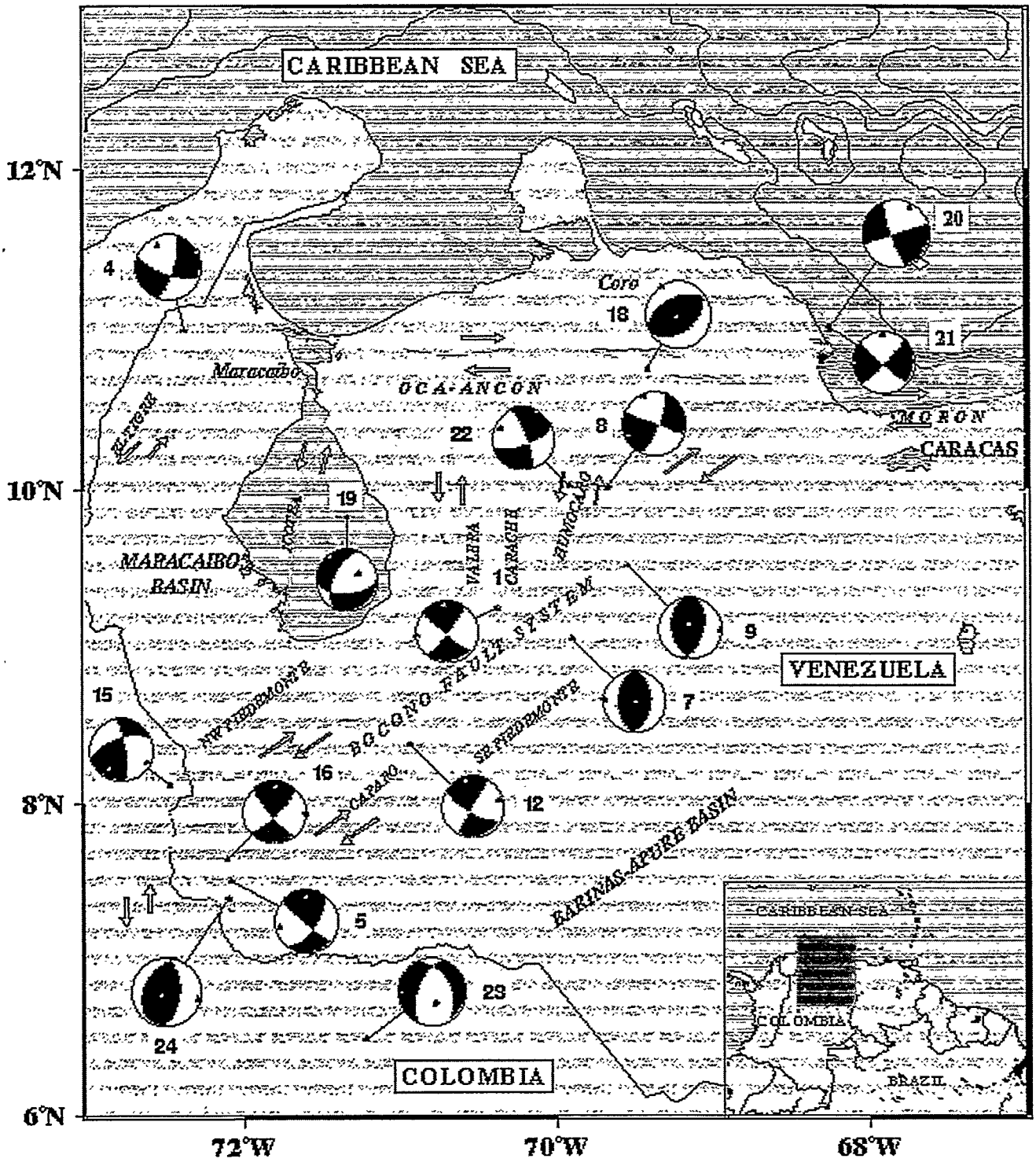

Figure 8 Analysis by focal mechanisms of earthquakes occurred in Eastern Venezuela since 1964. Dark quadrants focal mechanisms (spheres) indicate compressional arrivals. Filled and blank small circles correspond to P (compressional) and T (tensional) axes of focal spheres. Numbers refer to events reported in [2].

Stress field orientation resulting in a region where these lithospehric plates make contact, is an important factor to be considered for the understanding of tectonic processes induced by relative movement of plates. Complex tectonic environment of South American northwest has generated the discussion on main direction of compressive stress field in this area for over 20 years. From the studies performed, two main directions for maximum compressive stress are derived, both constistent with dextral movement of Caribbean and South America plates. First direction proposed for compressive stress field is East-West oriented, due to subduction of Nazca plate under South American plate. However, other authors report a northwest-southeast compression main direction, induced by subduction of Caribbean plate under South American plate, north of Colombia and northeast Venezuela.

Malavé research [2] divides the region into two zones with limit at 10° N, approximately. Southwest Venezuela, focal mechanims analysis suggests a compressive east-west stress field. However, focal mechanims of earthquakes, occurred northwest Venezuela, show a general rotation of P axes from norhtwest-southeast to north northeast-south southwest. In Figure 9, a projection of P and T axes focal sphere of focal mechanisms in lower hemisphere is given . Axes are traced in two groups: northwest Venezuela (left sphere) and southwest Venezuela (right sphere). First of these regions indicates a P axes rotation (maximum stress) from northwest-south to north northeast-south southwest, while in southwest region, P axes are oriented east-west. These directions serve as regional reference to establish maximum stress orientation of the area studied.

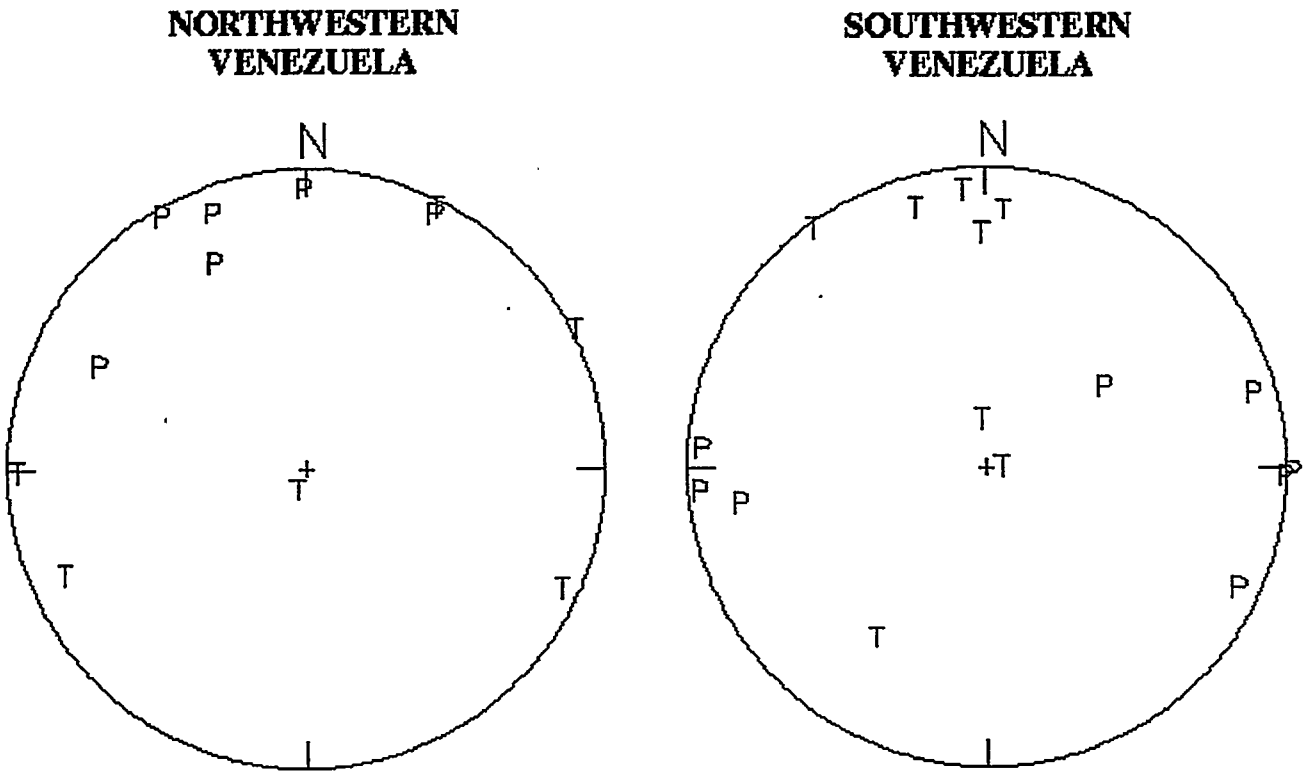

Figure 9 Projection of P and T axes focal sphere of focal mechanisms in lower hemisphere, determined in [2]. Axes are traced in two groups: northwest Venezuela (left) and southwest Venezuela (right).

3.2 Stress Direction in the Area Analyzed

3.2.1 Direction Determination by Core Analysis

A high number of production sand samples from the area studied has been used to perform a geomechanical characterization, and determine optimum expotation conditions, with sand production minimization. As a complimentary method in stress field characterization, several special tests such as AAA, SWAA and DSCA have been applied with the aim of determining minimum horizontal stress direction. Figure 10 summarizes average individual result of each technique applied. In general, minimum stress direction is consistent with directions regionally established.

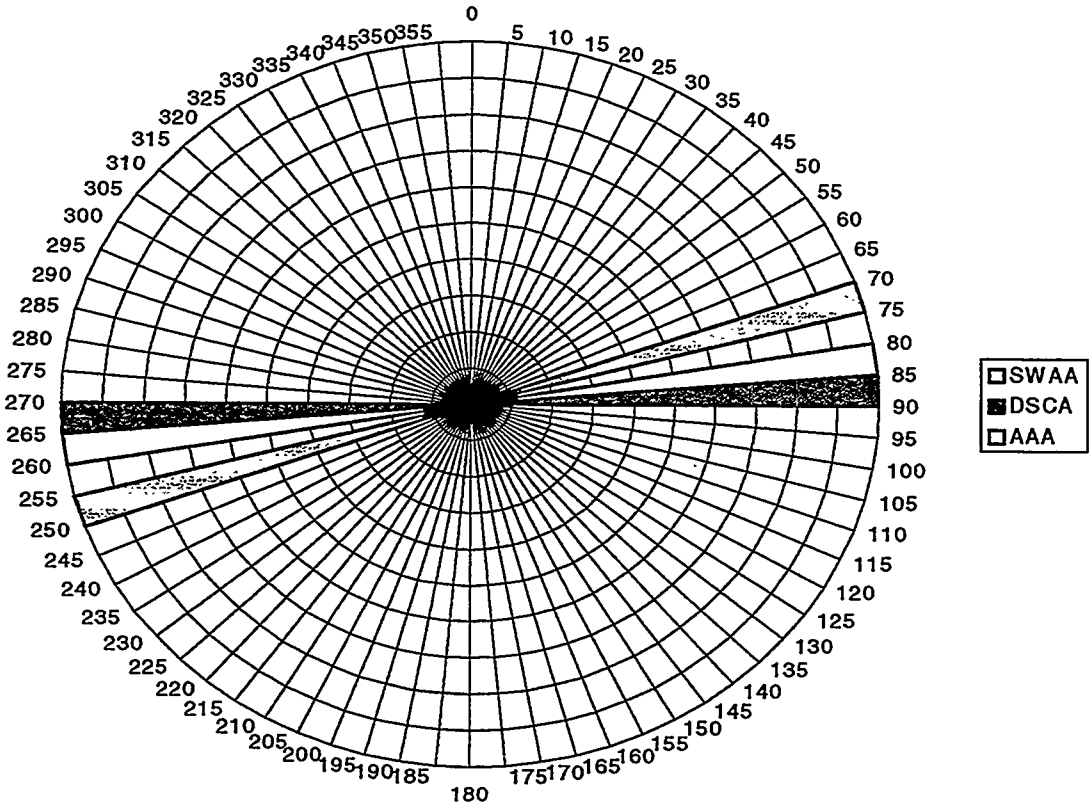

Figure 10 Direction of minimum horizontal stress by AAA, DSCA and SWAA.

3.2.1.1 ACOUSTIC ANISOTROPY ANALYSIS (AAA) IN WELL #9

In Figure 11 information of core in well #9, equivalent to σ_h direction is presentedat . This well is located near west fault of reservoir. As seen, there is a great dispersion of data taken from each test carried out at the indicated depth. In *average*, minimum horizontal stress direction with this technique corresponds to N 83° E ± 26°, which is consistent with general E-W direction, reported by focal mechanism analysis, southwest Venezuela. However, it was observed that at least one of the samples suggests a NW-SE direction for maximum stress, which is consistent with regional direction established for Lake Maracaibo basin.

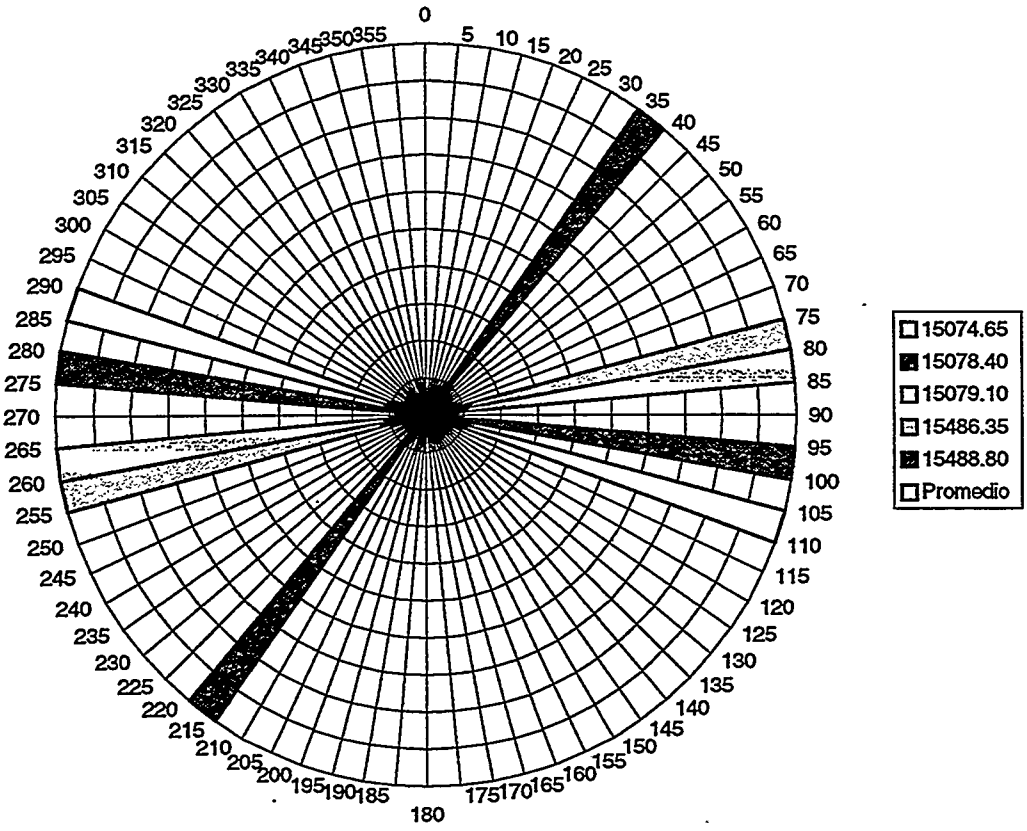

Figure 11 Direction of minimum horizontal stress by AAA 3780

3.2.1.2 SHEAR WAVE ACOUSTIC ANISOTROPY ANALYSIS (SWAA)

Results of SWAA evaluation in core of well # 9 are given in Figure 12. As shown, there is, again, a great dispersion of average direction data for σ_h. Average value is N 74° W ± 15°. In upper reading, this result is consistent with E-W direction reported by AAA.

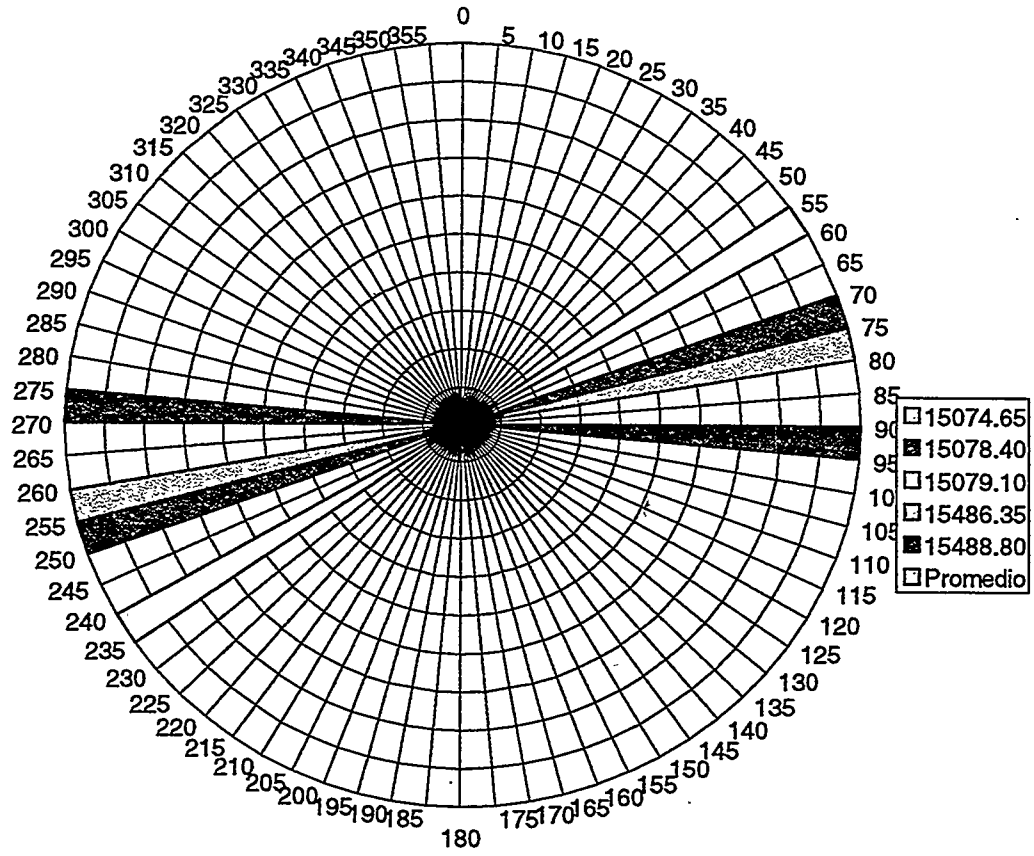

Figure 12 Direction of minimum horizontal stress by SWAA 3780

3.2.1.3 DIFFERENTIAL STRAIN CURVE ANALYSIS (DSCA)

Results of DSCA evaluation are presented in Figure 13. As seen, a great dispersion of average direction data for σ_h of N 89° W ± 23°. This is equivalent to a preferential E-W orientation. As in AAA and SWAA, some points of the samples analyzed suggest a direction consistent with two tendencies inferred from focal mechanisms.

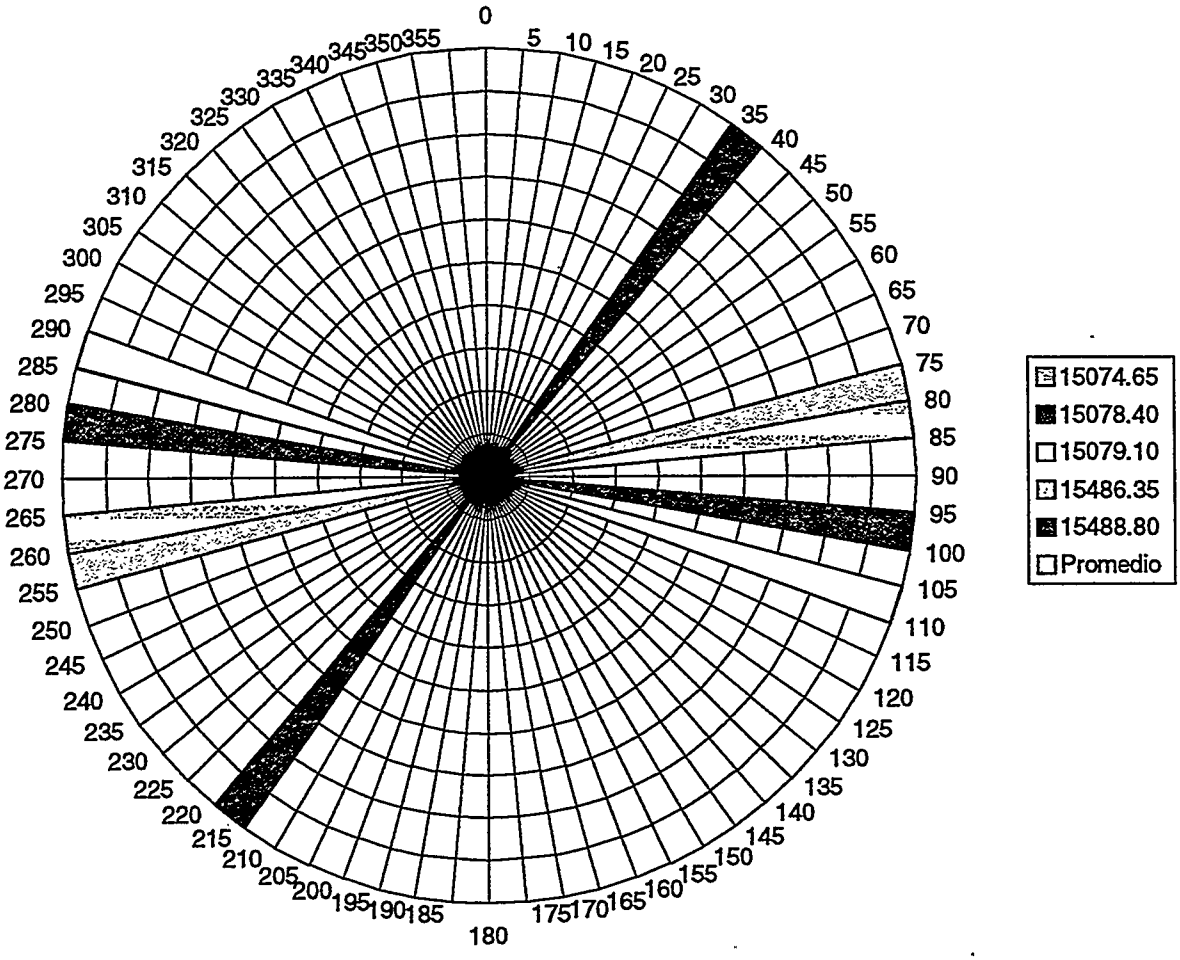

Figure 13 Direction of minimum horizontal stress by DSCA 3780.

3.2.2 STRESS DIRECTION BY PALEOMAGNETISM

Additional to field techniques, PDVSA has carried out two core orientation studies by paleomagnetism [3,4]. Main applications of this technique is in the determination of maximum horizontal stress, and sedimentation direction. Additionally, inferences can be obtained on magnitude relation of horizontal stresses. For information purposes, present study includes directions obtained.

3.2.2.1 ORIENTATION BY PALEOMAGNETISM IN WELL #10

Well #10 is located North of reservoir studied, around 0.5 km from reservoir limit fault. Orientation of σ_H generated by fractures caused by core sampling, corresponds to N 36° E direction. This orientation differs approx. 90° from direction observed in zones away from faults. This is a rotation that might be attributed precisely to close location of well to fault.

3.2.2.2 ORIENTATION BY PALEOMAGNETISM IN WELLS 3780 AND 3768

Both wells 3780 and 3768 are located near the reservoir limit fault. Maximum stress direction for these wells corresponds to an azimuth of N 79° E for 3768, and N 73° E for 3780. In both cases, this direction is consistent with focal mechanism direction, but different from regional tendency observed in wells away from faults. For illustrative purposes, in Figure 14 area rotation effect of maximum stress is shown as wells gets away from one of the faults of the area studied.

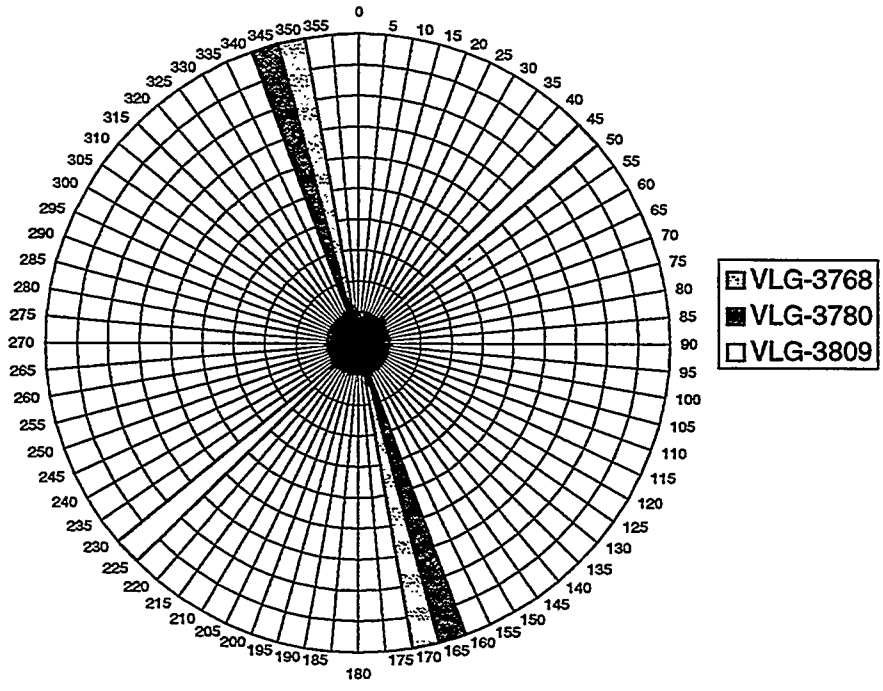

Figure 14 Direction of maximum horizontal stress in vertical wells of area studied. Wells # 3768 and 3780 are located near the reservoir limit fault.

3.2.3 DIRECTION DETERMINATION WITH FIELD TESTS

As part of sand control study in the area analyzed, several field techniques have been applied; namely: Anisotropy DSI® of company Schlumberger, acoustic image logs, and caliper well ovalization logs (dipmeter) of 4 or 6 arms. Below, the results, in chronological order, of this analysis.

3.2.3.1 ANISOTROPY DSI® IN WELL # 3785

In Figure 15, result of Dipole Sonic Imaging or Anisotropy DSI® analysis taken in well 3785 is shown. This technique measures tectonic stress direction based on principles similar to core technique known as Acoustic Anistropy Analysis o AAA [7]. The technique determines stress direction from anisotropy transit speeds of sonic waves, product of the microfractures induced by stresses acting on the rock.

Using a color scale, Figure 15 shows direction of maximum stress in function of depth from 15,100 ft to 17,200 ft. As seen, and based on this log information, maximum stress direction presents an abrupt variation near 90° of North-West to North general direction at an approx. depth of 5,938 ft.

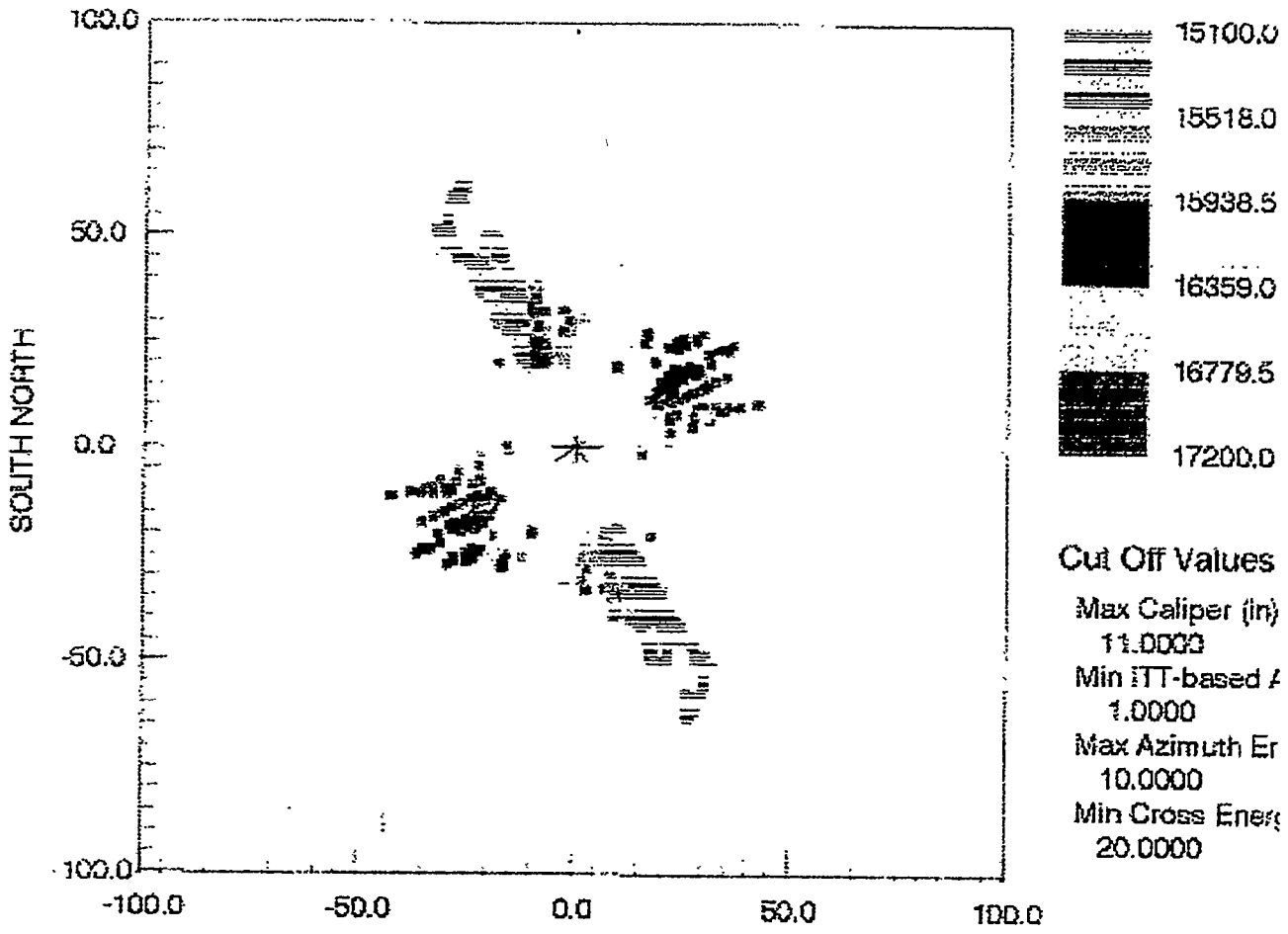

Figure 15 Direction of maximum stress, according to Anistropy DSI® log of well 3785.

3.2.3.2 LOGS OF ACOUSTIC IMAGES

Logs of acoustic images in open hole are used to detect new hole deformations known as breakout or ovalizations produced during drilling. As described in [6], these deformations are consequence of a combination of factors, such as stress local concentration due to removal of material around the hole, *in-situ* stresses, resistance of material, and pressure of drilling fluid (mud weight) on formation. Despite certain controversy on the best model to describe origin of ovalization [6], for present study, it is only necessary to know that, under certain conditions of deviation and structural dip of formation, a larger axis of ellipse describing an ovalization indicates the minimum horizontal stress. Moreover, since it is a direct function of stresses acting on formation, it is together with fracture direction, the best indicator to determine *in-situ* stress orientation.

In general, these ovalizations have variable extension, therefore, they can be detected both by mechanical (4 or 6 arms caliper) and acoustic means. With mechanical means, ovalizations are detected above 2 inches, compared to nominal diameter (bit diameter) of hole. On the contrary, acoustic images show a 0.5 in resolution, and therefore, they are more suitable for detection of new ovalizations in more resistent rocks. This fact implies that acoustic images can be employed to measure maximum horizontal stress magnitude.

For the area analyzed, a number of images logs has been taken to establish *in-situ* stress direction.

3.2.3.3 IMAGE LOG IN WELL 3794

In Figure 16, Figure 17, and Figure18, cross section obtained in acoustic image log taken in well 3794 is shown. In each image, presence of new ovalizations between 0.2" and 1" thick is observed. Direction of these ovalizations are indicators of minimum stress direction. As shown, as in Anistropy DSI®, a set of cross sections suggests the presence of stress rotation as well depth is increased.

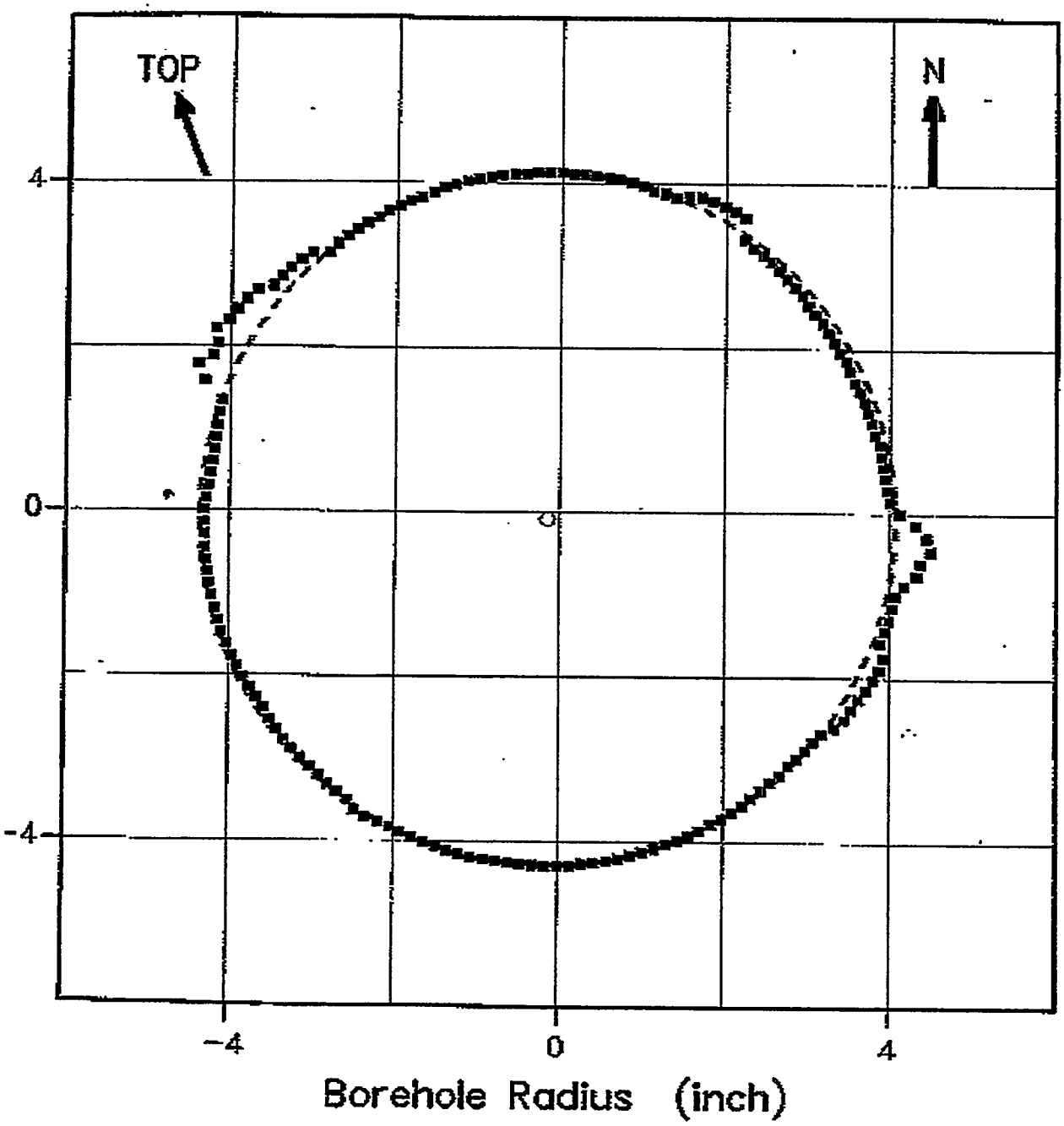

Figure 16 Cross section of acoustic image log of well 3794 @ 17,730 ft.

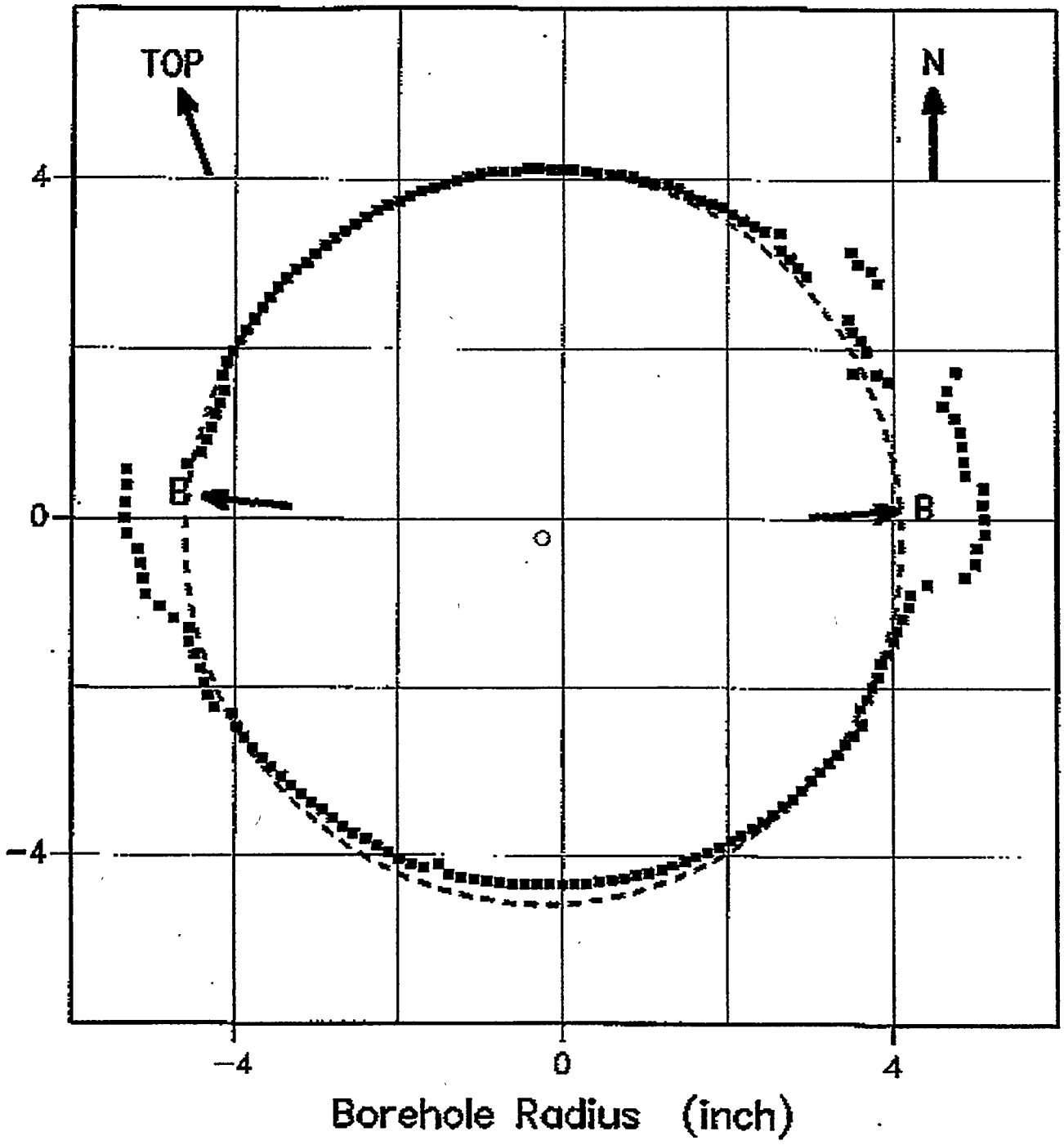

Figure 17 Cross section of acoustic image log of well 3794 @ 17,925 ft.

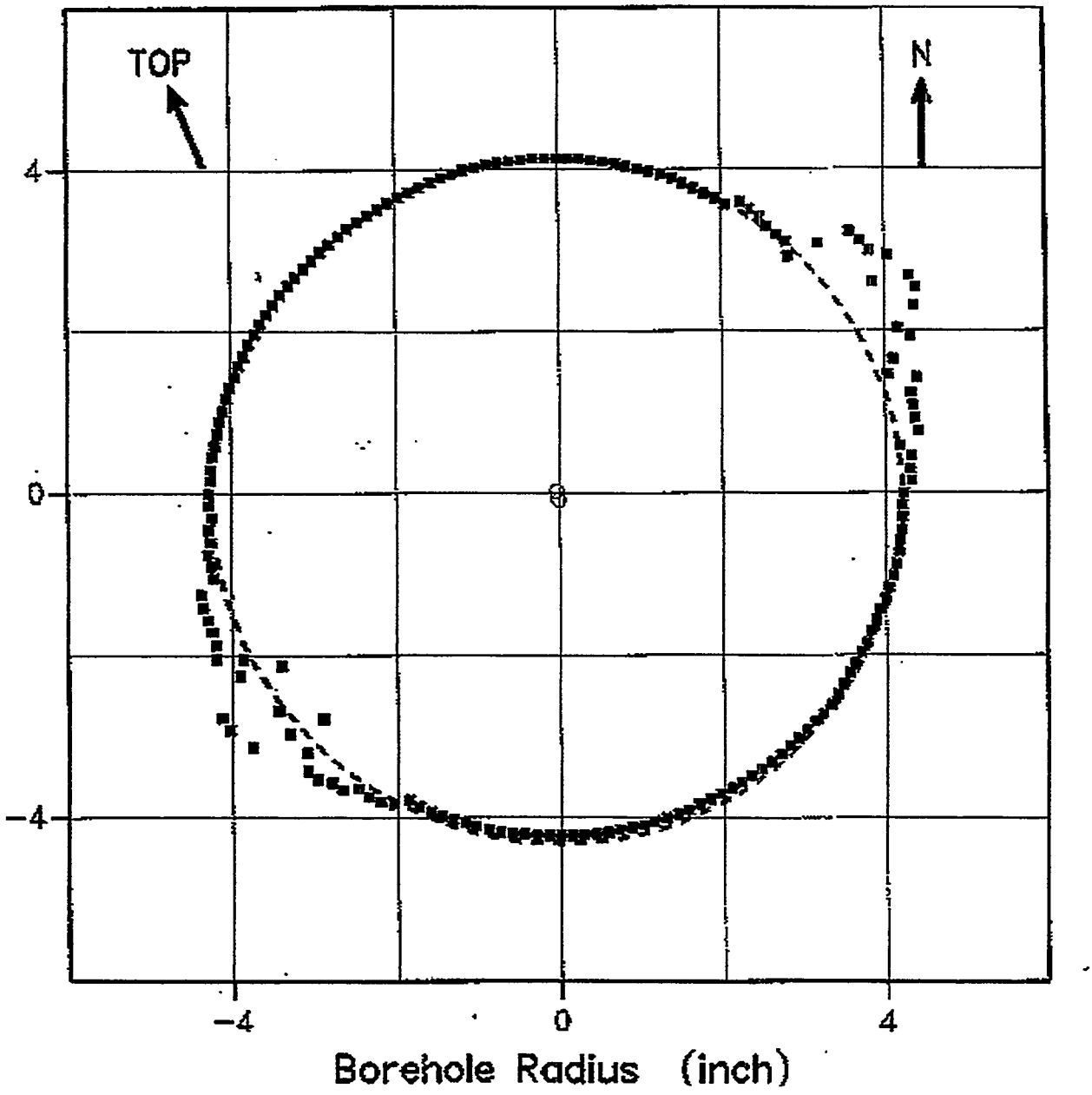

Figure18 Cross section of acoustic image log of well 3794 @ 18,925 ft.

However, it is worth mentioning that rotation direction is not consistent with reports from well 3785. In other words, rotation direction for maximum stress indicated by Anistropy DSI® is clockwise from North-West, while in cross section direction is Southeast-Northwest as depth increases. Of course, this rotation might be attributed to areal variation of stress rotation. It is to mention that using images, a measurement of maximum horizontal stress magnitude with method suggested by Zoback *et al.* [5] was performed. Results obtained with technique will be subject of another report, however, they in general indicate a higher value of 1.4 psi/ft for maximum horizontal stress gradient, consistent with results of microfracturing or leak-off analysis.

3.2.3.4 OVALIZATION ANALYSIS OF IMAGE LOG IN WELL 3809

In Figure 19 the frequency histrogram of ovalizations detected in image log taken in well 3809 is shown. The histrogram corresponds to direction of ovalizations in production well from 14,392 MDrkb ft to 16,415 MDrkb ft deep. The well is located northwest the reservoir near well 3776 away from main faults of reservoir.

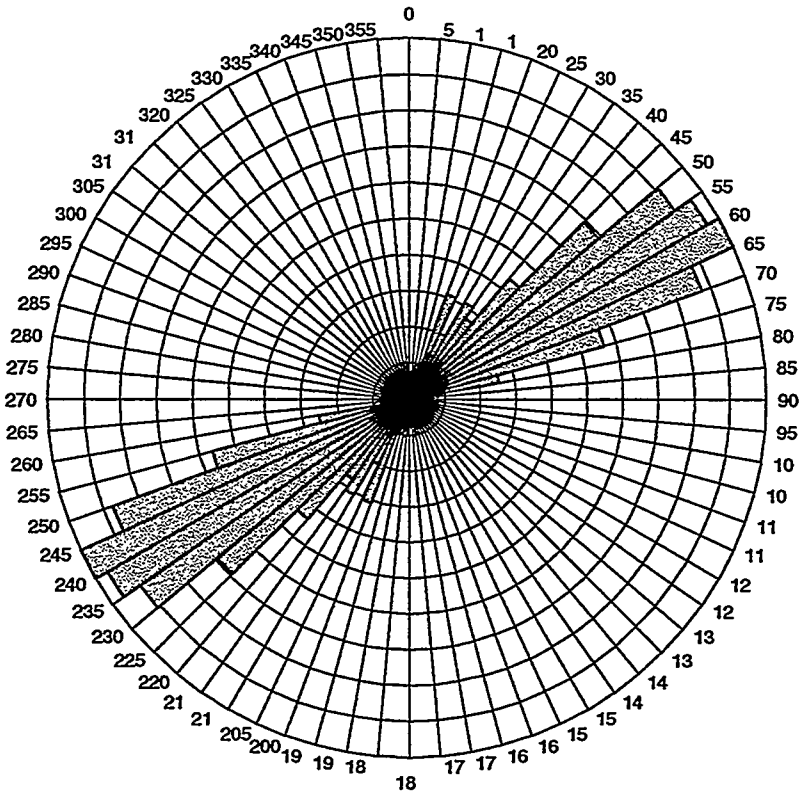

Figure 19 Frequency histogram of ovalization direction of well 3809, indicating σ_h direction.

As Figure 19 shows, average of stress direction readings observed indicates that minimum stress direction is N 49° E-S 41° O, corresponding to maximum stress direction of N 41° O - S 49° E. In azimuth, with respect to North, this means a direction of 49-230°. Different from results of previous methods, this image log did not show abrupt rotations of stress direction angle, as indicated by log Anisotropy DSI® of well 3785. Therefore, rotation in depth might correspond to a local phenomenon, *i.e.* a fault located near the well, that only affects variation in a certain extension.

4. Discussion of Stress in the Area Analyzed

4.1 Analysis of Magnitude

As inferred from results of density log integration with information on microfracturing, the stress field in the area studied represents a situation not reported worldwide. Magnitude components of stress field indicate that it is very probable that main stress ordering in the area studied corresponds to $\sigma_H > \sigma_h \approx \sigma_v$. This ordering represents the fundamental practices existing for developing a sand control strategy applying FracPack technique, given the feasibility of presenting horizontal hydraulic fractures. This suggests the need of limiting shotted section to control location of fracture, and ensure fracture effectiveness.

Although it is not currently possible to explain the reasons why of the high tectonic activity reported by stress level in the area studied, it is necessary to point out that in Lake Maracaibo basin, three tectonic plate systems converge, namely: Caribbean plate, South American plate and Nazca plate. Nature and location of borders of these plates is a matter of discussion among geologists [12]. However, it is expected that contact among these plates have a high compressive stress. Although especulations can be made on the origin of the high tectonic stress found in the area analyzed, opinion of a structure geologist and basin modelling are required to validate this hypothesis, which is out of the scope of the present study.

In function of hydraulic fracturing results of well 3815, in which no propagation of vertical fracture was detected, and the first cycle analysis, which showed the possibility of closing (at least) multiple fractures, presence of a tensor of deviated stresses with respect to vertical extension (well axis) is indicated. Presence of a deviated tensor with respect to vertical extension implies that care must be taken when interpreting results of stress direction obtained in AAA, SWAA tests, given the bidimensional nature of these techniques.

4.2 Analysis of Maximum Horizontal Stress Direction

One of the most complex aspects of stress field determination of the area studied consists in establishing a direction for this area. Areal variation divides reservoir into at least two zones, corresponding to those wells located near the reservoir limit fault, and those away from fault. In order to establish a reference to define outgoing direction, information of Lake Maracaibo basin wells was gathered providing a minimum stress direction reference in the region.

In Figure 20 regional tendency for Lake Maracaibo basin is shown. The tendency was established using induced ovalizations or fractures obtained from image logs of wells: 152 (6,000 ft deep), to

the North of Maracaibo city; 54 (10,000 ft deep) on the east coast south east of the Lake; and LSE-5018 (1,000 ft deep) on the east coast of lake. Regional tendency is observed showing a fan-like form covering at least 20° of deviation.

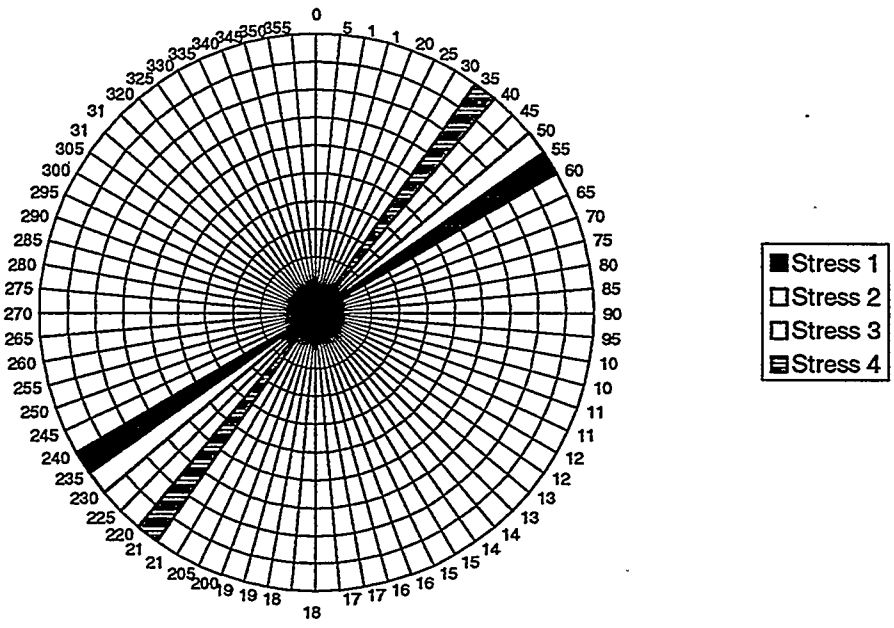

Figure 20 Direction of ovalizations (minimum stress) in wells located in Stress 1 zone, Stress 2 zone, Stress 3 zone, and well 3809, area of study.

Again, the tendency is consistent with orentation determinations obtained in wells away of reservoir limit fault. Noteworthy is that maximum (compressive) stress direction obtained in the focal mechanism study is consistent with direction obtained from acoustic images logs of Lake Maracaibo basin wells.

5. CONCLUSIONS AND RECOMMENDATIONS

From the information here presented, following conclusions are drawn:

I. Studies carried out up to now indicate that stress field in the study shows particular characteristic not previously reported for oil reservoir in Lake Maracaibo basin.

II. Stress regime is characterized by a low contrast between vertical stress (estimated by density log integration), and minimum horizontal stress estimated from open hole or cased hole microfracturing and leak-off tests. Maximum horizontal stress is estimated in 1.1 psi/ft.

III. From image logs and using Zoback technique to interpret ovalizations, gradient or higher value of maximum horizontal stress is 1.4 psi/ft.

IV. Minimum stress direction for the area studied is N 50° E, which is consistent with direction estimated by interpretation with other techniques applied in regions, such as focal mechanisms and ovalizations analysis of other basin reservoir geographically distributed (Mara Oeste, Barúa-Motatán, Tia Juana, among others). See Figure 20.

V. Results of paleomagnetism of open hole microfracturing tests performed in well 3815 are expected. However, preliminary interpretation suggests that stress field tensor is deviated with respect to vertical extension.

VI. From these conclusions following recommendations are derived within the sand control strategy for the area of study.

A. *Oriented Perforation.* If this methodology is implanted, perforations shall be oriented to N 40° W. This recommendation is for wells away from reservoir limit fault, due to the uncertainty with respect to maximum stress in wells near the fault.

B. *FracPack.* It is recommended to limit the height of shotted zone to sand thickness in wells treated with this technique. The recommendation is supported on the low feasiblity of the vertical extension of fractures, aiming to effectively control location of fractures.

C. *Horizontal Wells.* Horizontal wells in the area shall be oriented to maximum stress direction, according to what it is established in this study.

6. REFERENCES

1. Blundum de M y Muñoz, A. "Desarrollo de correlaciones núcleo-pérfil". Informe Técnico Maraven, Gerencia de Tecnología de Producción, MAR-IPTR-0246,97

2. Muñoz, A., et al. "Metodología Integrada para Análisis de Estabilidad de Hoyos", INTEVEP, S.A., Los Teques, INT-STE-00259,96

3. Eaton, B.A., "Fracture Gradient Prediction and its Application in Oilfield Operations", J. Pet. Tech. (Oct. 1969), 1353-1360.

4. Terzaghi, K., Peck, R.B., Mesri, G., "Soil Mechanics in Engineering Practice", 3era Edición, Jhon Wiley & Sons, Inc., New York, 1996.

5. "Open Hole Log Analysis and Formation Evaluation", Halliburton Logging Services, 1991

6. Fjaer, E. Holt, R., Horsrud, H.P., Raaen, A.M. y Risnes, R., "Petroleum Related Rock Mechanics", Elsevier, Amsterdam, 1992.

7. Terratek, S.A. "Caracterización Geomecánica de los núcleos de los Pozos 3780, 3768 y 3743", 1997

8. Terratek, S.A. "Caracterización Geomecánica de los núcleos del Pozos 3782", 1997

9. Castillo, E., et al. Caracterización Geomecánica de muestras de núcleo del pozo 3793, Campo Estudio, Área 2 Sur" INT-3980, 1997, Franquet, J. et al. "Análisis y Caracterización geomecánica del núcleo del pozo 3787, Área 2 Sur, Campo Estudio" INT-3529, 1997, INTEVEP, S.A., Los Teques.

10. Abasss, et al. en "FracPac Completion Services. Stimulation and Sand-Control techniques for high-permeability oil and gas wells", Halliburton Energy Services, Houston, 1994.

11. Abass, H., Hedayati, S. Soliman, M y Hunt, J., "Fracturing of Horizontal and Deviated Wells" en Stimulation Technology Review, Vol. 1, Halliburton Energy Services, Houston, 1994.

12. Malavé, G. "Deformación corticial y sismicidad superficial reciente en el Occidente de Venezuela: implicaciones tectonicas regionales", INT-03279, 1996

13. Van Alstine, D.R. "Paleomagnetic orientation of Eocene cores from Estudio Field Lake Maracaibo Wells 3743, 3780 y 3768 for Maraven, S.A.", Applied Paleomagnetics, Inc., April 1996.

14. Van Alstine, D.R. "Paleomagnetic orientation of Eocene cores from Well 3782, Lake Maracaibo.", Applied Paleomagnetics, Inc., Diciembre, 1996.

15. Zoback, M. y Peska, P, "In situ stress and Rock Strength in the GBRN/DOE Pathfinder Well, South Eugene Island, Gulf of Mexico, JPT, Vol. 47, N° 5, pp. 582, 1995 y referencias citadas.

Task 70 — DOE shall provide INTEVEP with information on the results of NIPER's thermal light oil program. This work deals with tracking DOE's Light Oil Steamflood at Naval Petroleum Reserve No. 3, Teapot Dome Field, Wyoming and laboratory research on light oil steamflooding, including in situ upgrading of the crude. Research is directed toward improving the understanding of the basic mechanisms responsible for enhanced light oil production using thermal methods and accelerating development and expansion of the resource base that is recoverable using this technology.

LIGHT OIL STEAMFLOOD RESEARCH—STEAMFLOOD LABORATORY DESIGN AND IN-SITU COMBUSTION PRINCIPLES/PRACTICES

by
Paul Ahner and Partha Sarathi
edited by
Arden Strycker

Abstract

This report presents the results of Task 70 research conducted as part of the Annex IV, a Thermal Oil Production Research agreement between the U.S. Department of Energy and the Venezuelan Ministry of Energy and Mines. The BDM Petroleum Technology as a subcontractor to BDM-Oklahoma conducted this research under DOE's thermal research program, whose goal is to improve the understanding of oil production by thermal methods and to help accelerate development and expansion of the resource base recoverable by thermal methods.

The original task statement outlined activities to evaluate DOE's Light Oil Steamflood at Naval Petroleum Reserve No. 3. However, this work has been done and described previously in Task 64. Consequently, the activities described here are updated to include two major components: (1) design and construction of a steamflood laboratory, and (2) the development of an in situ combustion handbook.

A steamflood research laboratory and a 3D physical model was built to accelerate development and expansion of the light oil resource base recoverable using steamflooding as the production technology. This was to be accomplished by improving the understanding of the basic light oil steamflood mechanisms and improving the predictive capability regarding horizontal well steamflooding performance. Although this work was terminated (November 1998) due to funding cuts, significant progress was made including construction of the research laboratory, a 3D physical model, software updating, shakedown runs and numerical simulation.

The objective of the in situ combustion handbook project is to provide under one cover the state of knowledge, prediction and practices of the in situ combustion (ISC) technology to operators and engineers who are unfamiliar with this aspect of thermal oil recovery technology.

The principle items to be addressed in the handbook include: (1) the fundamentals of the in situ combustion process, (2) evaluation of an ISC Prospect, (3) laboratory studies related to ISC process, (4) engineering of an ISC project, (5) operational practices, problems and solutions, and (6) case history of selected past projects and lessons learned from them.

The organization of the handbook emphasized practical aspects of the process. Important issues are clarified by providing examples drawn from past projects.

This work at **National Institute for Petroleum and Energy Research** was supported by the U.S. Department of Energy under contract DE-AC22-94PC91008 with BDM-Oklahoma Inc.

STEAMFLOOD LABORATORY

Background

Use of steam to recover heavy oil from unconsolidated sands is commercially successful and continues to be the leading enhanced oil recovery (EOR) production method (worldwide production is more than 1,200,000 bbl/day; U.S. production is 420,000 bbl/day, more than 60% of all U.S. EOR). Use of steam for light oil recovery is increasing (worldwide light oil steamflooding is producing more than 330,000 bbl/day; in the U.S., 2,500 bbl/day).

The United States has some large potential light-oil steamfloodable reservoirs: the multi-billion barrel oil resources of the diatomites and Monterey shales of the San Joaquin Valley in central California (sites of current light oil steamflooding pilots), and many of the shallow pressure-depleted oil-wet reservoirs of the Mid-Continent and Appalachian basins. Oil-wet reservoirs containing high pour-point paraffinic light crude are being considered for light-oil steamflooding because steam changes the wettability to water-wet conditions and provides the heat and pressure to overcome some primary production problems.

Successful research into light oil steamflooding has the potential to add the resources described above to our dwindling domestics reserves. The use of horizontal wells as steamflood injectors and producers can offer significant productivity advantages over vertical wells when developing both light oil and heavy oil fields since they can access a greater section of reservoir per well. For this reason and the fact that the horizontal to vertical well installation cost ratio has decreased to as low as 1.2 - 2.0, horizontal wells are becoming increasingly popular. Horizontal well operation has not yet been optimized to maximize production. Unequal pressure distributions at the "heel" and "toe" of the well (both ends of the horizontal section of well) can cause nonuniform sweep patterns when using horizontal wells as injectors. Numerical representation of horizontal wells regarding these heel and toe effects is still being developed. This project has the potential to offer both a simultaneous physical and numerical representation of horizontal wells in steamflood application which would offer a more reliable approach to predicting horizontal well behavior.

Thermal Recovery Research Objectives

The overall objective of this project was to accelerate development and expansion of the light oil resource base recoverable using steamflooding as the production technology. This was to be accomplished by:

- Improving the understanding of the basic mechanisms responsible for enhanced light oil production using thermal methods (including steam);
- Improving the predictive capability regarding horizontal well steamflooding performance which would be applicable to both light and heavy oil reservoirs.

Summary of Activities

The following activities were carried out during the past two years:

1. A steamflood research laboratory was constructed.
2. Updated software (Labview 4.0) was developed which provides control, real time display and monitoring of the experiments.
3. A more versatile, scaled, physical model which better meets industry's needs was designed and built. This model can:
   - Scale model both horizontal and vertical well pattern configurations in three dimensions including end effects and curved wells. This feature, along with numerical simulation allows the most current and most promising future well configurations to be evaluated.
   - Provide input to and calibrate numerical simulators. Present numerical simulator representation of the more complex well patterns is still questionable.
   - Allow for 1D, 2D, or 3D studies.
   - Be used in a vertical, tilted or horizontal position to model dipping reservoirs.
   - Use actual reservoir oil and rock, operate at field pressures, and operate at reservoir temperatures (up to 1,100 psi and 550° F) to better represent field operations.
   - Provide steamflood performance versus time regarding the 1) shape and progress of the steam swept volume and thermal profiles, the 2) instantaneous and cumulative steam oil ratio, and the 3) overall oil recovery.
   - Allow shorter experiments to be conducted to increase turnaround time and to improve cost effectiveness.
4. Three physical model runs were made for shakedown purposes to determine the heat loss characteristics of the model.
5. CMG-STARS numerical simulation of physical model performance was initiated in order to establish a common baseline between the numerical and physical simulations.

Hardware/Software Description

Steamflood Laboratory Apparatus

Building 87G at the Phillips Petroleum Research Center was chosen to house the steamflood laboratory. This building was chosen because it contains an isolated "safety cell" that has blowout panels to allow rapid, safe venting in the unlikely event of an equipment breach. The steamflood apparatus was built inside this safety cell and was remotely operated in the bay outside of the safety cell. The cooled, condensed products from the model were piped directly into a fume hood in the bay area where production weights and water-oil ratios could be recorded. Figure 70-1 shows a plan view of the physical layout. Figure 70-2 shows a layout of the equipment rack and the model.

The simplified steamflood apparatus, minus valves, heat tracing, pressure/temperature taps, saturation hardware and safety devices is shown in Figure 70-3. It is capable of pressures to 1100 psig, temperatures to 550° F, and steam flows to 360 cc/min CWE. Pressures were read by a single pressure transducer plumbed into a 48 port Scanivalve. The Scanivalve constituted a motorized 49 port valve which temporarily connects each port in sequence to a single pressure transducer.

Physical Model Description

The ASME approved model consisted of a 14" O.D. section of pipe with flanges on both ends. Steam feed and thermocouple access holes were installed on one side (Figure 70-4). In order to achieve a three dimensional flow regime, refractory cement was cast into the model to produce a rectangular void with dimensions of 10.5" wide by 4" high by 60" long (Figure 70-5). The refractory, with thermal properties similar to reservoir rock, simulated the heat losses to the roof and floor of the pay. The model held a total of 216 thermocouples in order to obtain a high resolution thermal profile between injector and producer. The horizontal wells consisted of 0.25" thin-wall stainless steel with a 400 mesh screened 0.086" slit cut into them using the relationship (Reference 1):

$$\text{slit width, inches (b)} = 2\,\pi\, r_{wm}$$

$$r_{wm} = r_{wp} / \partial$$

where r_{wp} = radius of field scale well and ∂ = scaling factor

This slit width of 0.086" represented a 6 inch well at a scaling factor of 220 or a 4 inch well at a factor of 150. Only the center 3 feet of the wells were slit with "well coolers" placed at both ends. These well coolers were installed to negate the artificial end effects that would be produced by the hot "unslitted" section of wells. An area of high potential heat loss, where the thermocouples pass through the steel shell was insulated with 1.5" thick teflon. At least 18 thermocouples were attached to the steel skin of the model to assess the heat losses during the runs. This heat loss data were used to calibrate the CMG-STARS representation of the physical model.

Computer Interface/Software Description

The monitoring, control and data storage functions were carried out by a Macintosh Quadra 950 computer, with an assortment of onboard (in the computer) and outboard cards. The Quadra used the following cards and auxiliary hardware.

- An onboard Greenspring four serial port expansion card that was used to communicate to various balances in the system, which monitored steam feed rate, production weights, etc.

- An onboard NB MIO 16x card/NB DMA 2800 card combination that connected to four outboard NB 64T AMUX cards and read a total of 256 channels. These channels were dedicated to temperature monitoring. The NB DMA 2800 card allowed high speed data collection.
- An onboard NB DIO 24 card to communicate with an outboard ER 16 relay card that controlled various solenoid valves.
- An onboard expansion card to communicate to an outboard expansion box that housed two Macintosh video cards and another NB MIO 16x card. The extra video cards allowed the Quadra to display screens on three monitors while the extra NB MIO 16x card read the pressure transducer signals from the Scanivalve.

Labview software programs were upgraded/developed to:

- Convert raw data into useful units;
- Monitor, display and store all temperature, pressure and flow rate data;
- Provide warning on at least 20 process variables when out of a specified range;
- Provide emergency shutdown capability on the crucial process variables;
- Display the steamflood front movement from all 216 model thermocouples in real time; and
- Automate the product collection system.

Summary of Runs

Four steamflood runs were made using water only saturated media to:

- Shakedown the system,
- Obtain baseline heat loss data for subsequent analysis using CMG-STARS numerical model, and
- Determine the practical lower steam feed rate to decide whether certain "ultra slow steam feed rate" scaling factors (Reference 2) could be applied to our model.

Since these were basically shakedown and water only baseline runs, little attempt was made to analyze them in detail. A qualitative description of these runs is given below.

Run 1 was a shakedown run and indicated some minor changes to the flowsheet that needed to be made. Runs 2 and 3 simulated a vertical injector/producer well pair in a 1/4 of a five spot pattern and a 400 md glass bead water saturated media. The system ran smoothly. A classic steam override pattern developed using steam feed rates around 30 cc/min CWE. After the override pattern was developed, steam rates were decreased to 1-3 cc/min to determine if ultra low flow scaling factors could be used. All forward progress of the steam front stopped at this point and the model began to cool, indicating that heat losses were too great to sustain a steamflood at these steam rates. This sudden cool down was expected to occur, since the model

was designed for high steam rates using the scaling factors of Pujol and Boberg (Reference 3). At these higher rates, heat loss has a lesser influence since the heat loss effects are overwhelmed. The ultra low flow rates were tested to clarify the limits of the model.

The last run was made using two horizontal wells arranged as shown in Figure 70-4 and Figure 70-5. A 10 Darcy coarse sand media and a much greater steam rate of 120 cc/min CWE was used. The thermal profiles from this run showed an almost uniform, rapid sweep between the two wells. The combination of high flows, high permeability and low viscosity liquid apparently caused this rapid pattern development in an almost plug flow fashion.

CMG-STARS Numerical Simulation

The first goal of the numerical simulation activities was to numerically simulate the heat loss characteristics of the physical model. After experimenting with some 2D numerical models, a 10 x 12 x 11 grid block numerical model was built and run to match the skin temperatures of the physical model during a steamflood run. Since the physical model is a cylinder and the numerical model is a 3D rectangle, a perfect numerical grid match to the physical model could not be made. To compensate, the thermal properties of the grid blocks around the packed bed were adjusted in order to achieve the temperature match at the skin of the physical model. After the temperature match was made, this numerical model would then serve as the baseline numerical model. This match has not yet been made, however.

IN-SITU COMBUSTION HANDBOOK
PRINCIPLES AND PRACTICES

Background

Previously, a handbook on steamflood operations was written and published (Reference 4) describing the basic elements in designing and implementing a field steamflood project. Mathematical formulas were kept to a minimum and descriptions were somewhat simplified to enable engineers less knowledgeable in steamflood operations to grasp the basic principles. This approach was used because the target audience were the smaller independent operators. Not only were books and journal articles reviewed from the public domain, but company handbooks and common practices among current operators were incorporated. The intent was to encourage those not currently injecting steam (particularly smaller independents) to review their own oil properties, and if appropriate, to expand their operations with some type of steam injection program.

The handbook for steamflood operations was tremendously popular, not only to U.S. independent operators, but to U.S. graduate students taking courses in EOR and to many international organizations also considering enhanced recovery by steam injection. Consequently, a similar project was initiated for in situ combustion. A handbook was to be developed on the in situ combustion process, reviewing past practices and providing guidelines (lessons learned) to those engineers looking for ways to increase production.

Work on the development of the handbook is completed. The handbook includes ten chapters including the introduction (Chapter 1). Chapter 2 describes the various in-situ combustion (ISC) processes. Chapter 3 is devoted to kinetic and combustion tube studies. The reservoir geological and site selection criteria for an ISC project are reviewed in Chapter 4. Chapter 5 presents a step by step approach for designing ISC projects. Case history of selected U.S. and non-U.S. combustion projects are presented in Chapter 6. Chapter 7 discusses in considerable detail the compressors and air plant requirements for a fireflood project. In Chapter 8 methods for igniting the reservoir are presented. Chapter 9 covers the well completion practices, operational problems and their solutions. This chapter also briefly touches upon the project monitoring issues. Chapter 10 considers the enriched air/oxygen fireflood requirements.

Following is a brief summary of these chapters included in the handbook. However, Chapters 9 and 10 are not included here, because they were not completed when this material was presented at the Annex IV meeting.

Chapter 1 - Introduction: The introductory chapter outlines the purpose, scope, and organization of the handbook and discusses the assets and liabilities of in situ combustion technology. Other sections focus on the history of the technology and the U.S. and global in situ combustion activities.

As outlined, the purpose of the handbook is to present the state-of-the-art knowledge and practices of the ISC technology in simple terms. The handbook is directed at independent operators and novice engineers who are unfamiliar with this oil recovery method. More specifically, the handbook includes:

- Documented the experience and lessons learned from the in situ combustion field projects of the last 45 years
- Summarized the role of combustion kinetics and combustion tube studies in establishing basic design parameters
- Detailed the steps involved in the selection of an in situ combustion field site and project design
- Provided guidance to equipment selection, installation, and operation
- Documented field problems, solutions and project monitoring requirements
- Detailed the well completion and ignition requirements
- Outlined the safety and other special considerations for oxygen/enriched air combustion field projects

Chapter 2 - Fundamentals of In Situ Combustion Process: This chapter reviews the different combustion processes and their recovery mechanisms.

In situ combustion is basically a gas injection oil recovery process. Unlike a conventional gas injection process, heat is used in an ISC process as an adjuvant to improve the recovery. The heat is generated within the reservoir (in situ) by burning a portion of the oil. The burning is sustained by injecting air or oxygen enriched gas into the formation. This process is also called a fireflood to connote the movement of a burning front within the reservoir. The oil is driven toward the producer by a vigorous gas drive (combustion gases) and water drive (water of combustion and recondensed formation water).

Based on the direction of the combustion front propagation in relation to the airflow, the process is classified as forward combustion or reverse combustion. In the forward combustion process, the combustion front advances in the general direction of airflow; whereas in reverse combustion, the combustion front moves in a direction opposite to that of the airflow. Only forward combustion is currently practiced in the field. The forward combustion is further categorized into 'dry combustion' and 'wet combustion'. In the dry combustion process, air or oxygen enriched air is injected into the reservoir to sustain combustion. The dry process is thermally inefficient because much of the heat generated during burning is stored in the burned sand behind the burning front and is not used effectively for oil displacement.

If water is injected together with air, much of the heat stored in the burned sand can be recovered by the water and transported forward, thus aid in improving recovery and process efficiency. Injection of water simultaneously or intermittently with air is commonly known as wet combustion. The ratio of the injected water rate to the air rate influences the rate of burning front advance and the oil displacement behavior. Wet combustion generally results in shorter project life and reduced compressor requirements compared to dry combustion.

The overall fluid transport mechanism in a combustion process is a highly complex sequence of gas drive (combustion gases), water drive (recondensed formation water and water of combustion, and in case of wet combustion the injected water), steam drive, miscible gas and solvent drive. The mechanisms of fireflooding are quite complicated, and there are many factors

that affect the operation, efficiency, and economics of the process. These factors are fully discussed in this chapter.

In addition to the aforementioned combustion processes, a number of variations to the basic combustion process have been proposed over the last 50 years and a few field-tested with mixed results. These variations were proposed to improve the effectiveness of the basic (dry or wet) combustion process under certain conditions. The suggested variations include: (1) heat wave process, (2) cyclic dry combustion, (3) cyclic wet combustion, (4) burn and turn (pressure up-blow down combustion or BP process), (5) steam-oxygen co-injection process, (6) steam chamber process, (7) COSH (combustion override split production horizontal well process), and (8) oxygen recycled produced gas process. To date, only the first four variations have been field-tested.

Chapter 3 - Kinetics and Combustion Tube Studies: Unlike steam injection processes, oil composition and rock mineralogy always play a major role on oil recovery in an ISC process. This is because the ISC process requires a chemical reaction between the crude oil and the injected air within the reservoir. The extent and nature of these chemical reactions as well as the heating effects they induce depends on the features of the oil-matrix system. The reservoir rock minerals and the clay content of the reservoir are known to influence the fuel formation reactions and their subsequent combustion. Hence a qualitative and quantitative understanding of ISC chemical reactions and their influence on the process is critical to the design of the process and interpretation of the field performance.

In contrast, steam injection processes are less sensitive to variations in oil composition and rock mineralogy. Large differences in oil composition are needed to effect changes by orders in magnitude of crude oil viscosity. Mineralogy mainly affects steam processes when water sensitive clays are present, or when high rates of rock dissolution occur.

This chapter presents an overview of the principal chemical reactions associated with the ISC process and describes the various experimental techniques and computational procedures employed to obtain the critical kinetic, process, and design information.

Chapter 4 - Evaluation of an In Situ Combustion Prospect: Several factors must be taken into consideration when evaluating candidate reservoirs for ISC application. These include site geology, reservoir rock and fluid properties, crude oil characteristics, and reservoir geometry. These variables are addressed in this chapter. Prospect screening criteria for ISC process is also presented.

In addition to favorable combustion characteristics of the crude oil, favorable geological characteristics of the reservoir are also critical. Based on an analysis of the geological features of the past U.S. fireflood project sites the following were concluded:

- The continuity of individual sand layers within the producing formation, especially in thin lenticular sand is a factor of major importance to the success of a fireflood. Failure of many past projects can be traced to lack of aerial continuity and the presence of compartmentalized reservoir sands.

- Reservoir depth is not critical to the technical success of the combustion process. Depth, however, does affect temperature, pressure, and well costs (and therefore, the economic success of the project).

- Structural altitude and dip are important considerations in the location of wells for a combustion project.

- Sand thickness is one of the more important parameters for the combustion process. Preferably the pay thickness should be at least five feet, but should not exceed 50 feet. It is preferable that very thin reservoirs (less than 8 feet thick pay) considered for fireflood contain multiple stacked thin sands separated by non-communicating vertical barriers.

- The actual value of permeability has very little effect on the mechanics of combustion. The degree to which a permeability profile correlate from one well to another is more important than the actual value of permeability.

- The economic success of a fireflood is dependent more on the actual value of the oil saturation-porosity product than on porosity alone. Porosity values lower than 0.2 are acceptable only if the oil saturation is greater than 0.4.

- The clay and metallic content of the rock, as well its surface area has a major influence on the economics and applicability of a fireflood in a reservoir.

- Geological factors such as the lenticularity and anisotropy must be taken into consideration in determining well spacing and orientation of flood patterns.

Chapter 5 - Engineering of an In Situ Combustion Project: Several variables are used to measure and control the performance of an ISC process. The most important parameters are fuel deposit, air flux, air injection rate, air-oil ratio, injection pressure, and oil recovery rate. Methods and equations to estimate these parameters are presented in this chapter. Three different techniques to engineer an in situ combustion project are presented and illustrated through examples. The methods discussed include: (a) Nelson-McNeil method (Reference 5), (b) Gates-Ramey volume burned method (Reference 6), and (c) Brigham-Sattman technique (Reference 7). Each of the methods are discussed in detail and explained through illustrated examples.

Chapter 6 - In Situ Combustion Case Histories: Since the early 1950's, more than 270 fireflood projects have been implemented in the U.S. and elsewhere throughout the world. A large number of field tests were conducted in reservoir situations that were not suited to fireflooding, and therefore, demonstrated where ISC should not be applied. Oil industry economics have changed considerably during the period in which the early field tests were conducted. Results that indicated an economic failure at one point in time might have considerable merit now. However, operational costs have generally increased, which makes it necessary to make a complete evaluation of each new prospect.

In this chapter, five firefloods were reviewed in detail to present the latitude to which this method has been used, from the very shallow low pressure reservoir of the General Crude's New Port Beach, California fireflood to Gulf's deep Heidelberg Cotton Valley Air Injection

Pressure Maintenance Project in Mississippi. The projects discussed include: (1) Mene Grande Oil Company's Miga P_{2-3} fireflood in Venezuela, (2) Chevron's (formerly Gulf) Cotton Valley air injection project (West Heidelberg Field, Jasper County, Mississippi), (3) Mobil's (formerly G.E. Kadane & Son) West New Port fireflood in Orange county California, (4) Oxy-Petroleum's (formerly Cities Service Co.) Bodcau fireflood in Boissier Parish, Louisiana, and (5) Husky Oil Company's Paris Valley combination (air-steam) fireflood in Monterey county California.

Each of the projects discussed present unique performance characteristics and operation problems. For each project, the project's outcome, reasons for the success or failure, operational problems and the operator's approach to mitigate the problems are presented.

Chapter 7 - Air Injection Plant: The air compression plant is probably the most important part of the surface facilities in a combustion project. Its role in an ISC project is to economically and continuously provide clean, dry, high-pressure air at the required rate to support and sustain combustion, while meeting environmental and safety requirements.

To achieve the stated objectives and to obtain the benefits of a trouble free operation, care must be exercised in selecting equipment, laying out correctly, and then maintaining the system in good working order. Poor operation and maintenance of the air compression-distribution system can result in compressor failure. Frequent air plant downtime resulting from compressor failure and explosion is one of the major causes of the economic failure of many past ISC projects.

The air compression plant consists essentially of one or more compressors with a power source (driver), control system, make air filter, intake air filter, inter- and after-coolers, separators, filters, dryers, fuel and lube oil storage tanks, interconnection piping, exhaust emission control equipment and distribution system to carry air to injection wells.

Several factors must be taken into consideration in the engineering of a trouble free air injection system for ISC operation. The air compressor is the heart of the compressed air system, and the selection of proper compressors for the application is critical. The engineer in charge of designing an air injection system must have a good understanding of the specific characteristics of different compressor types and the many factors that must be considered in the selection of compressors for ISC services. He must be familiar with the lubricant characteristics for air compressor service. The design requirements for the safe operation of a high-pressure air distribution system must also be understood.

This chapter provides guidance to the ISC project designer in the selection, purchase, operation, and maintenance of air compressors and related equipment. It also details an operator's experience with air compression distribution system explosions and preventive methods adopted to avoid future explosions.

Chapter 8 - Ignition: A fireflood operation is initiated by igniting the oil-in-formation. The ignition is generally initiated by supplying large amounts of heat, sufficient to elevate the formation temperature around the injection well to a value higher than the crude's ignition temperature.

Several different techniques are employed in the field to achieve ignition. These techniques can be divided into two categories, (1) spontaneous and (2) artificial. If the reservoir temperature is

high enough and the formation contain sufficiently reactive crude than it can be auto-ignited after a period of air injection without the need for any artificial ignition device. Alternatively, the oil-in-formation can be ignited using one or more of the many artificial techniques developed for this purpose, such as the electrical downhole heaters, gas fired downhole burners, catalytic heaters, hot fluid injection and chemical reactions.

This chapter briefly reviews the various techniques and devices employed in the field to initiate ignition. The equipment details and operation procedure for the gas fired burners and electrical heaters are presented.

REFERENCES

1. Scaled Physical Model Evaluation of Steam Injection with Non-Condensible Gas Additives in Saskatchewan and California Reservoirs. Saskatchewan Research Council, Petroleum Division, SSC File No. 006SQ.23440-9-9222, March 1993.

2. Kimber, K.D., S.M. Farouq Ali and V.R. Puttagunta. New Scaling Criteria and their Relative Merits for Steam Recovery Experiments. *J. Can. Pet. Tech.* (July-August, 1988), v. 27(4): p. 86-94.

3. Pujol, L., and T.C. Boberg. Scaling Accuracy of Laboratory Steamflooding Models. SPE Paper 4191, 43rd Annual California Regional Meeting, Bakersfield CA, Nov. 8-10, 1972.

4. Sarathi, Partha S. and David K. Olsen. Practical Aspects of Steam Injection Processes: A Handbook for Independent Operators. U.S. Dept. of Energy Report NIPER-580, DE92001070, October 1992.

5. Nelson, T.W., and J.S. McNeil. How to Engineer an In Situ Combustion Project. *Oil &: Gas J.* (June 5, 1961), v: 59(23): p. 58-65.

6. Gates, Charles F., and Henry J. Ramey. A Method for Engineering In Situ Combustion Oil Recovery Projects. *J. Pet. Tech.* (Feb. 1980), v. 32: p. 285-294.

7. Brigham, W.E., A. Satman, and M.Y. Soliman. Recovery Correlations for In Situ Combustion Field Projects and Applications to Combustion Pilots. *J. Pet. Tech.* (Dec. 1980), v. 32(12): p. 2132-2138.

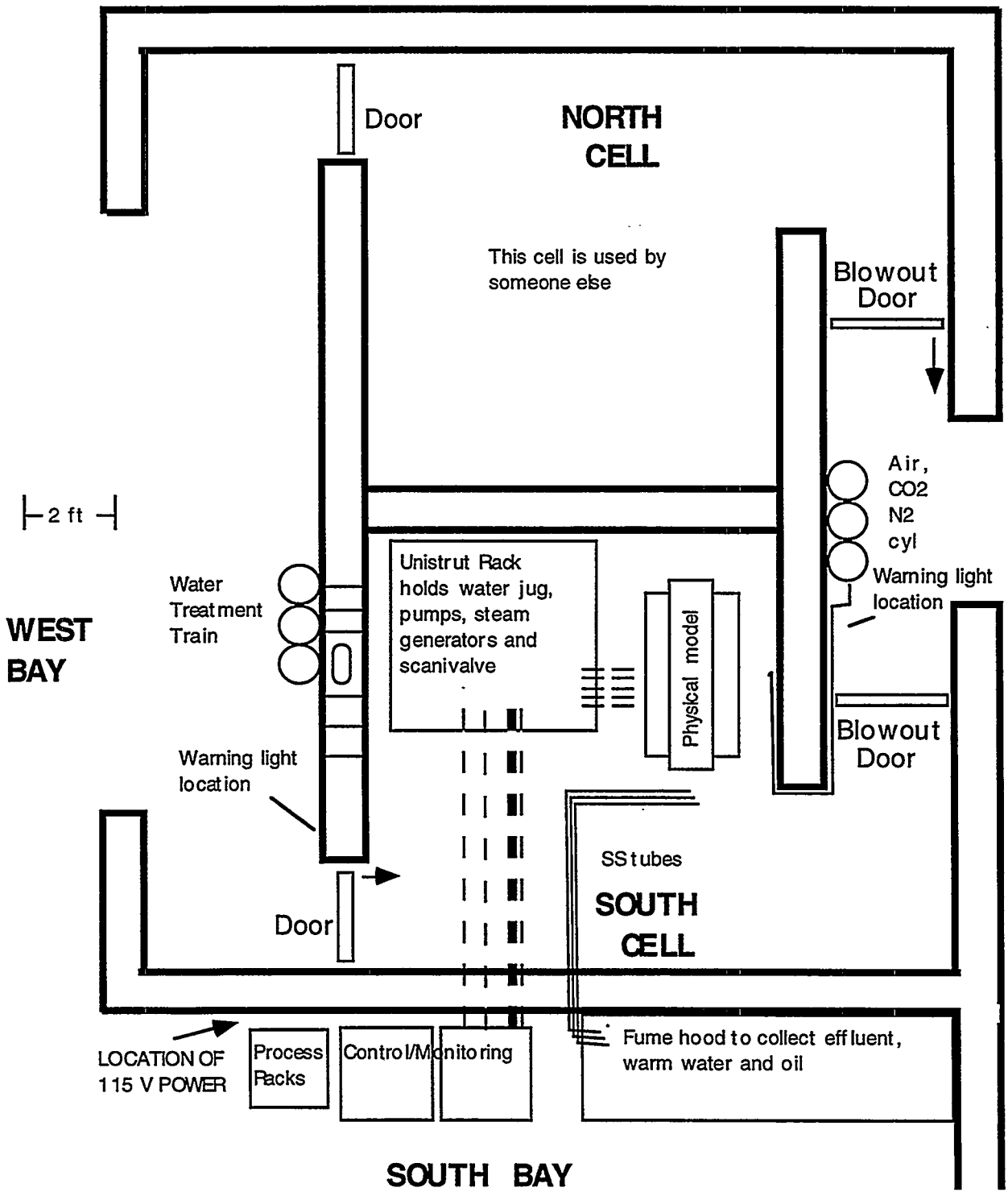

Dashed lines are overhead lines - these are mainly power/control/monitoring lines, there are stainless steel tubes running from the south cell to the fume hood.

Figure 70-1. Plan view of the steamflood laboratory.

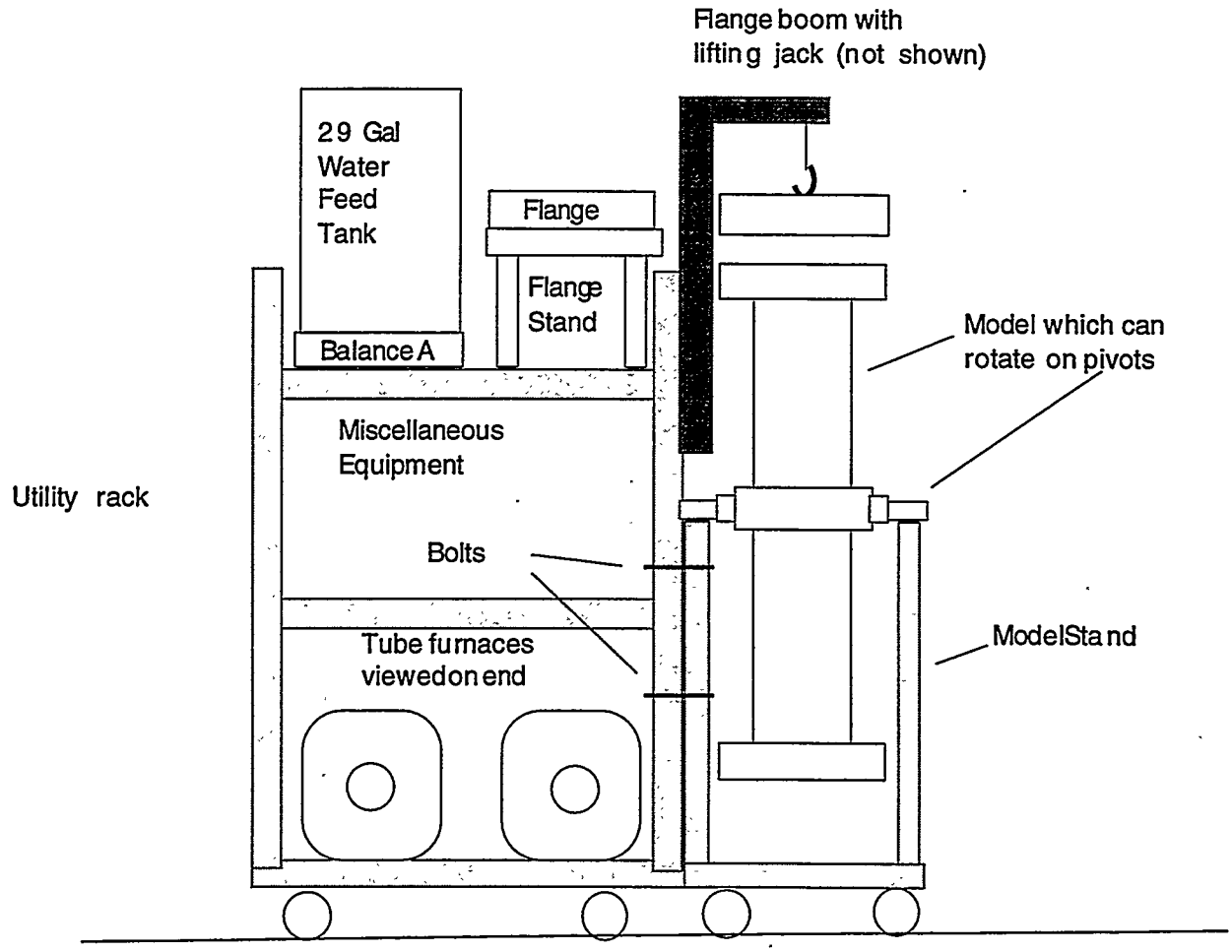

Figure 70-2. Side view layout of the steamflood flowsheet showing the utility rack, boom, and model stand.

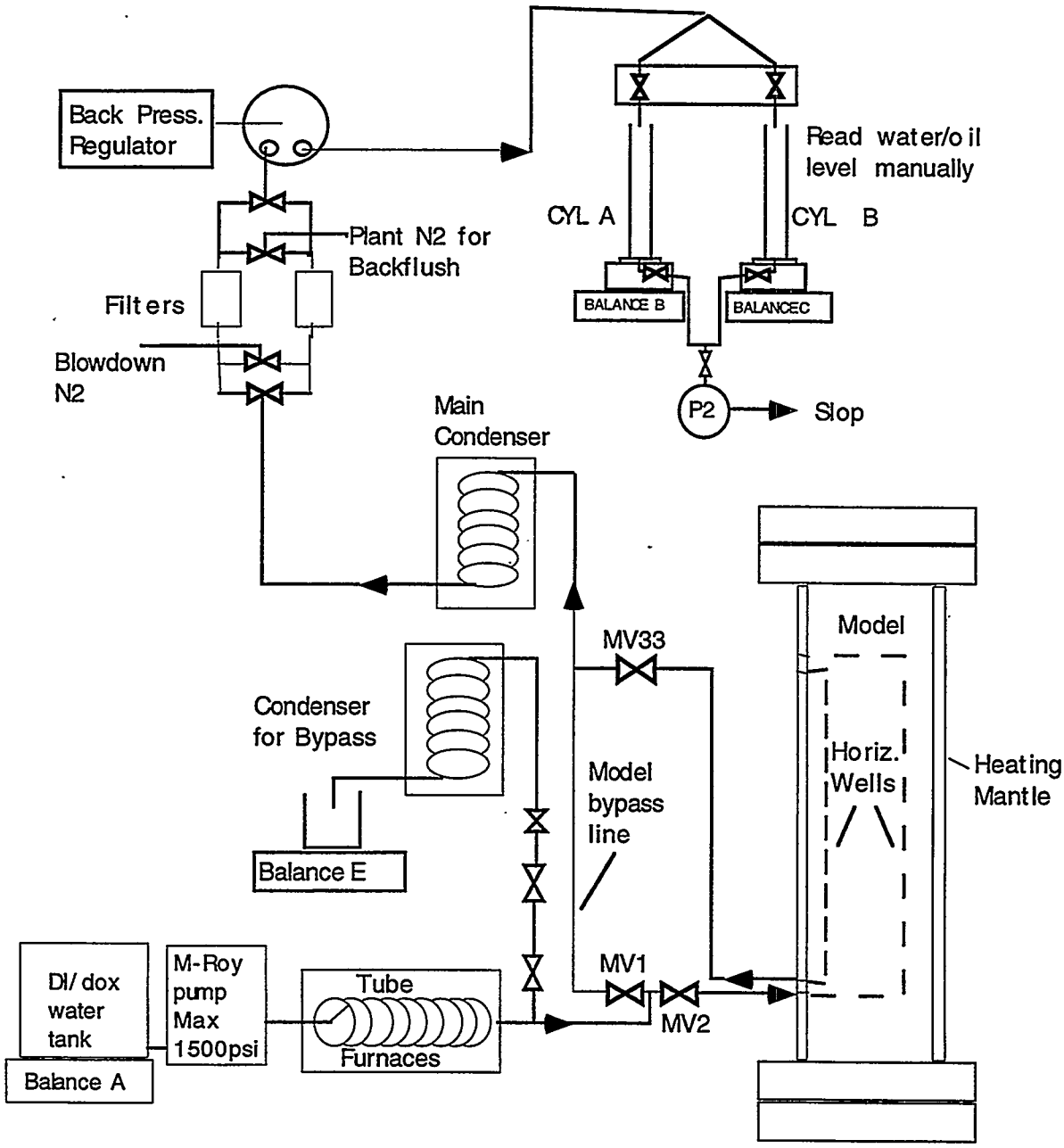

Figure 70-3. Simplified process flowsheet.

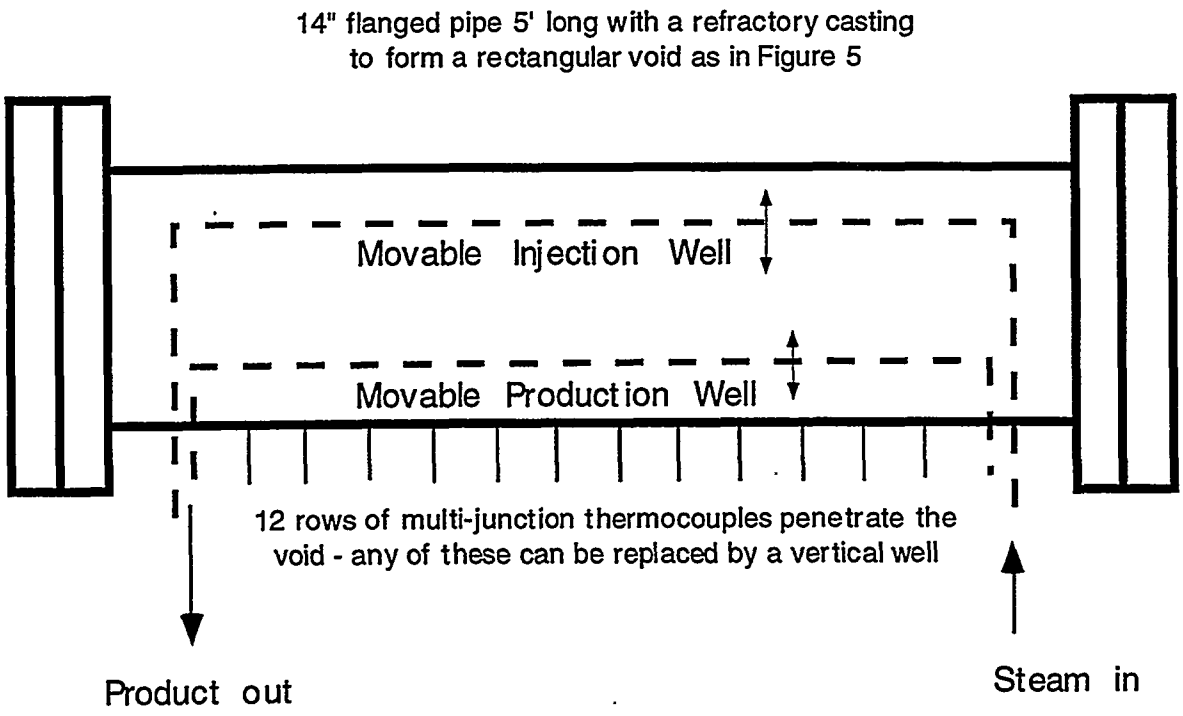

Figure 70-4. Simplified view of model - top view.

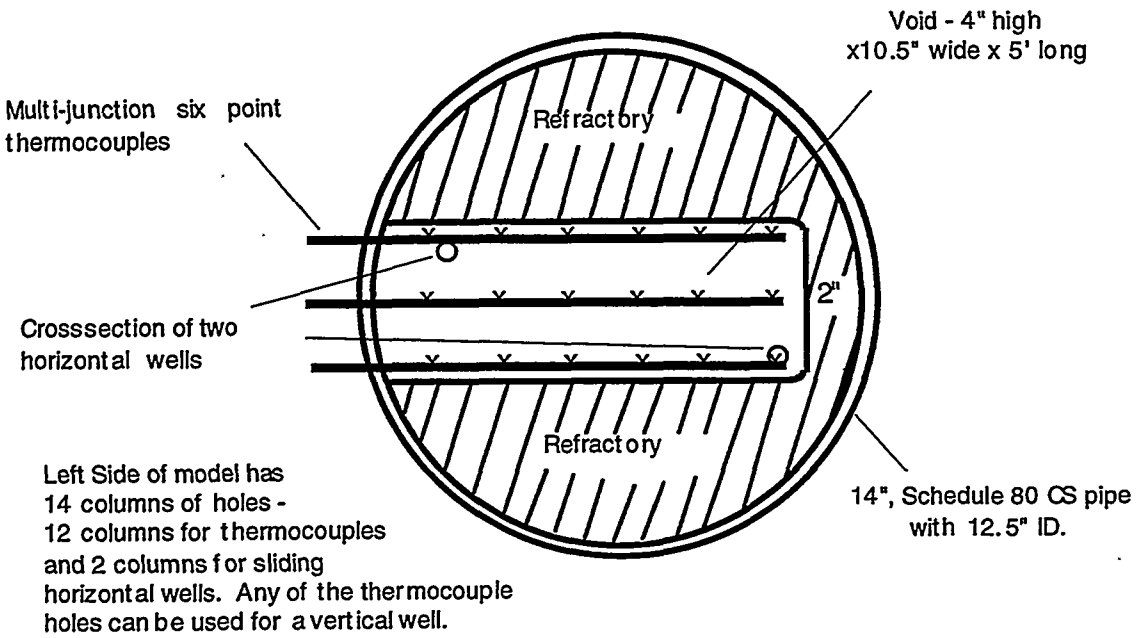

Figure 70-5. Cross section of model and refractory.

Task 71 — INTEVEP shall provide DOE with information on simulation and field results of heavy oil recovery by steam circulation in horizontal wells.

NUMERICAL SIMULATION OF PRODUCTION BEHAVIOR OF RECYCLING WELL LSE-4703

Belkis Fernández, Gilberto Venturini/PDVSA-Intevep

ABSTRACT

Over the last three years, horizontal well drilling technology has been applied in Venezuela both in light and heavy crude reservoirs. Application of this technology has generated satisfactory results in heavy crude reservoirs in the Orinoco Oil Belt, and in the traditional production areas in East and West Venezuela. However, in Western areas many reservoirs present a high level of depletion, and therefore, the well production potential is low. Meanwhile, in East Venezuelan reservoirs, successful results in production have been reported, due to high pressure and lower depletion.

Searching for alternatives to increase production of low productivity reservoirs, Maraven has tested a scheme of recycling low quality steam in horizontal wells. In the process, steam is injected at a lower pressure than reservoir pressure, in order to heat production system down the hole, to diminish crude viscosity, and to improve its movement. Using this technology, production of well LSE-4703, located in Tía Juana reservoir in Bolívar Coast, Zulia State, Venezuela, was programmed, allowing process evaluation in progress.

Objective of this paper is to present a summary of activities of the steam recycling process, and to evaluate results obtained in the first horizontal well LSE-4703.

To represent the process, a well model was developed, using a 3-D, three phase compositional simulator to simulate the steam recycling thermal process. Simulation results obtained show an improvement of well production response to steam alternate injection both in cold and hot production tests, reported prior to steam recycling process. Simulation allowed, by means of a sensitivity analysis, to determine optimal injection parameters to increase steam recycling scheme efficiency. It also allowed obtaining well production estimates for the next five years.

1. INTRODUCTION

Well LSE-4703 is located North-East of Lake Maracaibo, in Tía Juana field, Lagunillas reservoir, Zulia State (see Fig. 1). In February 1994, the well was first vertically drilled until 300', and then it was deviated until 1188' (930' TVD), with a 77° final inclination. An 8 1/2" horizontal hole was drilled until 2040' (1040' TVD). It was completed with a 5 1/2" slotted liner without gravel pack, placed from 1062' to 2040' (see Fig. 2).

Production equipment included a progressive cavity pump for well initial completion, and due to low production response, other exploitation choices were considered, such as steam-

assisted gravity drainage, sodium silicate injection in cold, and water alternate steam injection. Steam injection was not a proper alternative, since well is not gravel packed, and liner has neither expansion joint, nor seating nipples. Moreover, packing on which liner is hanged is not designed for high temperatures. Therefore, well injection had to be controlled and constantly supervised.

Based on this and searching for the most effective alternative to improve well production, a steam water recycling process was proposed. At present, five steam recycling cycles have been run, varying in each injection conditions in order to determine most appropriate operating conditions to optimize the process, and also to determine feasibility of applying the technology in the area.

To analyze field results of the steam recycling process, a well numerical simulation under this production scheme was done, and then sensitivity analyses were carried out. Variables considered in the analyses were production rate, injection pressure and steam quality. Production behavior was studied in each sensitivity in order to establish the effect on reservoir, well and surface behavior, caused by each condition.

2. RESERVOIR DESCRIPTION

Lower Lagunillas Reservoir belongs to Lagunillas Formation in Tía Juana field, under Maraven jurisdiction, north of Lake Maracaibo (see Fig. 1). It is a Lower Miocene formation, characterized by unconsolidated sands, which are 100 to 200 feet thick. Reservoir contains an original oil in place (OOIP) amounting MMbbls 350.4 and 3.7% of OOIP recoverable reserves. Petrophysical properties are: porosity: 36%, permeability: 1500 mD and initial water saturation: 17%.

Top of Lagunillas Lower Member is at 780 feet, with an initial pressure of 400 psi and 110°F. Presently, reservoir pressure has dropped to 250 psi. There are 88 wells drilled, 5 of which are inclined, and through them 5.5 MMbls of oil have been drained.
Fluid inside Lagunillas Lower Member shows characteristics presented in Table 1.

3. RESERVOIR PRODUCTION HISTORY

Average production of vertical wells drilled in Lagunillas Lower Member is around 50 bbl/d, producing in cold. Due to high viscosity, steam injection to reservoir has been necessary to increase well production up to 120% (140 bopd). However, average oil production under the same injection scheme is currently 100 bopd, due to reservoir depletion.

Because of low well productivity, it was proposed to drill well LSE-4703 horizontally, in order to improve remaining reserve drainage and productivity efficiency.

4. WELL HISTORY

In February 1994, well LSE-4703 was first vertically drilled with a 17 1/2" hole until 271', using a 13 3/2" liner at 250', a vertical hole from 12 1/4" to 300', and from there it was deviated to 1188' (measurement), 930' (vertical) with a 77° final inclination. A 9 5/8" liner was introduced and cemented at 1132' (measurement) to surface. An 8 1/2" horizontal hole was drilled to 2040' (measurement), 1040' (vertical). A 5 1/2" slotted liner was used to complete hole from 1062' to 2040' (measurement), hanged with a Baker 9 5/8" x 7" hydraulic packing, model ECP with no gravel pack, and no steam injection special equipment (expansion joints, nipples, etc). Completion was finished with the installation of a Griffin progressing cavity pump, model 300-TP-800 at 931' (measurement), 807' (vertical). Production expectations for this well were 522 bbl/d, having a 1378 feet horizontal length, but it only produced 71 bbl/d at 75 rpm.

Formation damage was assumed due to drilling mud. Therefore, a clean-up with sodium silicate was applied, circulating and injecting organic solvent to formation, but no increase in production was reported. Afterwards, 4723 tons of low quality steam (X = 56%) were injected at 800 psi injection pressure, and it was completed with mechanical pumping (Fig. 2). Production obtained reached 156 bopd, which then diminished to 60 bopd after 10 months.

Since no significant improvement of production response was obtained, compared to steam-injected vertical wells, well production was treated by recycling low quality steam inside horizontal section in order to heat the whole section with the steam, and improve crude movement in the pipe (see Fig. 3).

Injection conditions of recycling process in well LSE-4703 were established with CICLOPS program, determined by Maraven personnel. These conditions were: 50 ton/d of 20% quality steam, reaching well bottom with "zero" quality at 390°F, and an injection pressure of 200 psi. However, conditions had to be modified in field to optimize well contributions, depending on limits of temperature and well bottom pressure.

Well production expected during the process was 400 b/d. Estimate might increase depending on injection conditions. Field production response obtained oscillated between 340 and 170 b/d, after applying recycling process, and after 5 cycles in which injection conditions were varied (see Table 2). However, flow mechanism is unknown, since no relation between steam injection rate, and production was found. However, apparently at higher injection rate, higher production, but in those cases water entered too fast.
Consequently, a numerical simulation was performed to determine well behavior, and optimum injection parameters, as well as to increase understanding of flow mechanisms obtained inside the recycling well.

5. NUMERICAL MODELING

A numerical simulation was performed using the STARS simulator with the following characteristics:

1. It is tridimensional, and thermal
2. It is compositional, able to simulate multiphase flow
3. It has an implicit model
4. It includes options for analyzing effects of adjacent wells, having a flow model for horizontal, inclined and vertical wells both for injection and production processes.
5. It includes options for modeling wells with fluid recycling processes, showing a completion process exact to well LSE-4703.

Model applied presents characteristics described in Table 3.

The model discretization was based on the representation of well with YZ cells, where Y is the horizontal direction (Fig. 4).

Option for analyzing flow effects surrounding injection well, and displacement of fluid injected through annular space together with crude was also included. Fluid and rock data, as well as oil composition were obtained by PVT and core analysis of wells of an adjacent reservoir. Analyses allowed adjustments, using sensitivities of different parameters to represent Rs, GOR and water cuts, taking as reference historic results of wells in the zone.

6. MODEL CALIBRATION

6.1 Production before Steam Alternate Injection

To start simulation, the model was calibrated using production history of vertical well cold periods. Data obtained from PVT, viscosity, °API, GOR and water cut was verified, in function of well pressures and relative permeability curves, with which crude production, saturation and reservoir pressure declination adjustments were achieved (Fig. 5).

6.2 Production after Steam Alternate Injection

Historic adjustment of well LSE-4703 started during steam alternate injection. Injection rate and pressure, steam quality, soaking time, and production rates were established, and flowing bottom pressure was varied (Fig. 5). Table 4 presents conditions for steam alternate injection.

6.3 Production during Steam Recycling

Representation of recycling well was performed with a model, including fluid effect analysis of adjacent area of well. Two lines (according to scheme) were defined: First, a steam injection line with a 900 feet 2 3/8" in diameter horizontal section, with a steam

outlet at pipe end. Second line was in the annular space with a 908', 8 1/2" in diameter horizontal section having a 5 1/2" slotted liner. Vertical production pipe was included outside horizontal section.

For the simulation, effect occurring in the horizontal section was important, since effect in the inclined section is practically cancelled by pump position (located at the inlet of horizontal section) (Fig. 2).

Results of historic adjustment are given in Fig. 6. Differences observed in the graph correspond to BHP changes due to pumping system, which were mostly considered in the model, but in some cases average values were used in the recycling periods.

7. SENSITIVITY ANALYSIS

Once model adjustment was finished, different steam injection conditions were simulated to determine optimum conditions of recycling process. Parameters analyzed were injection rate and pressure, besides steam quality, with which different combinations among these three variables were evaluated.

First, quality and injection pressure values of 50% and 160 psi, respectively, were taken as base case, and different injection rates Qi between 10 and 60 ton/d were selected to obtain best Qi, based on the production response. Results are given in Fig. 7, indicating that for injection rates above 20 ton/d, the same production response will be obtained. With this injection rate value, a series of different pressures (between 80 and 160 psi) was selected to determine optimum injection pressure, considering responses obtained from oil *vs.* time accumulations, with which similar production responses for each study case were established (Fig. 8). Explanation for such behavior is attributed to process nature, since in this case only steam recycling is considered, and no steam is injected to formation. When this stage was finished and these two values were established, an optimum steam quality value Xi was also determined. Therefore, this parameter was varied from 0 to 90%. Results obtained were plotted in an accumulation *vs.* time graph (Fig. 9), which shows that for steam quality values higher than 30%, same production response is obtained.

8. PREDICTION OF PRODUCTION BEHAVIOR

With the sensitivity analysis using injection rate, pressure and steam quality parameters, a production behavior prediction was outlined for a 5 year scenario, from January 1996 to 2001, which allowed studying well behavior for determining the feasibility of applying low quality steam recycling process in the whole area.

Results obtained from prediction run are given in Table 5. They are also graphically shown in Figs. 10-12.

Fig. 10 presents results of well production behavior prediction, indicating that production rates are within 200 and 300 bopd in most of the period, implying a 120% increase of

production *vs.* average production before steam recycling cycle (120 bopd). In Fig. 12, results of water behavior prediction are plotted for. These values indicate that water cut does not overcome 60% for the period selected. Noteworthy is that these values indicate both formation water and water from steam injected.

At the same time, figures were prepared, representing different levels of pressure, temperature and viscosity, both in well and in adjacent areas. Figures will allow to better visualize possible way of varying those parameters during the recycling process, from the beginning to the end.

First case concerning pressure levels is presented in Figs. 13 and 14 for different planes, showing process influence concerning pressure. Pressure levels are observed varying from 50 to 450 psi for the initial case, in which 50 psi represents pressure at well bottom, and from 50 to 370 psi for the final case. In this case, pressure distribution near the well is shown, which is due to natural depletion of reservoir.

Results of temperature and viscosity distribution in similar production scenarios are given in Figs. 15 and 16, respectively.

9. CONCLUSIONS

1. Numerical simulation model reproduces very well current production behavior of well, compared to field test results.
2. Results obtained for prediction indicate a 120% increase of production, vs. the one obtained before recycling period.
3. Steam recycling process represents an efficient tool to improve well production behavior, accelerate drainage of remaining reserves, and reduce operating costs.
4. Optimum parameters of steam injection for a recycling scheme in horizontal wells of Lower Lagunillas reservoir are 20 ton/d steam rate, an 80 to 100 psi injection pressure and 30% quality steam.
5. Successful results obtained with simulation provide new options for developing low productivity reservoirs.

10. RECOMMENDATIONS

1. To develop and perform activities similar to the ones carried out in this study for crudes with different °API, located in other reservoirs, in order to expand the use of this process, which is a suitable alternative to increase well productivity and reduce operating costs.
2. To follow-up production of well LSE-4703 in order to verify behavior prediction values, determined in this study.

11. REFERENCES

1. Merchán, F.; Durán, A. Evaluación del pozos horizontal LSE-4703. Nota técnica. Ingeniería de Petróleo. División de operaciones de producción. Maraven, S.A., Lagunillas, March 1995.
2. Mendoza, H. Estimulación de pozo horizontal en Tía Juana (LSE-4703). División de operaciones de producción. Maraven, S. A., Lagunillas, May 1995.
3. Stars. Manual del usuario. Versión 96. CMG, Calgary, Canadá, 1996.
4. Therm. Manual del usuario. Intevep, S. A., Los Teques, 1987.
5. Reservoir Fluid Analysis Report. Well LL-525. Wright Petrolerum Laboratories. Tulsa, Oklahoma, January 1967.

TABLES

Table 1. Fluid properties

Bubble Pressure, Pb	690 psi
°API	9.6
Rs at Pb	68 SCF/STB
Bo	1.03 RB/STB
Viscosity at Tr, Pr	2300 cP
Viscosity at Tsc, Psc	49018 cP
Viscosity at Tsc, Pr	12800 cP

Tr, Pr: Reservoir conditions
Tsc, Psc: standard conditions (T = 86°F and P = 14.7 psia)

Table 2. Injection conditions of five recycling cycles

Cycle	X (%)	Injection rate (ton/d)	Pinj (psi)	Tinj (F)
1	40	33	160	360
2	27	26	106	330
3	23	52	165	365
4	36	16	81	310
5	22	30	98	320

Table 3. Characteristics of numerical simulation model

No. of blocks (areal)	1428
No. of layers (in Z)	7
Well location	Layer 4 (horizontal section)
Components	3 (dead oil, water and gas in solution)

Table 4. Injection conditions for steam alternate injection

Tons injected	4723 in 20 days
Injection pressure	800 psi
Injection temperature	520°F
Steam quality	56%
Soaking time	5 days

Table 5. Results of prediction

Cumulative Oil (Mbls)	456
Cumulative Gas (MMscf)	18.3
Cumulative Water (Mbls)	360

FIGURES

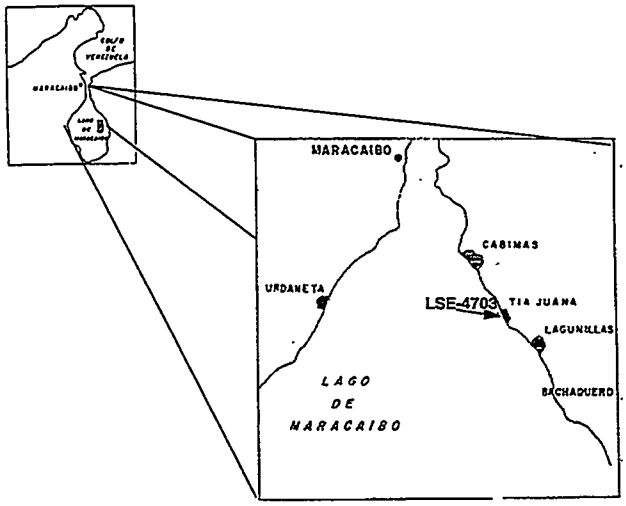

Fig. 1. Geographical location of well LSE-4703

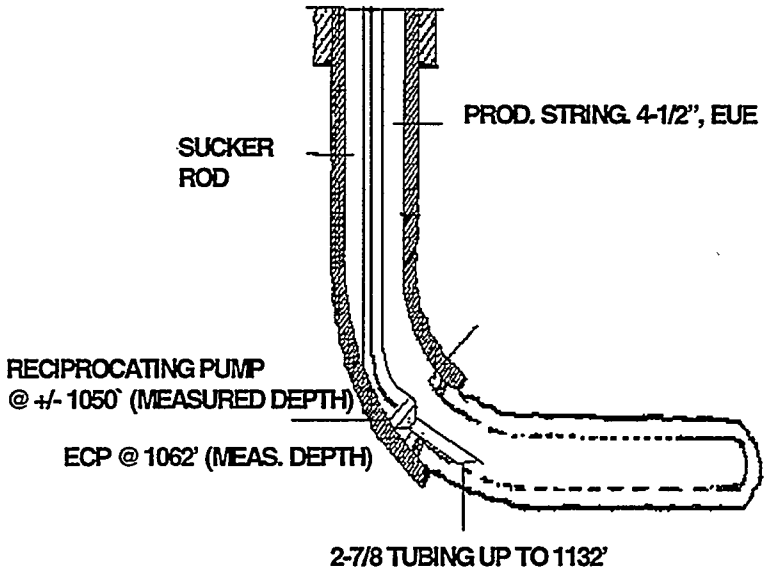

Fig. 2. Completion diagram of mechanical pumping

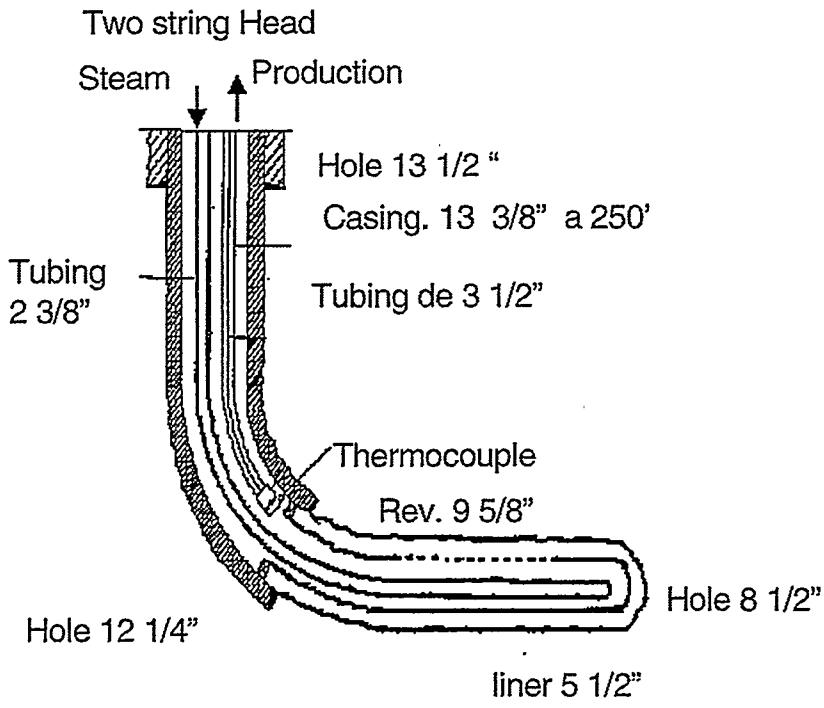

Fig. 3. Completion diagram of steam recycling

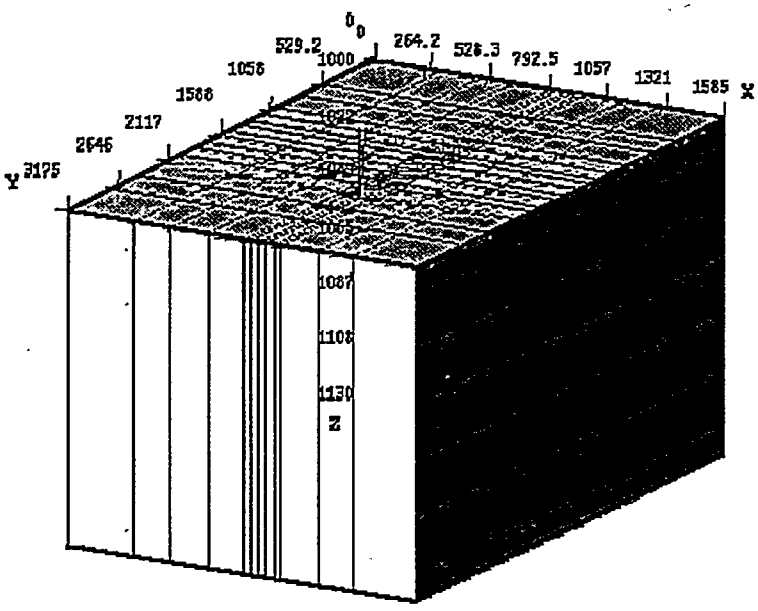

Fig. 4. Simulation grid

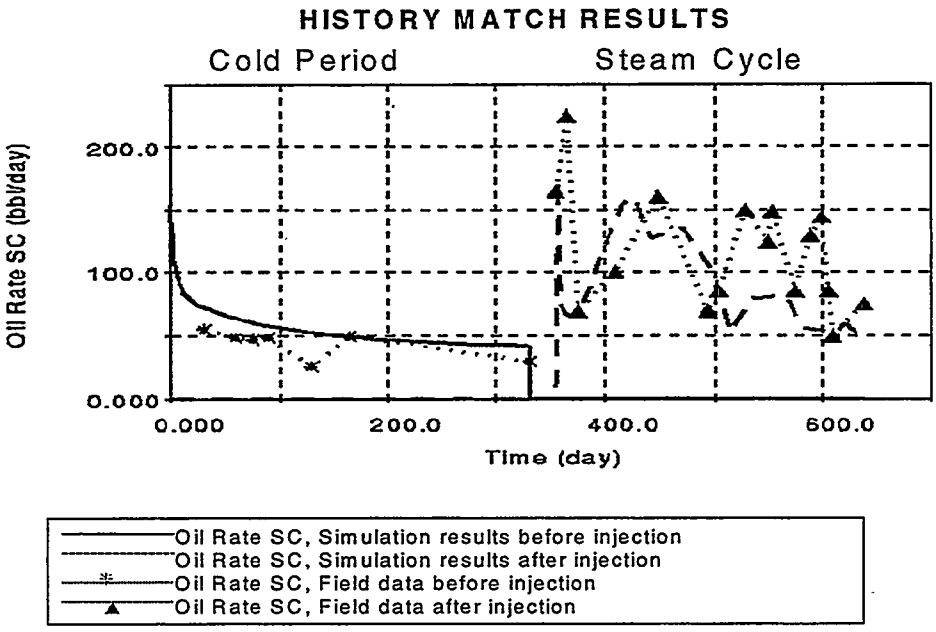

Fig. 5. Results of history match (Cold cycle followed by steam injection)

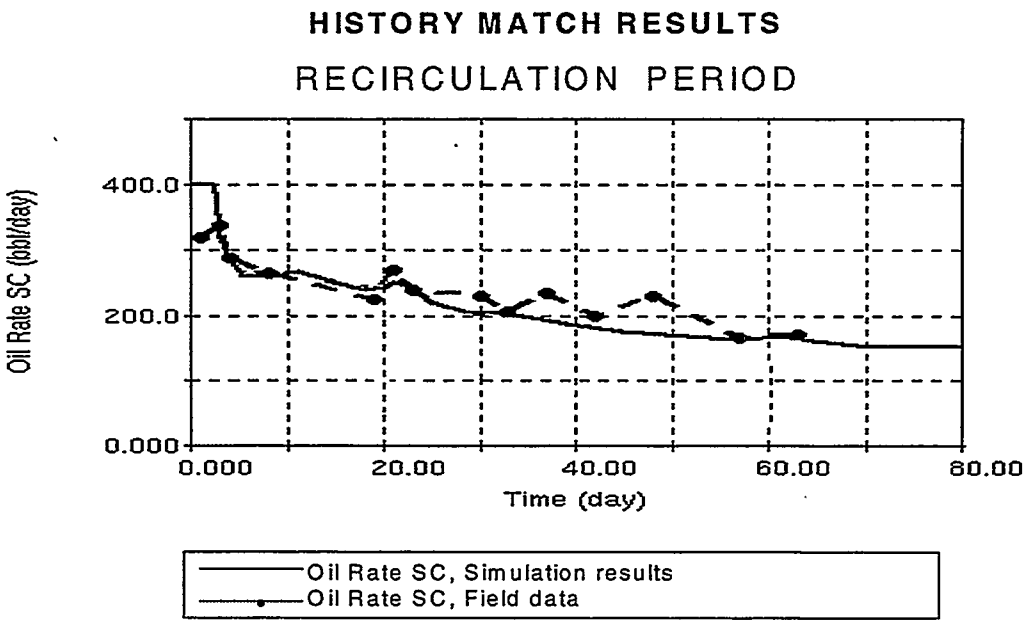

Fig. 6. Results of historic match (Steam recycling scheme)

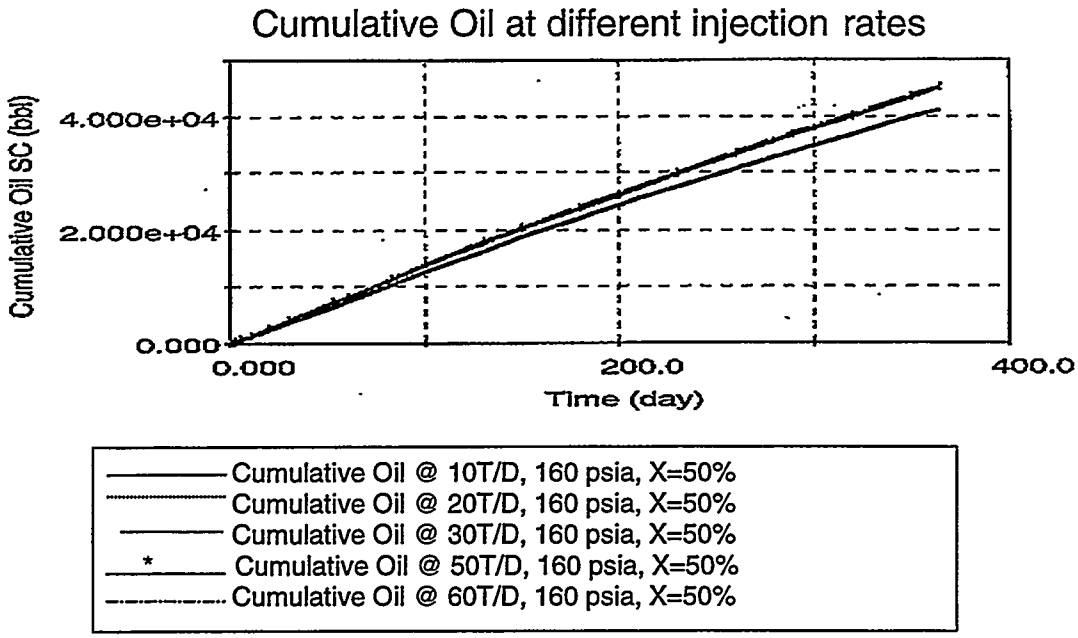

Fig. 7. Crude accumulated at different injection rates

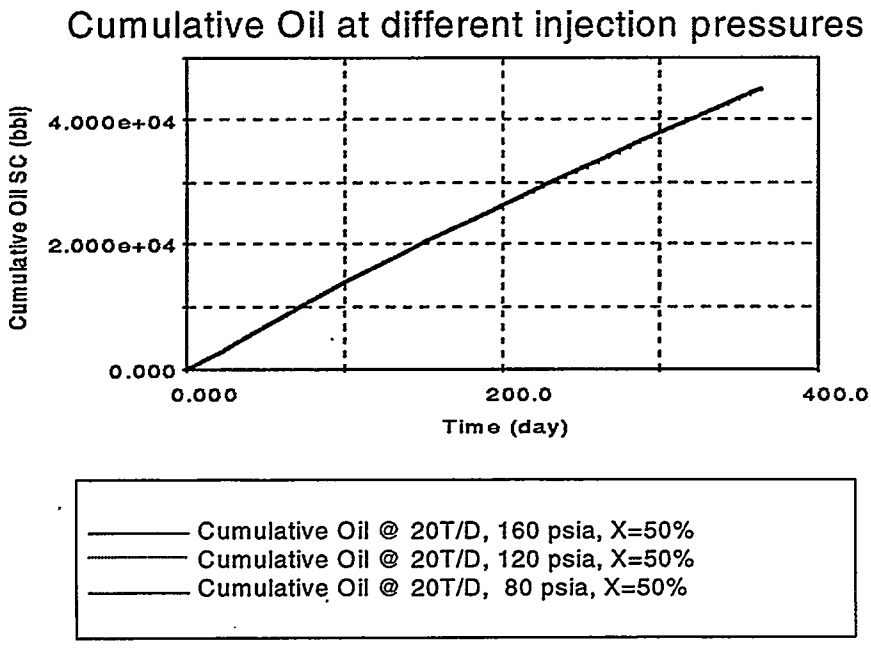

Fig. 8. Crude accumulated at different injection pressures

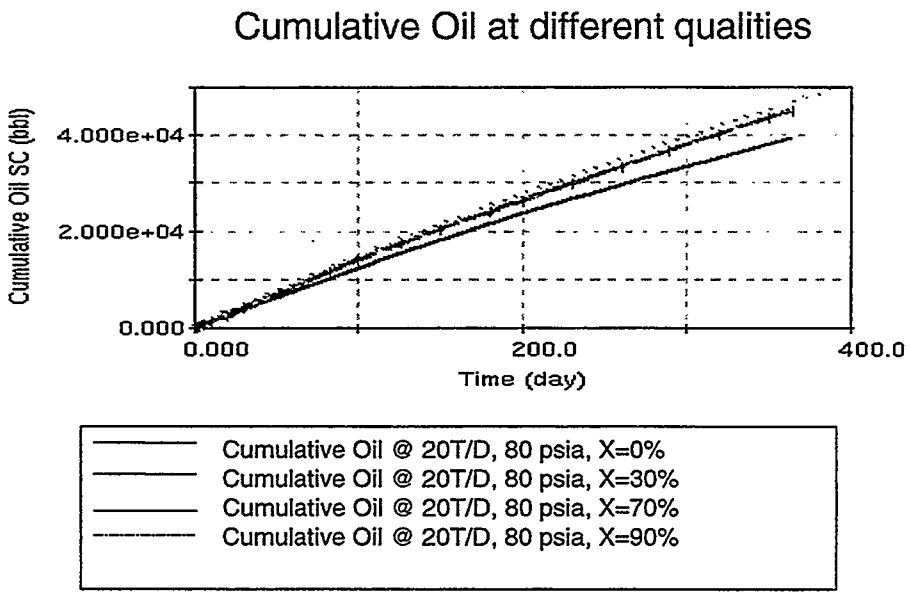

Fig. 9. Crude accumulated for different steam qualities

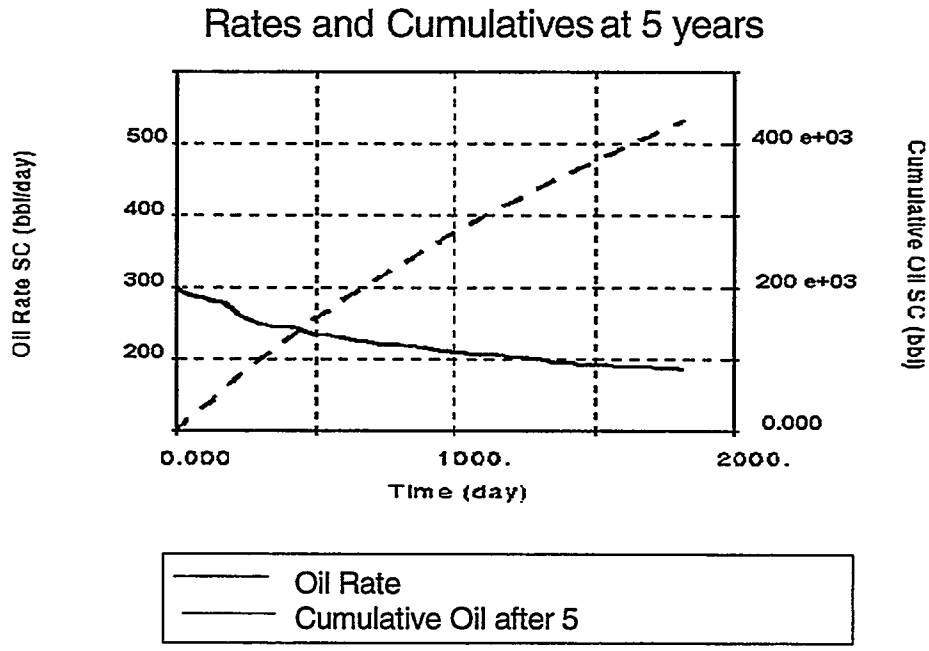

Fig. 10. Prediction of production behavior for 5 years (crude)

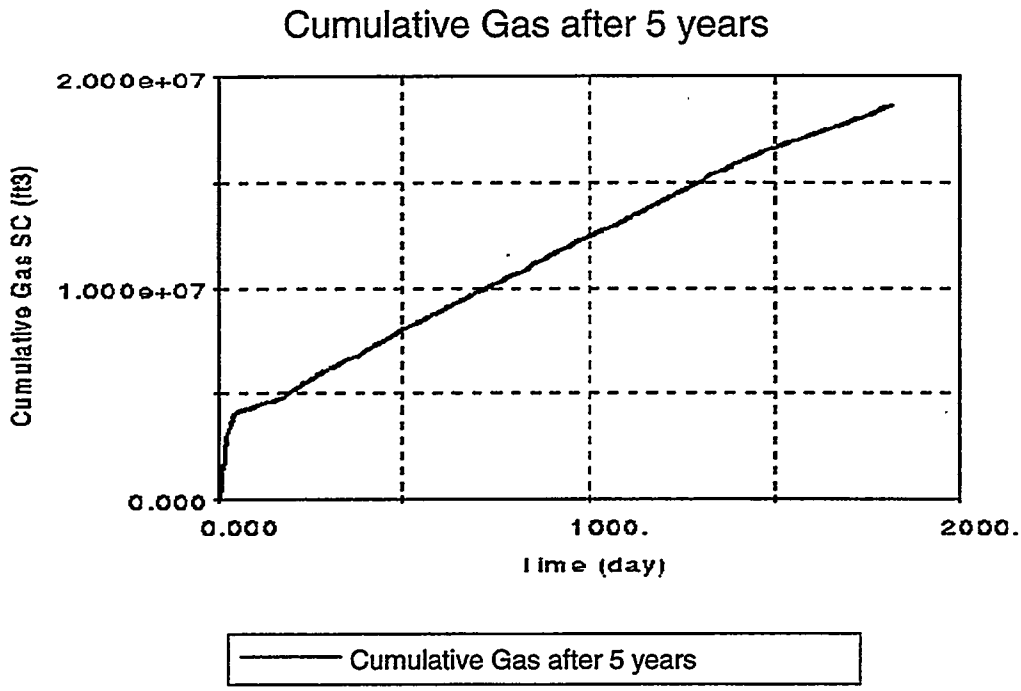

Fig. 11. Prediction of production behavior for 5 years (gas)

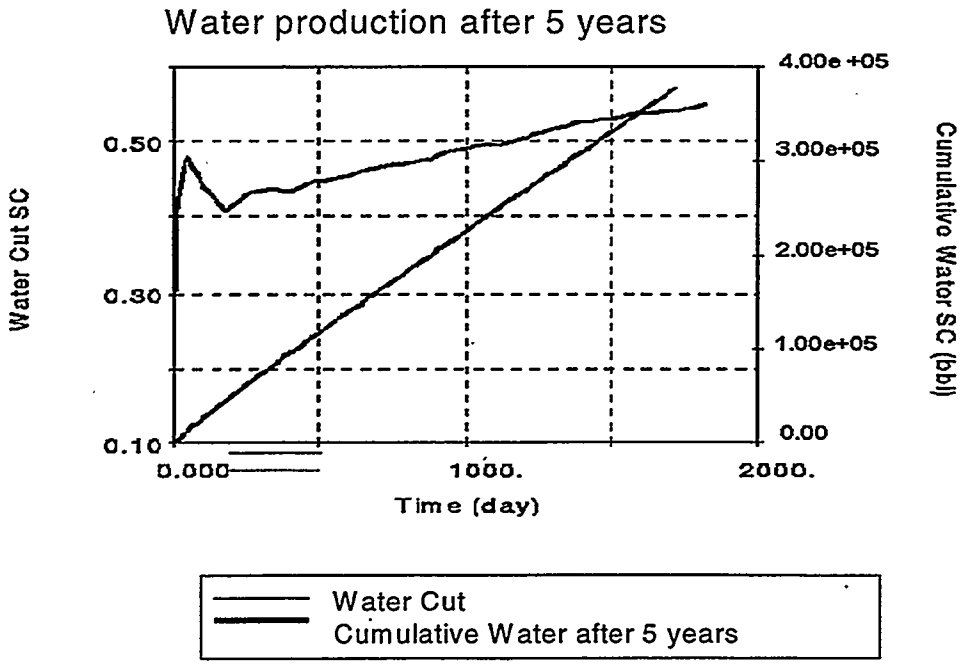

Fig. 12. Prediction of production behavior for 5 years (water)

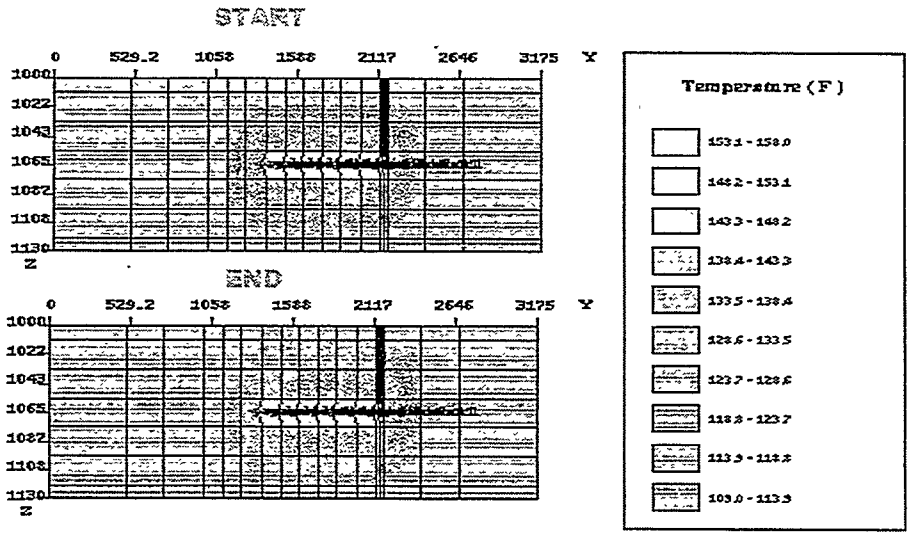

Fig. 5. Temperature levels in YZ plane

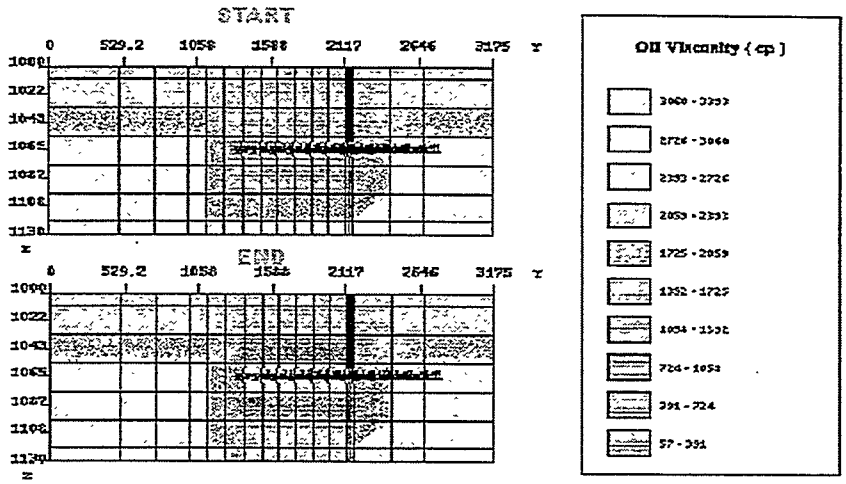

Fig. 16. Viscosity levels in YZ plane

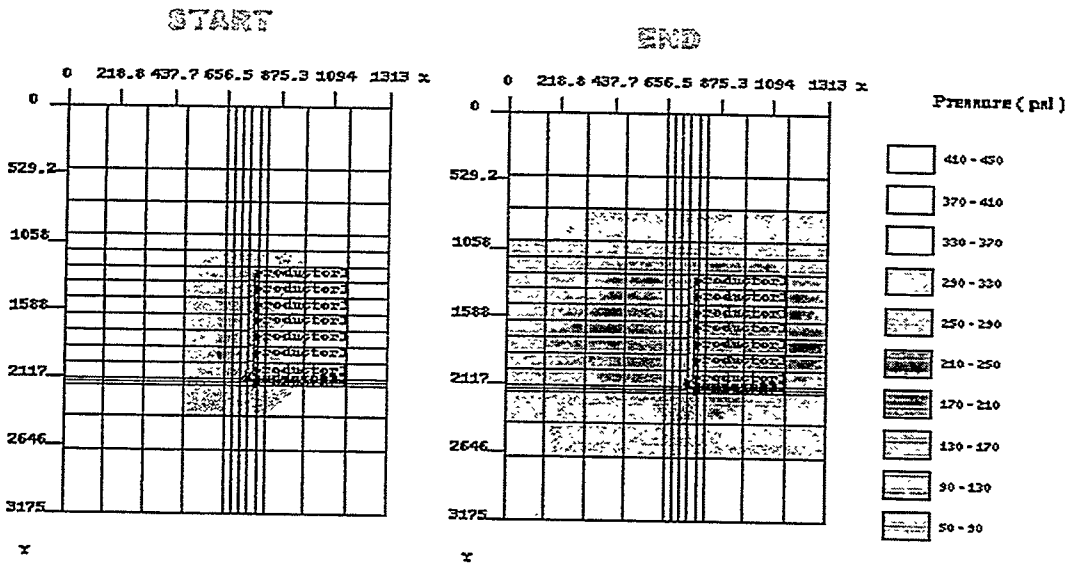

Fig. 13. Pressure levels in XY plane

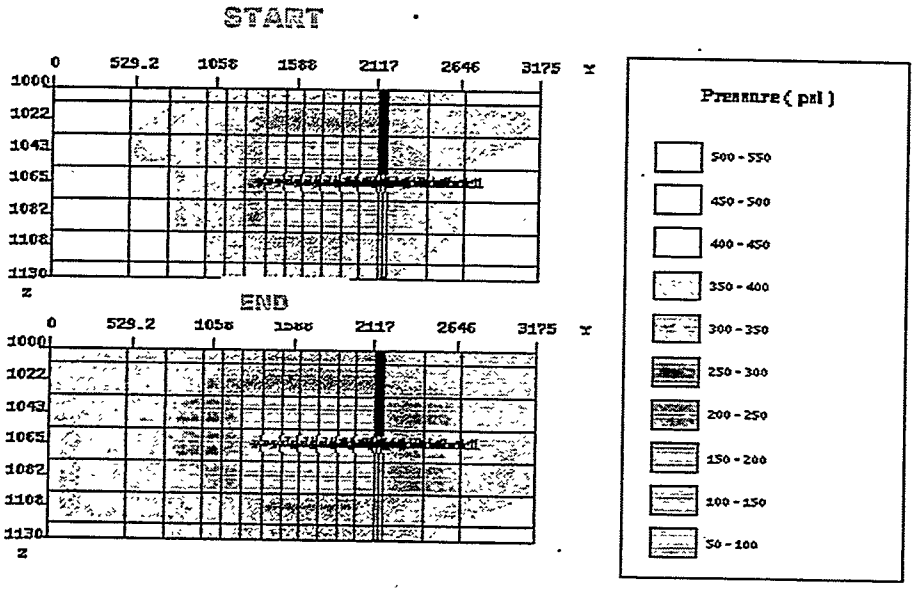

Fig. 14. Pressure levels in YZ plane

Task 72 – DOE/LLNL shall provide DOE with information on resistivity imaging from cross-borehole and surface-to-hole electromagnetic induction and use of this technology in cased wells

Progress in Crosswell Induction Imaging for EOR: Field System Design and Field Testing

B. A. Kirkendall, J. P. Lewis, S. L. Hunter, and P. E. Harben

1.1 Abstract

At Lawrence Livermore National Laboratory (LLNL), we are continuing our effort to develop improved crosswell low-frequency electromagnetic imaging techniques, which are used to map in situ steamflood and waterflood movement during enhanced oil recovery (EOR) operations. Toward this effort, we procured two new borehole-logging field vehicles, and developed and integrated new crosswell electromagnetic transmitter and receiver data acquisition and control systems into these vehicles. We tested this new acquisition system by conducting a suite of background measurements and repeatability experiments at the Richmond Field Station in Richmond, California. Repeatability of a given scan in which the receiver was fixed and the transmitter position was varied over 60 m in 0.2-m increments resulted in amplitude differences of less than 0.6% and phase differences of less than 0.54 deg. Forward modeling produced a resistivity map fully consistent with well log data from the Richmond Field Station. In addition, modeling results suggest (1) that residual high-conductivity saltwater, injected in 1993 and pumped out in 1995, is present at the site and (2) that it has diffused outward from the original target strata. To develop crosswell electromagnetic imaging into a viable commercial product, our future research must be a two-fold approach: (1) improved quantification of system noise through experiments such as ferromagnetic core characterization as a function of temperature, and (2) development of procedures and codes to account for steel-cased hole scenarios.

1.2 Introduction

The United States has extracted about 160-billion barrels of oil from its petroleum reserves over the past 130 years. Estimates indicate that this is only about one-third of the total U.S. reserves, but without enhanced extraction methodology, the bulk of these reserves will remain locked in the reservoir formations. To increase the fraction of reservoir oil available for extraction, U.S. oil companies must apply methods of enhanced oil recovery (EOR) to more and more fields.

In California, for example, where the oil is mostly a heavy viscous type, 55% of the oil currently produced comes from injecting steam, water, or gas into the reservoir to increase production by lowering the viscosity of this oil through heat and/or mixing. When production yields dwindle in primary reservoirs, often the first action taken by oil companies is to use hydrofracturing in producing horizons to increase output. Hydrofracturing can boost production by creating porous conduits for otherwise trapped oil to migrate to the producing well. Further recovery methods resort to longer term waterfloods, steamfloods, gasfloods, and chemicalfloods to sweep trapped oil to the producing wells. Although other methods employing in situ burning and microbes are in the early stages of development, waterfloods and steamfloods are the predominant means used at present.

It is of great economic importance to know where the steam or waterflood front is going during the EOR process. Channeling, bypass, and breakthrough into a nonproducing horizon can and often do occur. Since many steam and waterfloods operate for years at a time, companies can save money when a sweep problem is discovered early. Although sophisticated reservoir simulators

are often used to predict the migration of a steam or waterflood through the reservoir, the simulators are limited by (1) the relatively sparse borehole logs available and (2) precise knowledge of the regional geology and in situ rock properties of the reservoir.

Mapping the steam or waterflood with cross-borehole methods provides a means to monitor the progress of the EOR process before it reaches another well. The results from front mapping during the flooding process can also be incorporated into the reservoir simulator to further constrain the simulator with measured data from the reservoir.

LLNL pioneered the use of low-frequency cross-borehole electromagnetic imaging to monitor and map the progress of EOR steam and waterfloods. The operating frequencies of the transmitter are in the induction regime and, consequently, the method measures resistivity (or conductivity) contrasts in the reservoir since dielectric permittivity is negligible in the induction regime. The steam or waterflood lowers the resistivity of the formation in the regions that it infiltrates; images taken before, during, and after infiltration are compared to construct a map of the progress of this process. The imaging technique used in this study is depicted in Figure 1. Note that the transmitter and receiver systems are each housed in a specially designed field vehicle.

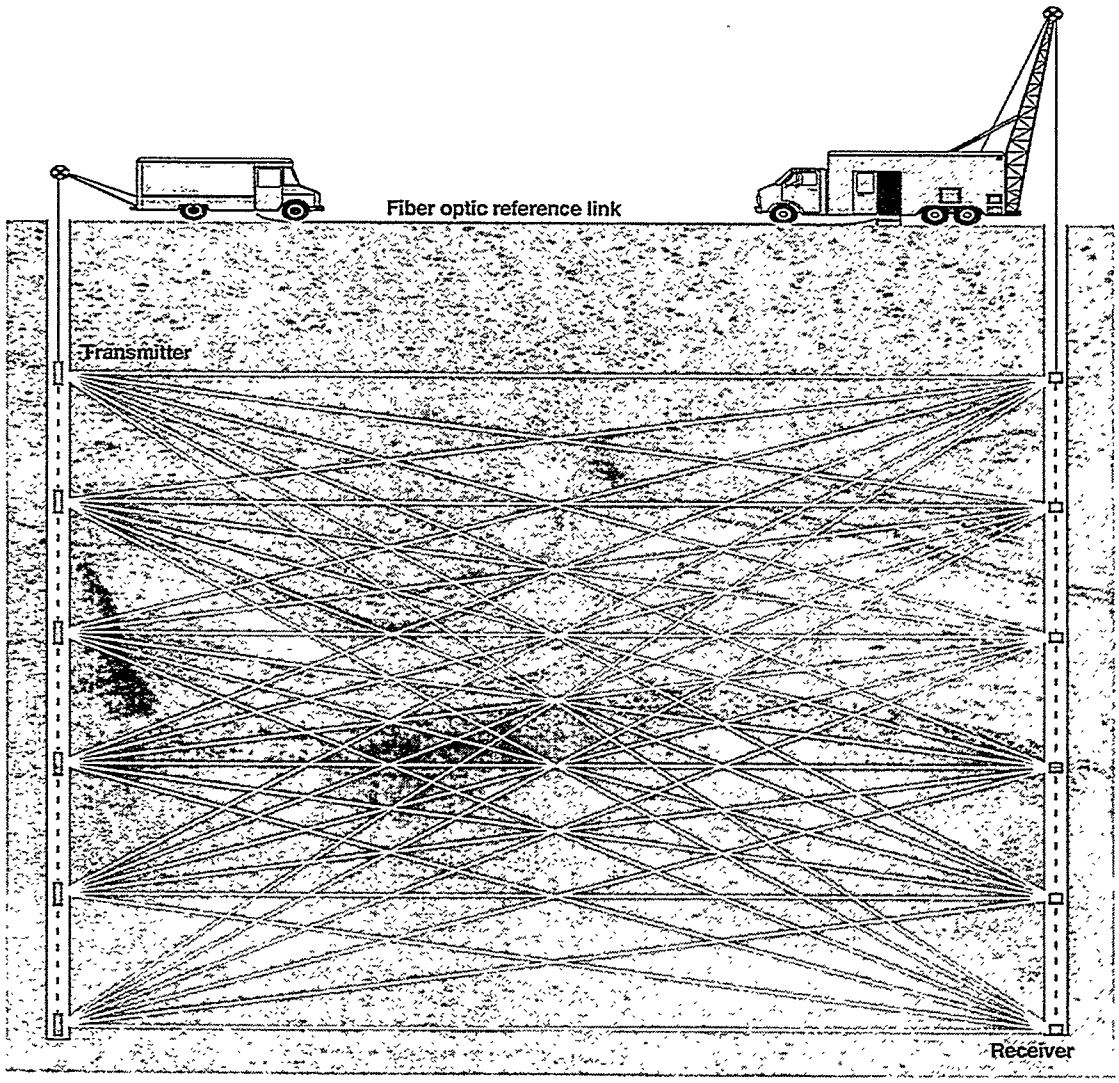

Figure 1. Pictorial representation of the crosswell logging procedure. Although the energy traced between wells does not physically follow raypaths, crosswell processing assumes distribution of such energy along straight conduction pathways.

The process of imaging an area begins with moving a transmitter over the entire length of the imaging zone so that the receiver can measure the in-phase and out-of-phase components of the signal that penetrate the formation between the two boreholes. These components are measured relative to the transmitter phase using a lock-in amplifier and a fiber-optic reference link to communicate transmitter phase information that is free of inductive coupling—a term that describes a "sneak path" that allows the transmitter signal to reach the receiver through the ground. The next phase in imaging an area consists of lowering the receiver to the next level, where the transmitter is again moved the entire length of the imaging zone so that the receiver can measure the transmitted signal through the formation. The data collected by this imaging process results in a set of measurements with transmitter and receiver positions as indicated by the white lines in Figure 1. An inversion algorithm is later applied to these data to reconstruct the formation resistivity profile between transmitter and receiver boreholes. Note that although the figure depicts straight rays between the transmitter and receiver to indicate the signal path, the true induction field measured by the receiver is influenced by a larger portion of the formation as a modification of a dipole magnetic field.

In this paper, we document the most recent efforts at LLNL to further develop the cross-borehole electromagnetic imaging technology as it applies to monitoring in situ EOR processes. We also describe our continued development of the field data-acquisition system. The first part of this paper details the acquisition system's design and functionality. This is followed by a discussion of the field tests and capability of this new acquisition system. Finally, we present the profiles acquired at the Richmond Field Station (RFS) and compare forward model results with well log and field data; the results of this comparison are another measure of system integrity.

1.3 Field Data-Acquisition System

The new crosswell electromagnetic imaging data-acquisition system is located in two large trucks, both obtained from the U.S. Department of Energy, Nevada Operations Office at the Nevada Test Site. These vehicles were excessed equipment previously used in big-hole logging for nuclear tests. Both vehicles were in nearly new condition, with less than 3000 road miles on the engines. The trucks were refitted as field vehicles to be used specifically for gathering and analyzing crosswell electromagnetic data. The receiver system is set up in a logging truck with a heavy-duty integrated 40-ft boom. The transmitter system is located in a bread truck. The transmitter truck was modified to include a generator, hydraulic system, winch, tailgate-mounted extendable hoist, and a swingable light-duty boom. This section details the modifications to the vehicles and the development and operation of the data acquisition system on each truck.

1.4 Receiver Truck

Figure 2 is a flowchart depicting the data links for the acquisition system located in the receiver truck (Figure 3), which has corresponding fiber-optic links to the transmitter truck, ethernet, voice communication, and dual analog signal receivers.

The TCP/IP protocol in the receiver truck operates under a LabVIEW virtual-data-acquisition instrument on a Windows Pentium PC platform. The signal analog link carrying information about the transmitter coil depth is input into the counter input of one of two National Instruments NB MIO-16X E-50 A/D cards; the other card accepts the receiver coil depth directly from the encoder. This depth information is displayed in the receiver truck and is input into the LabVIEW virtual instrument.

The analog receiver coil is essentially a ferromagnetic (mumetal) induction circuit with a dynamic frequency range from 20 Hz to 100 kHz, and is powered by a 12-V dc source. The data from the receiver coil is initially passed through a gain box with the options of signal gain or attenuation, and is then passed into a Stanford Research Systems pre-amplifier. (Electromagnetic energy can become highly attenuated in induction through conductive media, and can often require an amplitude gain to avoid problems with roundoff error and low signal resolution.) Next, the receiver-coil data are passed to a lock-in amplifier, along with the transmitter-current analog signal from the fiber-optic line. The lock-in amplifier uses the transmitter current waveform as the reference signal and detects receiver signals in-phase and out-of-phase; this is an effective method for accurately discriminating low-level signals in a noisy background. The lock-in amplifier is controlled though a GPIB interface on the receiver truck's Pentium PC.

All processing, data storage, and receiver-coil positioning is completed within the receiver truck.

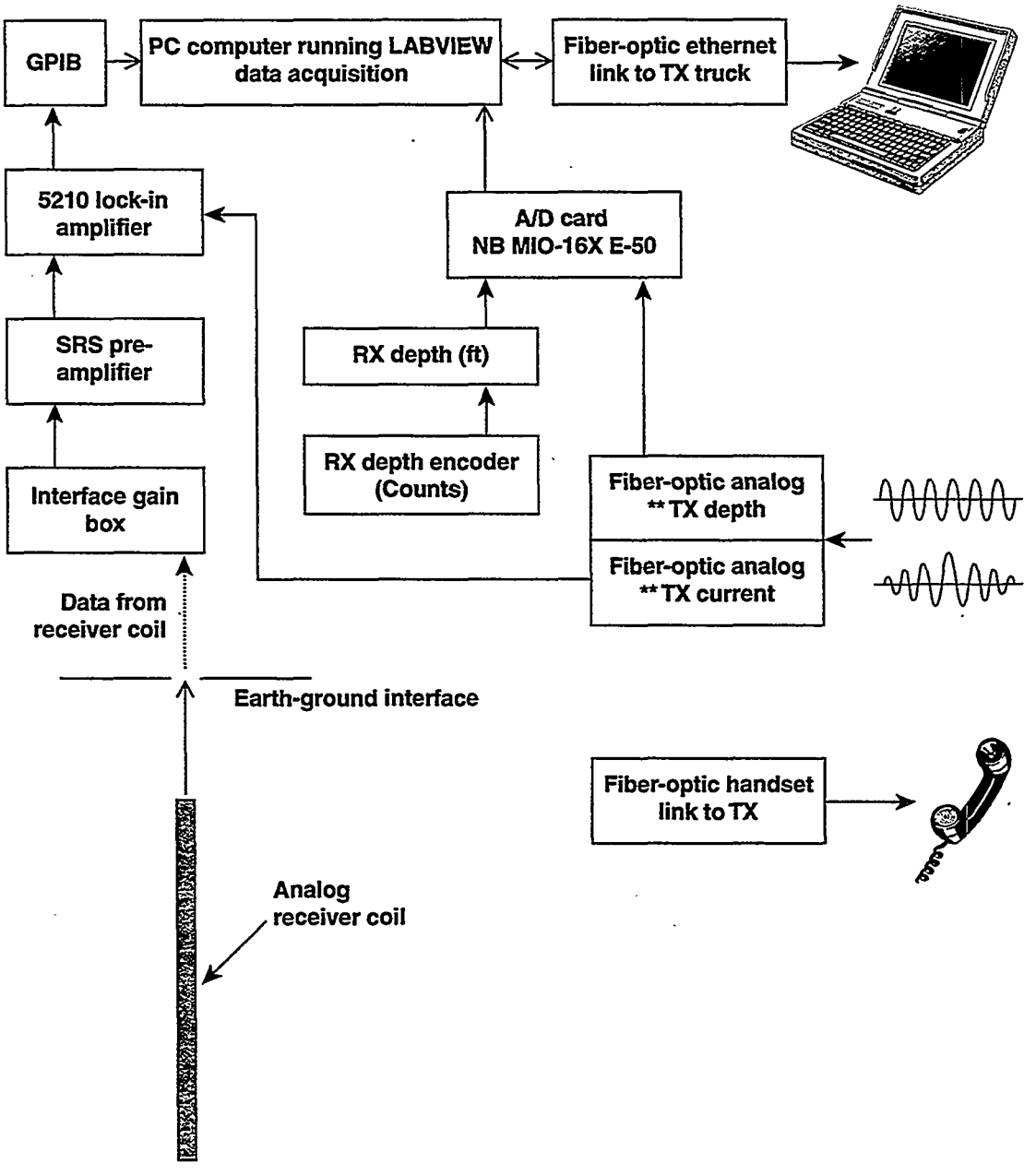

Figure 2. Flowchart of data links in the receiver truck. Fiber-optic cables provide rapid communication using light pulses, thereby eliminating inductive coupling with the acquisition system.

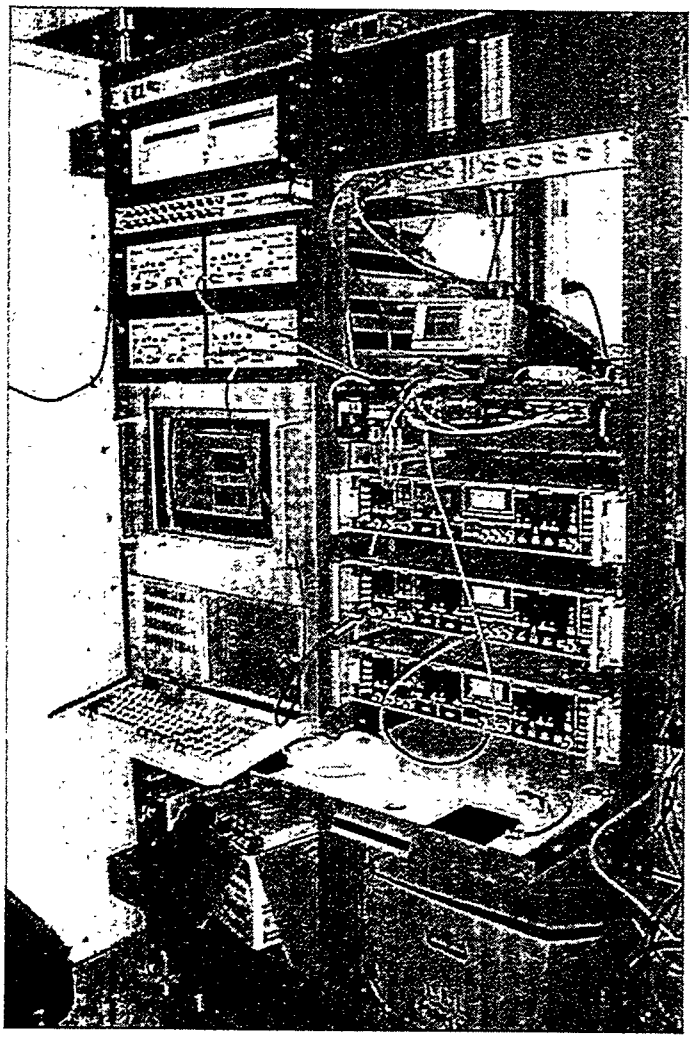

Figure 3. Inside the receiver truck. The fiber-optic chassis contains voice, ethernet, and analog communications. Three lock-in amplifier units are also shown; more than one may be simultaneously used in the presence of excessive signal noise.

In future design changes, we plan to modify the receiver truck so that it can fully operate the transmitter truck, thus making data collection more efficient.

The receiver truck (Figure 4) is a heavy duty 6 × 4 with a 65,000-lb load rating. The truck was used in logging the large nuclear explosive test holes at the Nevada Test Site. It has an integral boom that provides 40 ft of clearance between the shive center and the ground. Logging is accomplished through a retractable roof opening with the wireline path nearly vertical from the spool to the boom shive then over and back down to the borehole. The large winch has a capacity to hold 15,000 ft of 7 conductor, 15/32-inch wireline. The winch is hydraulically operated and is capable of line speeds from 1–200 ft per minute. The winch can pull line at 50 ft per minute with 10,000 lb of tension. The winch is rated for a maximum load of 20,000 lb. The winch air brake is rated at 10,000 lb line tension with the drum full and 14,000 lb with the drum empty and the cable fully extended. The mast, stabilizers, and outriggers are hydraulically operated and are rated at 14,000 lb of line pull with a safety factor of 3 applied to all components in the line-pull path.

The boom mast includes an integral 20,000-lb capacity loadcell and an encoder that resolves one turn of the shive into 512 increments, giving a position accuracy of about a tenth of an inch.

The truck has ac and dc lighting, air conditioning, and heating throughout. Power can be supplied by a 3-phase, 20-kV·A generator that is mounted below the logging cab of the truck.

1.5 Transmitter Truck

Figure 5 is a flowchart showing the transmitter truck's data links; three are active links with the receiver truck: the bidirectional voice communication link, the ethernet link, and the one-directional dual-analog signal-transmission links; all of which

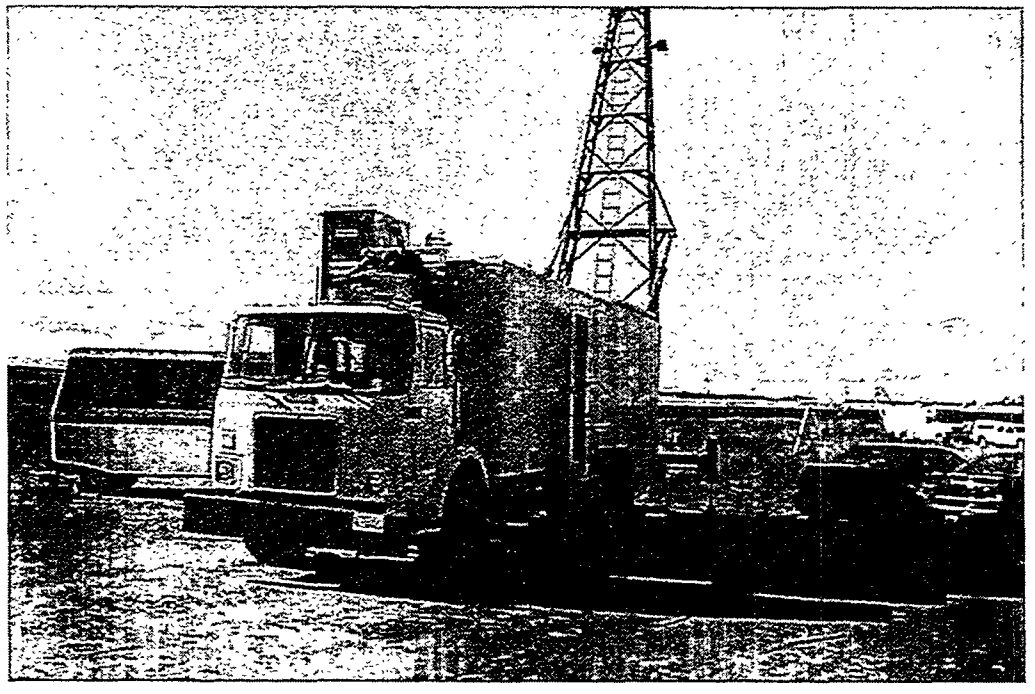

Figure 4. Logging mast fully extended on the receiver truck with the rear hydraulic stabilizer system activated. The large fuel capacity allows over 140 hr of operation in remote field sites. The transmitter truck is shown to the far right of the photo—a separation distance of 52 m.

are transmitted via fiber-optic cable to minimize inductive coupling with the system. The TCP/IP protocol is run under a software, or a virtual data-acquisition instrument developed from the LabVIEW software package, and is controlled by a Windows Pentium PC. The analog-signal-transmission lines carry information about the transmitter-coil depth and power to the receiver truck. The ethernet connection carries identical information, including the active TCP/IP link to the receiver truck; these ethernet data are used for separate calculations.

In crosswell electromagnetic imaging, high-resolution phase information is necessary to determine geophysical parameters, and this requires accurate depth information. Both the receiver and transmitter trucks are equipped with optical encoders, which pulse with milliradian accuracy; these pulses are then converted to downhole distances, which are sent simultaneously to the PC and analog signal links.

The analog signal sent to the PC uses the counter input of one of two National Instruments NB MIO-16X E-50 analog-to-digital (A/D) cards. The second A/D card accepts the transmitter power signal, which comes from two Crown amplifiers configured in push/pull operation; this configuration effectively doubles the voltage so that enough current can travel through the 1800 ft of cable to power the transmitter coil. The Crown amplifiers output an ac voltage proportional to the current driving the transmitter coil; spatial variance of ground conductivity partially determines the admittivity of the transmitter coil, and is thus necessary to monitor current change as a function of depth. The transmitter coil can be configured in two states: as an untuned LCR circuit for frequencies below 500 Hz, and as a tuned resonant circuit for a specific frequency higher than 100 Hz.

We are planning future improvements that include a general purpose interface bus (GPIB) connection, which controls the signal generator so that transmission signal modulation can be controlled from the receiver truck. Note that, in the current configuration, the transmitter PC displays real-time values of the transmitter depth and power so that the pulse modulation can be monitored in the transmitter truck.

As with the receiver truck, the transmitter truck was also procured from the Nevada Test Site. Previously, it was used as a general purpose field

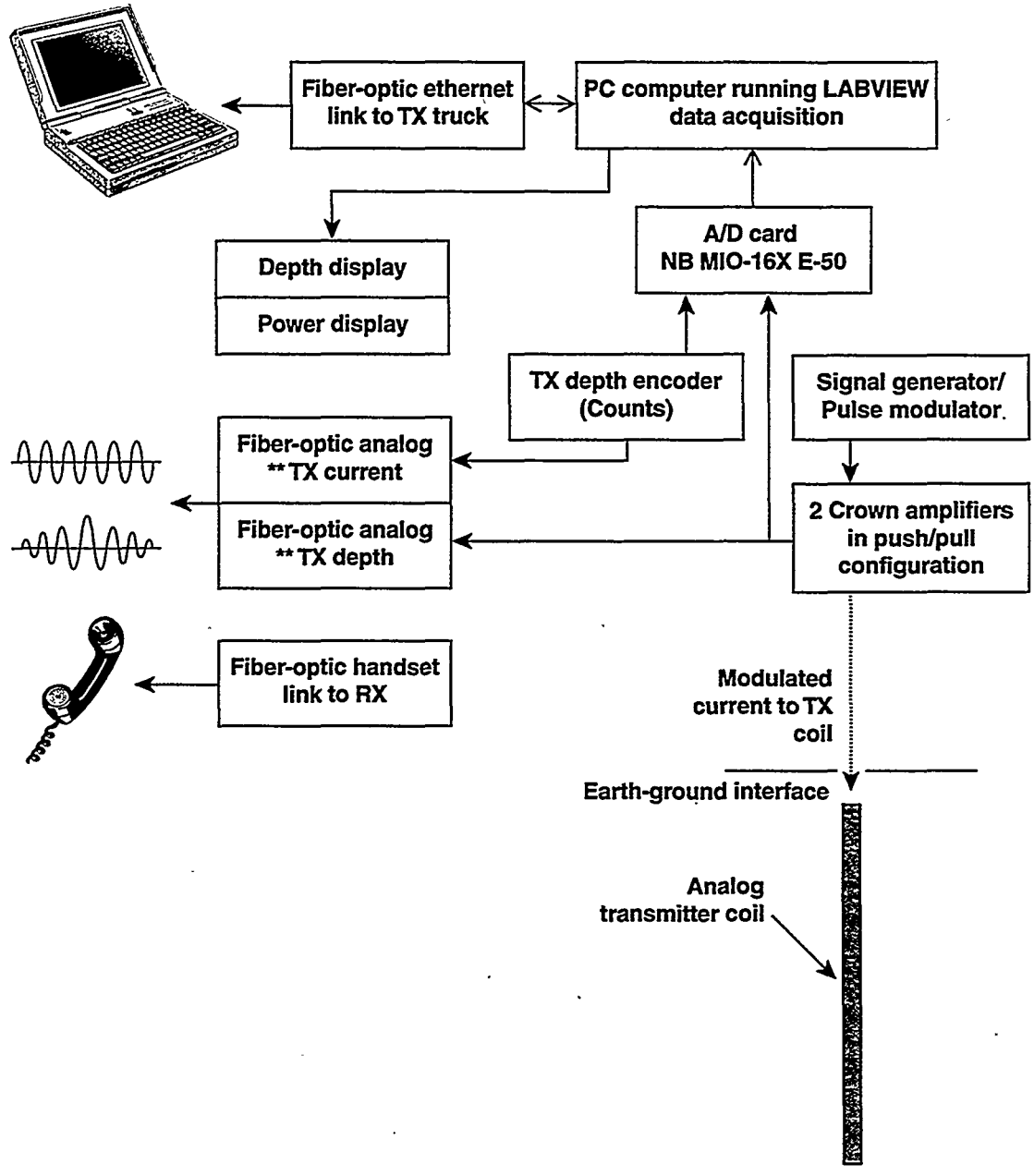

Figure 5. Flowchart of data links in the transmitter truck. Although future systems will use a GPIB interface to control the signal generator from the receiver truck, hydraulic control will remain under direct operator control.

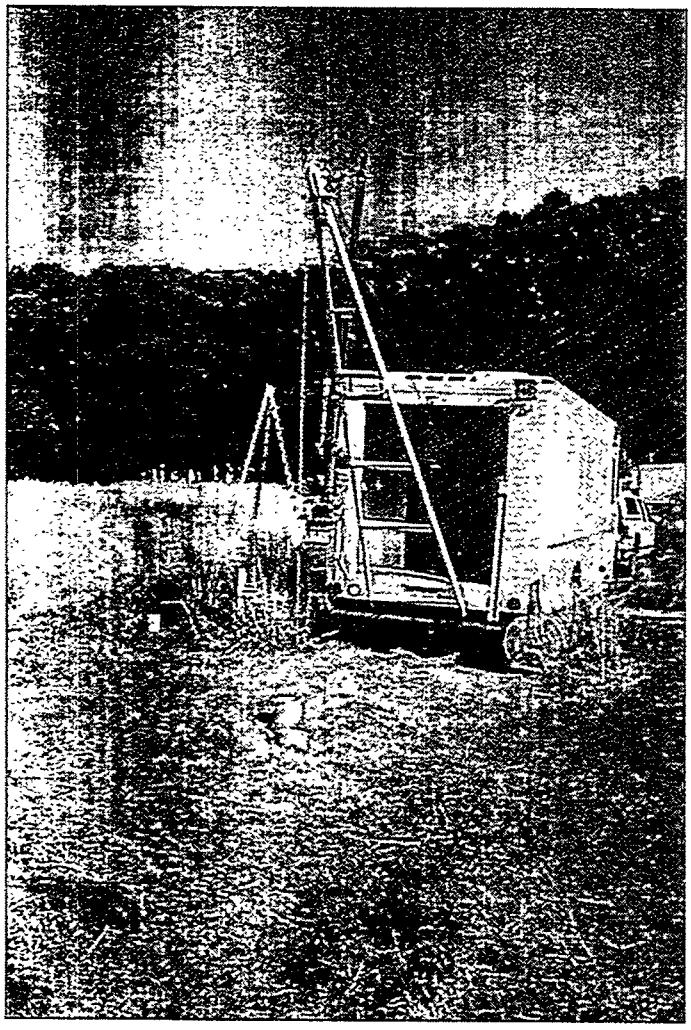

Figure 6. Rear view of the transmitter truck. The mast is controlled by a hydraulic boom on the port side of the truck. The borehole EMNW is located in the center of the picture.

vehicle (Figures 6 and 7). The truck is medium duty, with a 23,000-lb load rating.

We made major modifications to this vehicle so that it could serve as a transmitter platform. An integral A-frame boom was installed with 18 ft of ground clearance. A hydraulically operated winch, with its associated hydraulic reservoir, was installed. The winch drum has capacity to hold 3500 ft of 7 conductor 15/32-inch wireline. The winch is capable of wireline speeds between 10–100 ft per minute and has a maximum tension rating of 5000 lb. The winch brake is rated at 7500-lb line tension with an empty drum. The winch also includes a load cell measuring up to 10,000 lb pull and an encoder that divides one shive revolution into 512 increments. The position resolution is similar to the receiver truck, about 0.1 inch. The mast and outriggers are manually operated and are rated at a line pull of 10,000 lb with a safety factor of 5 applied to all components in the line pull path.

We also mounted a general purpose crane on the truck's extended rear bumper. This crane has a telescoping arm and full three-axis range of motion. The crane is controlled by electric motors activated by the operator's push buttons. The crane is used to support the A-frame during logging operations or can be used for special lifting and lowering tasks.

The truck has ac and dc power throughout as well as heating and air conditioning; ac power is provided by a PTO-driven, one-phase, 8-kV·A generator.

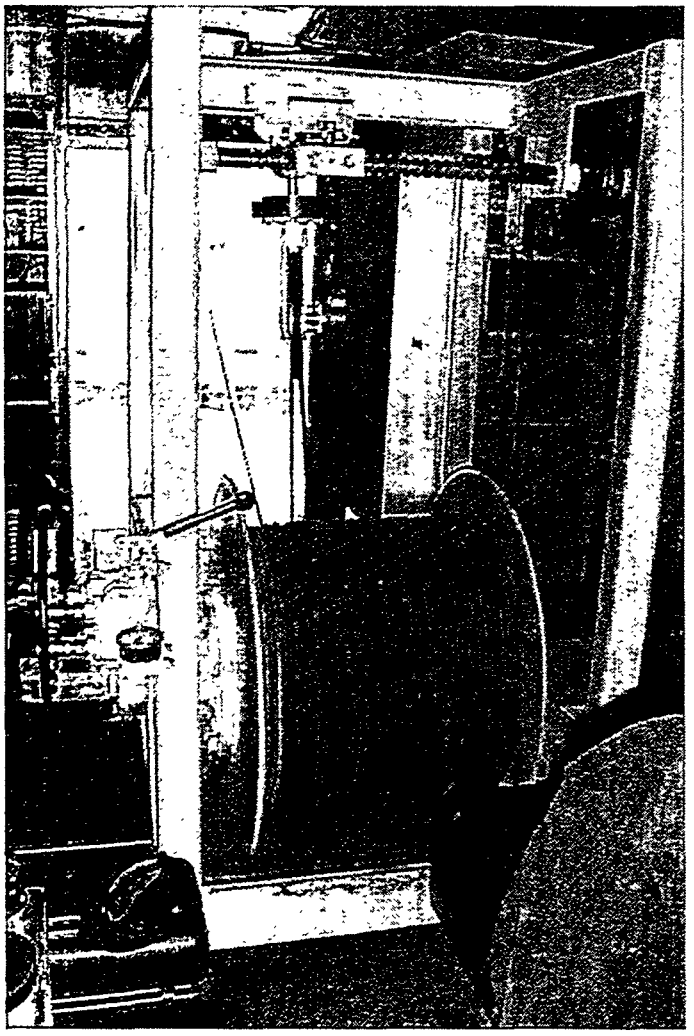

Figure 7. View from the inside of the transmitter truck. The winch in the center currently has 2400 ft of cable, with a capacity expansion. The optical encoder is attached to the shive wheel above the center of the spool. Hydraulic controls are on the center left.

1.6 Field Test Site

The RFS, which is located on land managed by the University of California, provided an ideal site for testing our new data-acquisition field system and for determining the extent of coherency between known modeling code and field data. The field site and test holes are shown in Figure 8. This experiment utilized wells EMNW, a 70-m-deep plastic-cased hole, OBSS, a 30-m-deep plastic-cased hole, and CAS1, a 30-m-deep steel-cased hole. Unequal well depth, as in this case, simply constrains our crosswell modeling attempts to the depth of the shallowest well. This experiment used well EMNW as the transmitter location and wells OBSS and CAS1 as the receiver locations. This geometry provided a steel-cased well within 10 m of a plastic-cased well for receiver locations, and a plastic-cased well at five times the distance for transmitter locations; this was a unique opportunity to examine induction through steel-cased wells. Although the RFS deployment acquired such data, the analysis includes the use and development of complex modeling procedures, which are beyond the scope of this paper.

The geological section of the RFS site can be divided into two primary units: a 40-m layer of unconsolidated deltaic deposits and a basement of sandstone or shale (Pouch, 1987). The unconsolidated deposits are primarily bay mud and clay with occasional layers of sand and gravel. One strata, at a depth of 30 m, was the target zone for a 1993 saltwater injection experiment. Mostly pumped out in 1995, the residual saltwater left a small but significant resistivity signature. According to Pouch (1987), the resistivity of the clay ranges from 5 to 20 ohm-m, whereas the sand and gravel ranges from 12 to 33 ohm-m.

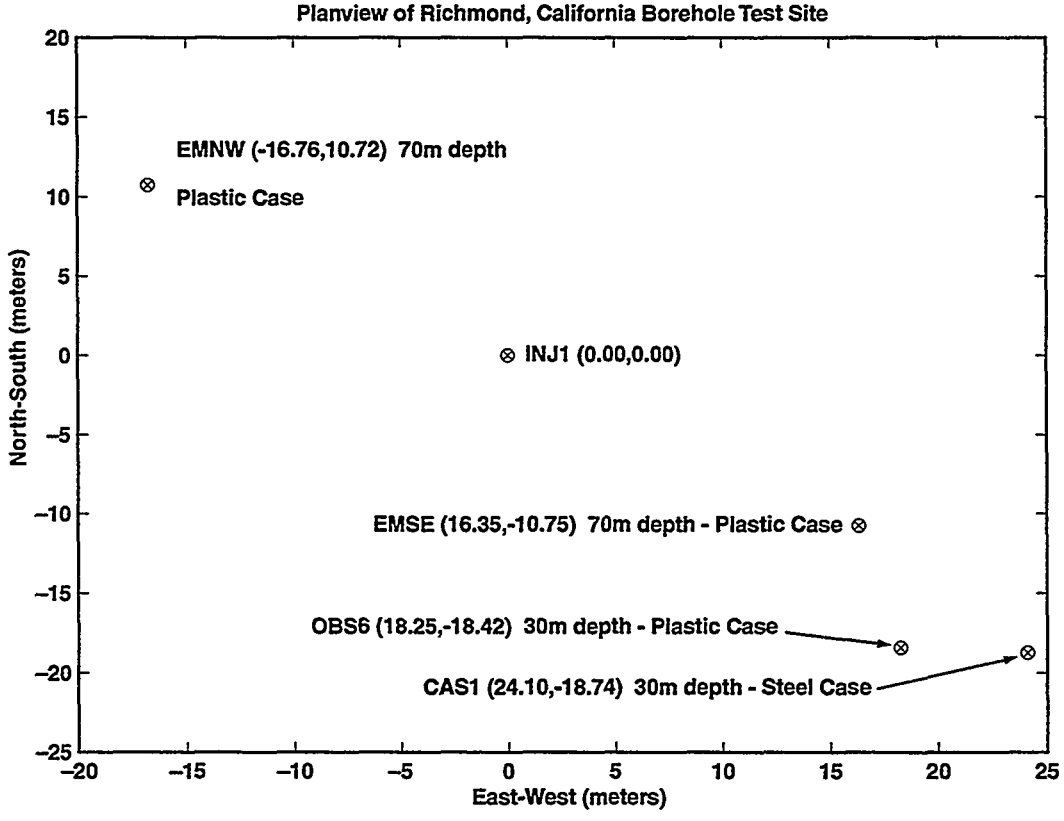

Figure 8. Planview of the Richmond Field Station. Well EMNW is used as the transmitter location and boreholes OBSS (plastic) and CAS1 (steel) are used for the receiver locations. Note the close proximity of wells OBSS and CAS1 in relation to EMNW; data acquired during this experiment will use this geometry in the analysis of the steel-cased-well scenario.

1.7 Calibration Procedure

Prior to interpretation, the receiver-coil voltage received at the lock-in amplifiers must be converted to an equivalent magnetic field due to a dipole of unit moment.This calibration procedure requires measuring the dipole moment of the transmitter and the phase correction factor for the complete crosswell system.

Since magnetic field intensity is assumed to be linearly proportional to the dipole moment, or strength, of the transmitter, the amplitude calibration is essentially the subtraction of this finite dipole moment to a unit moment. Ideally, the calibration setup would take place in the absence of *terra firma* (ground) since the ground affects the induction of the coil. One alternative is to use a modeling code to determine the effect of the ground on the measurements.

Calibration of the coils requires both the transmitter and receiver coils to be parallel and above the ground on nonmetallic platforms of a measured height. Initially, the separation is 15 m, and the current is just below saturation, approximately 20% of normal operating current. A stable reading of magnitude and phase is taken as the coils are increasingly separated until a $r1/3$ magnetic field decay can be shown. At this distance, approximately 40 m, the amplitude is increased to the normal operating current, producing a field proportional to the impedance of the driven system

$$\frac{V_{RX}}{I_{TX}} \cdot k = \frac{100 \cdot M}{r^3}, \qquad (1)$$

where

M = magnetic moment of transmitter,
r = TX/RX separation,
k = calibration factor,
V_{RX} = voltage at RX coil,
I_{TX} = source current.

Solving Eq. (1) for the unknown k
tion factor used to multiply each amplitude for unit dipole moment.

The phase calibration uses the same phase measurements as the amplitude calibration method, but extrapolates the phase for zero offset. Physically, zero offset implies measurement that is physically impossible to achieve because of saturation. The zero-offset phase measurement is subtracted from the theoretical value of 180 deg—for two parallel coils in air—and the result

1.8 System Test Results

Data Reproducibility

The RFS experiment allowed us to test the acquisition system in a number of ways; one of which was the repeatability measurements that offered a means to reveal any noise bias in the system. Results show that the phase and amplitude differences are less than 0.5 deg and 0.6%, respectively.

Figure 9 is a plot of the amplitude and phase of two equivalent profiles. The profiles are separated by two days and several setup and dismantling operations—a worst-case scenario. The phase discrepancy of approximately 0.5 deg is attributed to temperature: the first profile (day 1) had outside temperatures of 43°F, while the outside temperature during day 3 was 72°F. Additionally, system power on day 3 was kept on until a steady-state thermal equilibrium occurred, while on day 1, no system warm-up was allowed before repeatability measurements

Modeled Crosswell Data

One impetus for the RFS experiment was the potential to examine forward model coherency with field data. Forward models were run to match the field data to theoretical ground conditions. EM1D (Lee, 1986), a code that computes electromagnetic fields anywhere in an *N*-layered earth,

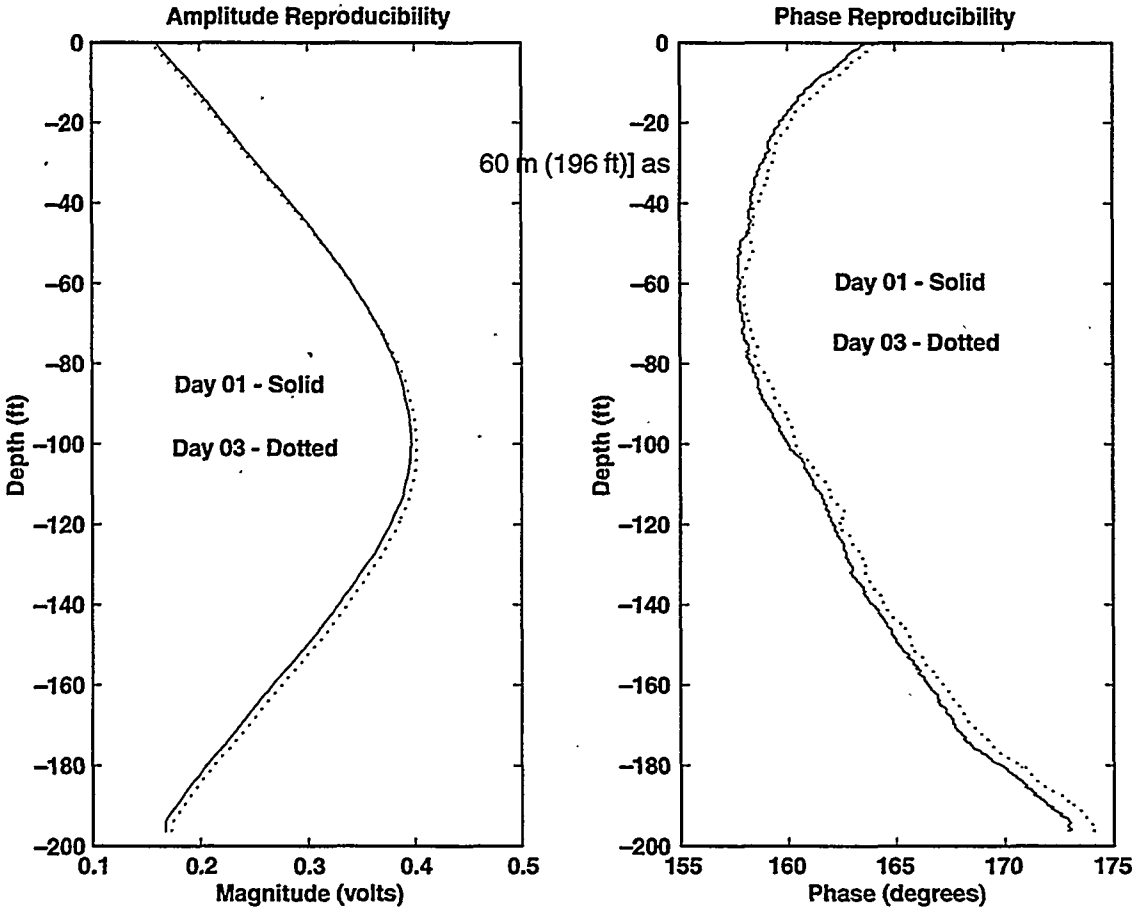

Figure 9. Results of system integrity tests. Using well EMNW [depth to surface: the transmitter-coil location and well OBSS [depth static: 30 m (93 ft)] as the receiver-coil location, two profiles separated by two days under worst-case scenarios were acquired to ascertain reproducibility.

was used to generate the dotted phase and amplitude models in Figure 10. In the earth model, a three-layered model, as described in Table 1, fits the phase quite accurately. Note, the next section describes information on well log versus forward model comparison.

Table 1: RFS model parameters.

Start depth (m)	End depth (m)	Resistivity (ohm-m)
0.0	19.0	8.7
19.0	36.5	9.2
36.5	∞	22.2

The phase is primarily a function of the layered conductivity and, therefore, is not expected to peak at the same depth. The amplitude model, however, has a maximum discrepancy of approximately $2 \times 10\text{–}4$ V, which is primarily due to error in the calibration process—most likely stemming from an error in the accepted value of the transmitter moment. Additional sources of error may also arise from the calibration process, when transmitter- and receiver-coil geometries are not accurately parallel.

Figure 11 plots the earth model found to optimally match the field data with the well log taken from the site in 1992. Immediately after the well log was taken, 55,000 gal of 1.0 S/m saltwater was injected into a 3-m-thick aquifer at a depth of 30 m. Since that time, pumping has removed a majority of the conductive water, although the residual

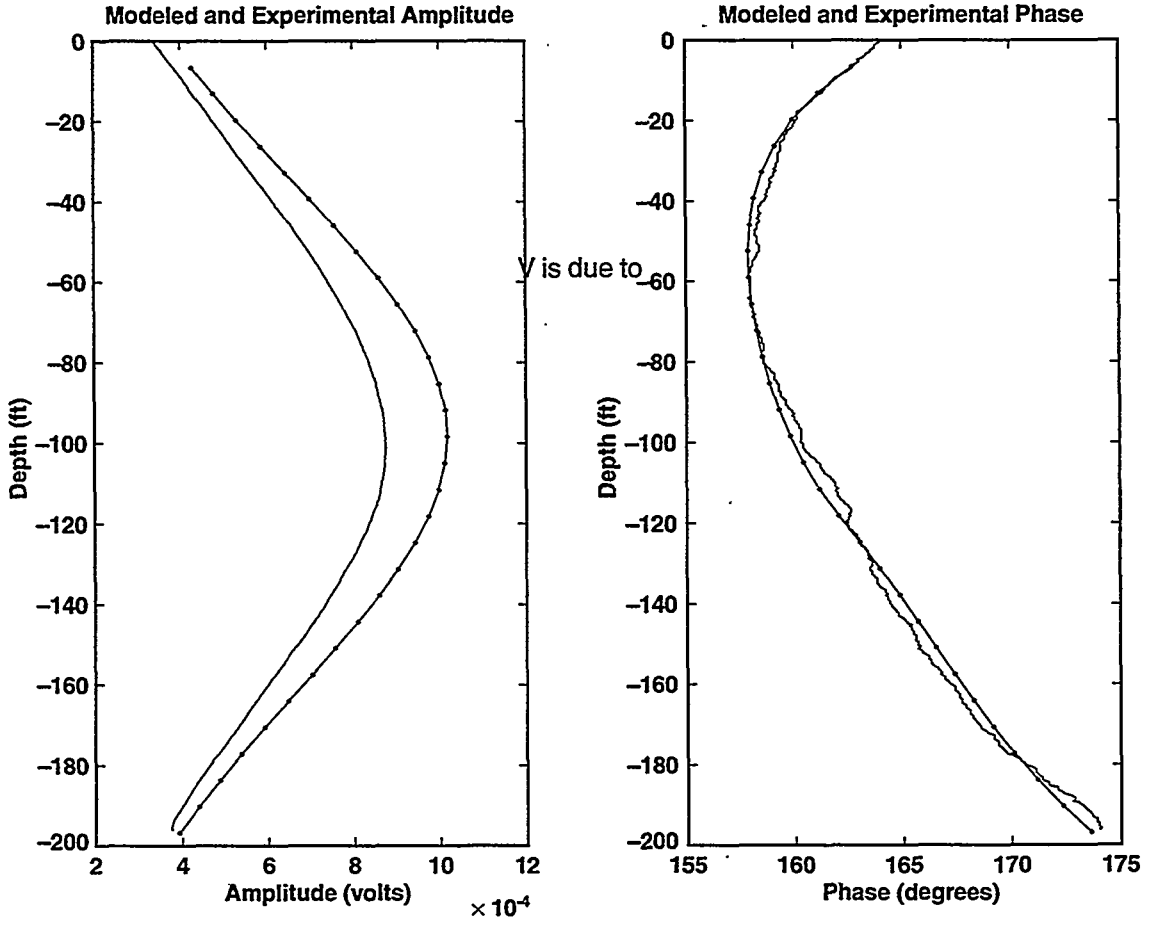

Figure 10. Comparison of EM1D forward model results (dotted) and acquired RFS field data (solid). The forward model was fit to the field data using a three-layered earth. See Table 1 for resistivity parameters as a function of depth. See Figure 11 for model comparison with well log data. The maximum amplitude discrepancy of 2×10^{-4} a calibration error, primarily due to an error in the measured magnetic moment of the transmitter. The phase discrepancy is 0.5 deg at the maximum, which is primarily due to system bias noise; this error is considered quite low.

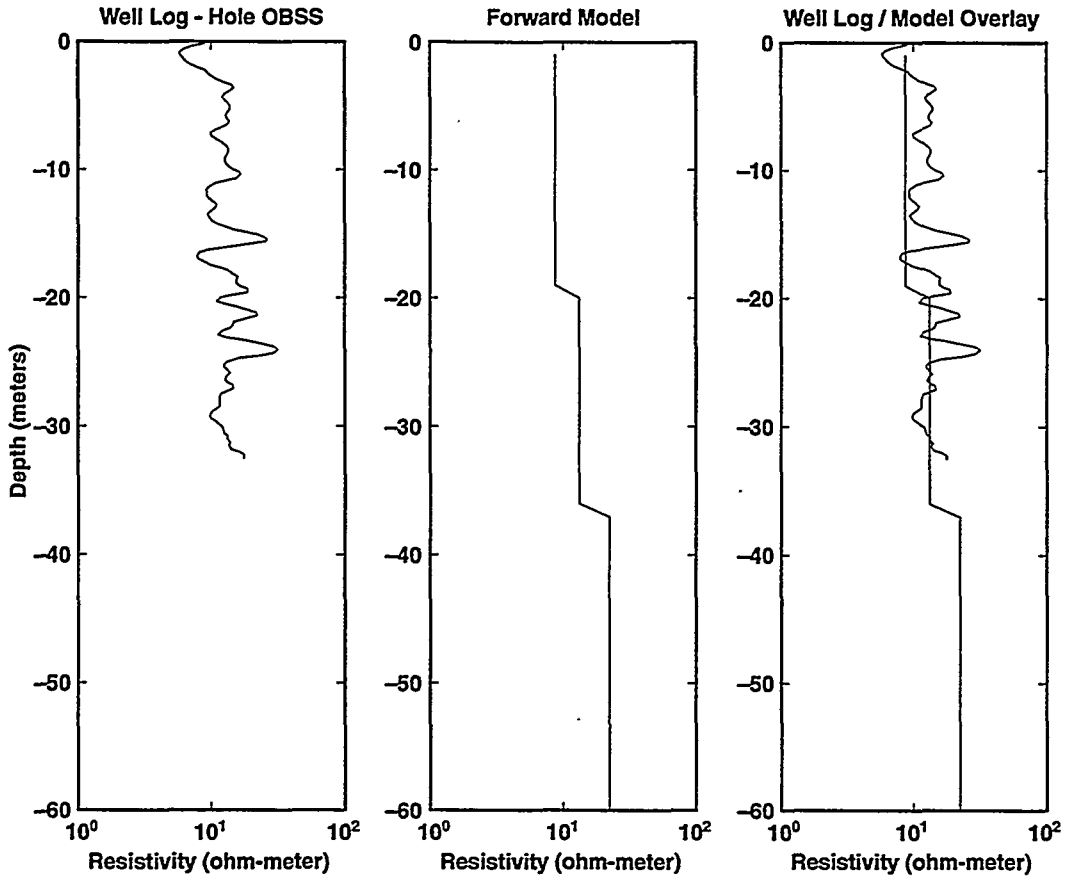

Figure 11. Comparison of well OBSS log data (left) to forward model (center). OBSS log data dates from 1993, acquired prior to a controlled spill; 55,000 gallons of 1.0 S/m saltwater was injected into a 3-m-thick aquifer at a depth of 30 m. In 1995, the salt plume was evacuated, although residual traces remain and are reflected in the several ohm-meter decrease offsets seen on the overlaid plot (right). Additionally, the forward model is extended to a depth of 60 m, as the model response at shallow depths depends on lower depths

appears to have spread through tidal forces to shallow depths, causing a decrease in the resistivity at shallow depths, and a gap of several ohm-m between the earth model and well log.

Inversion of Crosswell Data

The earth model in Figure 11 suggests that inversion of this crosswell data set would be rather uneventful. Indeed, a two-dimensional inversion code, EMINV2D (Alumbaugh, 1993), applied to a set of profiles produced a resistivity contour with little variation. The shallow-hole depth of 30 m did not allow the imaging of bedrock that begins at a depth of 40 m, and therefore, further inversion of these data were not pursued.

1.9 Conclusion

The crosswell low-frequency electromagnetic imaging program at LLNL has been upgraded to include two new borehole-logging field vehicles: one for signal transmission, and one for signal reception and data processing. In addition, a completely new and efficient data-acquisition system has been developed that relies on ethernet pr to transfer information through fiber-optic cable.

The RFS site provided a location to test the reproducibility, background noise, and abilities of the system, and also to collect data concerning a unique well configuration; a steel-cased well and plastic-cased well in close proximity, such that we

assume the formation between the two wells are identical. In addition, resistivity profiles were taken at the site and were matched with forward models. These models agree with well log data and show that the residual of a large saltwater plume injected into a 30-m depth strata early in 1993 caused a general resistivity decrease above a depth of 40 m.

A rapid calibration procedure was introduced and tested; during this calibration process, the accepted value of the transmitter moment appears to be slightly in error. It will be necessary to determine the moment to a higher degree of accuracy.

1.10 Future Research

A significant portion of the data acquired at RFS concerns the steel-cased well scenario; typical oil-well sites have one fiberglass well for monitoring, with the remainder are cased in carbon steel. Therefore, the potential commercial application of crosswell electromagnetic imaging depends on the development of procedure and modeling code that deals with electromagnetic transmission through steel casing.

Crosswell electromagnetic imaging ultimately depends on the inversion technique, which in turn depends on the quantification of system noise and bias. It is widely known that ferromagnetic behavior is dependent on temperature changes. The characterization of the ferromagnetic induction core, the center of the transmitter and receiver coils, as a function of temperature is one such step toward controlling bias. In addition, controlled laboratory experiments in which the subsurface is well characterized should assist in the development and testing of inversion techniques appropriate to electromagnetic phenomena.

1.11 Acknowledgments

We gratefully acknowledge the contribution of Mike Wilt and EMI Inc. (Richmond, CA) for the use of high-quality testing equipment, field assistance, and insightful advice. Additionally, Don Lippert, Jim Doeherty, and John Clyde of Lawrence Berkeley National Laboratory and Frank Morrison of the University of California, Berkeley, contributed valuable time and information concerning assorted axioms of borehole recovery theory.

1.12 References

Alumbaugh, D.L., 1993, "Electromagnetic Conductivity Imaging with an Interative Born Inversion," *IEEE Trans. Geoscience Remote*, 31(4), 758–763.

Lee, K.H., 1986, *Program EM1D*, Lawrence Berkeley National Laboratory, Berkeley, CA, fortran code, 1175 lines

Pouch, G.W., 1987, *Hydrogeological Site Assessment of the Engineering Geoscience Well Field at the Richmond Field Station, Contra Costa County, California*: M.Sc. thesis, Univ. of California at Berkeley, Berkeley, CA.

Image Reconstruction at a Heavy Oil Site in Lost Hills, California: Inversion Processing

Barry Kirkendall
Lawrence Livermore National Laboratory

2.1 Abstract

A waterflood initiated by Chevron Heavy Oil Division at the Lost Hills Truman Lease in California is notable for its low permeability geology. Lawrence Livermore National Laboratory is currently involved in a long term time-lapse multiple frequency electromagnetic characterization study using existing boreholes. Water is flooded into the eastward dipping unconsolidated sands at depths ranging from 500 – 650 meters. Regional induction logs and well sampling do not indicate the presence of waterflooding in the intended region, thus providing a strong case study for characterization using borehole electromagnetic imaging techniques.

Results show that the waterflood is using subsurface channels, either from regional stress fracturing or use of pre-existing Tulare formation lacustrine pathways. Images suggest that the current waterflood is not effectively moving the oil, although future difference images may show that small amounts of oil migration are involved. Laboratory results also show brine injection may induce a jump in resistivity for a short time until longer term injection can remove unique impurities in the soil matrix, discovered in laboratory core electrical analysis,which contribute towards this initial jump in resistivity after injection begins. This behavior can be seen in the calculated subsurface images.

Multiple frequency data is acquired which provides increased information on high penetration distance (a lower frequency advantage) and high resolution (a higher frequency advantage). As the waterflooding develops further, difference images will provide information on subsurface subsidence and higher resolution

2.2 Introduction

For a number of years, heavy oil has been produced with the aid of waterflooding from shallow unconsolidated sands in the San Joaquin Valley of central California. Characteristic of the area, most enhanced oil recovery (EOR) efforts such as waterflooding suffer from water bypass, inefficient sweep as a result of channeling and pre-existing fractures, and water override. The unsteady world oil market has dictated that low cost techniques be sought to make use of observation and production wells which allow greater sensitivity to produced and injected fluids than the traditional high cost lower resolution seismic techniques.

Electromagnetic (EM) techniques are sensitive to rock pore fluids within the subsurface. This contrasts with seismic techniques which are most sensitive to the rock matrix, or subsurface structure. EM crosswell techniques are therefore ideally suited to address the problems of EOR in a heavy oil environment due to the ability to discern between injection steam, injection fluids, and formation fluids. Traditionally, EM techniques have been employed in borehole logging. Recently, however, advances in computation ability and instrumentation make available crosswell and single-well configurations.

Crosswell EM induction is the chosen technique for Task 72, although currently, Lawrence Livermore National Laboratory (LLNL) is working with industry to develop instrumentation and computational software for a single-well EM induction tool. Both single-well and crosswell EM induction techniques provide an electrical conductivity distribution either in a cylindrical pattern or a two-dimensional plane between wells, respectively. This information is used by the field engineer to track subsurface fluids and control the recovery process.

The current long term study discussed was initiated from discussions between Dale Julander at Chevron and Barry Kirkendall at LLNL in 1999. The study includes a time-lapse, multiple frequency, crosswell EM survey of the Lost Hills, California Truman lease. LLNL is focused on the development and resolution increase of the inversion process, in characterizing noise due to production, injection, and hydraulic fracturing in an attempt to better understand the inversion process, and to develop and research practical methods to complete EM induction through steel casing. This report summarizes the inversion results from the first of several field deployments to Lost Hills, CA, and what we can ascertain about the waterflood and heavy oil reserves at the present time. Kirkendall (1999) describes the LLNL fiber optic based field system used in this study.

2.3 Inversion Study – Heavy Oil Site, Lost Hills, California.

2.3a Geologic Setting

The Lost Hills oil field is located along the crest of the Lost Hills anticline in California's San Joaquin Valley. This anticline is the southernmost segment of a northwest-trending segmented antiform that includes the Kettleman Hills anticlines and the Coalinga anticline to the north. It islocated on the western margin of the San Joaquin Basin and roughly parallels the trace of the San Andreas fault zone 20 miles to the west. The San Andreas system is thought to be the dominant control for structure in the western San Joaquin Valley oil fields (Miller et al., 1990).

The Lost Hills oil field was discovered in 1911, although substantial production did not occur until the mid to late 1960's. Presently, oil is produced via steam and waterflooding from a series of stacked oil sands ranging from the Miocene Monterey shales and diatomites to the Pleistocene Tulare sands. The Tulare Formation records the Pleistocene history of basin filling in the present-day San Joaquin valley. It is the first non-marine deposit to be preserved, unconformably overlying the marine Pliocene / Miocene Etchegoin Formation The unconformity at the underlying units contain numerous normal

faults which we feel are creating bypass conduits in the waterflood process, while the Tulare is largely unfaulted and has apparently filled in the older faulted eroded surface.

The Tulare records small- to medium-sized streams depositing loads in the lacustrine delta complexes at the western margin of Pleistocene Lake Corcoran. Because of the system's high energy, there are abundant clean sands throughout the field. Clay content is highly variable, depending on the facies type. Sand geometry is complicated but can generally be thought of as a series of discontinuous sheets and troughs. Well correlations must take into account the highly transitory depositional environment. Also, sedimentary packages can change dramatically within one steam pattern with a large resulting impact on fluid flow. Permeabilities range from a few hundred millidarcies in muddy sands to between 1000 and 3000 millidarcies in the clean sands. The total porosity ranges from 38 to 42% and displays little variability. Oil saturations range between 35 and 75% with a weighted average of 65%. The oil produced from Tulare sands is biodegraded and water washed; it ranges from 10 – 13 API gravity (Miller et al., 1990).

2.3b Site Description

Observation wells OB-7 and OB-8, located within the Truman lease, were drilled in August 1999 to depths of approximately 2500 ft. Figure 1 shows the highly deviated wells within the subsurface along with the location of the injection well; the depth interval investigated is between 1400 and 1700 ft.

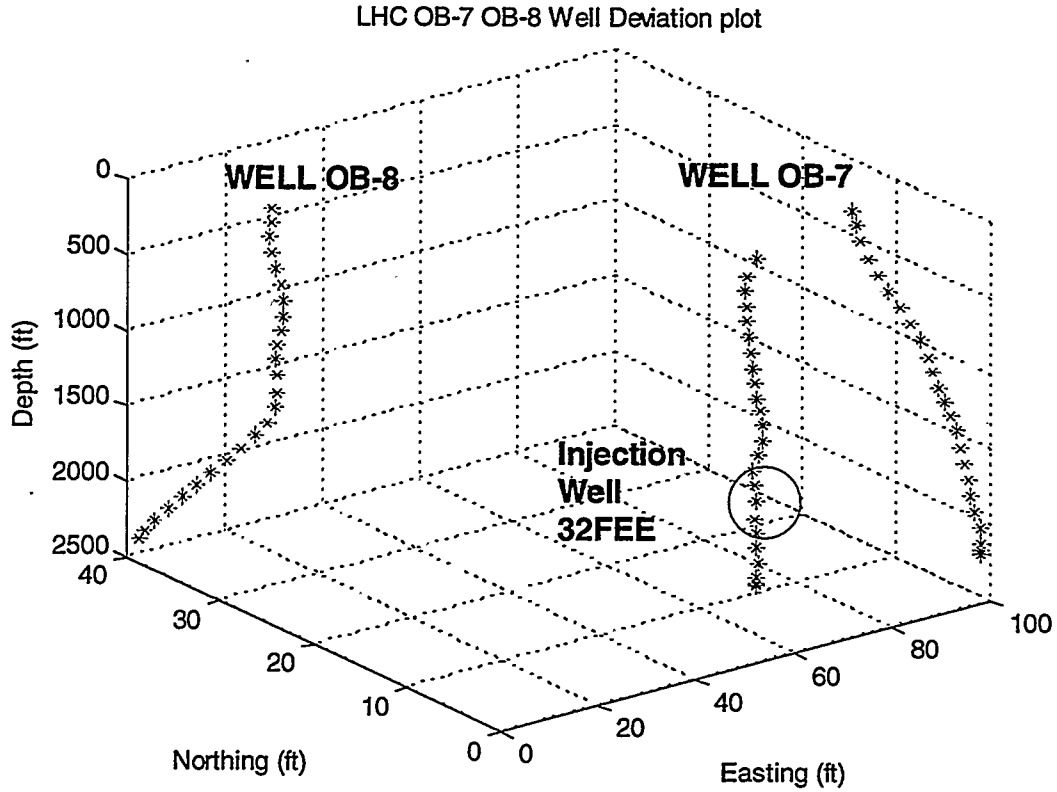

Figure 1: 3-Dimensional View of Chevron Wells OB-7 and OB-8. Note excessive well deviation at depths below 1500 ft. Inversion processing must account for this deviation. The circle region of the injection well represents the depth interval of water injection.

2.3c Objectives of EM Induction Surveillance

Waterflood processes initiated in November, 1997 in the Truman lease area. Initial induction logs for the injection and production wells in the area do not show any significant conductivity change due to the presence of highly conductive injection fluid. As a result, wells OB-7 and OB-8 were drilled in August, 1999 to help determine the flow patterns of injection fluids. In the core analysis of well OB-8, there was no indication of injection fluid present. LLNL and Chevron have since agreed to a long term surveillance of the OB-7 and OB-8 to attempt to track the injection fluid and ascertain the reasons for lack of these injection fluids in the induction logs and core samples. The crosswell survey is designed to examine the flow in the plane between OB-7 and OB-8. This method is quite sensitive to subsurface flow in individual layers.

In November, 1999, LLNL acquired full tomographic data within the depth interval 1400 – 1700 ft at both 2.0 kHz and 4.0 kHz source frequency. Waterflooding has been in effect since November, 1997 and has remained constant. Additionally, passive background noise was acquired at four depths near the injection region, and single- and dual-steel casing data was acquired at shallow depths within the interval 300 – 500 ft. This study will focus only on the inversion results from the tomography between 1400 and 1700 ft.

2.3d Crosswell Induction EM results

Figure 2 displays the short, medium, and long induction logs taken on November, 1999 at OB-7 and OB-8. Our inversion research uses dual two dimensional codes; one rapid cylindrically symmetric inversion for use in the field as an approximation (Alumbaugh, 1996), and one finite difference inversion (Newman, 1999) for use on a DEC Alpha supercomputer for high precision and control of parameters. The results of both images are shown below.

The cylindrically symmetric rapid two-dimensional inversion image calculates a somewhat different result than the finite difference image. This is due to certain limitations and assumptions made by the cylindrically symmetric inversion; the inclusion of smoothing parameters eliminate isolated inter-well conductive signatures, no account is taken for out-of-plane energy, breakdown occurs at rapid conductivity changes due to Born approximation, convergence does not typically occur beyond 3 skin depths (δ), and well deviation can not be accounted for. By comparison, finite difference inversion codes assume very little although computation expense is rather high.

Frequency is a trade-off between resolution and imaging distance. Images calculated at 4.0 kHz will typically have higher resolution than 2.0 kHz images, although the distances are greater in the 2.0 kHz case. As a result, note that the 4.0 kHz images have half the vertical extent of the 2.0 kHz images, and the resulting color legend is different for each frequency. One advantage of using multiple frequencies is the ability to accurately assess both high resolution and large probing depth at an area of interest.

Figure 3, the 4.0 kHz approximation inversion, and figure 4, the 2.0 kHz approximation inversion, both indicate a low conductivity zone between wells at depth of 480 meters. Figures 5 and 7 also indicate this anomaly with much higher resolution and accuracy, due to the high resolution, high computation expense approach. Laboratory measurements of OB-7 core samples indicate the conductivity of the injection brine saturated core to be approximately .48 Siemens/meter S/m or 2.0 -m, while the conductivity of the formation fluid such as the oil sands are approximately .23 S/m or 4.3 -m. This information suggests this area dominated by oil sands.

Conversely, the injection zone is situated at 480 meters depth within the injection well – referring to figure 1, this location occurs outside the plane between the wells and rather close to well OB-8. Based on analysis

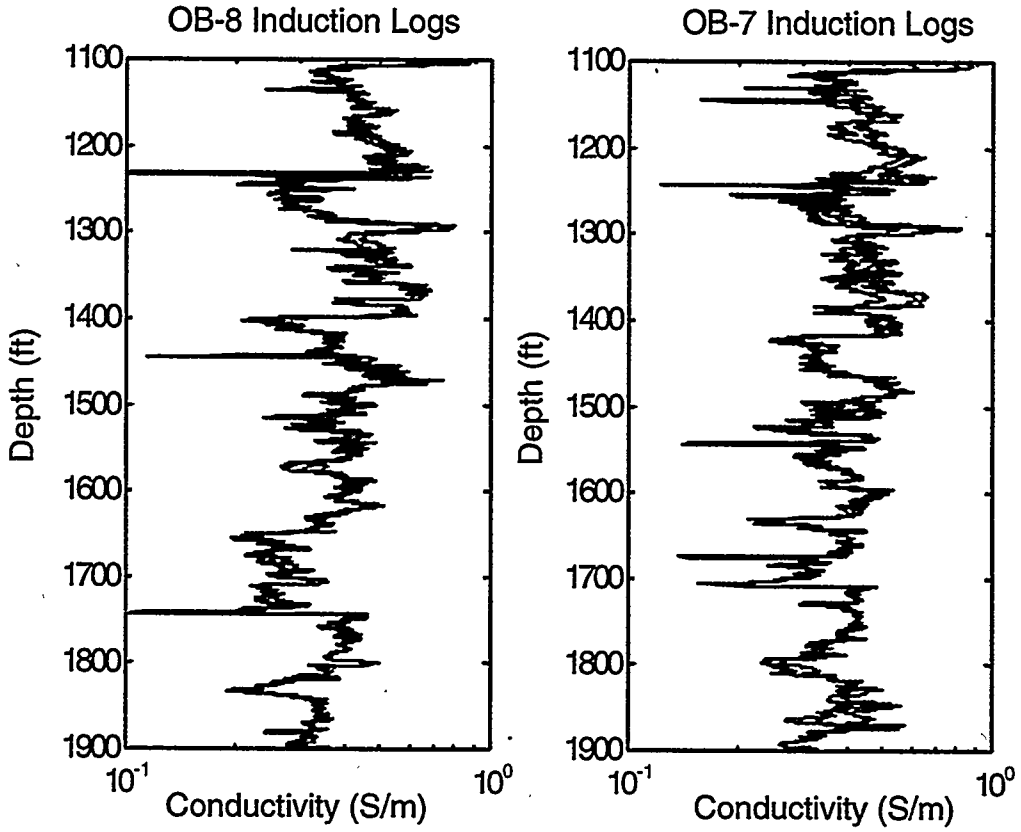

Figure 2: Short (30" - red), Medium (60" - green), and Long (90" - blue) Induction Logs for OB-7 and OB-8.

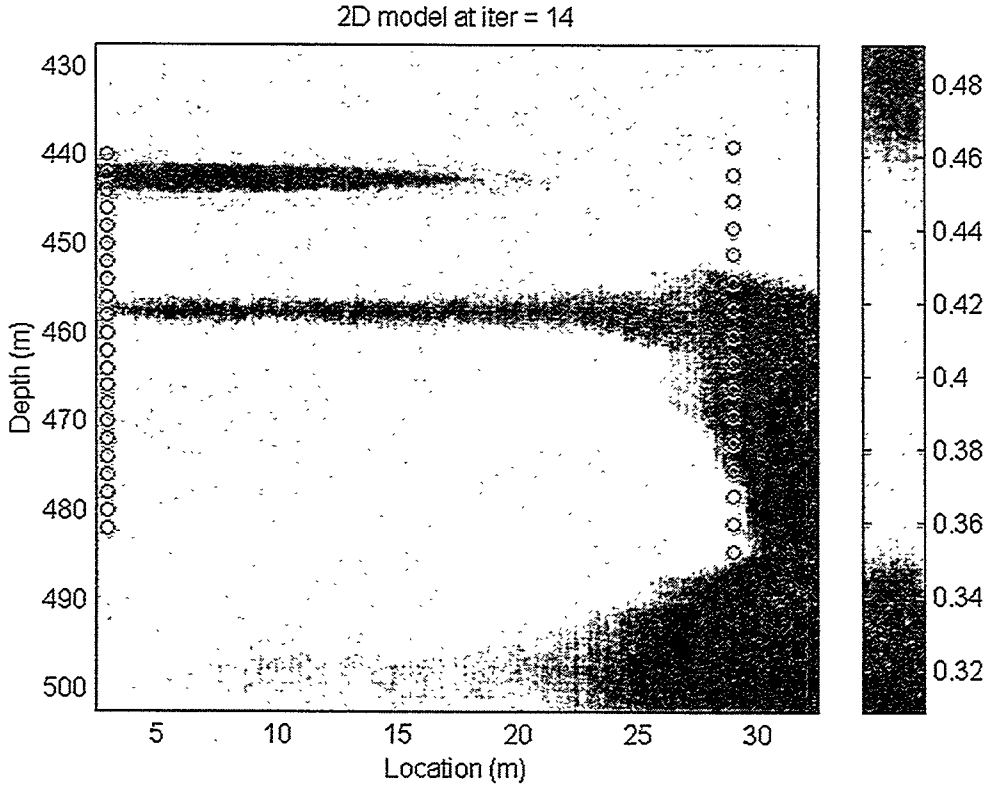

Figure 3: Cylindrically symmetric rapid inversion results for 4 kHz data. Iteration 26. ndver = 15, ndhor = 12, side = 5, z0 = 425, 22 transmitters [1400 – 1700 ft], 16 receivers @ 15ft intervals. Well OB-8 is represented with circles at x =0.0 m, well OB-7 with circles at x = 29.0 m.

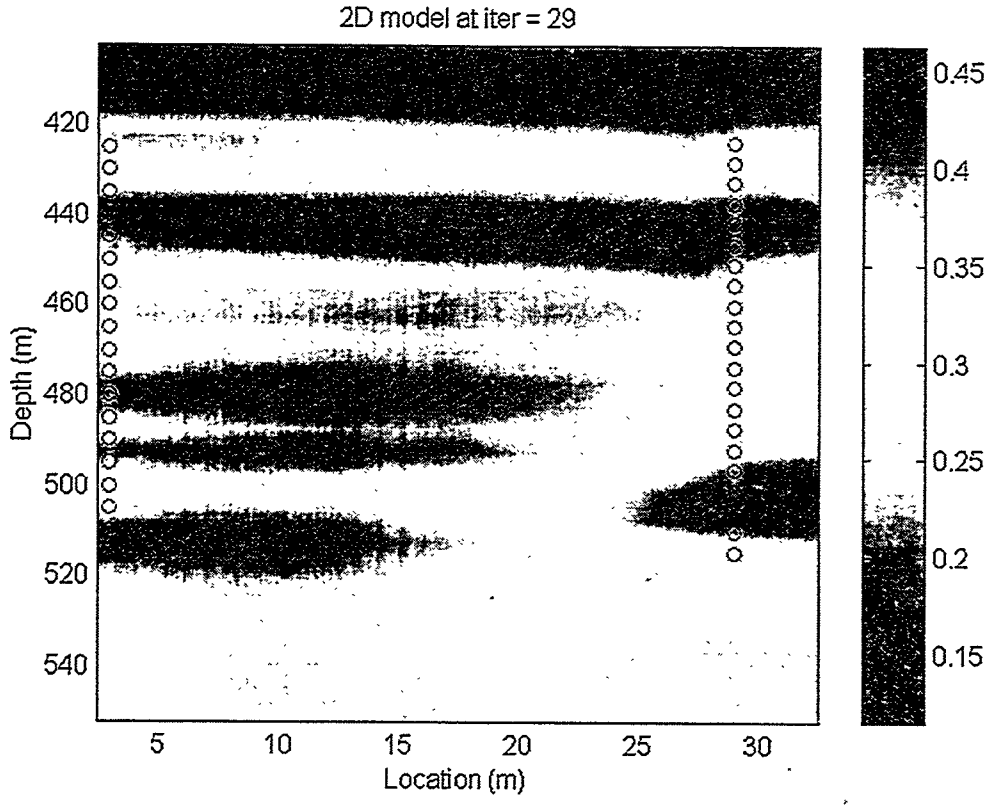

Figure 4: Cylindrically symmetric rapid inversion results for 2 kHz data. Iteration 30.ndver = 30, ndhor = 12, side = 5, z0 = 400, 21 transmitters [1450 – 1600 ft], 18 receivers @ 10 ft intervals. Well OB-8 is represented with circles at x = 0.0 m, well OB-7 with circles at x = 29.0 m.

of high resolution images, figures 5 and 7, this injection plume is flowing normal to the plane between the OB-7 and OB-8, either using a subsurface conduit caused by local stress fracturing or by a pre-existing Tulare lacustrine stream channel. In any case, it is clear that the injection fluid is not able to serve the intended purpose of moving the OIP. The waterflooding at this depth is ineffective due to the presence of subsurface flow conduits.

There is evidence based on figures 5 and 7 that brine injection fluid is present at well OB-7 at 440 - 455 meter depth. As there is no injection near this well, present modeling is determining whether this conductive signature is due to another subsurface conduit or an isolated pocket of formation fluid separate from the oil sands. Figures 6 and 8 illustrate the misfit during the inversion process for each frequency calculated.

2.4 Discussion and Conclusion

Waterflooding within the Tulare formation clearly is not reaching the intended target of the oil sands. Fractures known to exist normal to the fault range, and normal to the plane between the wells are likely providing a conduit for the injected brine. Further hydraulic fracturing may increase exposure to the oil-in-place (OIP), although in the presence of a high stress region such as the San Joaquin Valley, hydraulic fracturing may increase the effectiveness of existing fractures to remove injected brine by providing larger subsurface pathways.

This project will continue for the next calendar year with surveys repeated every 4 months for the continued monitoring of the waterflood and oil migration, as well as using difference images to detect subsidence and associated phenomena due to subsurface fluid migration. Preliminary results suggest that crosswell EM induction is seeing subsidence, although further processing of a data set newly acquired at Chevron is needed.

Results from this project have demonstrated that crosswell EM induction is a powerful tool in reservoir characterization and process monitoring. This technology is still in the developmental stages; we should expect future work to deal with horizontal coils, further resolution increases in the inversion process, and the development of single well field systems capable of dealing with steel casing.

The practical challenge is to incorporate technologies such as cross- and single-well EM induction with existing seismic in a cost effective manner. These technologies serve to improve the knowledge of reservoir geometry and to allow the engineer more control of secondary and tertiary recovery processes.

2.5 Acknowledgements

This project was funded by the U.S. Department of Energy through Fossil Energy research under contract number W-7405-Eng-48. We gratefully acknowledge project manager Tom Reid for his continued support. We also acknowledge Dale Julander, Kristin Castelucci, Jim Copeland, and Qiang Zhou of Chevron, Mike Hoversten of Lawrence Berkeley National Laboratory, Greg Newman of Sandia National Laboratory, David Alumbaugh of the University of Wisconsin, and Mike Wilt and Ping Zhang of Electromagnetic Instruments Inc for providing several inversion algorithms and advice.

2.6 References

Kirkendall, B, Lewis, J.P., Hunter, S.L.,Harben, P.E., *1999, Progress in Crosswell Induction Imaging for EOR: Field System Design and Field Testing*, LLNL Internal Report UCRL-133468, 14 p.

Miller, D, McPherson, J.G., and Covington, T.E., 1990, *Fluvo-Deltaic Reservoir, South Belridge Field, San Joaquin Valley, California, in Barwis*, J.H., McPherson, J.G., and Studlick, J.R. (Editors), *Sandstone Petroleum Reservoir, Springer-Verlag, NewYork, NY*, pp. 109-130

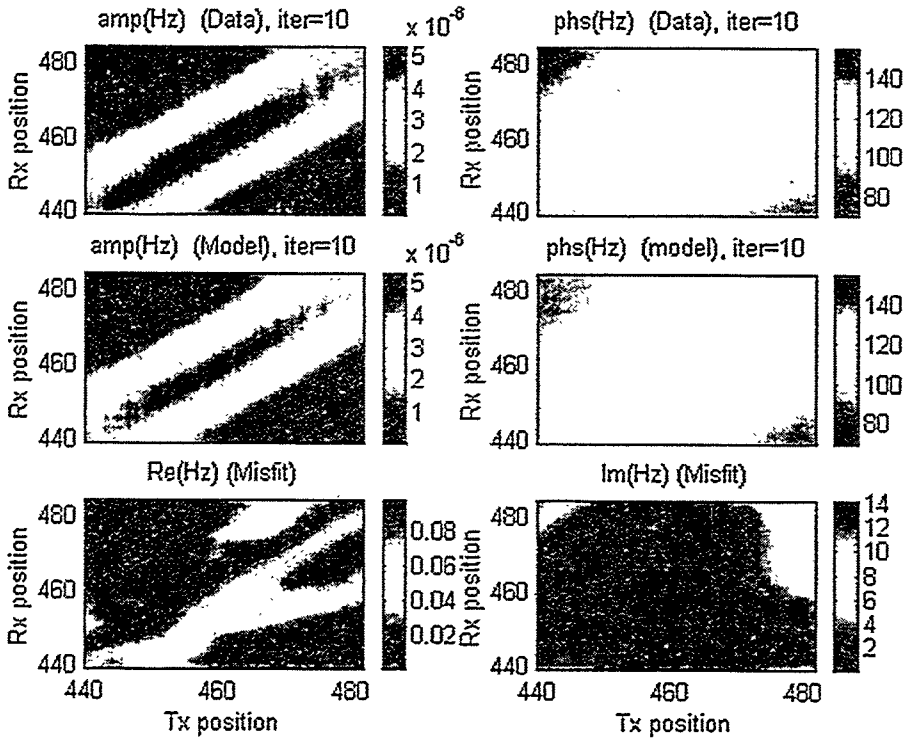

Figure 5: Inversion misfit matching for finite difference 4.0 kHz data, Lost Hills, California.

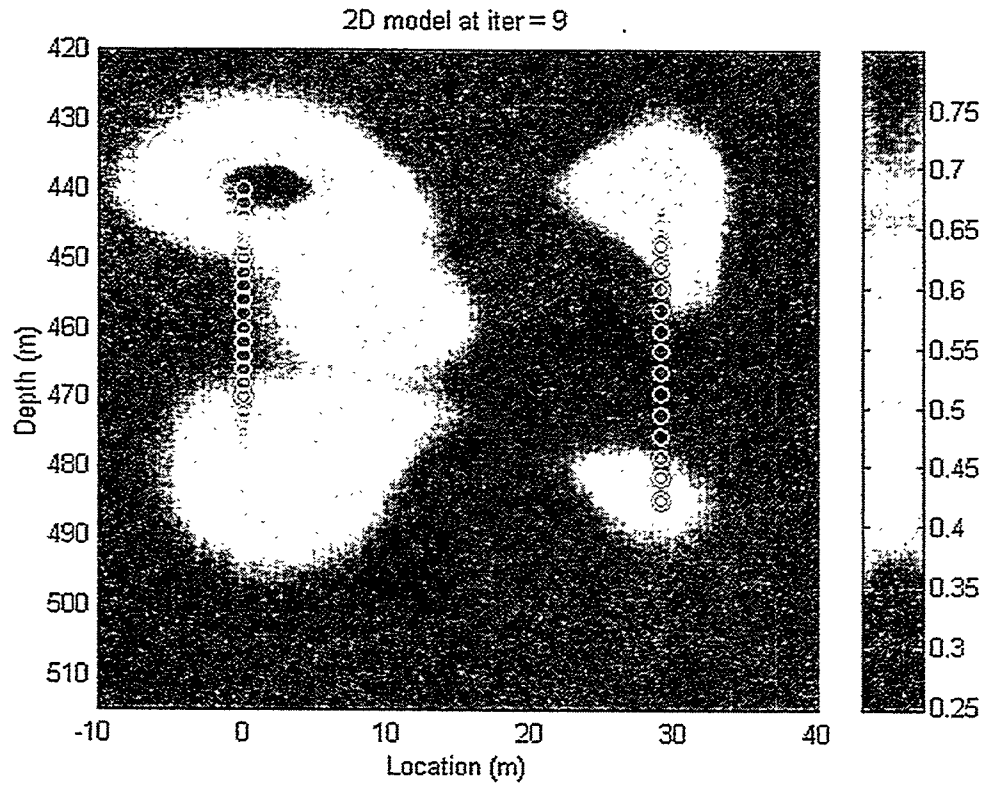

Figure 6: Finite Difference Inversion results for 4.0 kHz data, Lost Hills, California. Well OB-8 is represented with circles at x = 0.0 m, well OB-7 with circles at x = 29.0 m.

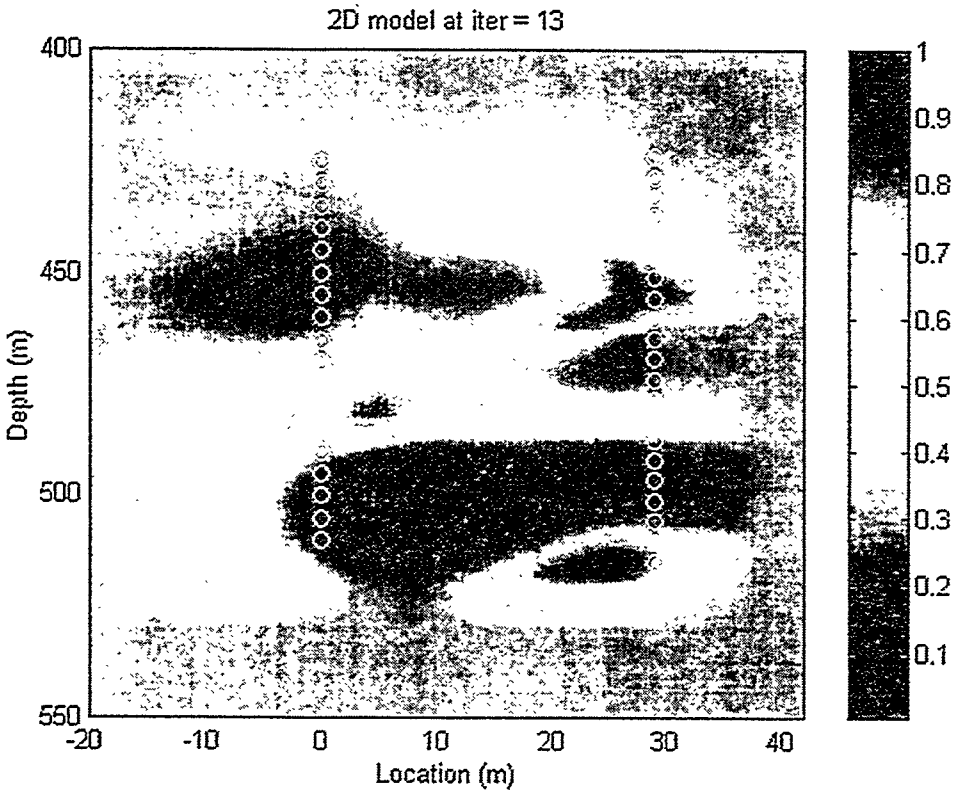

Figure 7: Finite Difference Inversion results for 2.0 kHz data, Lost Hills, California. Well OB-8 is represented with circles at x = 0.0 m, well OB-7 with circles at x = 29.0 m.

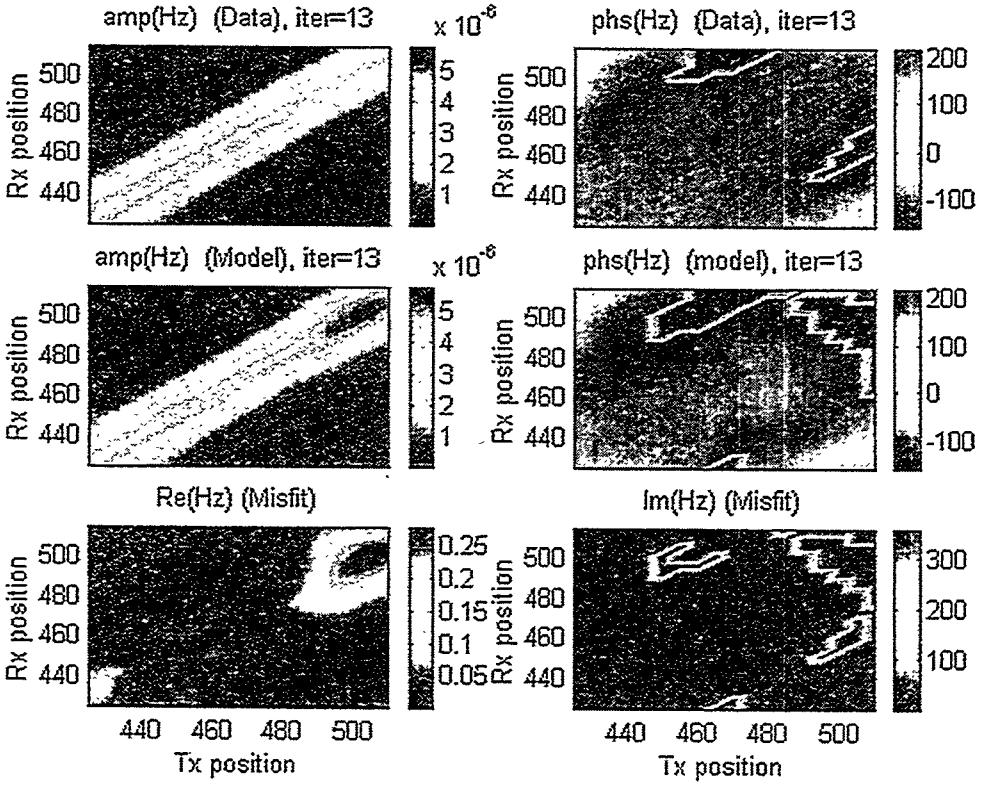

Figure 8: Inversion misfit matching for finite difference 2.0 kHz data, Lost Hills, California.

Task 73 — INTEVEP shall provide DOE with information on production mechanisms associated with heavy and extra heavy oil in unconsolidated formations. Simulation and laboratory results will be included.

Foamy Oil in Porous Media
Part I: Literature Review

A.M. KAMP

PDVSA Intevep, PO Box 76343, Caracas 1070-A, Venezuela
April 1999

Abstract

Oil containing a dissolved gas is called *supersaturated* when the dissolved gas concentration is higher than that corresponding to thermodynamic equilibrium at the existing temperature and pressure. Supersaturation is measured as the pressure difference between the equilibrium pressure at given saturation and the actual pressure. It is thought that the understanding of supersaturation is an important aspect in the understanding of *critical gas saturation*, which is the volume fraction of gas at which this becomes connected and starts to flow in the reservoir. High critical gas saturations are typical for foamy oil flow. It might be that high supersaturations are as well, but the connection with the high critical gas saturations is not well understood.

The objective of this report is to get a better understanding of the role of supersaturation and its importance in the process of modelling of foamy oil flow. After a introductory description of supersaturation, a very comprehensive literature review is presented, covering nucleation modelling (both nucleation of vapour and dissolved gas) and investigations on supersaturation in dissolved-gas/oil systems

1 Introduction

Foamy oils are typical for some of the Venezuelan and Canadian oil reservoirs. Typical characteristics of foamy oil are a low gas/oil ratio (GOR), a high primary recovery and high critical gas saturation. In order to do successful reservoir simulations for foamy oil producing reservoirs, it is important to understand the physics behind the production mechanisms. Recently some ideas have emerged on what happens in foamy oil. An idea that has wide support is that foamy oil is characterised by small bubbles that possibly move with the oil phase or are trapped in pore spaces. If these bubbles coalesce and form continuous gas, the primary production is over. Therefore it is important to understand how these tiny bubbles are created, at what pressure and

supersaturation they are created, how the size distributions are determined as well as the role of internal (such as the type of formation) and external (such as pressure draw down) factors on this all. Two keywords readily appear: supersaturation and nucleation. Both will be discussed in detail in this report.

A system containing a liquid and a dissolved (sometimes called condensed) gas is called *supersaturated*, when the amount of dissolved gas exceeds that corresponding to equilibrium at the existing pressure and temperature. The degree of supersaturation may conveniently be expressed as the difference between saturation pressure and the prevailing pressure.

Supersaturation is a dynamic phenomenon and supersaturated systems relax back to equilibrium in a finite amount of time. This happens by two processes, the first of which is the creation of free gas within the system by the *nucleation*[1] of bubbles and the second is *diffusion* of gas out of the system or into earlier created nuclei. Therefore, the understanding of supersaturation is connected to the understanding of both nucleation and diffusion, and a model for supersaturation is a model that captures nucleation and dissolved gas diffusion. A combination of both processes reduces, and finally annihilates, supersaturation.

Supersaturation is also a non-equilibrium property. Many of the classical analyses in reservoir engineering are based on static properties, such as for example PVT analyses. That type of characterisation does not permit the understanding of phenomena that are largely due to dynamic process, such as for example nucleation and supersaturation.

The term *supersaturation* should not be confused with *gas saturation*, which is the volume fraction of gas in the pore volume. The *critical supersaturation* can either be defined as the supersaturation at which the first bubble is nucleated or as the pressure difference at which the supersaturation no longer increases when the pressure is further decreased. The *critical gas saturation* is the gas saturation at which connected gas is created, covers several pore spaces and starts to flow in the porous medium. It is thought that these terms are however related, something which will be a further point of discussion in this report.

In practical applications, the phenomenon of supersaturation is well known by people who sometimes open a bottle of beer, champagne or cola. The sudden reduction of pressure that this induces causes the liquid to be

[1] In the following, we will sometimes refer to the term nucleation meaning the creation of a gas or vapour nuclei and the subsequent process of diffusion of gas into the created nuclei. Although diffusion and the creation of the actual nucleus are different processes, it is hard to draw a border between one and the other.

supersaturated with dissolved carbon dioxide gas. As long as a certain supersaturation persists, the liquid continues to generate bubbles, which subsequently grow by diffusion of dissolved gas into them, in order to reach a dissolved gas concentration that is in equilibrium with atmospheric pressure. Another well known application is deep water divers, who on ascending to the surface have to make decompression stops, so that the nitrogen which dissolved in the blood at the high pressure existing at great depths, can diffuse out of the blood into the lungs, without creating small bubbles in the body. In petroleum industry, supersaturation is foremost known in solution gas drive processes or production of foamy crude oils, and in problems with gas cut mud during drilling.

Gas phase formation in supersaturated liquids is a first-order phase transition, which occurs by bubble nucleation, growth and coalescence. Initially the created bubbles are small and far away from each other and coalescence is of no importance. The kinetics of the initial stage of the gas phase formation process is therefore describable only in terms of the rates of bubble nucleation and growth.

The supersaturation is one of the parameters that determine how much gas is dissolved in oil at a given moment. Since the viscosity of the oil is a strong function of the quantity of dissolved gas, the viscosity is also a function of supersaturation. Experimental observations also show that the size distribution of bubbles created by nucleation and diffusion depends on the degrees of supersaturation during the creation process. Possibly, the bubble size is also related to the critical gas saturation (the gas fraction at which the gas becomes connected), so that supersaturation and critical gas saturation may be connected.

This report covers a study of supersaturation and its relation to foamy oil flow. Its objective is to come to a better understanding of what supersaturation is and how it is related to gas saturation, critical gas saturation and foamy oil flow. Therefore a very comprehensive literature research has been carried out, covering partly the existing literature on nucleation of vapour and gas bubbles in dissolved-gas/liquid mixtures and most of the existing literature on foamy oil and solution gas drive related to supersaturation and critical gas saturation. Following the literature review, we underline some of the most pertinent observation that have been reported.

A partial verification is then attempted by using a framework for modelling of foamy crude oil, which has recently been proposed in Intevep (Hammond, 1997). Applying this framework to a rapid depressurisation experiment, actually conducted by Brigida Meza in Intevep, a model for the prediction of this experiment is obtained. Two different closure modelling are tested, one

conventional (such as used by Maini's group at PRI and in the STARS simulator), and one new and original. Predictions are made with both types of modelling. These predictions are then compared to the experimental data and conclusion about their validity are presented. Finally we present perspectives in the process of the development of a fully predictive model for foamy oil flow inside a reservoir.

2 Literature review

The existing literature may for convenience be separated in three parts: a first part which contains the theoretical description of nucleation of a vapour phase or of a dissolved gas in a liquid, a second part which treats the nucleation of gas bubbles in live, possibly foamy, oils and a third part on field observations of foamy heavy crude producing reservoirs. Although the first part does not directly relate to petroleum industry, it contains the basic description necessary for the oil-related part.

Although the process of nucleation of vapour bubbles by boiling (heat transfer) is not completely identical to the way nuclei are created from dissolved gas by pressure decrease (mass transfer), it has received more attention in the literature, and its understanding is useful for the understanding of the behaviour of dissolved gas. Supersaturation is therefore related to metastability limits of superheated liquid (e.g. Eberhart et al, 1974).

2.1 Nucleation and supersaturation in gas-liquid and vapour-liquid systems

Vapour-liquid

The theory of nucleation has initially been developed for description of nucleate boiling. The following processes govern nucleate boiling: heat transfer, mass transfer, liquid inertia, surface tension and viscous forces. Two asymptotic cases appear in the growth of a vapour bubble. In the early stages an inertia controlled solution (Rayleigh, 1917) applies, neglecting the heat transfer and taking only into account the dynamic or inertial effects. In this case, the bubble radius increases as a linear function of time. The large time solution is governed by heat and mass transfer, and has been studies by Plesset & Zwick (1954), Forster & Zuber (1954), Scriven (1959) and Bankoff (1964). The bubble radius then follows a square root dependence of the time.

The combined effects of liquid inertia, heat transfer, non-equilibrium effects and variable vapour density in the process of vapour bubble growth in constant and time dependent pressure fields has been investigated by Theofanous et al. (1969).
Reviews of these works can be found in Skripov (1974), Blander & Katz (1975) and Blander (1979).

The influence of surrounding bubbles on the rate of nucleation has been analysed by Deligiannis & Cleaver (1993). This influence is due to the wave action initiated by the growth of predominant bubbles and their relative motion with respect to the liquid. This affects the average pressure, which in its turn changes the critical work as determined by classical nucleation theory. The slip tends to reduce the nucleation rate, whereas the effect of bubble growth increases the rate of nucleation.

Simultaneous gas-vapour nucleation has been studied by Ward et el. (1970). The studied solution exists of a weakly soluble gas dissolved in a liquid, with the gas allowed to behave non-ideally. It is shown that, for a given temperature, the pressure at which the nucleation occurs in a gas-liquid solution increases as the gas concentration increases.
The superheat required to initiate the nucleation of a bubble in a pure liquid is usually defined as the difference between the temperature of the liquid at nucleation and the saturation temperature at the system pressure. A pure liquid becomes metastable, and nucleation becomes possible when the pressure is reduced below the vapour (saturation) pressure, so that the superheat is necessary positive for a pure liquid. As discussed above, the presence of a dissolved gas increases the nucleation pressure, so that in some cases homogeneous bubble nucleation is predicted to occur above the saturation pressure (Forest & Ward, 1978). The superheat then is negative.

Gas-liquid

In contrast to the numerous studies reported on nucleate boiling, the corresponding problem in mass transfer received less and later attention. Regarding mass transfer, one should expect a qualitatively similar behaviour to that of nucleate boiling: inertia control for high values of the driving force and diffusion control for low values of the driving force. The first part corresponds to the early stage in bubble growth and the latter part to a later stage.

Szekely & Martins (1971) present a theoretical analysis for the growth of a spherical gas bubble in a supersaturated liquid due to the diffusion of a solute. Liquid inertia, viscous effects, surface tension and mass transfer are taken into account. Writing the equations in a dimensionless form, they show that this

problem is characterised by a series of dimensionless numbers. The equations are solved numerically and comparing the full solution to the diffusion limited asymptotic solution, the validity range of the latter is determined. At low pressure, liquid inertia seems to play an important role and in this range their solution corresponds well to obtained experimental results.

After a paper by Rosner & Epstein (1972), which stressed the important of surface kinetics, Szekely & Martins (1973) published a paper which includes the joint effects of surface kinetics, liquid inertia, viscous forces and surface tension forces. They suggest the following asymptotic categories:

- *Diffusion* limited growth rate if the pressure in the bubble is close to the pressure in the liquid some distance from the bubble and the solute concentration is in thermodynamics equilibrium with the gas in the bubble. Bubbles in this regime exhibit parabolic growth rate;
- *Hydrodynamic* limited growth rate, including liquid inertia, surface tension effects and the transfer of viscous momentum. The solute concentration at the surface is then controlled by the pressure in the bubble, which is different from the pressure in the liquid. A departure from the parabolic behaviour discussed in the first item is then observed;
- *Surface kinetics* limited growth, where the solute concentration undergoes a discontinuity upon reaching the surface. In this case the solute concentration at the surface can not be determined by an equilibrium solubility relationship such as Raoult's or Henry's law, but the kinetics has to be solved.

Szekely & Martins conclude that inertial effects predominate in the early stages of growth but are probably only of practical importance in very low pressure systems. Viscous effects are only important for systems displaying very high viscosity such as glass melts and possibly heavy crude oils. Surface kinetics might play an important role over a wide range of conditions. The distinction between the viscous and the diffusion-limited regimes is also made by Toramaru (1995), who presents a numerical study of nucleation and growth of bubbles in viscous magmas. In another numerical study by the same author (Toramaru, 1989), a narrow depth interval is located, where nucleation takes place. Subsequently gas comes out of solution, not by nucleation, but by diffusional growth of bubbles. This study is carried out as a function of three dimensionless numbers, representing interfacial tension, diffusion and saturation pressure effects.

Ward et al (1985) studied the influence of vapour in gas nuclei in a dissolved gas in liquid solution, the gas concentration being near its saturation value. Previous theories assumed that the vapour concentration of liquid

solvent inside the gas bubble is negligible, as well as the so-called local equilibrium assumption, which says that the gas concentration at the bubble boundary may be taken as the equilibrium value corresponding to the conditions inside the bubble as the bubble evolves in size. Experimental evidence indicates that sometimes bubble can grow at concentrations lower than the saturation concentration, when a vapour phase is present in the bubble.

A model for supersaturated CO_2 solutions in water has been developed by Wilt (1986), examining the mechanisms of: homogeneous nucleation, heterogeneous nucleation at a smooth, planar interface and nucleation at interfaces conical and spherical cavities. The basis of his examination is classical nucleation theory as reviewed by Blander & Katz (1975) and Blander (1979) and extended by Ward et al (1970). His bubble stability theory builds on earlier work of Ward et al (1982).

Lubetkin & Blackwell (1988) present an experimental technique to count the number of bubbles created when the supersaturation of a solution is released. They show that this number of bubbles is closely related to the number of nuclei formed, thus allowing a quantitative test of nucleation theory. This is done by comparing their data to the heterogeneous nucleation model of Wilt (1986) which yields satisfactory agreement.

A literature review on nucleation modelling can be found in Lubetkin (1994).

2.2 Nucleation and supersaturation in oil/dissolved-gas systems

Kennedy & Olson (1952) present measurements on the supersaturation of methane and kerosene in the presence of silica and calcite crystals. Their observation show that the number of bubbles formed per second per unit area of surface crystal is a function of supersaturation only. They find the latter to be up to 700 psi. The frequency of bubble formation is observed to increase with increasing supersaturation. Silica and calcite crystals had identical effects and a small amount of water and crude oil had no effect on the results. At supersaturation lower than 30 psi, no bubble formation occurs within a time lapse of 138 hours. Based on their experimental observation Kennedy & Olson (1952) obtain a relation between the rate of pressure decline and the number of bubbles formed in the reservoir. In a later paper (Wieland & Kennedy, 1957), observations are extended to the measurements of bubble frequency in cores.

Wood (1953) repeats Kennedy & Olson's experiments using reservoir oil. He finds that at 27 psi supersaturation no gas bubbles had formed after 15

hours waiting. Stewart et al (1953, 1954) perform a systematic study of the role of supersaturation in oil recovery by solution gas drive in limestone. The supersaturation obtained was more than 20 psi at 10 psi/day pressure drawdown. The obtained recovery depended on the rate of pressure decline. Hunt & Berry (1956) present an experimental and theoretical study in order to determine the probability function of bubble nucleation time. They find that the mean rate of bubble formation increases rapidly with increasing supersaturation.

Other studies on the subject that are worth mentioning are those of Handy (1958) and Chantenever et al (1959). Wall & Khurana (1971, 1972) observe that for nucleation to occur, the liquid has to be supersaturated, higher rates of pressure decline being associated with greater degrees of supersaturation. They also observe the separate stages of bubble formation, growth and coalescence until the stage of connected gas.

A series of investigations has been carried out which touch upon the relation between supersaturation and critical gas saturation. These include the works by Dumoré (1970), Madaoui (1975), Abgrall & Iffly (1973) , Moulu & Longeron (1989) and Moulu (1989). In the latter, higher supersaturations are found at higher depletion rates. The number of bubbles created is larger and their size is smaller as the depletion rate is higher because of the higher supersaturations reached. The maximum supersaturation is found to occur after the nucleation of the first gas bubble. This phenomenon is also discussed by Aldea (1970) in the following way. When the pressure in live oil is lowered below the bubble point pressure, the oil becomes supersaturated. After the creation of the first bubble, which occurs at a pressure lower than the bubble point pressure, the gas dissolved in the oil starts to diffuse towards the bubble. Both this diffusion and further nucleation tend to force the system back to thermodynamic equilibrium. When the supersaturation is still low and few bubbles have been created, diffusion is slow because the distance to be covered by the dissolved gas molecules in order to reach a bubble is, on average, large. But when supersaturation increases and more bubbles are created, diffusion becomes faster. More gas gets out of solution and the saturation pressure (the pressure which would be in equilibrium with the actual concentration of dissolved gas) decreases faster. At the moment that the rate of decrease of saturation pressure becomes larger than the rate of decrease of actual pressure, the supersaturation starts to decrease. If the supersaturation has strongly decreased, the creation of new bubbles is nearly arrested and the diffusion can increase again, lowering the rate of decrease of the saturation pressure until both saturation pressure and actual pressure decrease at the same rate. Aldea (1970) also states that in heavy oils the obtained supersaturations are higher

than in light oils because of the fact that in the former the diffusion coefficient is lower.

The mechanics of bubble flow in heavy oil reservoirs is discussed by Islam (1990), who performs experiments on the flow of a foamy oil in capillary tubes and core flow experiments. Although supersaturation is not directly discussed in this paper, Islam finds that at higher pressure decline rates, smaller bubbles are found and higher recoveries. He does however not address the mechanisms through which smaller bubbles lead to higher recoveries.

The three research groups who have done probably the most work on supersaturation, critical gas saturation, nucleation, etc. in live oil systems, often in situations of solution gas drive and in foamy oil, are the groups lead by Firoozabadi (Reservoir Engineering Research Institute in Palo Alto, California), Yortsos (University of Southern California) and Maini (Petroleum Recovery Institute, Calgary).

Yortsos & Parlar (1989) study the response of a simplified solution gas drive system to an imposed supersaturation. They distinguish two parts: (i) nucleation; (ii) subsequent bubble growth. They show that nucleation events are likely to occur in the large pore bodies first, and that the supersaturation needed for the appearance of the first bubble should be largely independent of features unrelated to the porous media nature (such as, for example, the rate of pressure decline). The onset of nucleation is proposed to be that the local supersaturation exceeds the capillary barrier of capillary heterogeneities in the pore surfaces (such as cavities). The effect of pressure decline rate, according this model, would be in the activation of some crevices at given supersaturation, and not in modifying the kinetics of homogeneous nucleation. At small supersaturations, stable equilibrium gas bubbles in converging pore elements are possible. In this case a quasi-static percolation approach can be employed. For small pressure variations below the bubble point pressure, the growth process is mass transfer controlled; for larger pressure drops this is still the case, but diffusion is then no longer quasi-static.

A detailed study of multiple bubble growth is presented by Li & Yortsos (1994). The difference between gas phase growth in porous media and in bulk and between homogeneous and heterogeneous nucleation are stressed.

Data from experimental investigations in a micromodel correspond with the results of numerical simulations using Li & Yortsos's ideas (Li & Yortsos, 1995), although the agreement is less good on a microscopic level. It is among other things confirmed that the onset of nucleations occurs from different sites. Grow patterns of nucleation and growing gas in porous media was addressed by Satik et al (1995).

Firoozabadi et al (1992) measured supersaturation and critical gas saturation in two core samples containing a binary mixture of decane and methane. Their data show that pore structure could significantly affect the degree of supersaturation, the supersaturation in a porous medium with small pores being less than in a porous medium with larger pores. This observation might be linked to the fact that in cores with small pores a higher nucleation site density is present, so that the rate of nucleation is higher. They also find that even at high-pressure drawdowns, the supersaturation sometimes (in case of small pores?) becomes negligible. The supersaturation is proportional to the square root of the pressure decline rate (Firoozabadi & Kashchiev, 1993). Supersaturation and critical gas saturation seem to be connected: higher supersaturations imply higher critical gas saturation. This also implies that for larger pores and higher pressure draw downs, the critical gas saturation is higher. It is tempting to suppose that for higher supersaturation, smaller bubbles are created, which coalesce with more difficulty and therefore promote higher critical gas saturation.

In a reaction to Firoozabadi et al (1992), Saidi (1994) proposes that the degree of supersaturation be not related to whether pore sizes are small (lower supersaturation) or large (higher supersaturation), but rather to whether the pore size *distribution* is narrow or large. He states that low permeability porous media, with a narrow pore size distribution, favour gas dispersion and that high permeability porous media with a large pore-size distribution present less gas dispersion. Then he refers to Dumoré's experiments (1970), which show that dispersion develops more easily in large size pores than in smaller pores and concludes that this finding is in contradiction with the results of Firoozabadi et al (1992). In a reaction to Saadi's paper by Firoozabadi et al (1994), this point is not further touched upon.

Kashchiev & Firoozabadi (1993) propose a theoretical description of the kinetics of the initial stage of gas phase formation in supersaturated liquids at constant temperature. Using existing knowledge on bubble nucleation and growth, they set up a framework for the overall process of gas phase formation. They do this by building on existing modelling in other domains of new phase formation, such as crystallisation in melts and precipitation in solutions. Herein two different types of nucleation are distinguished: (i) progressive nucleation, where bubbles are continuously nucleated among growing bubbles, and (ii) instantaneous nucleation, where bubble nuclei are formed at once, so that later they only grow. Kashchiev & Firoozabadi arrive at the conclusions recapitulated in Table 1.

	Progressive nucleation	Instantaneous nucleation
Constant supersaturation	• Created gas volume is strong function of time and supersaturation • Induction time strong function of supersaturation	• Created gas volume is weaker function of time and supersaturation • Induction time weakly dependent on supersaturation
Steadily increasing supersaturation	• After a certain time delay the number of nucleated bubbles and the created volume increase sharply with time • Gas volume sensitive to supersaturation rate • Critical supersaturation weakly dependent on supersaturation rate • Critical supersaturation highly sensitive to effective surface tension	• The volume increases gradually with time • Gas volume less sensitive to supersaturation rate • Critical supersaturation dependent on supersaturation rate • Critical supersaturation not strongly dependent on effective surface tension

Table 1: Comparison of prediction of bubble nucleation and growth model for instantaneous nucleation and progressive nucleation at constant and steadily increasing supersaturation

Pooladi-Darvish & Firoozabadi (1997) perform constant withdrawal rate sand pack experiments. They observe low critical gas saturation, no flowing microbubbles, no mobility enhancement, and conclude that non-equilibrium effects are not dominant. These observations are different to those of Maini, Sarma & George (1993), but compatible with Firoozabadi & Anderson (1994). The absolute pressure measurements show a definite trace of supersaturation at short times, and the supersaturation seems to be somewhat lower in the light than in the heavy crude. Gas saturated silicone oil and heavy crude samples with same viscosity were flashed to atmospheric pressure. Smaller bubbles were observed in the heavy crude and they took longer to disassociate than in the silicon oil.

An investigation on the spatial development of gas saturation and pressure drop was carried out by Maini & Sarma (1994) and Maini, Sarma & George (1993). Although their observations (pressure gradient increases where gas saturation increases; pressure gradients are not constant but display a semi-periodical behaviour, probably due to local build up and liberation of free gas) are linked to supersaturation, this connection is not discussed in their paper.

Sheng et al (1995*a*, 1995*b*, 1996) presents a methodology for including non-equilibrium processes in foamy oil properties. In order to avoid nucleation modelling, they use a more ad hoc approach, where they assume that the increase of a macroscopic gas volume can be modelled as a power law function

of the time. Their total model furthermore includes the transport of four components: dissolved gas, solution gas (moving with the oil) , free gas (moving freely) and dead oil. They also modify the standard gas solubility obtained from PVT data, in order to replace the bubble point pressure by a lower nucleation threshold. The model needs matching with field data to tune the constants in the transfer relations between the components.

Kraus et al (1993) treat supersaturation through the assumption of a pseudo bubble point. In other words, they assume that the onset of creation of bubbles is not the bubble point pressure, but a slightly lower pressure that is called pseudo bubble point pressure. In order to achieve this, the data fit for the PVT data is adapted to fit the pseudo bubble point. Nucleation and diffusion modelling in thus not taken onto account.

A recent work on critical gas saturation and supersaturation is presented by Kamath & Boyer (1995). They separate the supersaturation in two components. The first is a capillary supersaturation: a static contribution which occurs because the oil phase has to be saturated with gas at the gas phase pressure and not at liquid phase pressure; The liquid phase pressure is lower than the gas phase pressure by the capillary pressure. The second supersaturation component is a dynamic component that reflects gas concentration gradients induced by finite pressure drawdowns. Kamath & Boyer performed drawdown experiments in cores, measuring gas saturation and supersaturation. By doing a shut-in experiment (keeping the core shut during several days and monitoring the pressure), they obtained the dynamic supersaturation, which equals the pressure rise during the shut-in experiment. They find that this supersaturation is approximately 6 psi, which is much lower than the total observed supersaturation. Therefore, they conclude that the dynamic supersaturation is small compared to the capillary supersaturation. Since the capillary supersaturation does not depend on the rate of pressure drawdown, they conclude that the critical gas saturation cannot be a strong function of the rate of pressure drawdown.

Claridge & Prats (1995) propose a model for the prediction of flow of foamy oil, which is based on the hypothesis of bubble coalescence and growth inhibition by asphaltene films on the bubble surfaces. They do however not address the topic of supersaturation.

Using the concept of supersaturation, Geilikman et al (1995) define a kinetic (or pseudo) bubble point, as the pressure at which the time derivative of the supersaturation becomes zero. This is the point at which the supersaturation starts to decrease, which is generally not equal to the pressure at which the first bubble is created. The kinetic supersaturation decreases with

an increasing ratio of diffusion coefficient of dissolved gas and viscosity of the liquid phase.
Using visual experiments of solution gas drive in a glass micromodel, Bora et al (1997) come to the following conclusions: (i) asphaltene constituents do not appear to play a significant role in nucleation and stabilisation of gas bubbles; (ii) heavy oil production is not accompanied by a large population of microbubbles; (iii) viscous coupling effects, sand production and wormhole effects might be important in heavy oil reservoirs. They also observe that the supersaturation at which the first bubble nucleates is system depend and varies between repeated tests in a same system. Higher supersaturations were required for the more viscous crude oils. Bubble nucleation happens at different locations and bubbles grow until they cover several pores. The supersaturation values necessary to initiate bubble nucleation were high for the deasphalted oils (up to 200 psi) and still higher for raw crude oils (up to 400 psi). Bubble nucleation happened on pore walls and impurities and sometimes on trapped water. Some nucleation sites only produced one single bubble while other were active during a longer time.

2.3 Field observations

In order to complete the preceding bibliography, we present some information on what has been reported from field data on foamy oil flow. Loughead & Saltuklaroglu (1992) report flow rates that exceed those predicted by Darcy's law (pseudo steady state radial flow) by a factor 10. Produced flow rates are reported to increase over a few years. Pressure transient tests were hard to interpret because of the complex flow regimes). This interpreting was done as showing evidence of channels. A material balance indicates high average gas saturation in the reservoir (i.e. a high critical gas saturation). Sand production generates cavities or channels, using earth stress and soil mechanics ideas consistent with easy failure.
Metwally & Solanki's (1995) present a similar work which is though less interesting than that from Loughead & Saltuklaroglu.

Maini (1996) presents a quite useful literature review, which however is somewhat short on primary data. He concludes that foamy crudes show higher primary recovery, low produced GOR and increasing recovery with drawdown pressure.
Smith (1988) also presents flow rates which are higher than predicted by Darcy's law and discusses "wormholing".

Mirabal & Gordillo (1996) present the results of an integrated study for the development of the MFB-53 reservoir, in Hamaca, Orinoco Belt in Venezuela, which includes experimental evaluation of the pseudoproperties of the crude as well as numerical simulation results. The mathematical model used by the authors includes in some degree the non-conventional characterisation obtained from the laboratory studies.

2.4 Observations by topic

In the following, some observations are recalled, sorted by topic.

Supersaturation and bubble creation

The bubble size seems to be smaller (Islam, 1990) and the rate of produced bubbles higher (Kennedy & Olson, 1952, Hunt & Berry, 1956, Moulu, 1989) if the supersaturation is higher. Since both nucleation and diffusion of dissolved gas are driven by supersaturation, this might indicate that when the supersaturation exceeds some limit value, the nucleation rate increases stronger than the diffusion. Then bubbles are created more easily (higher bubbles creation rate), but have less time to grow (smaller sizes) because the thermodynamic equilibrium is restored by nucleation and not by diffusional growth.

In case of pressure drawdown, the maximum supersaturation should be reached somewhere after the creation of the first few bubbles (Aldea, 1970).

Supersaturation and pressure drawdown

At a higher pressure draw-down, a higher supersaturation is reached (Wall & Khurana, 1971, Moulu, 1989, Firoozabadi & Kashchiev, 1993). This seems plausible in view of the preceding remarks and in view of the description of Aldea (1970). If the pressure drawdown is higher, then the rate of decrease of saturation pressure is lower than the rate of decrease of actual pressure. This goes on until the supersaturation becomes so high that nucleation becomes "explosive" and many bubbles are created.

Supersaturation related to oil density, viscosity and dissolved-gas diffusion constants

Although few observations have reported on this point, it seems that there is a definite connection between supersaturation and the viscosity and the density

of the oil (Pooladi-Darvish & Firoozabadi, 1997, Geilikman, 1995). Heavy and more viscous oils seem to lead to higher supersaturations. It is quite probable that these links also exist through a possible dependence of the diffusion coefficient of dissolved gas on the density and the viscosity of the liquid. Some of the explanations of why oil is foamy might be found in this point. Dissolved gas in heavy and viscous oils might have a small diffusion coefficient. Higher supersaturations are then reached and consequently, smaller bubbles will be created, which coalesce with more difficulty.

Supersaturation and critical gas saturation

There seems to be some evidence that higher supersaturations lead to higher critical gas saturations (Moulu, 1989, Firoozabadi & Kashchiev, 1993). Since a higher critical gas saturation means a higher primary recovery, high supersaturation might be an advantage from a production point-of-view. If higher pressure draw down leads to higher supersaturations, then reservoirs should be produced at high pressure drawdown.

Although this is highly hypothetical, we might imagine the following explanation: high pressure draw downs lead to high supersaturations, which in its turn lead to more bubbles and smaller bubbles; If we suppose that smaller bubbles have less chance to collide or to coalesce, then the formation of a connected gas phase would be delayed and the critical gas saturation would be higher.

Supersaturation and pore structure

Smaller pore sizes seem to lead to lower supersaturations (Firoozabadi et al, 1992). This can possibly be explained by the observation that the nucleation in a porous medium is mostly heterogeneous nucleation. The rate of bubble formation is then proportional to the number of nucleation sites, which is proportional to the total superficial area. The latter is higher (at equal pore volume) when the pores are smaller. There might be an important point in this when micromodels are used. In order to compare a real situation to a micromodel, both the porosity and the permeability should be equal. If for example the pores are larger in a micromodel than in a real formation, the processes of nucleation and growth will be different.

According to Saidi (1994), it is not the mean pore size that is important, but rather the width of the pore size distribution. Although his analysis is not completely convincing, he might have a point in stating that the form of the pore size probability distribution function is important.

Critical supersaturation

The assumption of a critical supersaturation or a pseudo bubble point (Kennedy & Olson, 1952, Wood, 1953, Kraus 1993, Bora et al., 1997) is widely accepted. Many variations are however found between different experiments and within the same experimental installation repeating similar experiments. This might be explained as follows. Bubble nucleation is a probability process that can *statistically* be described by a probability density, which depends on the supersaturation. For small supersaturations, the probability of bubble nucleation is low, but not zero. So at any finite supersaturation, a bubble might be nucleated.

It is also very difficult to eliminate impurities and to work with pure systems. Few small impurities can have a large influence of the behaviour of the system. An analogy can be drawn to the boiling of water. In pure systems, water can be heated to very high temperatures (superheats) before it starts to boil. In practice everyone knows that water at atmospheric pressure starts to boil at 100°C, because normally enough impurities are present at the walls of the container it is stored in, to start the nucleation process.

3 General conclusion and perspectives

A comprehensive literature review has been carried out. The main function of this literature research is to indicate what research has been carried out related to supersaturation, nucleation and diffusion. Due to the large quantity of publications (72) it was however not possible to discuss every single one of them in detail, nor to study the validity of all presented observations. A striking observation is that the knowledge about foamy oil is few and that the observations concerning the possible mechanisms for foamy oil behaviour are often contradicting.

The main conclusion of the literature review is the absence of experimentally validated statements like "foamy oils show more supersaturation than non-foamy oils" or "supersaturation is the key to the explanation of foamy oil behaviour". It seems though that supersaturation is related to critical gas saturation. And high critical saturations seem to be characteristic for foamy oils. There exist thus some vague ideas about connection between supersaturation and foamy oils.

It is however clear that the transfer of dissolved gas to free gas in the form of bubbles is initiated by the existence of supersaturation and tends to annihilate supersaturation. Supersaturation is therefore a necessary condition

for the creation of bubbles. It is however stressed that supersaturation is a dynamic state of the system, expressed by a composite variable as

$$s = p - p_{sat} = p - \frac{\xi}{K}$$

and not some parameter which indicates whether a crude oil is foamy or not.

Some other ideas are that dissolved gas molecules in viscous oils have low diffusion constants and thus diffuse very slowly to bubbles or connected gas surfaces. Very viscous (possibly foamy) oils might thus more easily be supersaturated than low viscosity oils. The existence of high supersaturation might also induce the creation of smaller bubbles, which might be related to the existence of high critical gas saturations since possibly small bubbles coalescence with more difficulty than large bubbles.

References

1. Abgrall E., Iffly R., 1973, "Etude physique des écoulements par expansion des gaz dissous", *Revue de l'IFP*, (Sept.-Oct.), **18**(5):667-692.
2. Acevedo S., 1997, "Estabilizacion de espumas de gas natural presentes en crudos de la faja petrolífera del Orinoco", *Informe final for Intevep EPYC*, Agosto 1997.
3. Aldea Gh., 1970, "Le mécanisme de récupération des huiles lourdes par expansion des gaz dissous", *Revue de l'IFP*, Dec., **25**(12):1403-1416.
4. Bankoff S.G., 1964, "", *Appl. Sci. Res.*, **12**:267
5. Blander M., Katz J.L., 1975, "Bubble nucleation in liquids", AIChE J., **21**:833-848.
6. Blander M., 1979, "Bubble nucleation in liquids", *Adv. Colloid & Interface Sci.*, **10**:1-32.
7. Bora R., Maini B.B., Chakma A., 1997, "Flow visualization studies of solution gas drive process in heavy oil reservoirs using a glass micromodel", *SPE Int. Thermal Operations and Heavy Oil Symposium* (Bakersfield, California, USA), 10-12 Feb., SPE 37519, pp 57-65.
8. Callaghan I.C. & Gould M., 1986, "Method for determining the stability of foam", *United States Patent*, **4.577.491**, 4pp.
9. Chatenever A., Indira M.K., Kyte J.R., 1959, "Microscopic observations of solution gas drive behaviour", *J.P.T.*, June:13-15.
10. Claridge E.L., Prats M., 1995, "A proposed model and mechanism for anomalous foamy heavy oil behaviour", Intern. Heavy Oil Symp., (Calgary, Canada), June 19-21, SPE 29243, pp. 9-20.

11. Deligiannis P., Cleaver J.W., 1993, "Influence of surrounding bubbles on the rate of nucleation", *Int. J. Heat & Mass Transfer*, **36**(15):3697-3701.
12. Dumoré J.M., 1970, "Development of gas saturations during solution gas-drive in an oil layer below a gas cap", SPE J. (Trans. AIME), **249** (Sept.):211-218.
13. Eberhart J.G., Kremsner W., Blander M., 1975, "Metastability limits of superheated liquids: bubble nucleation temperatures and their mixtures", *J. Colloid & Interface Sci.*, **50**(2):369-378.
14. Firoozabadi A., Ottesen B., Mikkelsen M., 1992, "Measurements of supersaturation and critical gas saturation", *SPE Formation Evaluation*, 7:337-344.
15. Firoozabadi A., Mikkelsen M., Ottesen B., 1994, "Reply to Discussion of Measurements of supersaturation and critical gas saturation", *SPE Formation Evaluation*, June, pp. 159-160.
16. Firoozabadi A., Anderson A., 1994, "Visualisation measurements of gas evolution and flow of heavy and light oil in porous media", SPE 28930, 1994 SPE Ann. Tech. Conf. & Exhibition (New-Orleans, LA).
17. Firoozabadi A., Kashchiev D., 1993, "Pressure and volume evolution during gas phase formation in solution gas drive processes", *SPE unsolicited paper*, SPE 26286, 36 pp.
18. Forest T.W., Ward C.A., 1978, "Homogeneous nucleation of bubbles in solutions at pressures above the vapour pressure of the liquid", *J. Chem. Phys.*, **69**(5):2221-2230.
19. Forster H.K., Zuber N., 1954, "", *J. Appl. Phys.*, **25**:474
20. Geilikman M.B., Dusseault M.B., Dullien F.A.L., 1995, "Dynamic effects of foamy fluid flow in sand production instability", Intern. Heavy Oil Symp., (Calgary, Canada), June 19-21, SPE 30251, pp. 113-124.
21. Hammond P.C., 1997, "A multiphase model for the flow of foamimg heavy crude oil in a porous medium with illustratice calculations", October 9, Intevep S.A., Venezuela.
22. Handy L.L., 1958, "A laboratory study of oil recovery by solution gas drive", *Petroleum Trans. AIME*, **213**:310-315.
23. Huerta M., Otero C., Rico A., Jiménez I.,de Mirabal M.& Rojas G., 1996, "Understanding foamy oil mechanisms for heavy oil reservoirs during primary production", SPE 36749, Annual meeting.
24. Hunt E.B., Berry V.J. Jr., 1956, "Evolution of gas from liquids flowing through porous media", AIChE J., Dec., pp. 560-567.
25. Islam M.R., 1990, "Mechanics of bubble flow in heavy oil reservoirs", 60th Californian Regional Meeting (Ventura, California, USA), April 4-6, SPE 20070, pp. 495-502.

26. Kamath J., Boyer R.E., 1995, "Critical gas saturation and supersaturation in low-permeability rocks", *SPE Formation Evaluation*, Dec., pp. 247-253.
27. Kashchiev D., Firoozabadi A., 1993, "Kinetics of the initial stage of isothermal gas phase formation", *J. Chem. Phys.*, 98(6):4690-4699.
28. Kennedy H.T., Olson C.R., 1952, "Bubble formation in supersaturated hydrocarbon mixtures", *Petroleum Trans. AIME*, **195**:271-278.
29. Kraus W.P., McCaffrey W.J., Boyd G.W., 1993, "Pseudo-bubble point model for foamy oils", *CIM 1993 Ann. Tech. Conf.*, Calgary, May 9-12.
30. Li X., Yortsos Y.C., 1995, "Visualization and simulation of bubble growth in pore networks", *AIChE J.*, **41**(2):214-222.
31. Li X., Yortsos Y.C., 1995, "Theory of multiple bubble growth in porous media by solute diffusion", *Chem. Engng. Sci.*, **50**(5):1247-1271.
32. Loughead D.J. & Saltuklaroglu M., 1992, "Lloydminster heavy oil production, why so unusual ?", paper 9, Proc. of the 9th Ann. Heavy Oil & Oil Sand Technology Symp. (Calgary).
33. Lubetkin S., Blackwell M., 1988, "The nucleation of bubbles in supersaturated solutions", *J. Colloid & Interface Sci.*, **26**(2):610-615.
34. Lubetkin S.D., 1994, "Bubble nucleation and growth", in: "*Controlled particle, droplet and bubble formation*", Colloid and Surface Engineering Series, ed. Wedlock D., Butterworth-Heinemann, Oxford.
35. Madaoui K., 1975, "*Conditions de mobilité de la phase gazeuse lors de la décompression d'un mélange d'hydrocarbures en milieux poreux*", PhD dissertation, Toulouse U., France.
36. Maini B.B., Sarma H.K., 1994, 'Role of non-polar foams in production of heavy oils' in Foams: Fundamentals and applications in the petroleum industry, *Adv. in Chem. Series*, **242**:405-420.
37. Maini B.B., Sarma H.K., George A.E., 1993, "Significance of foamy-oil behaviour in primary production of heavy oils", *J. Canad. Petrol. Technology*, **32**(9):50-54.
38. Maini B.B., 1996, "Foamy oil flow in heavy oil production", JCPT, **35**(6):21,22.24.
39. Metwally M., Solanki S., 1995, "Heavy oil reservoir mechanisms, Lindbergh and Frog Lake fields, Alberta, Part 1, Field observations and Reservoir simulation" , *CIM 46th Ann. Meeting* (Banff, Alberta), Paper 95-63.
40. Meza B., Kamp A.M., Huerta M., 1997, "Estudio de la estabilidad de espumas oleicas y su relación con la supersaturación", Internal report PDVSA Intevep, INT-4273.

41. Mirabal M, Gordillo, Fuenmayor M, Rojas G, Rodriguez H and R. Sanchez., 1996, "Integrated Study for the Characterization and Development of the MFB-53 Reservoir, North Hamaca-Orinoco Belt, Venezuela", *IV LAPEC* (Trinidad and Tobago).
42. Moulu J.C., Longeron D.L., 1989, "Solution gas-drive: experiments and simulations", *Proc. 5th European Symposium on IOR*, Budapest.
43. Moulu J.C., "Solution gas drive: experiments and simulations", *J. Petrol. Sci. & Engng.*, **2**:379-386.
44. Nishioka G., Ross S., 1981, "A new method and apparatus for measuring foam stability", *J. Colloid & Interface Sci.*, **81**(1):1-7.
45. Plesset M.S., Zwick S.A., 1954, "The growth of vapour bubbles in superheated liquids", *J. Appl. Phys.*, **24**:493
46. Pooladi-Darvish M., Firoozabadi A., 1997, "Solution gas drive in heavy oil reservoirs", *48th Ann. Tech. Meeting of the Petrol. Soc. of CIM* (Calgary, Alberta), June 11, Paper 97-113, 13 pp.
47. Rayleigh, 1917, "On the pressure developed in a liquid during the collapse of a spherical cavity", *Phil. Mag.*, **34**:94
48. Rosner D., Epstein M., 1972, "", *Chem. Engng. Sci.*, **27**:69.
49. Saidi A.M., 1994, "Discussion of measurements of supersaturation and critical gas saturation", *SPE Formation Evaluation*, June, pp. 157-158.
50. Satik C., Li X., Yortsos Y.C., 1995, "Scaling of single-bubble growth in a porous medium", *Phys. Rev.* E, 51(4):3286-3295.
51. Scriven L.E., 1959, "On the dynamics of phase growth", *Chem. Engng. Sci.*, **10**(1,2):1-13
52. Sheng J.J., Maini B.B., Hayes R.E., Tortike W.W., 1995*a*, "A non-equilibrium model to calculate foamy oil properties", *46th Ann. Tech. Meeting of the Petrol. Soc. of CIM* (Banff, Alberta, Canada), May 14-17, 12 pp.
53. Sheng J.J., Hayes R.E., Maini B.B., Tortike W.W., 1995*b*, "A proposed dynamic model for foamy oil properties", Int. Heavy Oil Symposium, SPE 30253, pp. 125-138.
54. Sheng J.J., Hayes R.E., Maini B.B., Tortike W.W., 1996 "A dynamic model to simulate foamy oil flow in porous media", *SPE Ann. Tech. Conf. & Exh.* (Denver, Colorado, USA), 6-9 Oct., SPE 36750, pp. 187-699.
55. Skripov V.P., 1974, "*Metastable liquids*", Wiley, NY.
56. Smith G.E., 1988, "Fluid flow and sand production in heavy oil reservoirs under solution gas drive", SPE Prod. & Eng. May, pp. 169-177.

57. Stewart C.R., Craig F.F., Morse R.A., 1953, "Determination of limestone performance characteristics by model flow tests", *Petroleum Trans. AIME*, **198**:93-102.
58. Stewart C.R., Hunt E.B. Jr., Schneider F.N., Geffen T.M., Berry V.J., 1954, "The role of bubble formation in oil recovery in oil recovery by solution gas drives in limestones", *Petroleum Trans. AIME*, **201**:294-301
59. Svrcek W.Y., Mehrotra A.K., 1982, "Gas solubility, viscosity and density measurements for Athabasca bitumen", *J. Can. Pet. Tech.*, July-August: 31-38.
60. Svrcek W.Y., Mehrotra A.K., 1989, "Properties of Peace River bitumen saturated with field gas mixtures", *J. Can. Pet. Tech.*, **28**(2): 50-56.
61. Szekely J., Martins G.P., 1971, "Non equilibrium effects in the growth of spherical gas bubbles dues to solute diffusion", *Chem. Eng. Sci.*, **26**:147-159.
62. Szekely J., Fang S.D., 1973, "Non-equilibrium effects in the growth of spherical gas bubbles due to solid diffusion - II", *Chem. Engng. Sci.*, **28**:2127-2140.
63. Theofanous T., Biasi L., Isbin H.S., Fauske H., 1969, "A theoretical study on bubble growth in constant and time-dependent pressure fields", *Chem. Eng. Sci.*, **24**:885-897.
64. Toramaru A., 1995, "Numerical study of nucleation and growth of bubbles in viscous magmas", *J. Geophys. Res.*, 100(B2):1913-1931.
65. Toramaru A., 1989, "Vesculation process and bubble size distributions in ascending magmas with constant velocities", *J. Geophys. Res.*, 94(B12):17523-17542.
66. Wall C.G., Khurana A.K., 1971, "Saturation: permeability relationships at low gas saturations", *J. Inst. Pet.*, **57** (Sept.):261-269.
67. Wall C.G., Khurana A.K., 1972, "The effects of rate pressure decline and liquid viscosity on low-pressure gas saturations in porous medium", *J. Inst. Pet.*, **58** (Nov.):335-345.
68. Ward C.A., Balakrishnan A., Hooper F.C., 1970, "On the thermodynamics of nucleation in gas-liquid solutions", *J. Basic Engng. (Trans. ASME)*, 92:695-704.
69. Ward C.A., Tikuisis P., Venter R.D., 1982, "", *J. Appl. Phys.*, **53**:6076.
70. Wieland D.R., Kennedy H.T., 1957, "Measurement of bubble frequency in cores", *Petrol. Trans. AIME*, **210**:122-125.
71. Wilt P.M., 1986, "Nucleation rates and bubble stability in water-carbon dioxide solutions", *J. Colloid Interface Sci.*, **112**(2):530-538.

72. Wood J.W. Jr., 1953, "*Bubble formation in Rangely field, Colorado*", MSc thesis, Texas A&M Univ., College station.
73. Yortsos Y.C., Parlar M., 1989, "Phase change in binary systems in porous media. Application to solution gas drive", 64th Ann. tech. Conf. & Exh. of the SPE (San Antonio, TX, USA), Oct. 8-11, SPE 19697, pp. 693-708.

Task 73

Part II

Foamy Oil Flow in Porous Media

D.D. JOSEPH[1], A.M. KAMP[2], R. BAI[1], M. HUERTA[2]

[1]Univ. of Minnesota, Dept. of Aerospace Engng. & Mech, 107 Akerman Hall
110 Union Street. S.E., Minneapolis, MN 55455, USA
[2] PDVSA Intevep, PO Box 76343, Caracas 1070-A, Venezuela

September 1999

Abstract

Certain heavy oils which foam under severe depressurization give rise to increased production and an increased rate of production under solution gas drive. The phenomenon seems to be related to the chemistry of these oils which not only stabilize foam but also stabilize dispersion of gas bubbles at lower volume ratios. We present here a mathematical model of this phenomenon which depends only on the velocity through D'Arcy's law, the pressure and the dispersed gas fraction. The theory governs only in situations in which the bubbles do not coalesce to produce the percolation of free gas. In this theory the bubbles move with the oil as they evolve. The main empirical content of the theory enters through the derivation of solubility isotherms which can be obtained from PVT data; modeling of nucleation, coalescence, bubble drag laws and transfer functions are avoided. The resulting theory is hyperbolic and nonlinear. The nonlinear equations for steady flow through a sandpack are solved by quadrature and give rise to good agreements between theory and the experiments of Maini & Sarma [1994] without fitting constants.

1 Introduction

In this paper a model is presented that is motivated by the need to explain anomalous features associated with production from reservoirs of so-called foamy oils. These oils are described by some of their properties of response to pressure declines; it is noted that they nucleate dispersed gas bubbles and display obvious foaminess in well head samples produced by solution gas drive in which oil and gas are produced by the drawdown of pressure (Huerta *et al.* [1996], Mirabal *et al.* [1996]).

When compared with the response of conventional oils, the response of foamy oils to drawdown of pressure is more favorable; primary recovery factor (percentage of the oil in the reservoir which can be recovered), the rate of production, the volume ratio of oil to gas which is recovered and the length of time that a given

pressure gradient or rate of production can be maintained are all increased substantially; the reasons for the favorable response of foamy oils in solution gas drive are not well understood and tentative explanations which have been put forward are controversial (see Maini [1996], Pooladi-Darvish and Firoozabadi [1997] and Sheng *et al.* [1999a] for recent reviews).

Foamy oils carry considerable amounts of dissolved gases in the condensed state. The relevant thermodynamic property for this is "gas solubility"; a function of temperature and pressure at equilibrium which gives the volume ratio of dispersed gas from the crude oil by outgassing. Tables of solubility of methane, carbon dioxide and other gases in various Canadian crude oils have been given by Svrcek & Mehrotra [1982], Peng *et al.* [1991] and others. The oils considered to be foamy evidently cavitate small dispersed bubbles which, under some conditions, are believed to move with the crude oil in which they are dispersed. Experiments done by Pooladi-Darvish & Firoozabadi [1997] have shown that bubbles which arise from depressurization of silicone oil and heavy crude of equivalent viscosity are very different; the bubbles in the silicone oil are larger and much more mobile than the ones in crude oil. Viscosity alone is not enough to demobilize dispersed gas; it is necessary to look at other properties like surface tension and surface active agents. Possibly there are surface active agents which are present naturally in foamy crudes which allow them to foam, but the precise agents, their composition and the mechanics by which they are released apparently have not been studied.

A "foamy oil" is a heavy oil which foams under rapid depressurization. Maini [1996] notes that "... The term "foamy oil" is often used to describe certain oils produced by solution gas drive which display obvious foaminess in wellhead samples. The primary production of heavy oil from several reservoirs in western Canada is in the form of an oil continuous foam. This foam resembles a chocolate mousse in appearance and often persists in open vessels for several hours ..." Foaming at a well head is a kind of foam formation analogous to the head on beer. To get such a head the pressure decline must be sufficiently severe to allow the bubbles which rise from outgassing of condensed gas in the bulk to accumulate at the free surface faster than they collapse. Perhaps there are surfactants in foamy oil which stabilize the films between the bubbles preventing collapse, promoting the buildup of the head. Foam stability measurements in the laboratory have shown that the foaminess of crude heavy oils is comparable to aqueous foams used for steam flooding applications (Sheng *et al.* [1996]). The outgassing of condensed gas will not lead to foam at the well head if the rate of depressurization is too low.

To create foam in a reservoir or in a sandpack it is necessary to depressurize rapidly enough to produce close packed solution gas bubbles which can undergo a topological phase change to stable films and plateau borders. This kind of "in situ" foaming of sandpacks has been achieved in the experiments of Maini and

Sarma [1994]. Gas and liquid move in lock step in these foams and lead to very high primary recovery factors. At the actual reservoir, gas fractions can be as low as 5 to 10% in oils which cannot foam but are well-dispersed and protected against coalescence, possibly by the same natural surfactants that might stabilize the foams.

In solution gas drive of foamy oil the depressurization of the sample leads to cavitation of small dispersed bubbles. The volume ratio of dispersed gas increases the volume of our composite fluid and it acts as a pump, gas coming out of solution pumps the fluid outward. This pumping action is well described by the continuity equation (4.4) which implies that in a closed volume v with boundary ∂v containing dispersed bubbles of volume fraction ϕ

$$\int_v \frac{1}{1-\phi}\frac{d\phi}{dt}dv = \oint_{\partial v} \mathbf{u}.\mathbf{n} \tag{1.1}$$

where $\mathbf{n}$ is the outward normal on ∂v and $\mathbf{u}$ is the velocity of our composite fluid.

The relative velocity of dispersed gas is important; if the bubbles coalesce and move relative to the oil more gas and less oil will be produced. Good recovery is sometimes described by a critical gas saturation value; this is the volume fraction of gas at which the gas becomes connected and starts to move. Maini [1996] identifies this critical saturation as a percolation limit, whilst Firoozabadi, Ottensen and Mikkelsen [1992] and Pooladi-Darvish and Firoozabadi [1997] identify this even by visual observation of bubbles in a viewing window. The values given by Firoozabadi *et al.* are about 5 times smaller than those given by Maini and his coworkers.

When the gas percolates, the good news about recovery is over; it is no wonder that all authors find that the critical saturation values are about the same as the primary recovery factors (which is the fraction of oil recovered by solution gas to oil in the reservoir) even when they disagree about definitions.

A few models of foamy oil flow have been put forward; each emphasize some special feature. One of the most recent models by Sheng *et al.* [1996], Sheng *et al.* [1999a] is a multiphase theory based on conservation laws with transfer from solution gas to evolved gas and from evolved gas to dispersed gas and free gas. Their theory does not seem to follow the curve of experimental values. They say that "... Published models include the psuedo-bubble point model (Kraus *et al.* [1993]), the modified fractional flow model (Lebel [1994]) and the reduced oil viscosity model (Claridge & Prats [1995]). Maini [1996] gave a detailed review and discussion of some of these models. These models have been used to history match heavy oil production, but their common weakness is that the dynamic processes which are

important features of foamy oil flow were not included properly. Although it may be possible to get an acceptable history match using these models, the predictive ability is likely to be limited..."

A more successful approach to modeling was recently advanced by Sheng *et al.* [1999b]. This model also requires the modeling of nucleation, bubble growth and disengagement of gas bubbles from the oil. The model ultimately leaves undetermined two adjustable parameters which fit the theory to experimental data better than previous models.

The present theory could be called a continuum mixture theory which is appropriate for foamy oil flow with dispersed gas of low mobility relative to the liquid and leads to three coupled nonlinear partial differential equations for $\mathbf{u}$, p and the gas fraction ϕ, five scalar equations in five unknowns. Our model has a few features in common with the excellent early work of Leibenson [1941] on the motion of gas saturated fluid in a porous media.

The model proposed here does not require information about nucleation, bubble growth, compressibility or forces which produce relative velocity. We put up a one-phase or mixture theory in which the dispersed gas is described by a gas fraction field in a single fluid in which the viscosity, density and mobility in D'Arcy's law all depend on the gas fraction. This fluid satisfies the usual D'Arcy law, and the continuity equation together with a kinetic (constitutive) equation required by the condensation and outgassing of methane (or other gases) in heavy crude. The theory depends only on parameters which can be measured in a PVT cell and sandpack. The virtue of the model is simplicity, but it can work only for relatively immobile dispersed gas bubbles in which divergence-free velocities are excluded (see the discussion following (4.4)). Certainly such a theory could not be expected to give rise to a percolation threshold or even to a critical gas fraction. We shall show that it can describe many features of solution gas drive of foamy oils in the regimes when the bubbles in the mixture are dispersed and even when they are trapped in foam.

It is our idea that the increased recovery and production are generated by the pumping of nucleating and growing gas bubbles embodied in (1.1). However recovery factors and production rates are not the same and we might test some ideas: if two foamy oils have the same viscosity, the one with higher solubility will have higher primary recovery and production rate; if two foamy oils have the same solubility, the one with lower viscosity will have a higher rate of production but a lower primary recovery. If the oil foams in situ, oil and gas move in lock step and the primary recovery factor increases while due to the increased viscosity of foam the rate of production decreases.

2 Solubility Isotherms

In the experiments of Svrcek & Mehrotra [1982] the pressure is dropped from p and T to p_{ref} and T_{ref} where in the experiments p_{ref} is atmospheric and $T_{\text{ref}} = 373.2°\text{K}$. It is assumed that all the gas in the live oil at p, T comes out. Defining now:

$V_g(p,T)$ is the volume of dispersed gas,
$V_l(p,T)$ is the volume of live oil,
$V^*(p,T)$ is the volume of dispersed gas which vaporizes from the condensed gas when p, T are dropped to $p_{\text{ref}}, T_{\text{ref}}$.

In this model we avoid all constitutive equations regarding nucleation rates and bubble growth. In our model we have only a mixture of liquid and dispersed gas, and the dispersed gas enters only through the volume fraction

$$\phi = \frac{V_g}{V_l + V_g}. \tag{2.1}$$

Equation (2.1) may be solved for

$$V_g = \frac{\phi V_l}{1-\phi}. \tag{2.2}$$

Svrcek and Mehrotra [1982] give volumetric solubility curves (CO_2 and methane in figure 2.1). In these figures

$$\hat{V} = V^*/V_l(p,T) \tag{2.3}$$

is the ratio between the volume of gas that can be evolved out of bitumen when the pressure is dropped to less than one atmosphere at a temperature of 100°C and the original volume of bitumen. We can assume that this tells you how much dispersed gas can come out of solution of condensed gas which is at a saturation value at any pressure and temperature. We are going to assume that this $\hat{V}$ determines the dispersed gas fraction ϕ following an argument put forward in what is to follow.

In the present approach we have no way to predict the size distribution of gas bubbles. This means that we are free to choose the size and distribution to measure $\hat{V}$ and the most convenient choice is when all the released gas is collected at the top of a PVT such as in the experiment of Svrcek & Mehrotra. Figure 2.2 describes such a depressurization experiment.

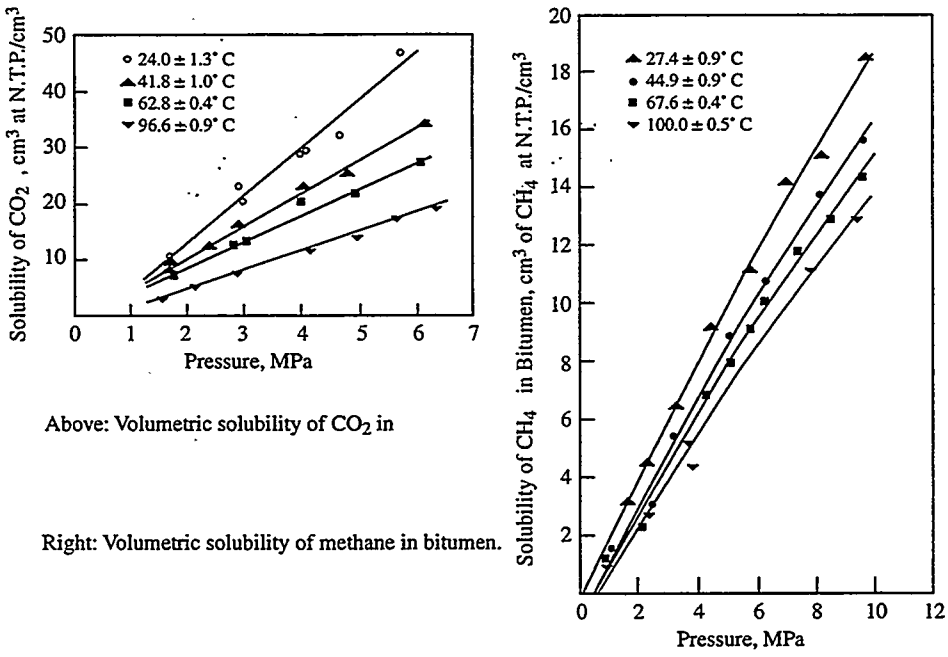

Above: Volumetric solubility of CO_2 in

Right: Volumetric solubility of methane in bitumen.

Figure 2.1: Solubility curves: $\hat{V}$ vs. p (Svrcek and Mehrotra [1982]).

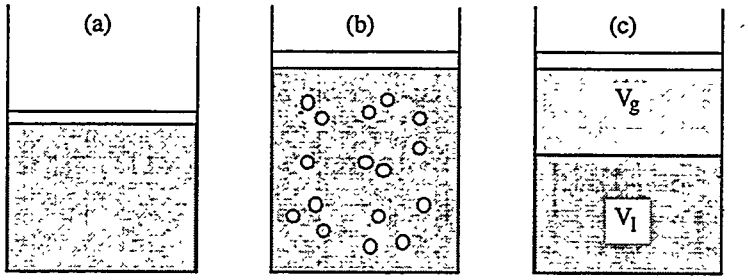

Figure 2.2: Depressurization experiment in PVT cell at constant temperature; the oil is indicated in dark gray, the gas in light gray. (a) Dissolved gas at pressure p and temperature T. (b) Just after the pressurization, pressure p_{ref} and temperature T_{ref}. (c) Finally all the gas percolates out and $\hat{V} = V^*/V_l$ can be measured.

Their data show that

$$p - p_{\text{ref}} = \hat{\gamma}(T)\hat{V} \tag{2.4}$$

where $\hat{\gamma} = dp/d\hat{V}$ is the slope of the solubility isotherms shown in figure 2.1. This slope is approximately constant. Here we have chosen p_{ref} as a small pressure at which a negligible amount of gas is dissolved in the oil. For practical purposes this could be standard (atmospheric) pressure.

2.1 Solubility Isotherms I

We first suppose that all the gas which comes out of solution is dispersed and does not percolate or foam. In the experiments in figure 2.1, we must suppose that the nucleation, growth and compressibility of gas bubbles are working, but these microstructural features are not monitored in these experiments which give only the solubility $\hat{V}$. This is also what we do in the mathematical model.

To convert (2.4) into a relation between p and ϕ at equilibrium we note that the total mass M of gas in the live oil is invariant, independent of p and T and

$$M = M_g(p,T) + M_c(p,T) \tag{2.5}$$

where

$M_g(p,T)$ is the mass of dispersed gas.
$M_c(p,T)$ is the mass of condensed gas.

Since the mass of condensed gas does not change when it is vaporized and assuming that this vapor is a perfect gas, we have

$$M_c = p_{\text{ref}} V^* / R T_{\text{ref}} \tag{2.6}$$

where R is the gas constant. From the same gas law

$$M_g = p V_g / R T. \tag{2.7}$$

Hence, from (2.5), (2.6) and (2.7) we have

$$M = \frac{p V_g}{RT} + \frac{p_{\text{ref}} V^*}{R T_{\text{ref}}} \tag{2.8}$$

and, using (2.3) and (2.4)

$$M = \frac{p V_g}{RT} + \frac{p_{\text{ref}}}{R T_{\text{ref}}} \left(\frac{p - p_{\text{ref}}}{\hat{\gamma}} \right) V_l. \tag{2.9}$$

We next introduce the bubble point pressure $\tilde{p}$ as the pressure at which there is no dispersed gas, all the gas is condensed in the live oil so that $V_g = 0; \tilde{V} \stackrel{\text{def}}{=} \hat{V}$ when $V_g = 0$ and from (2.4)

$$\tilde{p} - p_{\text{ref}} = \hat{\gamma}(T) \tilde{V} \tag{2.10}$$

where

$$\tilde{V}(\tilde{p}, T) = V^*(\tilde{p}, T) / V_l(\tilde{p}, T) \tag{2.11}$$

as in the cartoon of figure 2.3.

Since M is invariant, we may evaluate (2.8) at the bubble point

$$M = \frac{p_{\text{ref}}}{R T_{\text{ref}}} V_l(\tilde{p}, T) \tilde{V}(\tilde{p}, T). \tag{2.12}$$

Using (2.10) to eliminate $\tilde{V}$ in (2.12) and equating (2.12) and (2.9) we get

$$\frac{T_{\text{ref}}}{T} \frac{p}{p_{\text{ref}}} V_g + \left(\frac{p - p_{\text{ref}}}{\hat{\gamma}} \right) V_l(p, T) = \left(\frac{\tilde{p} - p_{\text{ref}}}{\hat{\gamma}} \right) V_l(\tilde{p}, T) \tag{2.13}$$

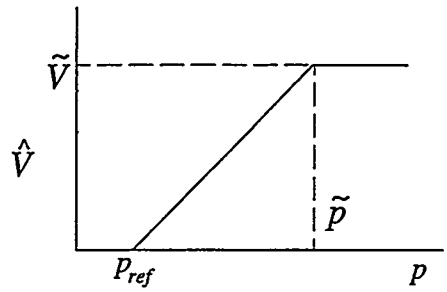

Figure 2.3: Solubility isotherm used in this model.

In most depressurization experiments the change of liquid volume due to outgassing and compressibility is small and $V_l(p,T) \approx V_l(\tilde{p},T)$. In this case the terms proportional to p_{ref} in (2.13) subtract out and after replacing V_g with $\phi V_l/(1-\phi)$ we get

$$\beta \frac{\phi}{1-\phi} = \frac{\tilde{p}-p}{p} \tag{2.14}$$

where

$$\beta = \frac{T_{\text{ref}}}{T}\frac{\hat{\gamma}}{p_{\text{ref}}} \tag{2.15}$$

is completely determined by the solubility isotherm in figure 2.1. Since the variation of T is small on an absolute scale, the values T/T_{ref} for the isotherms in figure 2.1 are just slightly larger than one.

The variable $\hat{V}$ is called *gas-oil ratio* and $\tilde{V}$ is the gas-oil ratio at saturation pressure. From (2.10):

$$\hat{\gamma}(T) = \frac{\tilde{p}-p_{\text{ref}}}{\tilde{V}}. \tag{2.16}$$

Substituting this value of $\hat{\gamma}$ in (2.15)

$$\beta = \frac{T_{\text{ref}}}{T}\frac{\tilde{p}-p_{\text{ref}}}{p_{\text{ref}}\tilde{V}}. \tag{2.17}$$

In most practical situations $\tilde{p} \gg p_{\text{ref}}$ so that from (2.17)

Oil	β
Lloydminster	3.40
Lindbergh	3.17
Cerro Negro	3.53

Table 2.1: Solubility coefficients for some heavy oils.

$$\beta = \frac{T_{\text{ref}}}{T} \frac{\tilde{p}}{p_{\text{ref}} \tilde{V}} \tag{2.18}$$

It is customary in the oil industry to characterize live oil by its saturation pressure $\tilde{p}$ and its gas-oil ratio $\tilde{V}$ at saturation pressure. By virtue of (2.18) one can calculate the solubility parameter β. Note that in most experiments p_{ref} is chosen as atmospheric pressure and T_{ref} as 60°F = 15.6°C.

Values for β for two Canadian heavy oils, Lloydminster and Lindbergh (Maini & Sarma, 1994) and for a Venezuelan heavy oil, Cerro Negro, are given in table 2.1. Graphs of the isotherm (2.14) for various values of β are shown in figure 2.5.

It can be noted that the solubility value for heavy crude oils from very different regions are very close, which indicated that they contain similar amounts of dissolved gases.

When ϕ and p satisfying (2.14) vary from point to point

$$\nabla p = \frac{-\beta p^2}{\tilde{p}(1-\phi)^2} \nabla \phi. \tag{2.19}$$

According to D'Arcy's law, $\mathbf{u} = -\lambda \nabla p$ where λ is the mobility of the foamy mixture in the porous media; hence the fluid flows up the bubble gradient toward regions in which there are more bubbles where the pressure is smaller.

Departures from the equilibrium solubility relation (2.14) are indicated as *supersaturation* or *subsaturation*. Defining the function

$$f(p, \phi) \stackrel{\text{def}}{=} \tilde{p} - p - \beta p \phi / (1 - \phi) \tag{2.20}$$

supersaturation ($f > 0$) corresponds to having more gas dissolved than there should be under thermodynamic equilibrium; subsaturation ($f < 0$) corresponds to having less gas dissolved than there should be under equilibrium. Supersaturation occurs when the pressure in the reservoir is drawn down, but the oil cannot evolve

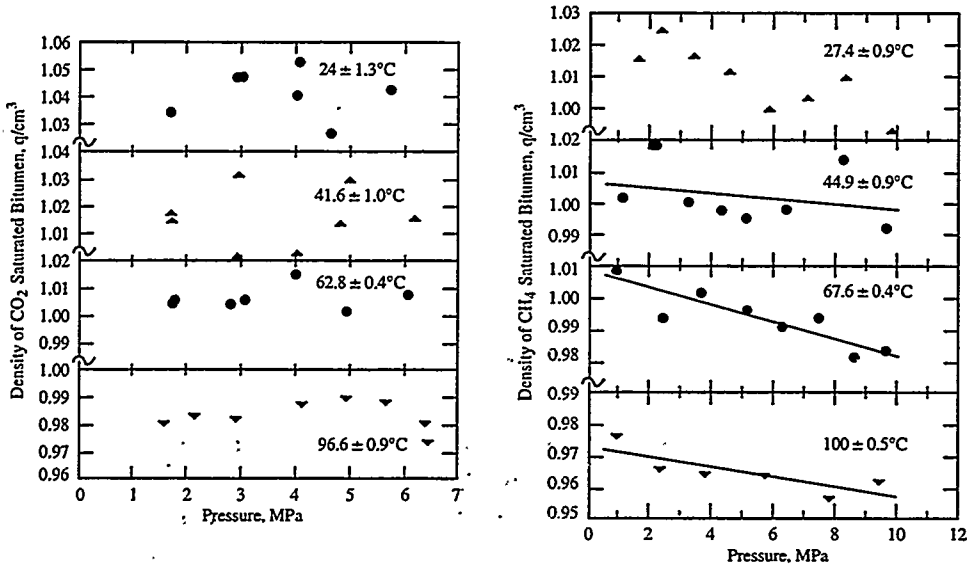

Figure 2.4: The density of bitumen and condensed gas mixtures. The density is nearly constant over very wide ranges of pressure. We can imagine that the mixture density is independent of pressure. Since gas solubility is a strong function of pressure; the density is also more or less independent of the fraction of dissolved gas at constant temperature (Svrcek & Mehrotra [1982]).

gas fast enough to keep up with the depressurization. Subsaturation, on the other hand, occurs when there is not enough gas available to dissolve in order to satisfy thermodynamic equilibrium at prevailing reservoir pressure and temperature. The function f in our theory is thus an indicator for departure from equilibrium solubility.

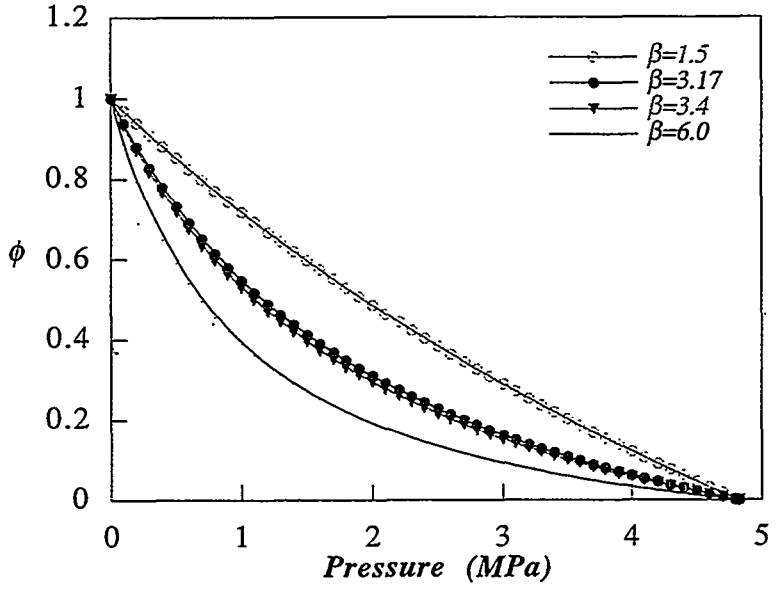

Figure 2.5: Graphs of the solubility isotherm (2.14) for various values of β. The limits of validity of the dispersed gas model can be roughly set at a close packing value, say $\phi_c = 0.68$. When $\phi > \phi_c$ some bubbles must touch and form foam film or to coalesce. This implies that results for drawdown greater than those for which $\phi = 0.68$ must take into account foaming and fingering of free gas.

2.2 Solubility Isotherms II

Consider a drawdown to atmospheric pressure $p_a = 10^6$dynes/cm^2 from a saturation pressure $\tilde{p} = 4.83 \times 10^7$dynes/cm^2 as in the experiment of Maini & Sarma [1994]. Using $\beta = 3.4$ for Lloyminster (from table 2.1) and evaluating the gas fraction of $\phi = \phi_a$ at atmospheric pressure we find

$$\phi_a = 0.93 \tag{2.21}$$

This is too much gas to exist as a bubbly dispersion; either the bubbly mixture passed into foam near to some outical value, say

$$\phi = \phi_c = 0.680 \tag{2.22}$$

or close packing or else some of the bubbles coalesced as free gas which fingers out of the sandpack. Probably foam and free gas both evolve at the outlet of a closed sandpack after a sudden drawdown to atmospheric from high saturation.

We may acknowledge the condition of close packing associated with change of phase to foam or free gas by rethinking and rewriting the derivation of (2.14) as

$$\beta \cdot \frac{\phi}{\phi_c - \phi} = \frac{(\tilde{p} - p_c) - (p - p_c)}{p - p_c} \tag{2.23}$$

where p_c is some pressure at which the gas fraction is ϕ_c. Equation (2.23) is in the same form as (2.14) with ϕ/ϕ_c replacing ϕ and $p - p_c$ replacing p.

We also note that the physics of supersaturation is complicated by the fact that bubbles cannot nucleate continuously and that the mechanism by which they nucleate is still not well understood. A bubble which might form in crude oil by the vaporization of dissolved gas at supersaturated conditions can be expected to satisfy Laplace's law

$$p_{vapor} - p = 2\gamma/R \tag{2.24}$$

where γ is surface tension (say 30 dynes/cm) and R is the bubble radius. Under mildly supersaturated conditions p is slightly smaller than the vapor pressure p_{vapor}; hence, R satisfying (2.24) cannot be very small.

It is argued that the vaporization of dissolved gas under supercritical conditions requires the simultaneous presence of undissolved gas hidden in crevices of impurities which are wet by gas preferentially. The curvature of the gas-oil interface in such a crevice is opposite to a bubble and it is controlled by capillarity rather than interfacial tension. The supersaturated dissolved gas vaporizes at the undissolved gas hidden in the crevice and the volume of the gas grows there until a bubble breaks away restoring the nucleation site to its original condition. The train of gas bubbles which emanate usually from a single site on a glass of beer as the gas comes out of the solution is a convenient example of outgassing at a nucleation site. The pore walls in a porous media are nucleation sites for outgassing of foamy oil. The possibility that asphaltenes in the oil are nucleation sites for dissolved gas is a current but unresoloved question.

In deriving (2.14), or (2.23), we have assumed the continuity of pressure across the bubble surface, ignoring the small pressure drop implied by (2.24).

In the sequel, we will base our analysis on the solubility isotherm I, given by (2.14), understanding that the theory is expected to lose validity when the drawdown is large enough to produce close packing. It is certain that we can achieve

better agreements with experiments by using β and ϕ_c as fitting parameters, but our purpose is better served by carrying the *ab initio* theory without any wiggle room through to conclusion.

3 Live oil and dead oil

Oil without dissolved gas is called dead oil. Oil saturated with dissolved gas is called live oil. The dissolved gas can be considered condensed and live oil is a mixture of miscible liquids, dead crude oil and condensed gas. The mixture of miscible liquids is like glycerin and water with the caveat that the oil and dissolved gas do not mix in all proportions; the fraction of dissolved gas at saturation is a function of temperature and pressure. The weight fraction of dissolved gases corresponding to figure 2.1 ranges from 0.3 to 6%. (See the tables in Svrcek & Mehrotra [1982]).

The viscosity of live oil can be orders of magnitude smaller than the viscosity of dead oil; the viscosity of live oil is a strongly decreasing function of the amount of dissolved gas in solution just as the viscosity of glycerol strongly decreases with the water fraction. In a pressure decline the viscosity of the live oil will increase because less gas is dissolved and because the presence of dispersed gas should increase the viscosity of the composite fluid.

We may seek to answer the question "what is the density of the dissolved gas in solution." We are not able to measure the density of the liquid gas in oil, but the density ρ of the mixture is available in data presented by Svrcek and Mehrotra and reproduced in figure 2.4. Let us note that this data shows that the density of the CO_2 in bitumen is a strong function of the pressure; hence figure 2.4 shows that the density of the not saturated bitumen is independent of the volume ratio Ψ of soluble gas in bitumen. Dissolved methane has a density only slightly different than bitumen (see figure 2.1). A theory of miscible mixtures which applies to live oil can be found in Chapter X of Joseph & Renardy [1992].

4 Model description

In this model we avoid all constitutive equations regarding nucleation rates and bubble growth. In our model we have only foamy oil and dispersed gas and the dispersed gas enters only through its volume ratio ϕ. The model combines D'Arcy's law, with a ϕ dependent mobility, a mass conservation law for ideal mixtures together with a constitutive equation governing the evolution of departures from equilibrium solubility. For out of equilibrium events gradients and time derivatives are crucial. The time derivatives which are used here have a material derivative

$$\frac{D}{Dt} = \alpha \frac{\partial}{\partial t} + \mathbf{u} \cdot \nabla \tag{4.1}$$

where α is the porosity. The continuity equation is given by

$$\frac{d\rho}{d\phi}\frac{D\phi}{Dt} + \rho(\phi)\text{div}\,\mathbf{u} = 0 \tag{4.2}$$

where

$$\rho(\phi) = \rho_g\phi + \rho_l(1-\phi) \approx \rho_l(1-\phi) \tag{4.3}$$

because $\rho_g \ll \rho_l$ where ρ_l is the density of live oil which depends only weakly on the volume ratio of dissolved gas. Combining (4.3) and (4.2) we find that

$$\frac{D\log(1-\phi)}{Dt} + \text{div}\,\mathbf{u} = 0 \tag{4.4}$$

Equation (4.4) restricts the theory to dispersions of low mobility relative to the suspending liquid. In any motion $\mathbf{u}(\mathbf{x}, t)$ of the composite which is divergence free $\text{div}\mathbf{u} = 0$, the dispersed gas fraction satisfies

$$\frac{D\phi}{Dt} = 0.$$

This implies that the volume ratio does not change on material particles of the composite fluid on divergence free motions.

Bubbles rising under gravity would lead to divergence free motions as would any motion of the bubbly mixture in which dispersed bubbles do not nucleate, diffuse or compress. Motions with non-zero divergence satisfy (1.1); the flux out of any closed volume, over which the div $\mathbf{u}$ does not sum to zero, must be non zero. This is the simplified way that our theory accounts for nucleation and diffusion.

Turning next to D'Arcy's law we let x increase in the direction of gravity. Then

$$\mathbf{u} = -\lambda\{\nabla p - \rho g \mathbf{e}_x\} \approx -\lambda\{\nabla p - \rho_l(1-\phi)\mathbf{e}_x\} \tag{4.5}$$

where

$$\lambda(\phi) = \kappa(\phi)/\mu(\phi) \tag{4.6}$$

is the mobility, $\mu(\phi)$ is the viscosity of live oil with dispersed gas of volume ratio ϕ and $\kappa(\phi)$ is the permeability.

4.1 Constitutive equations relating the dispersed gas fraction to the pressure

We are proposing models in which the basic variables are the pressure and dispersed gas fraction and are such that disturbed systems which are not forced will relax to equilibrium with pressure and temperature on the solubility isotherm $f(p,\phi) = 0$ given by (2.4). There are many possible ways to build models with the above properties. The simplest conceptual model with the desired properties is a first evolution model

$$\tau \frac{Df}{Dt} = -f \tag{4.7}$$

which guarantees that a disturbed stationary system will relax exponentially

$$f(p,\phi) = f(p,\phi_o) exp\left(-\frac{t}{\alpha\tau}\right)$$

Though (4.7) is conceptually simple, it is a mathematically difficult and strongly nonlinear problem when there is flow. This problem will be studied in a future work.

The most general *linear* evolution equation is assumed in the form

$$\tau \frac{Dp}{Dt} + \gamma\tau \frac{D\phi}{Dt} = f(p,\phi)$$

where $f(p,\phi)$ is given by (2.4) and τ and γ are to-be-determined constants. The determination of optimum values for γ and τ is a complicated problem which must involve mathematical analysis and comparisons of predictions with experiment. Here we take only some preliminary steps toward the solution of this problem.

4.2 Hyperbolic theory

In the work which follows we put $\gamma = 0$. The equation

$$\tau \frac{Dp}{Dt} = f(p,\phi) \tag{4.8}$$

is a Maxwell-like relaxation theory and τ is a relaxation time.

We shall show that the Maxwell type equation (4.8) leads to a hyperbolic system in which pressure changes propagate by waves. On the other hand, the equation in which the pressure derivative is neglected so that $\gamma\tau\frac{D\phi}{Dt} = f(p,\phi)$ leads to

parabolic propagation. The propagation of fronts of nucleating bubbles associated with the hyperbolic theory (4.8) is appealing and is our focus in this paper.

Collecting our equations, we have

$$\left.\begin{aligned} \tau\left(\alpha\frac{\partial p}{\partial t}+\mathbf{u}\cdot\nabla p\right) &= f(p,\phi) \\ &= \tilde{p}-p-\beta p\phi/(1-\phi)\,, \\ \frac{1}{1-\phi}\left(\alpha\frac{\partial \phi}{\partial t}+\mathbf{u}\cdot\nabla\phi\right) &= \operatorname{div}\mathbf{u}\,, \\ \mathbf{u} &= -\lambda\nabla p+\lambda\rho_l g(1-\phi)\mathrm{e}_x \end{aligned}\right\} \tag{4.9}$$

The parameters defining (4.9) are material parameters associated with solubility β in the function $f(p,\phi)$, porous material parameter α, mobility $\lambda(\phi)$, which is the ratio of permeability upon the viscosity of the foamy mixture, and the relaxation time τ. The relaxation time is a new parameter introduced here and it may be determined by wave speed measurements (see section 5).

The velocity $\mathbf{u}$ may be eliminated from (4.9). Thus,

$$\left.\begin{aligned} &\tau\left\{\alpha\frac{\partial p}{\partial t}-\lambda|\nabla p|^2+\lambda\rho_l g(1-\phi)\frac{\partial p}{\partial x}\right\}=\tilde{p}-p-\frac{\beta p\phi}{(1-\phi)}, \\ &\frac{1}{1-\phi}\left\{\alpha\frac{\partial \phi}{\partial t}-\lambda\nabla p\cdot\nabla\phi\right\}= \\ &\qquad -\operatorname{div}(\lambda\nabla p)-2\lambda\rho_l g\frac{\partial\phi}{\partial x}+\lambda'\rho_l g(1-\phi)\frac{\partial\phi}{\partial x} \end{aligned}\right\} \tag{4.10}$$

The system (4.10) is second order and should be solvable for two-end conditions. These conditions may be expressed in terms of p or ϕ or a combination of these. However, though it is clear that the pressure and superficial velocity ought to be continuous in the whole domain and at its boundaries, the continuity of ϕ is not required. We control and prescribe the pressure, or velocity. Suppose that we put the gravity terms in (4.10) to zero; then $(4.10)_1$ may be solved for ϕ and after substituion of the result in $(4.10)_2$ this becomes an equation in p alone. We solve the p equation; then $(4.10)_1$ gives ϕ in terms of p.

The system (4.9) may be regarded as describing the flow of a relaxing compressible fluid through a porous media. To see this, we replace ϕ with $\rho = \rho_l(1-\phi)$, using (4.3). Then (4.9) may be written as

$$\left.\begin{array}{c} \tau(\alpha\frac{\partial p}{\partial t}+\mathbf{u}\cdot\nabla p)=\tilde{p}-p-\beta p\frac{\rho_l-\rho}{\rho}, \\ \alpha\frac{\partial \rho}{\partial t}+\mathbf{u}\cdot\nabla\rho+\rho\,\mathrm{div}\,\mathbf{u}=0, \\ \mathbf{u}=-\lambda\nabla p+\lambda g\rho\mathbf{e}_x \end{array}\right\} \tag{4.11}$$

5 Constant state solutions

5.1 Constant state solutions and drainage

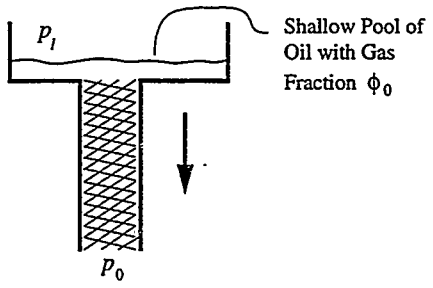

Figure 5.1: Sandpack enclosed in a pressure vessel set at pressure p_0. The supply of oil with dispersed gas fraction ϕ_0 keeps the small head at very small height. The oil and gas bubbles drain at a measured velocity u_0; then $\lambda(\phi_0)=\frac{u_0}{\rho_l g(1-\phi_0)}$

The constant state solution are uniform solutions p_0, $\phi_0, \mathbf{u}_0$ of (4.9), p_0 and ϕ_0 satisfying

$$f(p_0,\phi_0)=\tilde{p}-p_0-\beta p_0\phi_0/(1-\phi_0)=0 \tag{5.1}$$

and

$$\mathbf{u}_0=\mathbf{e}_x u_0, \quad u_0=\lambda(\phi_0)\rho_l g(1-\phi_0) \tag{5.2}$$

The constant state solution is a drainage flow; this flow may be used to determine the mobility $\lambda(\phi)$ (figure 5.1)

5.2 Perturbations of the constant state; wave speeds

If the perturbations $p', \phi', \mathbf{u}'$ of $p_0, \phi_0, \mathbf{u}_0$ are small, then

$$\tau\left(\alpha\frac{\partial p'}{\partial t} + u_0\frac{\partial p'}{\partial x}\right) + ap' + b\phi' = 0 \tag{5.3}$$

where

$$a = 1 + \frac{\beta\phi_0}{1-\phi_0}, b = \frac{\beta p_0}{(1-\phi_0)^2}$$

$$\frac{1}{1-\phi_0}\left(\alpha\frac{\partial\phi'}{\partial t} + u_0\frac{\partial\phi'}{\partial x}\right) - \operatorname{div}\mathbf{u}' = 0 \tag{5.4}$$

$$\mathbf{u}' = -\lambda_0\nabla p' - \lambda'\rho_l(1-\phi_0)g\phi'\mathbf{e}_x + \frac{\lambda_0\rho_l g\mathbf{e}_x\phi'}{2} \tag{5.5}$$

When gravity is unimportant, as in a vertical sandpack, these equations reduce to

$$\tau\alpha\frac{\partial p'}{\partial t} + ap' + b\phi' = 0 \tag{5.6}$$

$$\alpha\frac{\partial\phi'}{\partial t} + (1-\phi_0)\lambda_0\nabla^2 p' = 0 \tag{5.7}$$

We may eliminate p' or ϕ' from (5.6) or (5.7); in both cases we find the telegraph equation

$$\frac{\partial^2 p'}{\partial t^2} + \frac{a}{\tau\alpha}\frac{\partial p'}{\partial t} = c^2\nabla^2 p' \tag{5.8}$$

where

$$c = \left\{\frac{b(1-\phi_0)\lambda_0}{\tau\alpha^2}\right\}^{\frac{1}{2}}$$

is a wave speed. The waves are damped by the first derivative term in (5.8). If the relaxation time tends to zero then wave propagation gives way to diffusion

$$\frac{\partial p'}{\partial t} = \frac{(1-\phi_0)\lambda_0 b}{\alpha a}\nabla^2 p' \tag{5.9}$$

6 Sandpack experiments

Sandpack experiments are used as laboratory surrogates for the flow of oil and gas in porous reservoirs. In figure 6.1 a cartoon of a typical sandpack experiment copied from a paper by Sheng *et al.* [1996] is displayed. The pack may be loaded with sand from reservoirs.

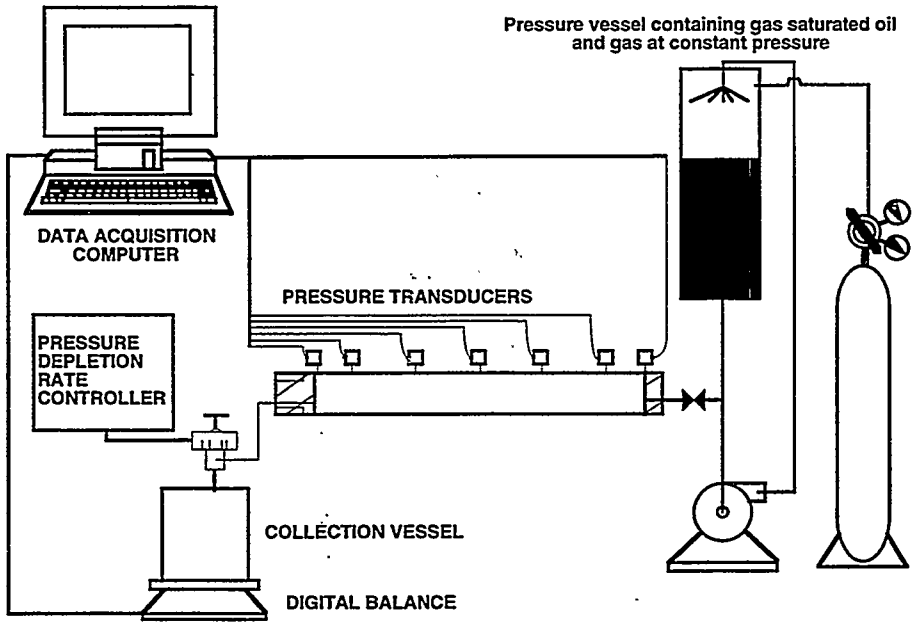

Figure 6.1: Cartoon of a sandpack experiment. Live oil can be injected at the inlet and a pressure depletion rate controller is at the outlet. Different experiments are described by prescribed conditions at the inlet and outlet.

Sandpacks provide an excellent way to get precise data under controlled conditions simulating flow in reservoirs; they are convenient for mathematical modeling because they lend themselves to one dimensional treatments. It is useful to look at these one-dimensional models for horizontal sandpacks in which gravity may be neglected and for vertical flow in which gravity may be important. In both these cases we have our governing equation (4.10) with $\nabla = e_x \partial/\partial x$. Terms proportional to gravity are put to zero in horizontal sandpacks.

Different experiments can be carried out in a sandpack corresponding to different conditions listed below.

Closed inlet. ($x = L$) $u(L,t) = 0$ hence, from $(4.9)_3$, we have

$$\frac{\partial p}{\partial x}(L,t) - \rho_l g\big(1 - \phi(L,t)\big) = 0 \tag{6.1}$$

A pressure gradient is generated by gravity in a vertical sandpack with a closed end at $x = L$. The liquid will be held in the pack by capillarity (which is not explicitly considered in this model) unless it is pushed out by nucleating bubbles.

Pressure drawdown at the outlet ($x = 0$)

$$p(0,t) = \tilde{p} - g(t) \tag{6.2}$$

where $g(0) = 0$ and $g(\infty) = p_\infty < \tilde{p}$. At $t = 0$ the sandpack has no dispersed bubbles and as $t \to \infty$ the pressure becomes uniform. A linear prescription of pressure depletion

$$\begin{aligned} &p = \tilde{p} - At \quad \text{for} \quad 0 \le t \le t_0 \\ &p = p_\infty \quad \text{for} \quad t > t_0 \end{aligned} \tag{6.3}$$

is useful for comparing fast (A large) and slow depletion (A small). The fastest depletion is a step change of pressure

$$p(0,t) = \tilde{p} - (\tilde{p} - p_\infty)H(t) \tag{6.4}$$

where $H(t)$ is the Heaviside function.

Prescribed velocity at the outlet

$$u(0,t) = -\lambda(\phi)\left\{\frac{\partial p}{\partial x}(0,t) - \rho_l g(1-\phi)\right\} \tag{6.5}$$

is prescribed at $x = 0$. If we withdraw very rapidly, $u(0,t)$ is large, the pressure at the inlet will decline, rapidly nucleating gas. In the limit, all of the material will be gas $\phi = 1$; physically one might think of dry foam.

Open inlet. If the pressure at the inlet is prescribed at a value greater than the final outlet, and both pressures are constant in time, then a steady flow of live oil from the reservoir at the inlet to the outlet will be established. It is then of interest to predict and monitor the gas fraction distribution $\phi(x,t)$ during the transient and the final steady state (see section 9).

7 Pressure decline in a closed horizontal sandpack

At $t = 0$ live oil with no dispersed bubbles fills the sandpack

$$\phi(x,0) = 0, p(x,0) = \tilde{p}, u(x,0) = 0 \tag{7.1}$$

The velocity vanishes at the closed inlet. Hence

$$\frac{\partial p}{\partial x}(L,t) = 0 \tag{7.2}$$

The pressure decline at the outlet is given by

$$p = \begin{cases} \tilde{p} - At, 0 < t < t_0 \\ p_0, \quad t > t_0 \end{cases} \tag{7.3}$$

where A represents the rate of decline.

From (4.10) we form the governing equations for $p - \tilde{p} = \pi(< 0)$.

$$\tau\left\{\alpha\frac{\partial \pi}{\partial t} - \lambda\left(\frac{\partial \pi}{\partial x}\right)^2\right\} = -\pi - \beta\frac{(\tilde{p}+\pi)\phi}{1-\phi} \tag{7.4}$$

$$\alpha\frac{\partial \phi}{\partial t} - \lambda\frac{\partial \pi}{\partial x}\frac{\partial \phi}{\partial x} + (1-\phi)\frac{\partial}{\partial x}\left(\lambda\frac{\partial \pi}{\partial x}\right) = 0 \tag{7.5}$$

Solutions of (7.1) through (7.4) will require numerical integration.

7.1 Telegraph equation

We may however hope to solve the linearized version of these equations, (5.6) and (5.7) with $\phi_0 = 0, a = 1, b = \beta\tilde{p}$. The governing telegraph equation is in the form

$$\frac{\partial^2 \pi}{\partial t^2} + \frac{1}{\tau\alpha}\frac{\partial \pi}{\partial t} = c^2\frac{\partial^2 \pi}{\partial x^2} \tag{7.6}$$

$$c = \left\{\frac{\beta\tilde{p}\lambda_0}{\tau\alpha^2}\right\}^{\frac{1}{2}} \tag{7.7}$$

and it can be solved relative to initial conditions at saturation

$$\pi(x,0) = 0 \tag{7.8}$$

$$\phi(x,0) = 0 \tag{7.9}$$

for $0 \leq x \leq L$, and to prescribed inlet and outlet conditions. At a closed inlet the velocity vanishes, hence

$$\frac{\partial \pi}{\partial x}(L,t) = 0. \tag{7.10}$$

At the outlet, we carry out a linear drawdown

$$\pi(0,t) = \begin{cases} -At, & 0 \leq t < t_0 \\ -At_0, & t \geq t_0 \end{cases} \tag{7.11}$$

The linearized theory is valid only for very small values of At_0. We must disallow step changes of π, however small. To see this, we note that the linearization of (7.4) around (7.8) and (7.9) gives rise to

$$\tau\alpha\frac{\partial \pi}{\partial t} = -\pi - \beta\tilde{p}\phi \tag{7.12}$$

so that ϕ is small only if $\frac{\tau\alpha}{\beta\tilde{p}}\frac{\partial \pi}{\partial t}$ is small, which cannot be true for step changes in π. Though conditions on ϕ are not required to solve the telegraphers equation system (7.6)–(7.11) for π, we find that the drawdown condition (7.11) implies that

$$\phi(0,t) = \frac{1}{\beta\tilde{p}} \begin{cases} At + \tau\alpha A, & 0 \leq t < t_0 \\ At_0, & t \geq t_0 \end{cases} \tag{7.13}$$

At $t = t_0$ there is a discontinuity of ϕ corresponding to the initiation of a stopping wave. Obviously the fraction of dispersed gas at the outlet is an increasing function of the drawdown rate A.

Turning next to the solution of (7.6)–(7.11), we change variables

$$\left.\begin{aligned} \pi &= -\alpha\tau A\theta \\ x &= c\tau\alpha\chi \\ t &= \tau\alpha T \end{aligned}\right\} \tag{7.14}$$

$$\frac{\partial^2\theta}{\partial T^2} + \frac{\partial\theta}{\partial T} = \frac{\partial^2\theta}{\partial\chi^2} \tag{7.15}$$

$$\theta(\chi,0) = 0 \quad \text{for} \quad 0 \le \chi \le l, \tag{7.16}$$

$$\frac{\partial\theta}{\partial\chi}(l,T) = 0 \tag{7.17}$$

$$\theta = \begin{cases} T, & 0 \le T < T_0 \\ T_0, & T \ge T_0 \end{cases} \tag{7.18}$$

where

$$l = L/c\tau\alpha \quad \text{and} \quad T_0 = t_0/\tau\alpha. \tag{7.19}$$

To solve (7.15)–(7.18) we introduce our auxiliary problem for

$$\psi \stackrel{\text{def}}{=} \frac{\partial\theta}{\partial T} \tag{7.20}$$

given $\psi(\chi,T) = \partial\theta/\partial T$, we may find

$$\theta(\chi,T) = \int_0^T \psi(\chi,T')dT' \tag{7.21}$$

by integration. After differentiating (7.15–7.17) with respect to T, we find that ψ satisfies

$$\frac{\partial^2\psi}{\partial T^2} + \frac{\partial\psi}{\partial T} = \frac{\partial^2\psi}{\partial\chi^2}, \tag{7.22}$$

$$\psi(\chi,0) \equiv 0 \quad \text{for} \quad 0 \le \chi \le l, \tag{7.23}$$

$$\frac{\partial\psi}{\partial\chi}(l,T) = 0 \tag{7.24}$$

$$\psi(0,T) = H(T) - H(T-T_0) \tag{7.25}$$

where $H(T)$ is a unit step function.

It should be understood that the solution does not rise above zero until it is struck by the wave moving with velocity c. Hence $\pi(x,t)$ is different from '0 only when $x < ct$ and $t < t*$ where $t*$ is the time of first reflection defined by

$$L = ct*$$

We will focus our attention on wave propagation to short times, $t < t*$ and $t < t_0$ where t_0 is the time at which the drawdown is stopped and we could choose this stopping time $t_0 < t*$ to be after the wave has reflected off the wall at $x = L$.

Short times mean that $T < T*$ and $T < T_0$. The functions $\theta(\chi,T)$ and $\psi(\chi,T)$ are different from zero only when $\chi < T$ and for short times we may replace (7.18) with

$$\theta(0,T) = T \tag{7.26}$$

and (7.25) with

$$\psi(0,T) = H(T)\,. \tag{7.27}$$

The solution of (7.22), (7.23), (7.24) and (7.27) can be found in Carlslaw and Jaeger [1949] in the form

$$\psi(\chi,T) = H(T-\chi)f(\chi,T) \tag{7.28}$$

where

$$f(\chi,T) = e^{-\chi/2} + \frac{\chi}{2}\int_{\chi}^{T}\left[\frac{e^{-\sigma/2}}{\sqrt{\sigma^2-\chi^2}}I_1(\frac{1}{2}\sqrt{\sigma^2-\chi^2})\right]d\sigma$$

and I_n is the Bessel function of imaginary argument such that $I_1(x) = dI_0(x)/dx$. The solution (7.28) is free of parameters and is plotted against χ for different values of T in figure 8.1(a).

We obtain $\theta(\chi,T)$ by integration (7.21), using (7.28); it is plotted against χ for different values of T in figure 8.2(a).

An important functional of the solution is the velocity $U(0,t)$ at the outlet which can be obtained from

$$\frac{\partial\theta(0,T)}{\partial\chi} = \int_0^T \frac{\partial\psi}{\partial\chi}(0,T')dT'$$

where

$$\frac{\partial\psi}{\partial\chi}(0,T) = -\delta(T)f(0,T) + H(T)\frac{\partial f}{\partial\chi}(0,T)$$

Hence

$$\frac{\partial\theta}{\partial\chi}(0,T) = -1 + \int_0^T \frac{\partial f}{\partial\chi}(0,T')dT' \tag{7.29}$$

where θ is plotted in figure 8.2. The velocity $u(0,t)$ at the outlet can be expressed in terms of (7.29) by

$$\begin{aligned} u(0,t) &= -\lambda_0\frac{\partial\pi}{\partial x}(0,t) \\ &= \frac{\lambda_0 A}{c}\frac{\partial\theta}{\partial\chi}(0,t/\alpha\tau) \end{aligned} \tag{7.30}$$

7.2 Rate of production

The rate of production of oil is the volume of oil leaving the outlet at $x = 0$ per unit time and is given by

$$\mathring{Q} = \text{Area } u(0,t)[1-\phi(0,t)] \tag{7.31}$$

where Area is the area of the sandpack and $\phi(0,t)$ is given by (7.13) for $t < t_0$. The cumulative production up to a time $\hat{t} < t_0$ is given by

$$\begin{aligned} Q_{\hat{t}} = \int_0^{\hat{t}} \mathring{Q}(t)dt = \\ \text{Area}\frac{\lambda_0 A}{c}\int_0^{\hat{t}} \frac{\partial\theta}{\partial\chi}(0,t/\alpha\tau)\left[1-\frac{A}{\beta\tilde{p}}(t+\tau\alpha)\right]dt \end{aligned} \tag{7.32}$$

For small values of $A/\beta\tilde{p}$, the cumulative production is a linearly increasing function of the drawdown rate A.

8 Diffusion

For small values of the relaxation time τ, the second time derivative in (7.6) becomes less and less important in the solution; the amplitude of the discontinuity in the solution decays to diffusion rapidly and the hyperbolic property of the solution is apparent only at very early times. The change of variables used in section 8 is not appropriate for the limit $\tau \to 0$. When $\tau = 0$, the linearized problem (7.6) reduces to

$$\alpha \frac{\partial \pi}{\partial t} = \beta \tilde{p} \lambda_0 \frac{\partial^2 \pi}{\partial x^2} \tag{8.1}$$

and (7.12) reduces to

$$\pi + \beta \tilde{p} \phi = 0 \tag{8.2}$$

This problem is subject to the initial condition (7.8) and (7.9), the inlet condition (7.10) and the outlet conditions (7.11). A new change of variables

$$\begin{aligned} \pi &= -\alpha A \theta, \\ x &= \sqrt{\beta \tilde{p} \lambda_0}\, \chi, \\ t &= \alpha T \end{aligned} \tag{8.3}$$

leads to the following parameter-free diffusion problem

$$\left.\begin{aligned} &\tfrac{\partial \theta}{\partial T} = \tfrac{\partial^2 \theta}{\partial \chi^2}, \\ &\theta(\chi, 0) = 0, \\ &\tfrac{\partial \theta}{\partial \chi}(L, T) = 0, \\ &\theta(0, T) = \begin{cases} T & (0 < T < T_0) \\ T_0 & (T > T_0) \end{cases} \end{aligned}\right\} \tag{8.4}$$

where

$$l = \frac{L}{\sqrt{\beta \tilde{p} \lambda_o}} \quad \text{and} \quad T_o = \frac{t_o}{\alpha}$$

We may form an auxilliary problem for

$$\psi = \frac{\partial \theta}{\partial T} \tag{8.5}$$

analogous to that (7.20)

$$\left.\begin{array}{l} \frac{\partial^2 \psi}{\partial T} = \frac{\partial^2 \psi}{\partial T^2} \\ \psi(\chi, 0) = 0, \end{array}\right\} \tag{8.6}$$

$$\frac{\partial \psi}{\partial \chi}(l, T) = 0, \tag{8.7}$$

$$\psi(0, T) = H(T) - H(T - T_0) \tag{8.8}$$

The solution of the ramp-up problem (8.4) may be obtained from the solution of the auxiliary by integration as in (7.21).

In the limit

$$l \to \infty \quad \text{and} \quad T_0 \to \infty,$$

equation (8.7) and (8.8) may be replaced by

$$\left.\begin{array}{ll} \psi(\infty, T) & = 0 \\ \psi(0, T) & = H(T) \end{array}\right\} \tag{8.9}$$

The solution of (8.6) and (8.9) is unique and is given by

$$\psi = \frac{1}{\sqrt{\pi T}} \int_0^{\chi} \exp\left(\frac{-\chi^2}{4T}\right) d\chi = \operatorname{erfc}\left\{\frac{\chi}{2\sqrt{T}}\right\} \tag{8.10}$$

The solution of the corresponding ramp up problem with $\theta(0, T) = T$ is given by integration of (8.10)

$$\theta(\chi, T) = \int_0^T \psi(\chi, T')\, dT', \tag{8.11}$$

Graphs of $\psi(\chi, T)$ and $\theta(\chi, T)$ which can be compared with figures 8.1(a) and 8.2(a) are given in figures 8.1(b) and 8.2(b).

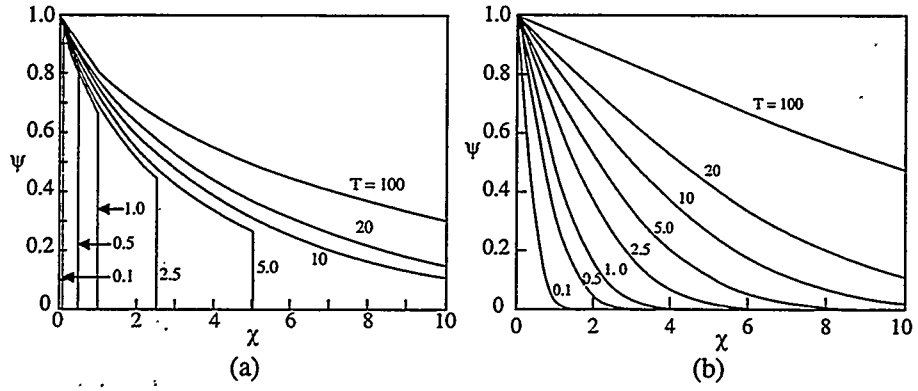

Figure 8.1: Comparison of wave propagation and diffusion for a step change in pressure $\psi(\chi,T)$: $\psi(\chi,T) = 0 \ \forall \ \chi$ when $T < 0$, $\psi(0,T) = H(T)$, $\psi(\infty,T) = 0$. (a) wave propagation: ψ satisfies (7.22) and is given by (7.28). (b) diffusion: ψ satisfies (8.6) and (8.9) and is given by (8.10).

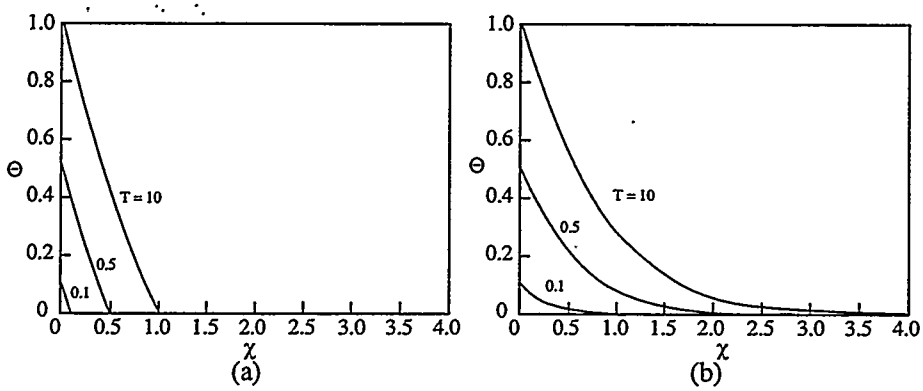

Figure 8.2: Comparison of wave propagation and diffusion for a ramp change in pressure: $\psi(\chi,T) = 0$ for $T < 0$, $\psi(0,T) = T$, $\psi(\infty,T) = 0$. (a) wave propagation: $\psi = \theta$ where θ satisfies (7.15), (7.16), $\theta(\infty,T) = 0$ and (7.26). (b) diffusion: $\psi = 0$ where θ is given by (8.11).

9 Steady flow in a horizontal sandpack

We drive foamy oil from a reservoir at saturation $\tilde{p}$ to another reservoir at the outlet pressure p_L. The dispersed gas fraction at the ends $\phi(0) = \phi_0$ and $\phi(L) = \phi_L$ are unknowns, not continuous at reservoir interfaces. It will be convenient to work with dimensionless variables

$$y = \frac{p}{\tilde{p}},\ \chi = x/L. \tag{9.1}$$

The dimensionless form of equations (7.4) and (7.5) for steady flow are

$$\hat{\tau}\Lambda(\phi)\left(\frac{dy}{d\chi}\right)^2 = \frac{y[1+(\beta-1)\phi]-1+\phi}{1-\phi}, \tag{9.2}$$

$$-\Lambda(\phi)\frac{dy}{d\chi}\frac{d\phi}{d\chi} + (1-\phi)\frac{d}{d\chi}\left\{\Lambda(\phi)\frac{dy}{d\chi}\right\} = 0, \tag{9.3}$$

$$\left.\begin{array}{r}(y,\phi) = (1,\phi_o) \text{ at } \chi = 0\\ (y,\phi) = (y_L,\phi_L) \text{ at } \chi = 1\end{array}\right\} \tag{9.4}$$

where

$$\Lambda(\phi) = \lambda(\phi)/\lambda(\phi_0)$$

and

$$\hat{\tau} = \frac{\tau\tilde{p}\lambda(\phi_0)}{L^2} \tag{9.5}$$

is a dimensionless relaxation time; the underlying sytem of equations is hyperbolic and accomodates discontinuous solutions only when $\tau > 0$.

Equation (9.2) may be written as

$$\frac{d}{d\chi}\left\{\Lambda(\phi)(1-\phi)\frac{dy}{d\chi}\right\} = 0,$$

hence

$$\Lambda(\phi)(1-\phi)\frac{dy}{d\chi} = C = constant. \tag{9.6}$$

Equation (9.6) says that the oil velocity

$$-\lambda\frac{dp}{dx}(1-\phi)$$

in steady flow is a constant independent of x. Combining (9.6) and (9.2) we get

$$\hat{\tau}C\frac{dy}{d\chi} = y[1+(\beta-1)\phi]-1+\phi. \tag{9.7}$$

Equations (9.6) and (9.7) together with the conditions (9.4) define the steady flow in a horizontal sandpack.

When the relaxation time τ vanishes, (9.7) reduces to the equilibrium isotherm $f(p,\phi)=0$ which means that the right hand side of (9.2) vanishes

$$y[1+(\beta-1)\phi]-1+\phi = 0 \tag{9.8}$$

Elimination of ϕ between (9.6) and (9.8) leads to a nonlinear first order differential equation in which the integration constant and the constant C are determined by the prescribed conditions (9.4). For the equilibrium case, the condition $y=1$ at $x=0$ implies that $\phi_0=0$ so that ϕ is continuous into the reservoir at $x=0$.

In the general case, (9.6) and (9.7) imply that

$$\frac{\hat{\tau}C^2}{\Lambda(\phi)(1-\phi)} = y[1+(\beta-1)\phi]-1+\phi \tag{9.9}$$

Evaluating (9.8) first at $\chi=0$ where $y=1$, we get

$$\frac{\hat{\tau}C^2}{\Lambda(\phi_0)(1-\phi_0)} = \beta\phi_0 \tag{9.10}$$

and then at $\chi=1$, we get

$$\frac{\hat{\tau}C^2}{\Lambda_L(1-\phi_L)} = y_L[1+(\beta-1)\phi_L]-1+\phi_L \tag{9.11}$$

Equations (9.10) and (9.11) determine C^2 and one relation between ϕ_0 and ϕ_L.

Equation (9.9) may be solved for

$$y = F(\phi) = \left\{ \frac{\hat{\tau} C^2}{\Lambda(\phi)(1-\phi)} + 1 - \phi \right\} / [1 + (\beta - 1)\phi] \tag{9.12}$$

After differentiating (9.12) with respect χ, replacing $dy/d\chi$ with (9.6), we get

$$\frac{C}{\Lambda(\phi)(1-\phi)} = F'(\phi)\frac{d\phi}{d\chi}$$

and

$$C\chi = \int_{\phi_0}^{\phi} \Lambda(\eta)(1-\eta)\, F'(\eta) d\eta. \tag{9.13}$$

A second relation between ϕ_0 and ϕ_L is implied by (9.13) when $\chi = 0$ and $\chi = 1$.

The case $\tilde{\tau} = 0$ is of special interest. In this case the relaxation to equilibrium in which the pressure and dispersed gas fraction lie on a solubility isotherm is immediate. In this case (9.13) may be written as

$$C\chi = -\int_{\phi_0}^{\phi} \beta \frac{\Lambda(\eta)(\eta - 1)}{[1 + (\beta - 1)\eta]^2} d\eta \tag{9.14}$$

where $\phi = \phi_L$ at $\chi = 1$.

To investigate the effects of the relaxation parameter $\hat{\tau}$ on steady flow we treat the case in which the mobility $\lambda(\phi)$ is a constant independent of ϕ; in this case $\Lambda = 1$ and (9.13) reduces

$$C\chi = (1-\phi)F(\phi) + \int_{\phi_0}^{\phi} F(\eta) d\eta + C_0 \tag{9.15}$$

where

$$C\chi = \frac{\hat{\tau} c^2}{\beta} \ln \frac{1 + (\beta - 1)\phi}{1 + (\beta - 1)\phi_0} \frac{1 - \phi_0}{1 - \phi} + \left(\hat{\tau} c^2 + \frac{\beta^2}{(\beta - 1)^2} \right) \times \left(\frac{1}{1 + (\beta - 1)\phi} - \frac{1}{1 + (\beta - 1)\phi_0} \right) + \frac{\beta}{(\beta - 1)^2} \ln \frac{1 + (\beta - 1)\phi}{1 + (\beta - 1)\phi_0} \tag{9.16}$$

where $\phi = \phi_L$ at $\chi = 1$.

10 Comparison with the experiments of Maini & Sarma [1994]

Maini & Sarma [1994] reported results of experiments in a sandpack like that shown in figure 6.1 where pressure at inlet and outlet are controlled. A table of properties of the sandpack is given in Table 10.1. "Prior to the start of the flow experiments, each oil sample was cleaned of its suspended materials. The oil was then recombined with methane gas in the recombination equipment at a pressure of 4.83MPa." They did steady flow experiments using Lloydminster and Lindbergh crude oil in which the inlet pressure was at saturation

$$p = \tilde{p} = 4.83MPa = 4.83 \times 10^7 dynes/cm^2$$

varying the "drawdown" pressure at the outlet.

Table 10.2 gives the properties of the two "live" oils at saturation.

Parameter	Value
Length (m)	2.0
Cross-sectional area (m^2)	16.1×10^{-4}
Sand size (μ m)	74–105
Porosity (fraction)	0.33
Pore volume (mL)	1062
Permeability (μm^2)	3.35
Confining pressure used (MPa)	14.0

Table 10.1: Properties of the Porous Medium.

Oil	Density (g/cc)	Viscosity (Poise)	Core Average ϕ at maximum drawdown	β
Lloydminster	0.968	30.07	0.138	3.40
Lindbergh	0.978	39.70	0.148	3.17

Table 10.2: Properties of "live oil" at saturation.

The pressure distribution along the core sample which was measured in steady flow by Maini and Sarma [1994] is shown in figure 10.1 and 10.2. Six pressure transducers were placed at intervals along the pack. Each transducer measures the

pressure drop between two taps equally spaced along the pack; the pressure drop across two taps is called a "differential pressure." The plots given in figures 10.1 and 10.2 are of straight line segments between pressure taps.

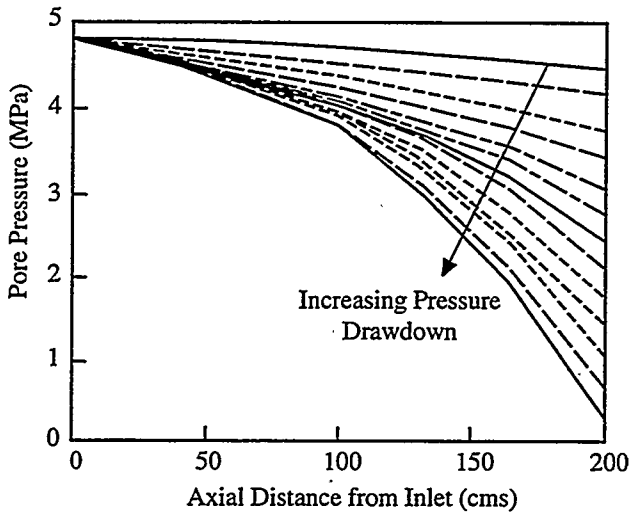

Figure 10.1: (Maini & Sarma, 1994). Pressure distributions in steady flows of Lindbergh oils at various pressure drawdowns.

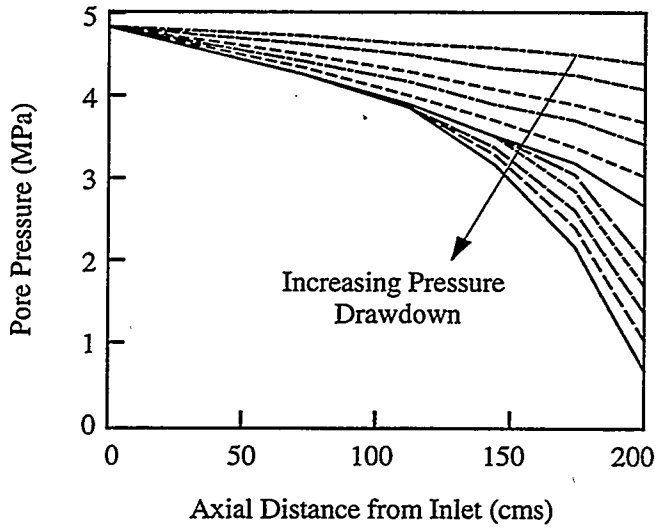

Figure 10.2: (Maini & Sarma, 1994). Pressure distributions in steady flow of Lloydminster oils at various pressure drawdowns.

Comparison of theory with the experiments of Maini and Sarma [1994] requires that we input a mobility function $\lambda(\phi) = k/\mu(\phi)$ which was not given by them. We are going to take $k = 3.35$ to be the constant value given in Table 10.1 and we will express

$$\mu(\phi) = \mu_0 m(\phi) \tag{10.1}$$

where μ_0 is the viscosity of live oil at saturation (given in Table 10.2) when $\phi = 0$ and of course $m(0) = 1$. The viscosity of the dispersion should grow with ϕ and, even more, the viscosity of oil istelf should increase when dissolved gas is released to the dispersion. However the viscosity of foamy oils in porous media is an unsettled subject and even the sign in the change of viscosity is controversial (see Sheng, *et al.* [1999a]).

We are going to use the celebrated empirical formula of Thomas [1965]

$$m(\phi) = 1 + 2.5\phi + 10.05\phi^2 + 0.00273\mathrm{e}^{16.6\phi} \tag{10.2}$$

for the viscosity of a dispersion of solid spheres of uniform size. This formula gives good results for small and moderate values of ϕ, say $\phi < 0.5$, which is not too close from a statistically well-packed array. Various empirical formulas for dispersions of solid spheres have been proposed and are compared in the paper of Poletto and Joseph [1994]. It can be said that none of these formulas is accurate near the well-packed condition which in fact develops a rheology more complicated than can be described by an "effective" viscosity.

The viscosity of well dispersed spherical bubbles might be described by the viscosity of a similar dispersion of solid spheres. In any case the expression 10.1 and 10.2 cannot be expected to hold for values of $\phi > 0.68$, and they may not hold for values of $\phi > 0.4$. It is of interest to evaluate if good agreement between theory and experiment can be achieved by choosing an appropriate viscosity function.

We are first going to compare theoretical pressure distributions of the equilibrium theory with $\tau = 0$ with the measured distribution as given in figure (10.1) and (10.2). The conparison will be given for drawdown in three cases, from 4.83MPa to (1) 0.75 MPa, (2) 1 MPa and (3) 3 MPa. Our attention is directed to Lloydminster and Lindbergh oils for which the solubility isotherms are given in figure 2.5.

To evaluate the response to a pressure drawdown it is useful to look at the maximum gas fraction in the sandpack. This will occur at the outlet where the pressure is lowest and $\phi(L) = \phi_L$. From figure 2.5 we find the values given in table 10.3.

	p_L(MPa)	$\phi_L(\beta = 3.4)$	$\phi_L(\beta = 3.4)$
(1)	0.75	0.615	0.632
(2)	1	0.53	0.547
(3)	3	0.152	0.161

Table 10.3: The outlet gas fraction with drawdown pressures.

From these values we may conclude that foamy and free gas will certainly occur at the outlet in case (1) and possibly in case (2). Case (3) should be well in the region of validity for non-foaming bubbly mixtures and the Thomas equation (10.2) should work if the assumptions that dispersed bubbles act like dispersed solid spheres when they are not closely packed; the Thomas equation might work for (2) but it will not work for (1) (see figure 10.8).

It is perhaps helpful to note that the last exponential terms of (10.2) accounts for less than 10% of $m(\phi)$ when $\phi < 0.268$.

The exponential term in the Thomas formula should not be used when ϕ indicates close packing. The viscosity of close packed solid spheres could tend to infinity but dispersed bubbles would foam or form free gas when close packed and the increase in the effective viscosity would be more moderate than for solid spheres. The value of ϕ for which a more moderate than exponential increase would be expected is not known but we might anticipate a value near $\phi = 0.5$. In fact we find excellent agreement with the observed distributions of pressure when we use the full Thomas formula (10.2) in drawdowns to 1MPa and 3MPa and a truncated version of Thomas' formula with the exponential neglected

$$\mu = \mu_0(1 + 2.5\phi + 10.05\phi^2) \tag{10.3}$$

for drawdown to $\phi_L = 0.75$ MPa. These comparisons are exhibited in figures 10.3, 10.4, 10.5 and 10.6. Figure 10.3 is our theoretical result for Lloydminster oil which can compare with the experimental result given in figure 10.2.

A more detailed comparison of theory and experiment is shown in figures 10.4, 10.5 and 10.6. The observed pressure is slightly higher for Lloydminster than Lindbergh in the cases p_L = 1MPa and p_L = 0.75MPa but is smaller for p_L = 3MPa. In all cases the assumption that the mobility λ is constant underpredicts the pressure. Good agreements between theory and experiments is achieved with oil fitting under the assumption that mobility varies with ϕ as $\lambda = k/\mu(\phi)$ with k given in table 10.1, μ_0 given in table 10.2 and $\mu(\phi)$ given by the Thomas expression (10.2) and (10.3).

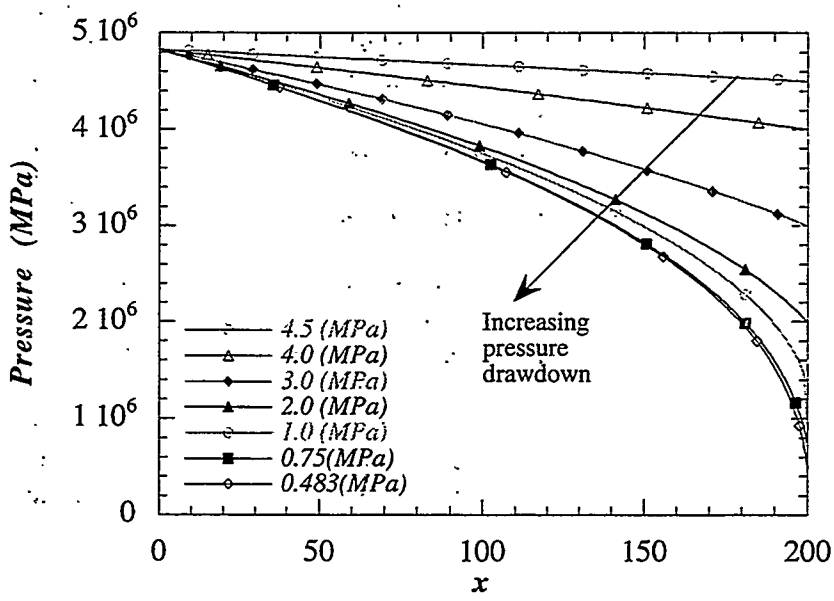

Figure 10.3: Theoretical pressure distributions in steady flows of oil (with $\beta =$ 3.4 and variable $\mu(\phi)$ as in (10.2)) at pressure drawdowns to values greater than 0.75 and the truncated formula (10.3) from 0.75 to 0.483 MPa. This figure can be compared with the experimental result shown in figure 10.2.

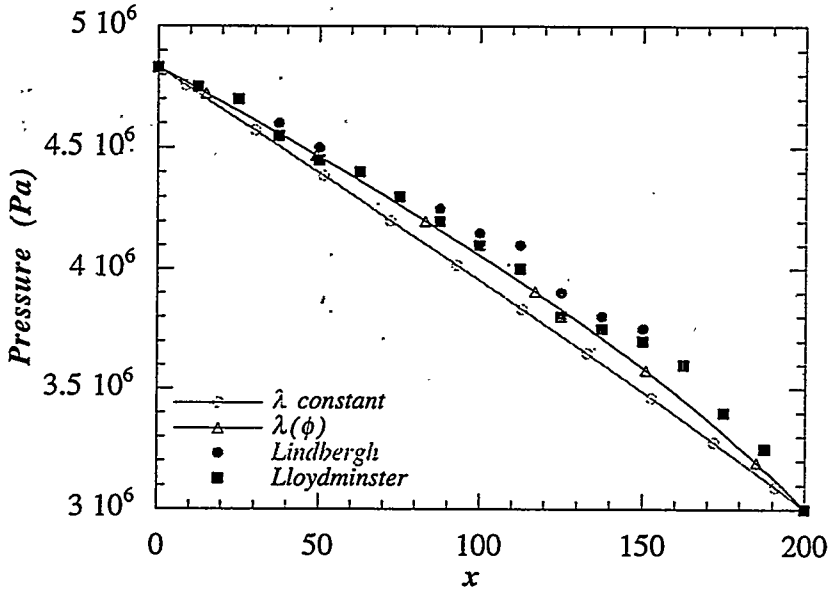

Figure 10.4: Comparisons of the theoretical and experimental pressure distributions at drawdown pressure p_L =3MPa. $\beta = 3.4$ is used in the theory for both constant and variable oil viscosity μ.

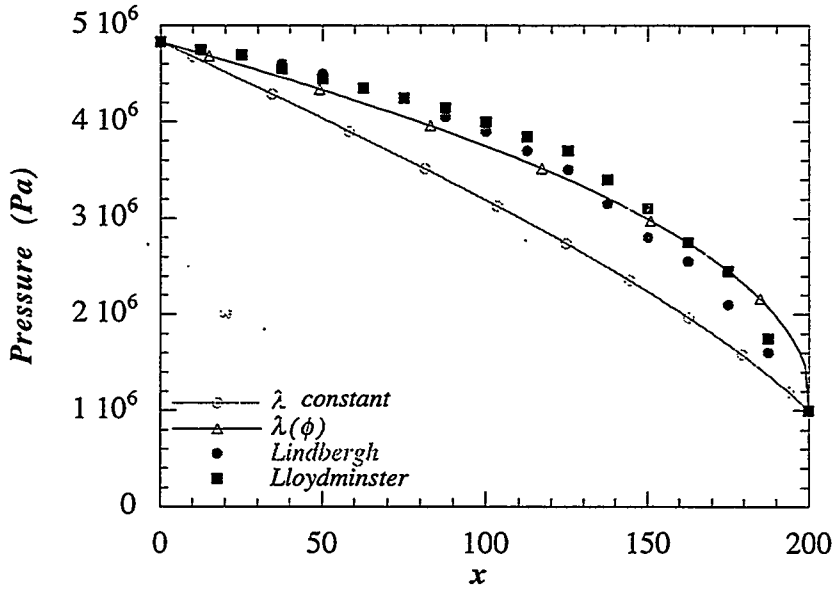

Figure 10.5: Comparisons of the theoretical and experimental pressure distributions at drawdown pressure $p_L = 1$MPa. $\beta = 3.4$ is used in the theory for both constant and variable oil viscosity μ.

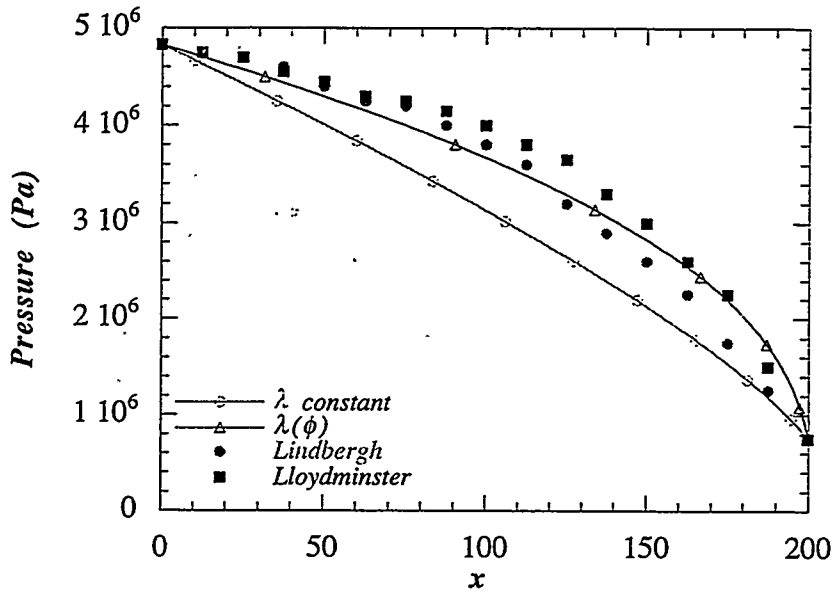

Figure 10.6: Comparisons of the theoretical and experimental pressure distributions at drawdown pressure $p_L = 0.75$MPa. $\beta = 3.4$ is used in the theory for both constant and variable oil viscosity μ.

In figure 10.7 we compared the theoretical prediction for the pressure when $\beta = 3.17$ (Lindbergh) and $\beta = 3.4$ (Lloydminster); the differences are very small with slightly higher value of p when $\beta = 3.17$.

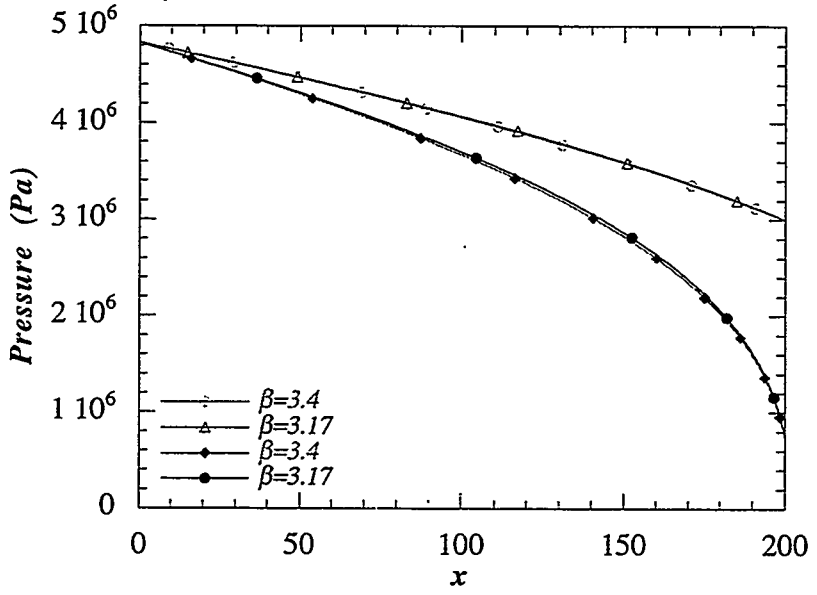

Figure 10.7: Comparisons of theoretical pressure distributions with Lloydminster ($\beta = 3.17$) and Lindbergh ($\beta = 3.4$) oils at drawdown pressure $p_L = 0.75$ MPa and 3 MPa. For the same drawdown pressure, the pressure difference is not significant with different β.

Figure 10.8 compares theoretical and experimental values (Maini & Sarma [1994] figure 2) for the oil production rate (10.4) as a function of the pressure drawdown. The volume flow rate is given by

$$\mathring{Q} = \text{Area } [-\lambda(\phi)\, dp/dx\, (1-\phi)] \tag{10.4}$$

where the area is $16.1 \times 10^{-4} m^2$ (table 10.1) and the quantity in the brachials is the constant oil velocity (see (9.6)). The mass flow rate is obtained by multiplying (10.4) by the oil density $\rho_o = 0.968$ g/cc and converting to experimental units. The production rate is over predicted when $\lambda = \lambda_o$ is constant. The exponential term in the Thomas expression under predicts when the oil foams. The agreement between

theory and experiment with variable $\lambda(\phi)$ using expression (10.1) and (10.2) and no fitting parameters is excellent.

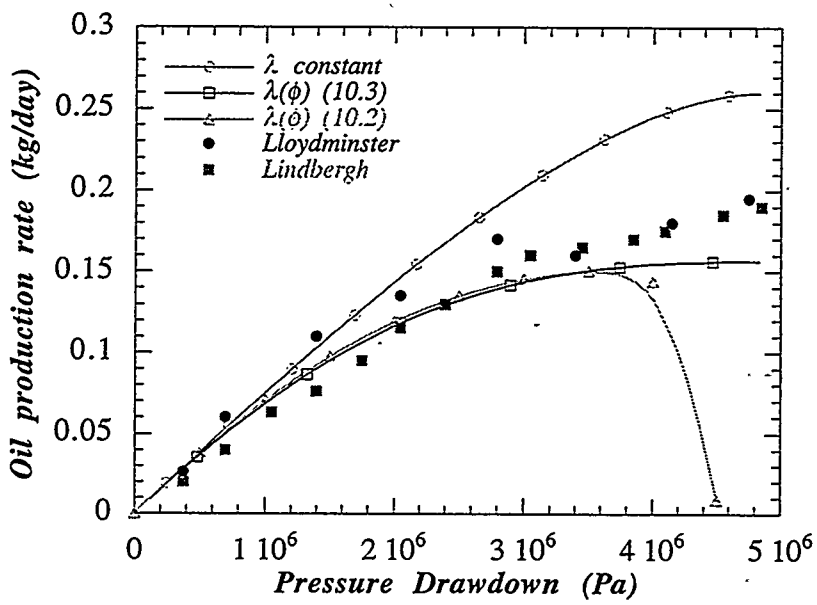

Figure 10.8: Comparisons of oil production rates in steady flows at various pressure drawdowns.

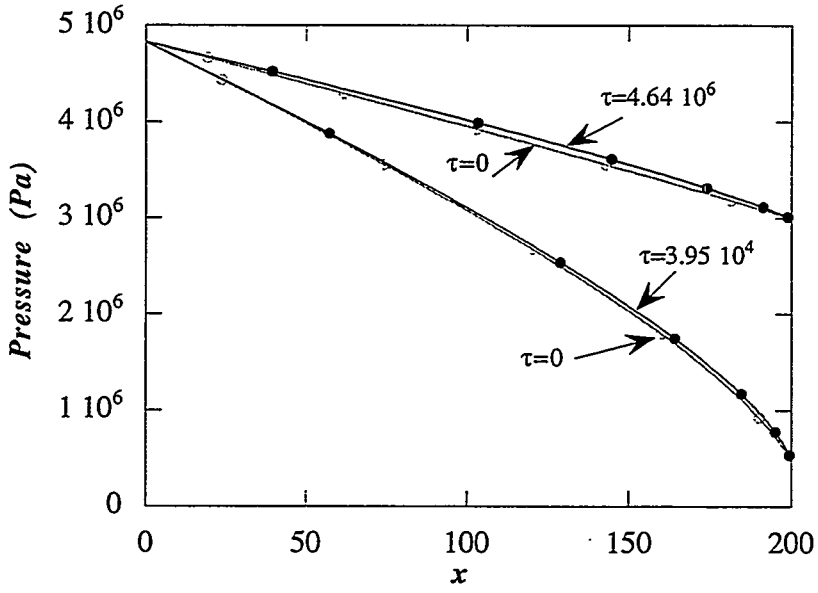

Figure 10.9: Comparisons of theoretical pressure distributions with different relaxation time τ at $\beta = 3.4$ and constant oil viscosity. The maximum relaxation time that can be reached is $\tau = 4.64 \times 10^6$ when drawdown pressure $p_L = 3$MPa and $\tau = 3.95 \times 10^4$ when drawdown pressure $p_L = 0.75$MPa. There is no significant pressure difference for the different τ.

In figure 10.9 we show the results of our investigation of the influence that has the relaxation times τ. Our hope to back out τ from the steady flow experiments was not realized. The solution ceases to exist when $\phi = 1$, as it should and the difference in the pressure distribution in the region in which a relaxation solution exists is smaller than the errors in the experiments.

We turn next to the blow down experiment of Maini and Sarma [1994] (their figure 9, our figure 10.10). They describe their experiment as follows (the emphasis indicated is ours).

> A different type of experiment was needed to estimate the total recovery potential of solution gas drive. This experiment started with the sand pack at maximum "live oil" saturation. The pack was allowed to blow down to atmospheric pressure through the outlet end, and the inlet end remained closed. Figure 9 shows the recovery and pressure-drop behavior. *More than 20% of the original oil was recovered in this primary depletion experiment.* The value is surprisingly high for the viscous oil system and suggests that the critical gas saturation was much higher than what would be measured by an external gas drive experiment. Typically, the external drive experiments in such systems show the critical gas saturation to be less than 5%. Therefore, this experiment also suggests that a mechanism is present in heavy-oil systems to increase the critical gas saturation. *We suggest that this mechanism is the formation of an oil-continuous foam.*

We have already remarked that the solubility isotherm with $\beta = 3.4$ or 3.17 leads to dispersed gas fractions of the order 0.93; foaming is inevitable.

10.1 Blowdown experiment

The blowdown experiment is unsteady. The experiments shown in figure 10.10 show that the pack is still producing oil after 200 hours; the terminal steady and uniform state has not been achieved.

The results of the experiments at early times are not accurate enough to test our theory of hyperbolic propagation. Morever, the blowdown leads to foam and connected gas, a regime to which our theory should not apply.

We have the idea that after hours, wave propagation has decayed to diffusion, and that as a preliminary to a complete study of the nonlinear transient problem we could examine the idea that some information could be obtained from the diffusion theory given in section 8 modified to take into account the presence of a fixed wall. We solved the following problem

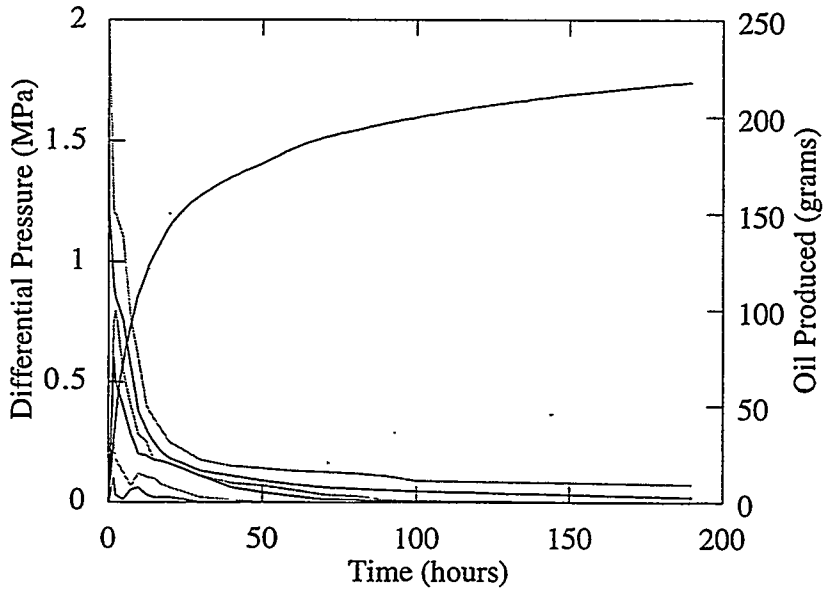

Figure 10.10: (Maini & Sarma, 1994). Change in the pressure drop across different core segments and cumulative oil production with time during the blowdown experiment with the Lloydminster system.

$$\left.\begin{aligned} \frac{\partial p}{\partial t} &= \frac{\beta\tilde{p}\lambda_o}{\alpha}\frac{\partial^2 p}{\partial x^2}, \\ p(x,0) &= \tilde{p}, \\ p(0,t) &= p_L\left[1-H(t)\right], \\ \frac{\partial p}{\partial x}(L,t) &= 0 \end{aligned}\right\} \qquad (10.5)$$

where $\beta = 3.4, \tilde{p} = 4.83$MPa, $\lambda_o = k/\mu_o, k = 3.35 \times 10^{-8} cm^2$, $\mu_o = 30$ poise, $\alpha = 1/3$, $\beta\tilde{p}\lambda_o/\alpha = 11/20 = 0.55$ and $p_L = 0.1$MPa. The problem (10.5) was resolved numberically and the results were displayed in figure 10.11. The differential pressure distributions predicted by the diffusion theory follow the qualitative trends observed in the experiments. The oil produced is given

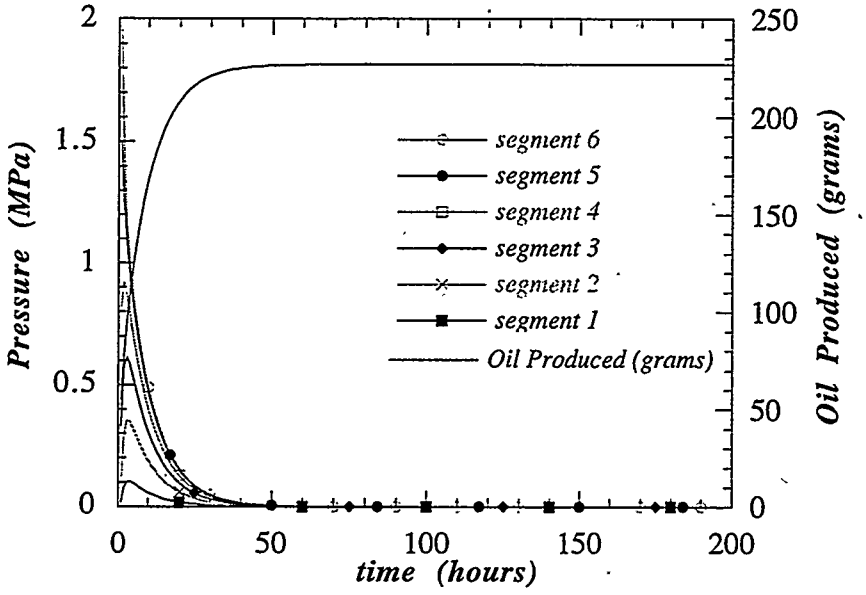

Figure 10.11: Change in the pressure drop across different core segments and cumulative oil production with time during the blowdown with the linearized Lloydminster system.

$$\rho_o Q(t) = \rho_o \int_o^t \mathring{Q}(t)\, dt \tag{10.6}$$

where

$$\mathring{Q} = \text{-Area } \lambda(1-\phi)\, dp/dx \tag{10.7}$$

is evaluated at $x = 0$, the open end of the sandpack. The theory overpredicts the cumulative productin because blowdown produces large amounts of connected gas which is not allowed in the theory.

11 Conclusion and discussion

The theory which we have developed could be called a continuum mixture theory for foamy oils flow with dispersed gas of low mobility relative to the liquid which

leads to three coupled nonlinear partial differential equations for $\mathbf{u}, p$ and the gas fraction ϕ, five scalar equations in five unknowns.

The model proposed here does not require information about nucleation, bubble growth, liquid compressibility or forces which produce relative velocity. We put up a one-phase or mixture theory in which the dispersed gas is described by a gas fraction field in a single fluid in which the viscosity, density and mobility in D'Arcy's law all depend on the gas fraction. This fluid satisfies the usual D'Arcy law, and the continuity equation together with a kinetic (constitutive) equation required by the condensation and outgassing of methane (or other gases) in heavy crude. The theory depends only on parameters which can be measured in a PVT cell and sandpack. The virtue of the model is simplicity, but it can work only for relatively immobile dispersed gas bubbles in which divergence-free velocities are excluded (see the discussion following (4.4)). Certainly such a theory could not be expected to give rise to a percolation threshold or even to a critical gas fraction. We have shown that it can describe many features of solution gas drive of foamy oils in the regimes when the bubbles in the mixture are dispersed and even when they are trapped in foam.

The equations of our theory are highly nonlinear and the underlying system is hyperbolic giving rise to propagating bubble fronts, and experiments to check the predicted wave speeds have as yet to be carried out. When the wave speeds are known, we may calculate a relaxation time which is a material parameter of our theory.

We solved linearized versions of our equations for the pressure drawdown in a sandpack with one end closed and were able to resolve the nonlinear flow for steady flow in an open sandpack by quadrature. The solutions of the steady flow problem depend only weakly on the relaxation time which when put to zero gives rise to our equilibrium solution. The results of the equilibrium theory are in excellent agreement with the experiments of Maini & Sarma [1994] when the mobility is chosen for a constant permeability and a viscosity given by Thomas' [1965] celebrated expression for the viscosity of a dispersion of solid spheres.

The theory given here is in the spirit of applied mathematical modeling and though it depends strongly on empirical data through and only through our solubility constant β, it is without fitting parameters.

More work can and should be done with this theory, but the results given here go far toward establishing that a simple theory, based on the dispersed gas fraction, avoiding complicated modeling of nucleation, bubble growth, transition to free gas and complicated transfer functions, can capture many of the essential features of foamy oil flow.

12 Appendix

In this appendix we carry out an analysis of equations (4.10) for type; we show that under the usual conditions the system is hyperbolic with x, t plane tesselated by nonintersecting characteristic lines.

Putting the gravity related term to zero (4.10) can be written as

$$\tau\alpha\frac{\partial p}{\partial t} - \lambda\tau\left(\frac{\partial p}{\partial x}\right)^2 - \tilde{p} + p + \frac{\beta p\phi}{1-\phi} = 0 \qquad (12.1)$$

$$\alpha\frac{\partial \phi}{\partial t} - \lambda\frac{\partial p}{\partial x}\frac{\partial \phi}{\partial x} + (1-\phi)\lambda'\frac{\partial \phi}{\partial x}\frac{\partial p}{\partial x} + \lambda(1-\phi)\frac{\partial^2 p}{\partial x^2} = 0 \qquad (12.2)$$

where $\lambda' = d\lambda/d\phi$. To analyze this system we use the method of simple jumps. To put the system into canonical form we need to form a quasilinear system in which the highest derivatives are linear and (12.1) is not quasilinear. We can get a quasilinear system by differentiating (12.1) with respect to x, writing

$$p' \stackrel{\text{def}}{=} \frac{\partial p}{\partial x}$$

Then

$$\tau\alpha\frac{\partial p'}{\partial t} - 2\lambda\tau p'\frac{\partial p'}{\partial x} + \frac{\beta p}{(1-\phi)^2}\frac{\partial \phi}{\partial x} - \lambda'\tau(p')^2\frac{\partial \phi}{\partial x} + p' + \frac{\beta p'\phi}{1-\phi} = 0 \qquad (12.3)$$

$$\lambda(1-\phi)\frac{\partial p'}{\partial x} + \alpha\frac{\partial \phi}{\partial t} + \left[\lambda'(1-\phi)p' - \lambda p'\right]\frac{\partial \phi}{\partial x} = 0 \qquad (12.4)$$

Now we look for solutions which allow for simple jumps of the derivatives of p, p' and ϕ assuming that p, p' and ϕ are continuous. These (characteristic) lines are designated as

$$\psi(x,t) = \text{const} \qquad (12.5)$$

and we seek the explicit form of the function ψ.

Now define a notation for a simple jump across the line $\psi(x,t) = \text{const}$

$$[\![\circ]\!] = (\circ)_1 - (\circ)_2$$

The jump equations corresponding to (12.3) and (12.4) are

$$\tau\alpha\left[\left[\frac{\partial p'}{\partial t}\right]\right] - 2\lambda\tau p'\left[\left[\frac{\partial p'}{\partial x}\right]\right] + \left(\frac{\beta p}{(1-\phi)^2} - \lambda'\tau(p')^2\right)\left[\left[\frac{\partial \phi}{\partial x}\right]\right] = 0 \quad (12.6)$$

$$\lambda(1-\phi)\left[\left[\frac{\partial p'}{\partial x}\right]\right] + \alpha\left[\left[\frac{\partial \phi}{\partial t}\right]\right] + \left(\lambda'(1-\phi)p' - \lambda p'\right)\frac{\partial \phi}{\partial x} = 0 \quad (12.7)$$

The derivatives are discontinuous across but not along characteristic lines. Hence

$$(\tau\alpha\psi_t - 2\lambda\tau p'\psi_x)[\![p'_\psi]\!] + \left(\frac{\beta\phi}{(1-\phi)^2} - \lambda'\tau(p')^2\right)\psi_x[\![\phi_\psi]\!] = 0 \quad (12.8)$$

$$\lambda(1-\phi)\psi_x[\![p'_\psi]\!] + \left\{\alpha\psi_t + \left(\lambda'(1-\phi)p' - \lambda p'\right)\psi_x\right\}[\![\phi_\psi]\!] = 0 \quad (12.9)$$

Equations (12.8) and (12.9) may be solved for the jumps if and only if

$$\left(\alpha\psi_t + \left\{\lambda'(1-\phi)p' - \lambda p'\right\}\psi_x\right)\left(\tau\alpha\psi_t - 2\lambda\tau p'\psi_x\right) - \lambda(1-\phi)\psi_x^2\left\{\frac{\beta\phi}{(1-\phi)^2} - \lambda'\tau(p')^2\right\} = 0 \quad (12.10)$$

On the line $\psi = \text{const}$

$$d\psi = \psi_x\,dx + \psi_t\,dt = 0$$

Hence

$$-\psi_t/\psi_x = \frac{dx}{dt} \equiv \mathring{x} \quad (12.11)$$

After inserting (12.11) into (12.10) and some algebraic rearrangements, we find that

$$\alpha\mathring{x} + \frac{p'}{2}\left[3\lambda - \lambda'(1-\phi)\right] = \pm\left\{\frac{\lambda\beta\phi}{\tau(1-\phi)} + \left(\lambda^2 + (\lambda')^2(1-\phi)^2\right)\frac{(p')^2}{4} - \frac{1}{2}\lambda\lambda'(1-\phi)(p')^2\right\}^{1/2} \quad (12.12)$$

If the quantity under the square root is positive, there are two roots for $\mathring{x}$ which define the characteristics. If the mobility is independent of ϕ

$$\lambda' = 0$$

then there are always two roots and the original system is strictly hyperbolic.

The analysis just given does mean that discontinuities in p and ϕ are not allowed as we saw already in the linearized analysis leading to the telegraph equation. The underlying system is not quasilinear and the existence of shock waves in the solution set is an open question.

$$\left(-\alpha\mathring{x} + \lambda'(1-\phi)p' - \lambda p'\right)\left(-\tau\alpha\mathring{x} - 2\lambda\tau p'\right) - \lambda(1-\phi)\left\{\frac{\beta\phi}{(1-\phi)^2} - \lambda'\tau p'^{\,2}\right\} = 0 \quad (12.13)$$

$$\alpha^2\mathring{\mathring{x}}^2 + \mathring{x}\left[2\alpha\lambda p' - \alpha\lambda'(1-\phi)p' + \alpha\lambda p'\right] - 2\lambda p'\left[\lambda'(1-\phi)p' - \lambda p'\right] - \frac{\lambda\beta\phi}{\tau(1-\phi)} + \lambda\lambda'(1-\phi)p'^{\,2} = 0 \quad (12.14)$$

$$\alpha^2\mathring{\mathring{x}}^2 + \alpha p'\mathring{x}\left[3\lambda - \lambda'(1-\phi)\right] - \lambda\lambda' p'^{\,2}(1-\phi) + 2\lambda^2 p'^{\,2} - \frac{\lambda\beta\phi}{\tau(1-\phi)} = 0 \quad (12.15)$$

$$\left\{\alpha\mathring{x} + \frac{p'}{2}\left[3\lambda - \lambda'(1-\phi)\right]\right\}^2 - \frac{p'^{\,2}}{4}\left[3\lambda - \lambda'(1-\phi)\right]^2 - \lambda\lambda' p'^{\,2}(1-\phi) + 2\lambda^2 p'^{\,2} - \frac{\lambda\beta\phi}{\tau(1-\phi)} = 0 \quad (12.16)$$

$$\left\{\alpha\mathring{x} + \frac{p'}{2}\left[3\lambda - \lambda'(1-\phi)\right]\right\}^2 - \frac{\lambda^2 p'^{\,2}}{4} - \frac{p'^{\,2}\lambda'^{\,2}}{4} (1-\phi)^2 + \frac{1}{2}\lambda\lambda'(1-\phi)p'^{\,2}\frac{\lambda\beta\phi}{\tau(1-\phi)} = 0 \quad (12.17)$$

Acknowledgement. The work of D.D. Joseph was supported in part by the DOE, Department of Basic Energy Sciences, the NSF under Grant Opportunities for Academic Liasons with Industry and the Minnesota Supercomputer Institute. We wish to thank Prof. G.I. Barenblatt for bringing Leibenson [1941] to our attention and for helpful discussion.

References

1. Carlslaw and Jaeger 1969 *Operational Methods in Applied Mathematics,* Oxford University Press (2nd ed).

2. Claridge, E.L. and Prats, M. June 19-21, 1995 "A Proposed Model and Mechanism for Anomalous Foamy Heavy Oil Behavior," paper SPE 29243 presented at the International Heavy Oil Symposium, Calgary, AB *Proc.*, 9-20; also the unsolicited manuscript of SPE (USMS) 29243, 1994.

3. Firoozabadi, A., Ottesen, B., & Mikkelsen, M. December 1992 "Measurement of Supersaturation and Critical Gas Saturation", SPE Formation Evaluation, 337–344.

4. Huerta, M., Otero, C., Rico, A., Jiménez, I., De Mirabal, M. & Rojas, G. October 6-9, 1996 "Understanding Foamy Oil Mechanisms for Heavy Oil Reservoirs during Primary Production", paper SPE 36749, presented at the 1996 SPE Annual Technical Conference and Exhibition, Denver, Colorado, 671–685.

5. Joseph, D.D. 1990 Fluid dynamics of viscoelastic liquids, Springer-Verlag. *Appl. Math Sciences*, **84.**

6. Kataoka, T., Kitano, T., Sasahara, M., & Nishijima, K. 1978 "Viscosity of particle filled polymer melts," *Rheol. Acta* **17**, 149– 155.

7. Kraus, W.P., McCaffrey, W.J., & Boyd, G.W. 1993 "Pseudo-Bubble Point Model for Foamy Oils," paper CIM 93-94 presented at the 44th Annual Technical Conference of the Petroleum Society of CIM, Calgary, AB, May 9-12.

8. Lebel, J.P. March 2, 1994 "Performance implications of various reservoir access geometrics", Paper presented at the 11^{th} *Annual Heavy Oil & Oil Sands Tech. Symp..*

9. Leibenson, L.S., 1941 The motion of gas-saturated fluid in a porous media. Bulletin, USSR Acad. Science, ser. giography & geophysics, No. 3.

10. Maini, B.B., June 1996 "Foamy Oil Flow in Heavy Oil Production," *JCPT* 35, No. 6, 21-24.

11. Maini B.B. & Sarma, H. 1994 "Role of Nonpolar Foams in Production of Heavy Oils," in: "Advances in Chemistry Series" **242**: 405–420.

12. Metzner, A.B. 1985 "Rheology of suspensinos in polymeric liquids," *J. Rheol.* **29**, 739–735.

13. de Mirabal, M., Gordillo, R., Fuenmayor, M., Rojas, G., Rodriguez H. & Sanchez, R. April 23–26, 1996 "Integrated Study for the Characterization and Development of the MFB-53 Reservoir, North Hamaca-Orinoco Belt, Venezuela", paper SPE 36095, presented at the Fourth Latin American & Caribbean Petroleum Engineering Conference, Port-of-Spain, Trinidad & Tobago.

14. Peng, D.Y., Fu, C.T., Bird, G.W. & Hsi, C. August, 4-9, 1991 "Effect of Gas components on thermodynamic properties of Alberta Heavy Crudes and Bitumens," in: 5th Unitar Heavy Crude & Tar Sands International Conference, Caracas, Venezuela, Proc. 1: 47-55.

15. Poletto M. & Joseph, D.D. March/April 1995 Effective density and viscosity of a suspension, it J. Rheol. **39(2)**, 323-343.

16. Pooladi-Darvish M. & Firoozabadi, A. June 11, 1997 "Solution gas drive in heavy oil reservoirs", paper no. 97-113, presented at the 48th Annual Technical meeting of the Petroleum Society of CIM in Calgary, Canada.

17. Sheng, J.J., Hayes, R.E., Maini A.B. & Tortike, W.S. 1996 A dynamic model to simulate foamy oil flow in porous media, SPE 36750.

18. Sheng, J.J., Maini, B.B., Hayes R.E. & Tortike, W.S. May 1999a "Critical Review of foamy Oil Flow", *Transport in Porous Media,* **35,2**, 157-187.

19. Sheng, J.J., Hayes, R.E., Maini, B.B. & Tortike, W.S. May 1999b "Modeling Foamy Oil Flow in Porous Media", *Transport in Porous Media,* **35,2**, 227-258.

20. Svrcek, W.Y. & Mehrotra, A.K. 1982 Gas solubility, viscosity and density measurements for Athabasca bitumen, *J. Canadian Petroleum Technology*, **21**,(4) 31–38.

APPENDIX A

Short text of the Tenth Amendment to Annex IV of the Implementing Agreement Between the Department of Energy of the United States of America and the Ministry of Energy and Mines of the Republic of Venezuela iii the Area of Enhanced Oil Recovery Thermal Processes signed by the Project Managers on September 30, 1996.

Tenth Amendment and Extension to Annex IV

Agreement Between Jesue Boulivar (INTEVEP) and Thomas B. Reid (DOE)
Tasks to be Performed under Annex IV
October 1, 1996 – September 8, 1998

Task 68 - DOE shall provide INTEVEP with results from the SUPRI research on heavy oil. This includes flow properties, in-situ combustion, foam flow in porous media, and reservoir evaluation methods. In situ upgrading through thermal methods will be part of Task 68.

Task 69 - INTEVEP shall provide DOE with information on Geomechanical Modeling of unconsolidated formations. This includes studies on borehole stability in vertical and horizontal wells.

Task 70 - DOE shall provide INTEVEP with information on the results of NIPER's thermal light oil program. This work deals with tracking DOE's Light Oil Steamflood at Naval Petroleum Reserve No. 3, Teapot Dome Field, Wyoming and laboratory research on light oil steamflooding, including in situ upgrading of the crude. research is directed toward improving the understanding of the basic mechanisms responsible for enhanced light oil production using thermal methods and accelerating development and expansion of the resource base that is recoverable using this technology.

Task 71 – INTEVEP shall provide DOE with information on simulation and field results of heavy oil recovery by steam circulation in horizontal wells.

Task 72 - DOE shall provide INTEVEP with information on resistivity imaging from cross-borehole and surface-to-hole electromagnetic induction using research conducted by Lawrence Livermore National Laboratory. The research will include reservoir characterization and front tracking in steam and waterflooded petroleum reservoirs using crosshole tomography. In addition, research will be conducted on application of the technology in steel cased wells. A final task involves a summary of research on the application of electrical and electromagnetic heating for heavy oil recovery.

Task 73 INTEVEP shall provide DOE with information on production mechanisms associated to heavy and extra-heavy oil in unconsolidated formations. Simulations and laboratory results will be included.

Thomas B. Reid — Sept 30, 1996 (Date)

Jesus Bolivar — SEPT. 30, 1996 (Date)

APPENDIX B

Full text of tile Agreement For Energy Cooperation Between the Department of Energy of the United States of America and the Ministry of Energy arid Mines of the Republic of Venezuela, signed October 13, 1997.

AGREEMENT

FOR ENERGY COOPERATION

BETWEEN THE DEPARTMENT OF ENERGY OF

THE UNITED STATES OF AMERICA

AND

THE MINISTRY OF ENERGY AND MINES OF

THE REPUBLIC OF VENEZUELA

The Department of Energy of the United States of America (DOE) and the Ministry of Energy and Mmes of the Republic of Venezuela (MEM), hereinafter "the Parties":

CONSIDERING

The interest of the Parties in strengthening the bilateral cooperation for the development, application and sustainable use of conventional energy (especially fossil fuels), energy efficiency, and renewable energy;

The importance that the Parties, assign to the exchange of information, experiences, and points of view regarding the development and analysis of energy systems, the design and implementation of energy regulatory regimes, the dissemination of ,energy technology information, and the design, development and improvement of energy information systems;

The Parties desire to promote regional energy cooperation through information exchange, analysis and forecasting, and cooperative activities within the framework of hemispheric energy cooperation and integration

The importance the Parties assign to the contribution by conventional energy (especially fossil fuels), energy efficiency and renewable energy to increase the energy diversity and security of supply, to promoting sustainable development and opportunities for economic interaction, as well as to. the contribution of technology to the rational and ecologically acceptable development of all phases of energy activity, including evaluation of resources and energy production, transportation, processing distribution and end use;

The Agreement between the Government of the United States of America and the Government of the Republic of Venezuela for Scientific and Technological Cooperation signed October 13, 1997;

The Agreement between the Parties for Cooperation in the Field of Energy Research and Development signed March 6, 1980, and extended September 8, 1993 for a term of five years (hereinafter the Energy R&D Agreement), and the Parties interest in continuing certain Implementing Agreements under the Energy R&D Agreement (hereinafter referred to as "Project (Annexes") and undertaking new cooperative activities in the field of energy research and development.

Have agreed as follows: .

ARTICLE I
SCOPE AND OBJECTIVES

1. The purpose of this Agreement is to establish a framework for cooperation between the Parties in activities of mutual interest to promote the rational development and rise, of conventional energy (especially fossil fuels), energy efficiency and renewable energy, and such other topics as the Parties may agree.

2. Cooperative activities under this Agreement will be conducted on the basis of equality, reciprocity, and mutual benefit to the "Parties".

ARTICLE II
FORMS OF COOPERATION

Cooperation between the Parties under this Agreement may include, but need not be limited to the following activities:

A Exchange of information, analyses and forecasts pertaining to the Parties' energy sectors, including short-, medium-, and, long-term forecasts;

B. Development of joint studies and projects to facilitate energy planning, the formulation of policies related to energy production and end-use, the establishment of regulatory systems, and the promotion of trade and investment opportunities that foster greater productivity, sustainable, and reliability of energy supply and energy markets.

C. Design of training activities and educational materials for strengthening institutional capacities and promoting the cleaner and more rational use of conventional energy (especially fossil fuels), energy efficiency, and renewable energy;

D. Exchange of scientific and technical information, and results and methods of research and development on a periodic basis in a manner agreed to by the Joint Steering Committee established by Article 3 (D):

E. Organization of seminars and other meetings on agreed energy topics;

F. Survey visits by specialists to the agencies and facilities of the Parties;

G. Cooperation on the evaluation and development of renewable energy resources and on integrated planning of energy resources;

H. Conduct of program for the exchange and training of personnel from the Parties' energy sectors;

I. Exchange of information and collaboration to identify sources of Financial support for the development of studies, energy analyses and conduct of projects specifically intended to promote the rational and ecologically acceptable use of conventional energy (especially fossil fuels), energy efficiency and renewable energy;

J. Assistance in the purchase or loan of equipment needed to carry out specific activities undertaken under this Agreement;

K. Joint projects including experiments, test, design, analysis and other collaborative technical activities;

L. Exchange of materials, instruments, components, and equipment for testing and;

M. Such other activities as the Parties may agree in writing.

ARTICLE III
MANAGEMENT

A. The Secretary of Energy and of the United States of America and the Minister of Energy and Mines of the Republic of Venezuela each will designate senior Principal Coordinators, representing their respective countries, to coordinate activities under this Agreement. The Principle Coordinators will jointly plan and coordinate cooperative activities and report annually to the Minister and the Secretary, respectively. The Principal Coordinator may establish Joint Committees to assist them in the activities under this Agreement.

B. The Minister and the Secretary will review progress of the work under this Agreement when they meet. The Principal Coordinators, or the joint committees, will appoint Project Managers for each Project Annex established under Article 4.

C. The Principal Coordinators will meet annually, or as otherwise mutually agreed, alternatively in Venezuela and the United States. The Principal Coordinators may invite representatives of other organizations within their countries to attend the meetings and serve as advisers to assist in the planning and conduct of cooperative activities undertaken under this Agreement.

D. The Joint Steering Committee (JSC) established under the Energy R&D Agreement will continue supervising the implementation of the ongoing Annexes I, IV, X, XIV, XV, XVI and XVII under the Energy R&D Agreement and other new cooperative energy research and development activities.

ARTICLE IV
PROJECT ANNEXES

1. When the Parties agree to undertake a cooperative activity or an activity which may give rise to intellectual property, the Parties will execute a Project Annex. Each will include provisions for carrying out the activity as well as appropriate provisions pertaining to technical scope, intellectual property as defined in Annex A of this Agreement, management, total costs, cost sharing, schedule and other issues as appropriate.

2. The following Project Annexes which were entered into pursuant to the Energy R&D Agreement shall continue in effect until work undertaken is completed subject to the term and conditions of this Agreement or until this Agreement expires or is terminated in accordance with Article 12.

A. Project Annex I, Joint Characterization of Heavy Crude.

B. Project Annex IV, Enhanced oil Recovery Thermal Process.

C. Project Annex X, On-Site Training of Petroleum Engineers.

D. Project Annex XIV, Exchange of Energy Related Personnel.

E. Project Annex XV, Oil Recovery Information and Technology Transfer.

F. Project Annex XVI, Oil And Petrochemical Ecology and Environmental Research.

G. Project Annex XVII, Drilling Technology.

ARTICLE V
ASSIGNMENT OR EXCHANGE OF PERSONNEL

The following provisions shall apply concerning assignment or exchange of personnel under this Agreement:

A. Each Party will make best efforts to ensure that personnel to be assigned to or exchanged with the other Party. have the necessary qualifications skills and competence to perform the activities planned under this Agreement.

B . Each assignment or exchange of personnel will be agreed in writing.

C. Each Party will be responsible for the salaries, insurance, travel expenses, and allowances to be paid to its personnel.

D. Each Party will provide assistance to the personnel from the other Party (including accompanying relatives when appropriate) in matters such as lodging and administrative formalities related to the trips on mutually acceptable and reciprocal basis.

E. The personnel from each Party who are visiting the other Party will conduct themselves as agreed to in the specific assignment or exchange agreement.

ARTICLE VI
EXCHANGES OF EQUIPMENT

The following provisions shall apply concerning exchanges of equipment pursuant to this Agreement:

A. By mutual agreement, a Part may provide equipment to be utilized in a joint activity. In such case, the sending Party shall supply, as soon as possible, a detailed list of the equipment to be provided together with the relevant specifications and appropriate technical informational documentation related to the use, maintenance, and repair of the equipment.

B. Title to the equipment and necessary spare parts supplied by the sending Party for use in joint activities shall remain in the sending Party, and the property shall be returned to the sending Party upon completion of the joint activity, unless otherwise agreed in writing.

C. Equipment provided pursuant to this Agreement shall be brought into operation at the host established only by mutual agreement between the Parties.

D. The host establishment shall provide the necessary premises, shall provide for utilities such as electric power, water and gas, and normally shall provide materials to be tested, in accordance with the agreed technical requirements.

E.. The responsibility and expenses for the transport of the equipment and materials from the United States by plane or ship to an authorized port of entry in Venezuela convenient to the ultimate destination, and also the responsibility for its safekeeping and insurance en route shall rest with DOE.

F. The responsibility and expenses for the transport of the equipment and materials from Venezuela by plane or ship to an authorized port of entry in the United States convenient to the ultimate destination, and also the responsibility for its safekeeping and insurance en route shall rest with MEM

G. Equipment provided pursuant to this Agreement for use in joint activities shall be considered to be scientific, not having commercial character, and each Party shall make its best effort to obtain duty free entry

ARTICLE VII
EXCHANGES OF INFORMATION

The following provisions shall apply concerning exchanges of information pursuant to this Agreement: .

A. Each Party will, according to its legal authority, make available to the other the information which is relevant for complying with the activities in the Agreement and which can be made available in terms of the laws and regulations of each country as long as this information is reasonably accurate and is adequately documented. The Parties will not exchange business-confidential information of any nature unless agreed upon in writing. Information can be designated as business-confidential if the person or institution having the information may derive economic benefit or may obtain a competitive advantage over those who do not have it, the information is not generally known or publicly available from other sources, and the owner has not previously made the information available without imposing in a timely manner an obligation to keep it confidential. The Parties agree that exchange information which is not business-confidential as defined in this Article can be broadly disseminated.

B. The use and application of any information supplied, exchange, or developed by the Parties will be the responsibility of the receiving Party. The issuing Party does not guarantee, that the information is suitable for any purpose.

C. In the eventuality that any information which is generated, exchanged, or submitted under this Agreement is identified in a timely manner as business-confidential information, each Party and its participants will protect such information in view of the pertinent administrative laws, regulations, authorities and practices.

E. No provision in this Agreement can obligate the Parties to allow access to information that is restricted for any reason, or when one Party considers it essential for national security, the safeguard of national resources or the competitiveness for public or private companies, research centers, or laboratories.

F.

ARTICLE VIII
INTELLECTUAL PROPERTY

The provisions for the protection and transfer of intellectual property are established in Annex A to this Agreement, "Intellectual Property," which constitutes an integral part of this Agreement and is applicable to all cooperative activities performed under the Agreement.

ARTICLE IX
SECURITY OBLIGATIONS

The Parties agree that no information or equipment requiring protection in the interests of national defense or foreign relations of either Party and classified in accordance with the applicable national laws and regulations shall be provided under this Agreement, In the event that information or equipment which is known or believed to require such protection is' identified in the course of cooperative activities undertaken under this Agreement; it will be brought promptly to the attention of the appropriate. officials and the Parties will consult concerning the need for, and level of appropriate protection to be accorded such information or equipment

ARTICLE X
GENERAL PROVISIONS

A. Unless otherwise agreed by the Parties in writing, all expenses resulting from cooperative activities under this Agreement will be paid by the Party that incurs them,

B. Each Party will conduct the activities provided for in this Agreement subject to its respective laws and regulations and will provide financial resources subject to the availability of appropriated funds and personnel.

C. This Agreement shall, as of the date of , signature, supersede the Energy R&D Agreement, provided however that the Annexes (I, IV, X, XIV, XV, XVI and XVII) initiated under the Agreement are continued in effect and shall be subject to, and form an integral part of this Agreement.

ARTICLE X1
SOLUTION OF DISPUTES

All questions related to the interpretation of this Agreement will be solved by agreement of the Parties.

ARTICLE XII
ENTRY INTO FORCE, DURATION, MODIFICATION, AND TERMINATION

A This Agreement will enter into force upon signature and will remain in force for five (5) years unless it is modified or terminated pursuant to the terms established in this Agreement. Unless one of the Parties notifies the other Party in writing of its intention to terminate this Agreement at least six months before its expiration this Agreement will be automatically extended for an additional five-year Period.

B. This Agreement may be modified or extended by written. agreement of the Parties.

C. Either of the Parties may terminated this want upon ninety (90) days written notice to the other Party. The termination of thus Agreement will not affect the completion of' activities initiated but not completed during its term.

Done at the City of Caracas on the 13th day of the month of October, nineteen ninety-seven, in two versions in English and Spanish, both texts being equally authentic

BY THE DEPARTMENT OF ENERGY OF THE UNITED STATES OF AMERICA

Federico F. Pena
Secretary of Energy

BY THE MINISTRY OF ENERGY AND MINES OF THE REPUBLIC OF VENEZUELA

Erwin Jose' Arrieta Valera
Minister of Energy and Mmes

ANNEX A
INTELLECTUAL PROPERTY

A. The Parties shall ensure adequate and effective protection of intellectual property created or. furnished under this Agreement and relevant Project Annexes. The Parties agree to notify one another in a timely fashion of any inventions or copyrighted works arising under this Agreement and to seek protection for such intellectual property in a timely fashion. Rights to such intellectual property. shall be allocated as provided in this Annex. .

B. Scope

1. This Annex is applicable to all, cooperative activities undertaken pursuant to this Agreement, except as otherwise specifically agreed by the Parties or their designees.

2. For purposes of this Agreement, "intellectual property" shall have. the meaning found in Article 2 of the Convention Establishing the World Intellectual Property Organization, done at Stockholm, July 14, 1967.

3. This Annex addresses the allocation of rights and interests between the Parties. Each Party shall ensure that the other Party can obtain the rights to intellectual property allocated in accordance with this Annex, by obtaining those rights from its own participants through contracts or other legal means, if necessary. This Annex does not otherwise alter a prejudice the allocation between a Party and its nationals, which shall be determined by that Party's laws and practices.

4. Disputes concerning intellectual property arising under this Agreement should be resolved through discussions between the concerned participating institutions, or; if necessary, the Parties or their designees.. Upon mutual agreement of the Parties, a dispute shall be submitted to an arbitral tribunal for binding arbitration in accordance with the applicable rules of international law. Unless the Parties or their designees agree otherwise is writing the arbitration rules of the Untied Nations Commission on International Trade Law (UNCITRAL) shall govern. .

5. Termination or expiration of this Agreement shall not affect rights or obligations under this Annex.

6. Cooperative activities will not be entered into where the purposes of the activities is to produce inventions in the following areas, or where there is a possibility of producing inventions in the following areas, until such time as inventions in these areas are considered patentable subject matter by both Parties:

1. drinks and food products for humans and animals;
2. medicine of all kinds, and

3. pharmaceutical and chemical preparations, reactions and compounds.

C. Allocation of Rights

1. Each Party shall be entitled to a nonexclusive, irrevocable, royalty free license in all countries to translate, reproduce, and publicly distribute scientific and technical journals articles, reports and books directly arising from cooperation under this Agreement. All publicly distributed copies of a copyrighted work prepared under this provision shall indicate the names of the authors of the work unless an author explicitly declines to be names

2. Rights to all forms of intellectual property, other than those described in Paragraph C.1 above shall be allocated as follows:

   (i) Visiting researchers for example scientists visiting primarily in furtherance of their education, shall receive intellectual property rights under the policies of the host institution. In addition, each visiting researcher named as an inventor shall be entitled to national treatment with regard to awards, bonuses, benefits, or any other rewards, in accordance with the policies of the host institution.

   (ii) (a) For intellectual property created during joint research, for example, when the Parties, participating institutions, or participating personnel have agreed in advance on the scope of work; each Party shall be entitled to obtain all rights and interests in its own country. Rights and interests ins third countries will be determined in Project Annexes. If research is not designated as "joint research" in the relevant Project Annexes, rights to intellectual property arising from the research will be allocated in accordance with paragraph C.2(i) above. In addition, each person named as an inventor shall be entitled to national treatment with regard to awards, bonuses, benefits or any other rewards in accordance with the policies of the participating institutions.

   (b) Notwithstanding paragraph C.2(ii)(a) above, if a type of intellectual property is available under the laws of one party but not the other Party, the Party whose laws provide for this type of protection shall be entitled to all rights, and interests worldwide. Persons named as inventors of the property shall nonetheless be entitled to national treatment with regard to awards, bonuses, benefits, or any other rewards in accordance with the policies of the participating institutions of the Party obtaining the rights.

D. Business-confidential Information

In the event that information identified in a timely fashion as business-confidential is furnished or created under this Agreement, each Party and its participants shall protect such information in accordance with applicable laws, regulations, and administrative practices. Information may be identified as "business-confidential" if a person having the information may derive economic benefits from it or may obtain a competitive advantage over those who do not have it, the information is not

generally known or publicly available from other sources, and the owner has not previously made the information available without imposing in a timely manner an obligation to keep it confidential.